# ADVANCED RADIO FREQUENCY IDENTIFICATION DESIGN AND APPLICATIONS

Edited by **Stevan Preradović**

# Contents

# Preface

Radio Frequency Identification (RFID) is a modern wireless data transmission and reception technique for applications including automatic identification, asset tracking and security surveillance. As barcodes and other means of identification and asset tracking are inadequate for recent demands, RFID technology has attracted interest for applications such as logistics, supply chain management, asset tracking, and security access control. Due to the flexibility and numerous advantages of RFID systems compared to barcodes and other identification systems, RFID is now becoming crucial for mass market.

Patronization of RFID technology by major retail chains like Wall Mart, K-Mart, USA Department of Defence, and similar consortia in Europe and Asia has accelerated the progress of RFID technology significantly in the new millennium. As a result, significant advancement on RFID technology has been gained within a short period of time. This book focuses on the advances in RFID tag antenna and ASIC design, novel chipless RFID tag design, security protocol enhancements along with some novel applications of RFID.

The book is divided into two sections. The first section of the book presents the theory and design of RFID tags – physical layer. The second section of the book focuses on novel RFID applications as well as tag-to-reader communications protocol development and enhancement.

Since most RFID tags comprise of an antenna and chip (ASIC), the design of both are presented in the first section of the book. The initial chapter presents the basic the theoretical concepts of RFID and also introduces the operating range evaluation of RFID systems since reading range is an important factor when installing an RFID system. The following chapters focus on tag antenna design. The most commonly used antenna for RFID tags is the dipole antenna and a novel technique for matching the antenna impedance with the input impedance of the ASIC is presented. Following are novel antenna structures based on miniaturized fractal and Hilber-curve antennas and metamaterial based antennas. Novel fractal structures and metamaterials enable the minituarization of passive UHF tag antennas compared to those that can be found on the market. The design of novel small antennas for metal proximity use is presented with a comprehensive parametric study focusing on the design concepts of these antennas.

Following the chapters focusing on tag antenna design are chapters which present a low-power baseband processor for UHF passive tags and the interaction of electrostatic discharge and RFID which is hardly ever presented in RFID books but plays an important role in any digital circuit design. The first section of the book is finalized by a chapter focusing on a new and exciting type of RFID called Chipless RFID. Chipless RFID has the potential to replace the barcode since it has no ASIC for it. In this book, a fully printable chipless RFID tag based on multiresonators is presented, which encodes data into the spectrum therefore creating its own spectral signature.

The second section of the book focuses on new and advanced applications of radio frequency identification. The second section starts with one of the most common applications of RFID – privacy and product maintenance and tracking. In the first chapter of the second section the RFID protocols and their classification are presented. Previously presented works on security and managing hacking attacks on RFID systems are surveyed and new techniques and measures in increasing the privacy of RFID systems are presented. The following chapters focus on the use of RFID for localisation and positioning applications. Novel applications such as the use of RFID for mobile robot positioning and the detection of unexploded ordnance at military firing ranges are presented. Advances in RFID tag identification processes and protocols at the RFID reader end along with the reordering of localisation objects for RFID tag databases are presented. The second section of the book is finalized with the design and implementation of a multi-protocol UHF RFID platform which enables the designers to have an almost universal test platform before actual RFID system implementation is conducted in order to save cost.

This book is intended for readers who are already familiar with RFID and wish to gain information on novel designs and cutting edge RFID technology. This book also provides substantial theoretical and technological background and explanation of RFID for those readers who are new to the field of RFID and wish to embark into this exciting and ever expanding field.

<div align="right">

**Stevan Preradović**
Monash University,
Australia

</div>

# Part 1

# Advanced RFID Tag Design

# Operating Range Evaluation of RFID Systems

Peter. H. Cole, Zhonghao Hu and Yuexian Wang
*The University of Adelaide*
*Australia*

## 1. Introduction

Operating range is one of the most significant criteria in evaluating the performance of RFID systems, especially UHF RFID systems. That is because a longer operating range can create more potential application opportunities and ensure a more reliable performance. The operating range is determined by the whole RFID system design rather than just a part of it. Hence, it is worth doing some analysis to find out the methods for evaluating the operating range and which factors, in an overall system design, may play a key role in improving the operating range. In order to achieve this target, this chapter provides in Section 2 an RFID technology background by explaining some relevant terminologies in the antenna performance. The considerations of designing tag antennas in reality are described in Section 3. Then Section 4 and Section 5 analyse two limitations 1) threshold power in exciting a transponder, and 2) sensitivity of a reader, in achieving a successful communication between the transponder and the reader. Section 6 summarises the existing work in the literature on analysing the operating range of UHF RFID systems. The existing work is based on either theoretical analysis according to the Friis equation or totally experimental analysis in real RFID systems. The experimental analysis is a direct solution but may be expensive in cost and time. The limitations of using the Friis equation are given in Section 7. In order to overcome these limitations, Section 8 provides a novel method for evaluating the operating range of RFID systems via a scattering matrix. Lastly the key factors in designing a long operating range RFID systems are identified in Section 9.

## 2. Fundamental parameters of antennas and the friis equation

### 2.1 Power transmission in a tag

Fig. 2 shows a Thevenin equivalent circuit of an antenna in its receiving mode. $Z_{ant} = R_{ant} + jX_{ant}$ is the input impedance of the antenna in which $R_{ant}$ is composed of loss resistance $R_l$ and radiation resistance $R_r$. The receiving antenna is connected to its load $Z_c = R_c + jX_c$ by a transmission line of which the characteristic impedance is $Z_0$. $V_{in}$ is the induced voltage caused by the incident wave. In the diagram the induced voltage is represented by a peak value phasor. The source causes a current represented by a peak value phasor I to circulate in the direction shown through all elements of the circuit.

If the receiving antenna shown in Fig. 2 is a tag antenna, then the load presented to the tag antenna is a chip. In fact, the transmission line between the tag antenna and the chip is very short, hence the antenna output impedance at port $AB$ is nearly the same to the transferred impedance at port $A'B'$. Fig. 1 is thus simplified to Fig. 2, in which the symbols representing
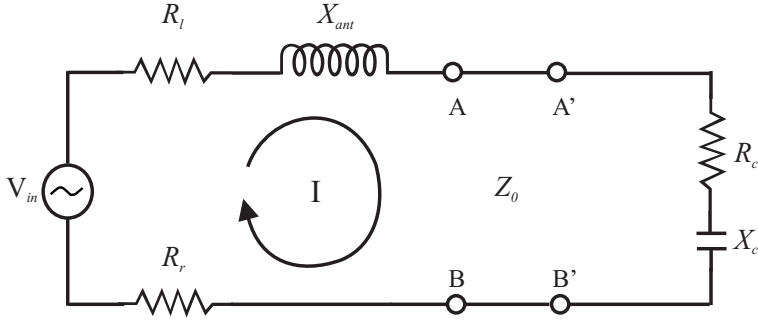
Fig. 1. Thevenin equivalent of a receiving antenna.
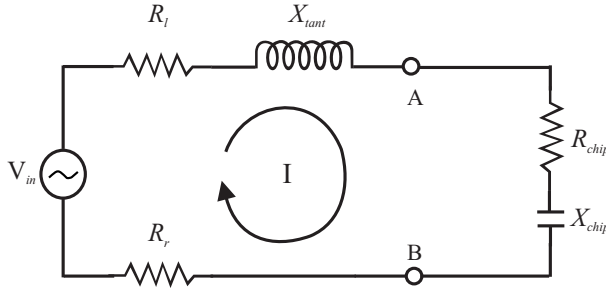


Fig. 2. Thevenin equivalent of a transponder.

the impedance elements are rewritten to keep correspondence with the situation here. $Z_{chip} = R_{chip} + X_{chip}$ is the impedance of the chip presented to the tag antenna. $Z_{tant} = R_{tant} + X_{tant}$ is the tag antenna's output impedance. $R_{tant}$ is composed of loss resistance $R_l$ and radiation resistance $R_r$.

The phasor representing the circulating current is given by

$$I = \frac{V_{in}}{R_{tant} + R_{chip} + j(X_{tant} + X_{chip})} \tag{1}$$

The power captured by the tag (chip and tag antenna) is expressed as follows

$$P_{tag} = \frac{|I|^2(R_{chip} + R_{tant})}{2} = \frac{|V_{in}|^2(R_{chip} + R_{tant})}{2(R_{tant} + R_{chip})^2 + 2(X_{tant} + X_{chip})^2} \tag{2}$$

The power delivered to the chip is given by

$$P_r^{chip} = \frac{|I|^2 R_{chip}}{2} = \frac{|V_{in}|^2 R_{chip}}{2[(R_{tant} + R_{chip})^2 + (X_{tant} + X_{chip})^2]} \tag{3}$$

The load impedance for maximum power transfer is the complex conjugate of the antenna impedance. Thus in this case

$$R_{chip} = R_{tant} \tag{4}$$

$$X_{chip} = -X_{tant} \tag{5}$$

The total power captured is then $\frac{|V_{in}|^2}{4R_{tant}}$ according to Equation 2. Half of the power is delivered to the load which is the maximum available power $P_A = \frac{|V_{in}|^2}{8R_{tant}}$. The other half is consumed by the antenna in the form of scattered power and ohmic losses. If the antenna is lossless which means that $R_l = 0$ so $R_{tant} = R_r$, the backscattered power is $\frac{|V_{in}|^2}{8R_r}$.

When the impedance is unmatched whether or not the antenna is a lossless antenna, the chip can only get part of the maximum available power, the ratio of the power $P_r^{chip}$ delivered to the unmatched load to the maximum available power $P_A$ is then

$$\frac{P_r^{chip}}{P_A} = \frac{4R_{tant}R_{chip}}{(R_{tant} + R_{chip})^2 + (X_{tant} + X_{chip})^2} \tag{6}$$

We can use the identity $|Z_{chip} + Z_{tant}|^2 - |Z_{chip} - Z_{tant}^*|^2 = 4R_{tant}R_{chip}$ to write the result above as

$$\frac{P_r^{chip}}{P_A} = \frac{|Z_{chip} + Z_{tant}|^2 - |Z_{chip} - Z_{tant}^*|^2}{|Z_{chip} + Z_{tant}|^2} = 1 - |\frac{Z_{chip} - Z_{tant}^*}{Z_{chip} + Z_{tant}}|^2 = 1 - |\theta|^2 \tag{7}$$

where $\theta = \frac{Z_{chip} - Z_{tant}^*}{Z_{chip} + Z_{tant}}$ is defined as the reflection coefficient in many publications (Karthaus and Fischer, 2003; Fuschini et al., 2008; Fuschini et al., 2007), but we notice that the expression of $\theta$ here is not analogous to a reflection coefficient as defined in most text books because of the conjugate symbol in the numerator. Hence, we would rather just call it the theta parameter. It has the property that its magnitude squared is the fraction of the available source power that is not delivered to the chip.

Using the circuit of Fig. 2 and our definition of the theta parameter, we may derive the expression for the current I.

$$I = \frac{V_{in}}{2R_{tant}}(1 - \theta) \tag{8}$$

The sum of the powers dissipated within and backscattered from the tag antenna becomes

$$P_{sum}^{tag} = \frac{|I|^2 R_{tant}}{2} = \frac{|V_{in}|^2}{8R_{tant}}|1 - \theta|^2 = P_A|1 - \theta|^2 \tag{9}$$

The backscattered power into the air becomes

$$P_{bs}^{tag} = \frac{|I|^2 R_r}{2} = \frac{|V_{in}|^2}{8R_{tant}}\frac{R_r}{R_{tant}}|1 - \theta|^2 = P_A e_r|1 - \theta|^2 \tag{10}$$

where
$P_A$ = the maximum available power of load,
$e_r = \frac{R_r}{R_{tant}}$ is known as the radiation efficiency.

## 2.2 Effective area

The power capturing characteristics of a receiving antenna can also be described in terms of effective area, which is defined as the ratio of the available power at the terminals of the receiving antenna to the power flux density of a plane wave incident on the antenna on

condition that the polarisation of the receiving antenna and the impinging wave is matched. In mathematical form, it is shown as Equation 11 (Balanis, 2005).

$$A_e = \frac{P_r}{W_i} \tag{11}$$

where
$A_e$ = effective area (m$^2$),
$P_r$ = available source power (W),
$W_i$ = power density of incident wave (W/m$^2$).

### 2.3 Effective length

The induced voltage $V_{in}$ of the receiving antenna shown in Fig. 2 can also be expressed in terms of the antenna effective length.

In order to provide clarity in the definition of the concept of effective length, we introduce as shown in Fig. 3 the definitions of input current and induced voltage for a general antenna.
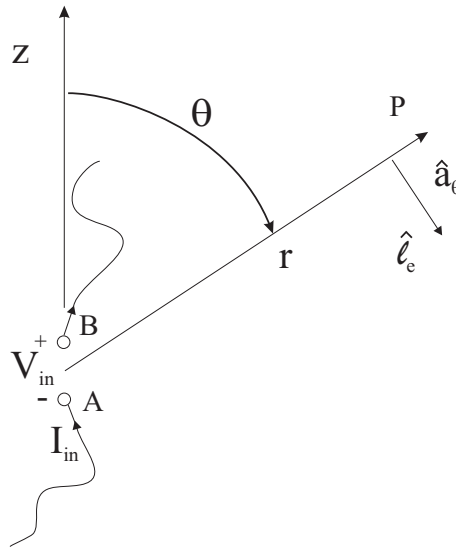
Fig. 3. Coordinate used in the definition of effective length.

The general antenna we consider is excited, when it is driven, by injecting a peak value phasor input current $I_{in}$ at two terminals A,B, shown in Fig. 3. These terminals are also used as the output terminals for the induced voltage $V_{in}$ sensed as shown in Fig. 3 when the antenna receives a signal from an incident field.

Without loss of generality, we place in Fig. 3 terminal $B$ directly above terminal $A$, and establish a spherical polar co-ordinate system with its origin at the midpoint at the interval $AB$, and the reference $z$ axis for the polar angle $\theta$ in the direction from A to B (other satisfactory co-ordinate systems could be defined, but the one being defined here has the advantage of being defined in a clear way).

It is noted that the antenna need not be a wire antenna. All that is needed is that it have terminals A,B allowing the definition of an input current and of a terminal voltage, and a

co-ordinate system for describing the far field.

We note that the far electric field will be in the direction $\hat{\mathbf{a}}_\theta$ and we will be defining an effective length vector $\mathbf{l}_e$ to be in the same direction as $\hat{\mathbf{a}}_\theta$ and to have a magnitude to be defined shortly. The value of the effective length vector $\mathbf{l}_e$ is determined by far-zone field $\mathbf{E}_a$ radiated by this antenna (Balanis, 2005).

$$\mathbf{E}_a = -j\eta \frac{kI_{in}}{4\pi r} \mathbf{l}_e e^{-jkr} \tag{12}$$

where $k$ is the free space propagation constant and $\eta$ is the characteristic impedance in free space.

For a uniform incident electric field represented by a peak value phasor $\mathbf{E}^i$, using the reciprocity theorem, the voltage $V_{in}$ induced at the terminal of a receiving antenna which is shown in Fig. 2 depends on the same effective length of the antenna as shown in Equation (13) (Balanis, 2005) below.

$$V_{in} = \mathbf{E}^i \cdot \mathbf{l}_e \tag{13}$$

## 2.4 Gain

Gain is one of the parameters that describe an antenna's radiating ability. The absolute gain of an antenna (in a given direction) is defined as the ratio of the power density of an antenna radiated to a certain far field point to the power density at the same point which would be radiated by a lossless isotropic emitter. It is expressed as

$$g = \frac{4\pi r^2 W_{rad}}{4\pi r^2 W_{rad}^i} = \frac{W_{rad}}{W_{rad}^i} \tag{14}$$

where $g$ is the gain of the subject antenna, $r$ is the distance from the antenna to a point in far-field zone, which should be lager than $2D^2/\lambda$, ($D$ is the largest dimension of the subject antenna). $W_{rad}$ is the radiation density generated at that point by the subject antenna (Balanis, 2005), $W_{rad}^i$ is the power density of the lossless isotropic emitter.

The physical meaning of gain is related to the two factors: (1) directivity $D_d$ and (2) radiation efficiency $e_r$ (Balanis, 2005). Gain can also be expressed in the other form Equation 15 by means of these two factors.

$$g = D_d \times e_r \tag{15}$$

Besides the expression of gain in terms of absolute value as introduced above, another two forms are also widely used. These are dBi and dBd. $G_{dBi}$ is the form of gain which is written in decibels (dB). In mathematical forms, it is shown

$$G_{dBi} = 10\log_{10} \frac{W_{rad}}{W_{rad}^i} = 10\log_{10} g \tag{16}$$

Clearly, the reference is still a lossless isotropic emitter. The concept of dBd is similar to dBi. The only difference is that the reference object is changed to a lossless half wavelength dipole antenna instead of a lossless isotropic antenna. Therefore, gain in dBd can be expressed as Equation 17.

$$\begin{aligned}
G_{dBd} &= 10\log_{10} \frac{W_{rad}}{W_{rad}^d} \\
&= 10\log_{10}\left(\frac{W_{rad}}{W_{rad}^i} \times \frac{W_{rad}^i}{W_{rad}^d}\right) \\
&= 10(\log_{10} g - \log_{10} g_d) \tag{17}
\end{aligned}$$

where $W_{rad}^d$ is the radiation density of the half wavelength dipole antenna and $g_d$ is the gain of the dipole which is 1.64. In terms of dBi, it is 2.15dB. Hence, Equation 17 becomes

$$G_{\text{dBd}} = G_{\text{dBi}} - 2.15\text{dB} \tag{18}$$

## 2.5 EIRP and ERP

In order to avoid the effects brought by RFID power transmitter to other radio wave devices, many countries impose regulations on the power usage. The radiated power limitation is usually expressed in terms of "EIRP" and "ERP". EIRP and ERP are the acronyms of Equivalent Isotropic Radiated Power and Effective Radiated Power respectively. The regulators do not care about how much power actually is radiated from the reader antenna, although the limitation is described in terms of power. What they really care about is the maximum power density.

The radiation power density of a reader antenna at a distance $r$ can be expressed as Equation 19.

$$W_{rad} = \frac{P_t^{rant} g^{reader}}{4\pi r^2} \tag{19}$$

where $P_t^{rant}$ is the input power to the reader antenna, and $g^{reader}$ is the gain of this antenna. The radiation density caused at the same distance $r$ by a lossless isotropic emitter with input power $P_{EIRP}$ is given in Equation 20.

$$W_{rad} = \frac{P_{EIRP}}{4\pi r^2} \tag{20}$$

The $P_{EIRP}$ that achieves for a lossless isotropic emitter at a given distance the same radiation density as the antenna of gain $g^{reader}$ and input power $P_t^{rant}$ is given by

$$P_t^{rant} = \frac{P_{EIRP}}{g^{reader}} \tag{21}$$

ERP is a similar concept to EIRP, however, the reference emitter is changed to a lossless half wavelength dipole instead of a lossless isotropic emitter. The absolute gain of a lossless half wavelength dipole is 1.64. Therefore,

$$P_t^{rant} = \frac{1.64 P_{ERP}}{g^{reader}} \tag{22}$$

The EIRP and ERP has the following relationship, derived by Equation 21 and Equation 22.

$$P_{EIRP} = 1.64 P_{ERP} \tag{23}$$

## 2.6 Polarisation

The electric field vector at a point may trace a curve as a function of time. The type of the curve can be used to classify polarisation patterns. Generally, polarisation can be classified into three types which are linear, circular or elliptical polarisation.

When the receiving and transmitting antennas are polarised in the same pattern, the receiving antenna can capture the maximum power emitted from the transmitting one. However, in general, the polarisations of these communicating antennas working in the same system are different, which causes polarisation mismatch.

Polarisation efficiency is involved to evaluate this mismatch. This factor is defined as the

ratio of the actual power received by an antenna to the possible maximum received power which can be accomplished by optimising the matching condition between the polarisation of incident wave and that of receiving antenna. In mathematics, it is expressed as Equation 24 (Balanis, 2005),

$$e_p = \frac{|\mathbf{l}_e \cdot \mathbf{E}^i|^2}{|\mathbf{l}_e|^2 |\mathbf{E}^i|^2}$$

(24)

where
$\mathbf{l}_e$ = vector effective length of the receiving antenna which has been introduced in Subsection 2.3,
$\mathbf{E}^i$ = incident electric field.
UHF RFID systems usually adopt linearly polarised antennas as tag antennas because of their low cost and easy fabrication. However, most RFID systems are used to detect mobile items, for example, in the RFID application of supply chains, the cargo on which is mounted a tag will be transported along a supply chain. If the reader antenna is linearly polarised, it is possible that the tag antenna and the reader antenna can be aligned orthogonally to each other. When that happens, the reader will not be able to read or program RFID tags. Hence, RFID reader antennas often adopt circular polarisation to ensure in most of the cases the system can perform correctly. As a result, the polarisation efficiency between a reader antenna in circular polarisation and a tag antenna in linear polarisation is 0.5 i.e. -3dB.

### 2.7 The Friis transmission equation

After introducing the fundamental parameters for describing an antenna, the Friis transmission equation commonly used in designing and analysing communication systems is given in Equation 25. This equation relates the power delivered to the load of a receiving antenna $P_r$ to the available power $P_t$ from a transmitter which is placed at a distance $r > 2D^2/\lambda$ in free space, where $D$ is the largest dimension of either antenna.

$$P_r = P_t(1 - |\Gamma_t|^2)(1 - |\Gamma_r|^2)g_t g_r (\frac{\lambda}{4\pi r})^2 e_p$$

(25)

In Equation 25, $\Gamma_t$, $\Gamma_r$ are the reflection coefficients of the transmitting antenna and the receiving antenna respectively, $g_t$ and $g_r$ are the gain of the transmitting and the receiving antenna respectively, as defined in Subsection 2.4, and $e_p$ denotes the polarisation efficiency which is explained in Subsection 2.6.
If the two antenna's impedances are perfectly matched to their source or load and their polarisation is matched as well, an ideal form of Equation 25 is expressed as follows.

$$P_r = P_t g_t g_r (\frac{\lambda}{4\pi r})^2$$

(26)

Equation 25 is an idealised form of the Friis transmission equation. When this equation is applied in analysing RFID systems, a few changes should be made according to the special needs of RFID systems, which are identified in Section 7.
In addition, the factor $(\frac{\lambda}{4\pi r})^2$ which is defined as the path gain describes the dependence of the power received by the transponder on the wavelength and the distance $r$. Normally, this factor is much less than 1, and we speak of there being a loss. However, this path loss occurs in free space. Most of RFID systems are installed in a building or even a room. Therefore, the path loss in a more complicated environment should be considered before applying it to an RFID system. The evaluation of the in-building path loss has been described in Section 7.

## 3. Tag antenna design

In Section 2, a few fundamental parameters such as gain, impedance match, polarisation etc, in designing antennas are discussed. Besides those parameters, some other parameters e.g. the antenna size, cost and deployed environment should be considered as well if the antenna is expected to be used in reality. Usually, the tag antenna design is more limited by those parameters required by the reality than the reader antenna design, hence only the tag antenna design is discussed in this section. The parameters required by the reality are discussed respectively in the three following itemisations.

- *Size*

  Generally for tag antennas the smaller the better. However, the small size will also affect other factors, such as gain, impedance match and bandwidth. Most of the commercial tags are less than 140mm×40mm.

- *Applied environment or attached objects*

  Definitely, an RFID system will not be deployed in free space. The applied environment especially when a tag is attached to a metallic object will have a critical impact on the performance of the RFID system because of the metallic boundary conditions. As a result, a solution to this problem is needed before completing an antenna design.

- *Cost*

  Generally speaking, a 96-bit EPC inlay (chip and antenna mounted on a substrate) costs from 7 to 15 U.S. cents (RFID Journal, 2010). Low cost tags are always required by the industry for a wide range of applications. One of the possible solutions to reduce the cost significantly is the use of printed electronics, especially printed silicon electronics, which is out of the scope of the work in this chapter. Cole et al. (2010) give more details of the printed electronics and its costs.

Unfortunately and not surprisingly, the factors discussed in this section and the antenna parameters discussed in Section 2 are interacting and usually are not positively related. Some tradeoffs, depending on the system requirements, should be made during the antenna design.

## 4. Threshold power of a transponder

Chips require a minimum power or voltage to be operated which are called threshold power or threshold voltage. Generally, the threshold power is about $100\mu$W (Finkenzeller, 2003) but can be even less down to $16.7\mu$W (Karthaus and Fischer, 2003). If the distance between a tag and a reader is too far for the tag to collect more power than the threshold, that tag is unable to be detected. The amount of power or voltage, which can be collected by transponders at a certain distance, depends on the tag antenna design which is briefly discussed in Section 3. Apparently, this threshold is critical to evaluate the reading range of an RFID system and it is definitely decided by the chip IC design. As shown in Figure 4, a typical transponder IC consists of several principal components which are decoder, voltage multiplier, modulator, control logic and memory unit. Each component's power consumption or power transfer efficiency can influence the threshold power. These factors are discussed in the subsections below.
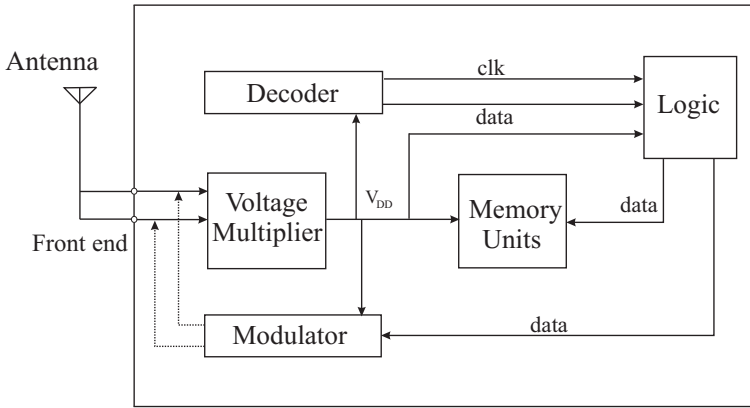
Fig. 4. Block chart of a transponder.

### 4.1 Modulator

The power transfer efficiency influenced by impedance matching situation has been analysed in Subsection 2.1. If the ideal impedance match is obtained which means the chip input impedance is the complex conjugate of the antenna impedance, half of the captured power is delivered to the chip, the other half is consumed by the antenna linked to the chip. However, in this case, the signals carrying backscattered power are all in the same phase and magnitude, and cannot carry any information. Therefore, a modulator is employed in the chip circuit to adjust the front-end impedance into two different states, $Z_{chip1}$ and $Z_{chip2}$. Hence, phase or magnitude of the backscattered wave can be changed to form a useful signal back to the base station antenna. The input RF power to the chip becomes Equation 27.

$$P_{r,1,2}^{chip} = P_A(1 - |\theta_{1,2}|^2) \tag{27}$$

where
$\theta_{1,2} = \frac{Z_{chip1,2} - Z_{tant}^*}{Z_{chip1,2} + Z_{tant}}$,
$P_A$=maximum available power.

The power reflected from the chip for backscattering also then varies between two states according to Equation 10. In terms of the modulation modes, ASK (Amplitude Shift Keying) or PSK (Phase Shift Keying) could be employed. For ASK, the amplitude difference of the backscattered wave between the two states brought by $\theta_1$, $\theta_2$ should be large enough to allow the reader to tell them apart. Similarly, for PSK, the phase difference of the backscattered wave between the two states brought by $\theta_1$, $\theta_2$ should be large enough to allow the reader to tell them apart. The difference of the two states determines the error probability.

As a result, the $\theta$ parameter is a decisive factor in designing an RFID system. It determines through Equation 27 how much RF power is distributed to the chip rectifier to be converted into dc power and through Equation 10 how much RF power is assigned to backscatter to the reader for it to decode under a particular modulation mode either ASK or PSK. The optimisation of the two states of $\theta$ depending on the modulation modes to achieve the best usage of the RF power received by the transponder is discussed by Karthaus and Fischer (2003). The selection of the two states of $\theta$ under either ASK mode or PSK mode for obtaining reading range oriented RFID system or bit-rate oriented RFID system is reported by Vita et al.

(2005). The task of optimising the factor of $\theta$ is out of the scope of the work in this chapter. Hence, it is not discussed further.

## 4.2 Rectifier efficiency

Once the RF power is received, it will be transmitted to the inside circuit, including voltage multiplier, decoder, control logic and memory units. However, the RF power cannot be used by these components directly and the induced voltage in the terminal of the tag antenna is too small to excite the circuit. As a result, a voltage multiplier is needed to rectify the ac current to dc, and to enlarge the induced ac voltage. This process definitely brings power loss due to the diode and capacitor composing of multiplier. The ratio of dc power produced by the voltage multiplier to the input RF power is called rectifier efficiency. Clearly, threshold power will be increased by a low rectifier efficiency. It was reported that rectifier efficiency ranged from 5-25% (Finkenzeller, 2003). For example, Karthaus and Fischer (2003) achieved a 18% rectifier efficiency. However, with the recent years development of semiconductor technology and circuit design, rectifier efficiency has been improved significantly. Nakamoto et al. (2007) even made the factor to be 36.6%.

## 4.3 Memory chosen

The threshold power, can be divided into two types: 1) the threshold power for reading and 2) the threshold power for programming. Those two types of threshold power are also related to the memory which is used to store data in the transponder. The data carriers, currently applied, can be categorised into the three types of RAM, EEPROM as well as FeRAM. A comparison among these memories is made below:

- *RAM*

  This kind of memory can store data only temporarily. When the voltage supply disappears, the stored data is lost. This form of memory can be used in a passive tag as a temporary information storage when the tag is being read or written. Additionally, it can also be applied in an active tag.

- *EEPROM*

  Compared to RAM, EEPROM is a long-term storage memory which can provide reliable data for around ten years (Finkenzeller, 2003). The reading operation with this memory needs a relative low supply voltage which is usually below 5V (Finkenzeller, 2003; Karthaus and Fischer, 2003). Che et al. (2008) even succeed in lowering the threshold voltage to be 0.75V. Moreover, a considerably large voltage (around 17V) is needed to activate the tunnel effect, so that data can be written. Although a charging pump is integrated into the circuit to provide this large voltage and EEPROM is used widely as an RFID tag memory, it still has two serious weakness. Firstly, the power consumption of programming is much lager than that of reading due to the large voltage needed in writing. As a result, the tag integrated with EEPROM cannot be read and written at the same range. Usually, the writing range is only about 20% of the reading range. Secondly, the programming is a time-expensive operation due to the tunneling principle (Nakamoto et al., 2007). In general, it needs 5-10ms for each single-bit or multiple-bit operation.

- *FeRAM*

  FeRAM is invented to solve the weaknesses which are faced by EEPROM. The ferroelctric effect is taken advantage of to store data and achieve a balanced power consumption in both reading and programming. In particular, Nakamoto et al. (2007) addressed this

unbalanced reading and writing barriers by employing FeRAM memory. The writing time is also improved to $0.1\mu$s (Finkenzeller, 2003; Nakamoto et al., 2007). A 4m operating distance approximately balanced in reading and writing was derived for a 4W EIRP transmitted power. The actual input power of both working modes is nearly the same which are $13\mu$W in reading and $15.7\mu$W in writing. The writing speed of FeRAM is 100 times faster than that of EEPROM. However, FeRAM has not been widely used in place of EEPROM because FeRAM cells are difficult to combine with CMOS processes, since a high temperature treatment is needed to crystallise the memory materials (PZT or SBT) into ferroelectric phases before the cell is connected to the CMOS (Finkenzeller, 2003; Lung et al., 2004).

Table 1 provides a comparison among the three memories (Finkenzeller, 2003; Fujitsu, 2006).

| Comparison parameters | RAM | EEPROM | FeRAM |
|---|---|---|---|
| Size of memory cell | $\sim$ | $\sim 130(\mu m)^2$ | $\sim 80(\mu m)^2$ |
| Lifetime in write cycles | $\infty$ | $10^5$ | $10^{10} \sim 10^{12}$ |
| Read cycle (ns) | $12 \sim 70$ | 200 | 110 |
| Write cycle | $12 \sim 70$ns | $3 \sim 10$ms | $0.1\mu$s |
| Data write | Overwrite | Erase + Write | Overwrite |
| Write voltage (V) | 3.3 | $15 \sim 20$ | $2 \sim 3.3$ |
| Energy for Writing | $\sim$ | $100\mu$J | $0.0001\mu$J |

Table 1. Comparison among RAM, EEPROM and FeRAM.

In conclusion, as long as the modulation mode, the rectifier efficiency, the dc power needed by the chip circuit and the type of memory units are known, the threshold power of transponder can be derived. In particular, Karthaus and Fischer (2003) made a tag which could be read at a distance of 4.5m under only 500mW ERP radiated power. In this case with on-wafer measurements, the rectifier efficiency was established to be 18%, the dc power consumed by the chip circuit was $2.25\mu$W ($1.5\mu$A, 1.5V). As a result, the minimum input RF power for operation is $12.5\mu$W ($\frac{2.25\mu W}{18\%}$). The threshold RF power for reading is the sum of the minimum backscattered power ($4.2\mu$W) derived by Karthaus and Fischer (2003), and the minimum input RF power ($12.5\mu$W). However, the threshold power for programming is much larger than that for reading because an EEPROM memory is chosen which choice leads to an unbalanced operating range between reading and programming. The optimisation of all factors discussed in this section is beyond our work, so they will not be discussed further in this chapter.

## 5. The reader sensitivity

Young (1994) gave the mathematical expression of a general receiver's sensitivity, and is reproduced as follows.

$$Sen = (S/N)_{min}kTB(NF) \tag{28}$$

where
$Sen$ = sensitivity,
$(S/N)_{min}$ = the minimum signal to noise ratio required to demodulate the replying signal,
$k$ = Boltzman's constant,
$B$ = bandwidth of the receiver,
$NF$ = noise factor of the receiving equipment,
$T$ = absolute reference temperature used in the definition of the noise factor.
In the case of an RFID reader the sensitivity can be influenced by several additional factors

including receiver implementation details, receiver gain, communication protocol specifics and interference generated both within the reader and externally by other users of the spectrum. A figure for sensitivity is usually available from the reader manual, and is commonly -70dBm. However, for passive tags the sensitivity is usually good enough for detecting the backscattered signal (Nikitin and Rao, July 2006), and the range is limited by tag excitation, not receiver sensitivity.

## 6. The literature review on the existing work in evaluating operating range

Significant work has been done in evaluating operating range of RFID systems recent years. Griffin et al. (2006) reported two radio link budgets based on the Friis equation. The first budget links the power received by a chip to the power radiated from a reader antenna. The second budget establishes the relationship between the power received by the reader from the backscattered power of the tag and the power radiated from the reader antenna. The contribution of Griffin et al. (2006) is to add a new factor named as gain penalty in the modified Friis transmission equation. The gain penalty shows to what extent the materials close to the tag can reduce the antenna's gain. However, Griffin et al. (2006) assumes the tag antenna's impedance is always matched to the chip. This is not an accurate assumption because 1) the requirement of the modulation needs at least one state of impedance mismatching, 2) the existence of electro-magnetically sensitive materials in close proximity to the tag will critically vary the output impedance of the tag antenna (Dobkin and Weigand, 2005; Prothro et al., 2006).

Nikitin and Rao (December 2006) introduced a new method in describing and measuring the backscattered power from the tag antenna by means of radar cross section (RCS) based on the Friis transmission equation in free space. Compared with the study by Griffin et al. (2006), the impedance mismatch occurring in the tag and caused by the modulation is considered. The RCS of a meander line dipole antenna in three different situations is investigated by assuming the antenna is placed in free space. The three situations are 1) the antenna is loaded with a chip, 2) the antenna is shorted and 3) the antenna is open circuit. The measurement of the RCS was thus conducted in an anechoic chamber after background substraction. However, when the tag is deployed in a more complicated environment than in free space, this method is not applicable.

Jiang et al. (2006) proposed another concept *response rate* in evaluating the operating range of an RFID system by experiments. Most of the exciting readers support a "poll" mode, wherein the reader continually scans for the presence of RFID tags. For example, a reader sends $N$ polls within a second, and counts the number of the responses ($N_r$) from the particularly tag being observed. Therefore, the response rate from that tag is defined as $\alpha = N_r/N$. The larger the response rate is, the more probability the tag will be read. By placing the tag in different positions each time in a complex environment, and counting the response rate of the tag, the readable probability of the tag in various positions can be derived. The optimum position could be found and this optimisation definitely involves the influence of the environment. In addition, people can even place many tags in the complex environment at one time and get the response rate of each tag by experiments. The method not only considers the effects from the environment but also the effects from the mutual coupling among the tags.

Hodges et al. (2007) optimised the position where the tag should be attached on each bottle of wine within a case containing six identical bottles based on a modified response rate test. The test is modified by setting a threshold response rate and attenuating the transmitting power from the reader programmablly to meet that threshold response rate. Then the RF margin for

the tag in each location on the wine bottle is tested and the optimum location is determined. According to the discussion above, the existing work is based on either theoretical analysis according to the Friis equation or totally experimental analysis in a real RFID system. The experimental analysis is a direct solution but may be expensive in cost or in time. In addition, the limitation of using the Friis equation is also obvious in that it cannot deal with a complex environment. More details of the Friis equation's limitation in evaluating the operating range of an RFID system are given in Section 7.

Furthermore, the simulation tools such as Ansoft HFSS or CST can accomplish a full wave analysis on the transmission between two antennas or among multiple antennas. A complex environment can be built in the simulation model and considered in the simulation process. The accomplishment of the simulation is definitely dependent on the computing ability of the equipment used. The influences of the environment on the antenna gains and input impedance can be obtained directly, hence people may argue that the Friis equation could still be used combining with the simulation results about the antenna impedance and gain which is similar to what Griffin et al. (2006) did by involving a gain penalty, but the path loss caused in the propagation cannot be obtained directly which is required by the Friis transmission equation. Hence, we totally abandon the Friis equation but turn to evaluating the reading range of an RFID system in any environment by a scattering matrix which takes all the relevant matters into account. More importantly, a scattering matrix can be obtained by both simulation and experiments. This novel method in evaluating the operating range of an RFID system is introduced in Section 8.

## 7. Interpretation and limitations of the Friis transmission equation in an RFID perspective

In Subsection 2.7, a common form of the Friis transmission equation is given in Equation 25. In addition, Equation 25 is simplified to Equation 26 in an ideal condition. In this section, the physical meaning of each factor in the Friss transmission equation and its usage is interpreted in an RFID perspective. With respect to the radio wave communication between a reader and a passive tag, it is known that the reader firstly interrogates the tag, which is named as forward-link. Then, the tag receives the power from the interrogating wave and makes use of this power to backscatter a signal to the reader, which process is named as backward-link. The Friis transmission equation may be used once in each link. We therefore discuss the use of the Friis transmission equation in the two links respectively and identify its limitations in analysing operating range of an RFID system.

### 7.1 Forward link

In the forward-link, the reader antenna is in the transmitting mode. Conversely, the tag antenna is in the receiving mode. The Friis transmission equation used in this link is written as follows according to Equation 25.

$$P_r^{chip} = P_t^{reader}(1 - |\Gamma_{rant}|^2)(1 - |\theta|^2)g^{reader}g^{tag}\frac{1}{pl}e_p \tag{29}$$

$P_t^{reader}$ represents the available source power from the reader generator, which has been designed to produce optimum power into a load of real impedance $Z_0$ and has been connected to the reader antenna by a cable of characteristic impedance $Z_0$. $P_r^{chip}$ is the power received by the chip. $\Gamma_{rant}$ is the reflection coefficient between the reader antenna and the reader which

is expressed in Equation 30a. $Z_{rant}$ is the input impedance of the reader antenna, $Z_0$ is the characteristic impedance of the transmission line connected to the reader antenna, which is usually 50Ω. $\theta$ is the parameter the magnitude squared of which describes the fraction of the available source power not delivered to the tag circuit as defined in Subsection 2.1 and rewritten in Equation 30b in which $Z_{chip}$ is the chip impedance, $Z_{tant}$ is the output impedance of the tag antenna and $Z_{tant}^*$ is conjugate to $Z_{tant}$. $g^{reader}$ and $g^{tag}$ are the gains of the reader antenna and the tag antenna respectively. The path gain factor $(\frac{\lambda}{4\pi R})^2$ in Equation 25 is changed to be $\frac{1}{pl}$, since the RFID system considered here is not assumed to be operated in free space but a more practical and complex environment.

$$\Gamma_{rant} = \frac{Z_{rant} - Z_0}{Z_{rant} + Z_0} \tag{30a}$$

$$\theta = \frac{Z_{chip} - Z_{tant}^*}{Z_{chip} + Z_{tant}} \tag{30b}$$

The expression of the power input into the reader antenna is given in Equation 31 according to Equation 21.

$$P_t^{rant} = P_t^{reader}(1 - |\Gamma_{rant}|^2) = \frac{P_{EIRP}}{g^{reader}} \tag{31}$$

where $P_{EIRP}$ is the equivalent isotropic radiated power which meaning is given in Subsection 2.5. The involvement of $P_{EIRP}$ is because the maximum power allowed to be radiated is usually described in terms of $P_{EIRP}$. According to Equation 31, Equation 29 becomes:

$$P_r^{chip} = P_{EIRP}(1 - |\theta|^2)g^{tag}\frac{1}{pl}e_p \tag{32}$$

The maximum value of $P_r^{chip}$ is obtained when $P_{EIRP}$ is set to be maximum which is regulated differently in different countries and regions. To make the tag readable, $P_r^{chip}$ has to be larger than the threshold power for operating the chip, which was discussed in Section 4.

In Equation 7, another form of $P_r^{chip}$ is given in terms of maximum available power $P_A$ and the theta parameter $\theta$, which is rewritten as follows.

$$P_r^{chip} = P_A(1 - |\theta|^2) \tag{33}$$

### 7.2 Backward link
In the backward-link, the tag antenna is in the transmitting mode. Conversely, the reader antenna is in the receiving mode. The Friis transmission equation used in this link is written as follows.

$$P_r^{reader} = P_{sum}^{tag}(1 - |\Gamma_{rant}|^2)g^{reader}g^{tag}\frac{1}{pl}e_p \tag{34}$$

where $P_r^{reader}$ is the power received by the reader and $P_{sum}^{tag}$ is the sum of the powers dissipated within and backscattered from the tag antenna. The expression of $P_{sum}^{tag}$ has been given in Equation 9 which is rewritten in Equation 35. The path loss factor remains the same as that in Equation 32, since the propagating path in the forward link is the same as in the backward link.

$$P_{sum}^{tag} = P_A|1 - \theta|^2 \tag{35}$$

Solving for $P_r^{chip}$ according to Equation 35 and Equation 33 gives:

$$P_r^{chip} = \frac{1 - |\theta|^2}{|1 - \theta|^2} P_{sum}^{tag} \tag{36}$$

Substituting Equation 36 into Equation 29, another expression of $P_{sum}^{tag}$ is derived.

$$P_{sum}^{tag} = P_t^{reader}(1 - |\Gamma_{rant}|^2)|1 - \theta|^2 g^{reader} g^{tag} \frac{1}{pl} e_p \tag{37}$$

Substituting Equation 37 into Equation 34, then

$$P_r^{reader} = P_t^{reader}[(1 - |\Gamma_{rant}|^2)|1 - \theta|g^{reader} g^{tag} \frac{1}{pl} e_p]^2 \tag{38}$$

Equation 38 establishes the relationship between the power transmitted from the reader $P_t^{reader}$ and the power received by the reader $P_r^{reader}$ after the transmitted wave is backscattered from the tag antenna. $P_r^{reader}$ has to be larger than the sensitivity of the reader which was introduced in Section 5.

According to Equation 31, $P_t^{reader}$ is replaced by $P_{EIRP}/[(1 - |\Gamma_{rant}|^2)g^{reader}]$, Equation 38 becomes:

$$P_r^{reader} = P_{EIRP}(1 - |\Gamma_{rant}|^2)g^{reader}[|1 - \theta|g^{tag} \frac{1}{pl} e_p]^2 \tag{39}$$

**7.3 Limitations in implementing the Friis transmission equation**

In Subsections 7.1 and 7.2, the power transfer between the transponder and the reader in the forward and backward link is established in Equation 29 and Equation 38 by means of the Friis transmission equation.

However, there are a few limitations in implementing the Friis transmission equations for evaluating the operating range of an RFID system, if the system is deployed in a very complex environment, e.g. 1) when a tag is mounted on a metallic item or a liquid item, or 2) when the testing environment contains a lot of metal reflectors. The reasons of the limitations are given as follows.

1. *Far field condition*

   To implement the Friis transmission equation, the two antennas in communication should be sufficiently far away from each other. The distance between them should be larger than $2D^2/\lambda$, where $D$ is the largest dimension of either antenna, and $\lambda$ is the free space wavelength at the resonant frequency. However, when an RFID system is placed in the very complex environment as mentioned before, the reader antenna has to be very close to the tag in order to read it. Hence, the distance between them is not sufficient to meet the far field criterion.

2. *Gain and impedance variation*

   In the Friis transmission equation, the gain and input/output impedance of the tag/reader antenna are involved. However, again the RFID system is placed in a very complex environment. The gain pattern and impedance will vary from the intentionally designed values. The effects brought by metals in proximity to a tag antenna to the antenna's output impedance and gain are discussed by Griffin (2006) and Dobkin (2005). It would be possible to investigate those effects by means of simulation or experiments, but that would require effort.

3. *Unknown path loss factor*

As shown in Equation 31 and Equation 38, path loss factor $\frac{1}{pl}$ is still unknown. If the RFID system is deployed in free space, $\frac{1}{pl}$ is equal to $(\frac{\lambda}{4\pi r})^2$, where $r$ is the distance between the two communicating antennas. Most RFID systems are not deployed in free space but in an in-building environment consisting of many obstacles in the signal propagating path, and the system may be composed of multiple readers and tags. Because of the obstacles in building-environment where an RFID system is deployed, there are more losses brought by path obstruction, reflection, multi-path propagation, absorption and other attenuation effects. In addition, there are also more losses brought by the interaction between the multiple readers and tags.

The analysis of path loss of a dense reader environment was given by Leong (2008). The path loss in dB of a two-antenna RFID system (one tag antenna, one reader antenna) in building is introduced (Rappaport, 2002):

$$PL(\text{dB}) = PL(d_0) + 10 \times n \times \log_{10}(\frac{d}{d_0}) \tag{40}$$

where $d_0$ is an arbitrary reference distance; $n$ is a value that depends on the surroundings and building type; $d$ is the distance between the reader antenna and the tag antenna. The reference distance $d_0$ should be selected to be much smaller than the size of the building, so that the reflection in this small distance is not significant and the path loss in this small distance $d_0$ can be considered approximately equal to the path loss in free space.

Path loss represented by Equation 40 is a rough evaluation of the general case of an RFID system in building. It does not have the universality of all situations and especially is not suitable for defining the path loss factor in complex environments, e.g. metallic items in near proximity to a tag.

Based on the limitations in implementing the Friis transmission equation in evaluating the operating range of an RFID system, a novel method by means of the scattering matrix is therefore proposed in Section 8.

## 8. The use of S-parameters in analysing the operating range of RFID systems

### 8.1 Formula derivation

We consider the two antennas (a reader antenna and a tag antenna) transmission system to be a two port system, as shown in Fig. 5, in which the reader and chip are connected to the reader antenna and the tag antenna by transmission lines of which the characteristic impedance is $Z_0$. In Fig. 5, the reader antenna is represented by the two thick lines in the dashed circle for which the input impedance, taking into account the coupling between the antennas, is $Z_{rant}$, and the tag antenna is represented by the two thin lines in the dashed circle for which the output impedance, taking into account the coupling between the antennas, is $Z_{tant}$. The resistance of the reader $R_{reader}$ is deliberately designed to be equal to $Z_0$ (50$\Omega$). In addition, the transmission line between the tag and the chip is very short.

In the following discussion, we will make use of scattering parameters to establish the relationship between the power received by the chip and the power transmitted from the reader antenna. All the values involving voltage and current are represented by peak value phasors.
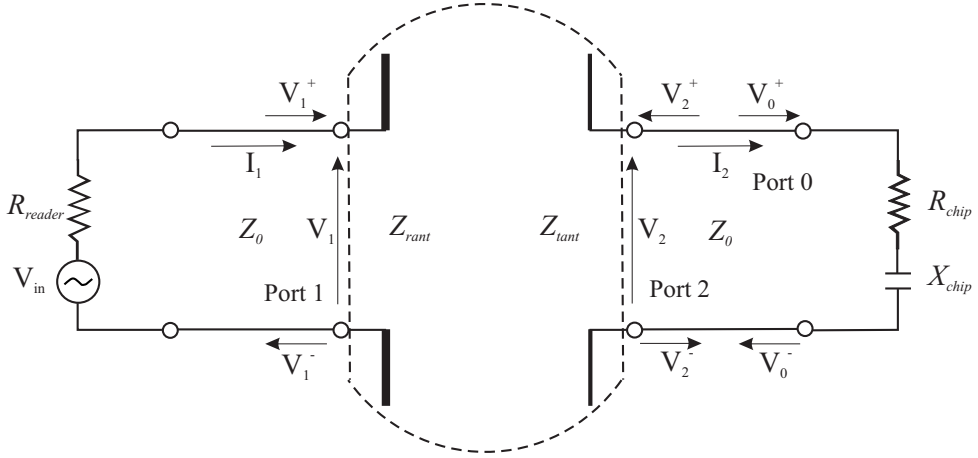
Fig. 5. Two port junction representing coupled antennas in an RFID system.

On the right side of Fig. 5, the voltage $V_0$ and current $I_0$ at the load port are expressed in Equation 41.

$$V_0 = V_0^+ + V_0^- \tag{41a}$$

$$I_0 = I_0^+ + I_0^- \tag{41b}$$

The current $I_0^+$ and $I_0^-$ can also be expressed by the voltage in and out of the load port as shown in Equation 42.

$$I_0^+ = \frac{V_0^+}{Z_0} \tag{42a}$$

$$I_0^- = -\frac{V_0^-}{Z_0} \tag{42b}$$

The ratio of $V_0^-/V_0^+$ is equal to the reflection coefficient looking into the chip impedance from the terminal of the transmission line, which is written as follows.

$$\frac{V_0^-}{V_0^+} = s_L = \frac{Z_{chip} - Z_0}{Z_{chip} + Z_0} \tag{43}$$

The power received by the chip $P_r^{chip}$ is obtained by Equation 44.

$$P_r^{chip} = \frac{|I_0|^2}{2} R_{chip} = \frac{1}{2}\left|\frac{V_0}{Z_{chip}}\right|^2 R_{chip} = \frac{|V_0^+ + V_0^-|^2 R_{chip}}{2|Z_{chip}|^2} = \frac{|V_0^+|^2 |1 + s_L|^2 R_{chip}}{2|Z_{chip}|^2} \tag{44}$$

As mentioned before, the transmission line between the chip and the tag antenna is very short (its length is nearly zero), hence, $V_0^+ = V_2^-$ and $V_0^- = V_2^+$. Then Equation 43 becomes

Equation 45. In addition, replacing $V_0^+$ in Equation 44 by $V_2^-$, Equation 46 is derived.

$$\frac{V_2^+}{V_2^-} = s_L = \frac{Z_{chip} - Z_0}{Z_{chip} + Z_0} \tag{45}$$

$$P_r^{chip} = \frac{|V_2^-|^2 |1 + s_L|^2 R_{chip}}{2|Z_{chip}|^2} \tag{46}$$

Similarly, on the left side of Fig. 5, the voltage $V_1$ and current $I_1$ on the port one is expressed in Equation 47.

$$V_1 = V_1^+ + V_1^- \tag{47a}$$

$$I_1 = I_1^+ + I_1^- \tag{47b}$$

The current $I_1^+$ and $I_1^-$ can also be expressed by the voltage in and out of the port one as shown in Equation 48.

$$I_1^+ = \frac{V_1^+}{Z_0} \tag{48a}$$

$$I_1^- = -\frac{V_1^-}{Z_0} \tag{48b}$$

The ratio of $V_1^- / V_1^+$ is equal to the reflection coefficient $\Gamma_{rant}$ which is expressed in Section 7 and rewritten as follows.

$$\frac{V_1^-}{V_1^+} = \Gamma_{rant} = \frac{Z_{rant} - Z_0}{Z_{rant} + Z_0} \tag{49}$$

The power transmitted from the reader antenna $P_t^{rant}$ is obtained by Equation 50.

$$
\begin{aligned}
P_t^{rant} &= \frac{1}{2}\text{Re}(V_1 \cdot I_1^*) = \frac{1}{2}\text{Re}[\frac{1}{Z_0}(V_1^+ + V_1^-)(V_1^+ - V_1^-)^*] \\
&= \frac{1}{2}\text{Re}[\frac{1}{Z_0}|V_1^+|^2(1 + \Gamma_{rant})(1 - \Gamma_{rant})^*] = \frac{|V_1^+|^2}{2Z_0}(1 - |\Gamma_{rant}|^2)
\end{aligned}
\tag{50}
$$

A scattering matrix can be built according to the simplified two port system shown in Fig. 5 as below.

$$\begin{bmatrix} V_1^- \\ V_2^- \end{bmatrix} = \begin{bmatrix} s_{11} & s_{12} \\ s_{21} & s_{22} \end{bmatrix} \begin{bmatrix} V_1^+ \\ V_2^+ \end{bmatrix} \tag{51}$$

According to the above matrix, the $V_1^-$ and $V_2^-$ can be written into Equation 52.

$$V_1^- = s_{11}V_1^+ + s_{12}V_2^+ \tag{52a}$$

$$V_2^- = s_{21}V_1^+ + s_{22}V_2^+ \tag{52b}$$

Substituting the first of Equation 45 and Equation 49 into Equation 52, solving for $V_1^- / V_1^+$ and $V_2^- / V_1^+$ gives

$$\frac{V_1^-}{V_1^+} = \Gamma_{rant} = s_{11} - \frac{s_{12}s_{21}s_L}{s_{22}s_L - 1} \tag{53}$$

$$\frac{V_2^-}{V_1^+} = \frac{s_{21}}{1 - s_{22}s_L} \tag{54}$$

Hence,

$$V_2^- = V_1^+ \frac{s_{21}}{1 - s_{22}s_L} \tag{55}$$

Equation 53 illustrates how the impedance mismatch in the transponder and the testing environment considered in the S parameters affect the reflection occurring between the reader and the reader antenna.

Inserting Equation 55 into Equation 46:

$$P_r^{chip} = \frac{|V_1^+|^2 |s_{21}|^2 |1 + s_L|^2 R_{chip}}{2|1 - s_{22}s_L|^2 |Z_{chip}|^2} \tag{56}$$

Equation 56 demonstrates that the power received by the chip is partially related to $|V_1^+|^2$. The value of $|V_1^+|^2$ can be defined by the combination of Equation 31 and Equation 50 as follows:

$$P_t^{rant} = \frac{|V_1^+|^2}{2Z_0}(1 - |\Gamma_{rant}|^2) = \frac{P_{EIRP}}{g^{reader}} \tag{57}$$

Then Equation 56 becomes:

$$P_r^{chip} = \frac{P_{EIRP}}{g^{reader}}|s_{21}|^2 \frac{R_{chip}Z_0}{|Z_{chip}|^2} \frac{|1 + s_L|^2}{(1 - |\Gamma_{rant}|^2)|1 - s_{22}s_L|^2} \tag{58}$$

In Equation 57, $\frac{|V_1^+|^2}{2Z_0}$ represents the available source power from the reader generator. The product of this power and $(1 - |\Gamma_{rant}|^2)$ denotes the power radiated from the reader antenna. This radiated antenna power can be expressed in terms of $P_{EIRP}$ by multiplying by the gain of the reader antenna $g^{reader}$. If $P_{EIRP}$ is set to be the maximum power specified by regulations, then Equation 57 tells us that no matter what the reflection between the reader antenna and the transmission line is, the reader antenna can always be made to radiate the same amount of power $\frac{P_{EIRP}}{g^{reader}}$ by adjusting the available source power $\frac{|V_1^+|^2}{2Z_0}$.

Finally, the power received by the chip is represented by means of scattering parameters which can be obtained by the simulation tools or experiments. The complex environment in which the RFID system is deployed can be built in the simulation model and considered in the simulation process. In terms of experiments, the environment is certainly considered. $P_{EIRP}$ is specified by the regulations in different countries and regions separately. In Australia, this factor is equal to 4W or 36dBm as introduced before. $g^{reader}$ is dependent on the reader antenna deployed. $s_L$ can be calculated by Equation 43. The reflection occurring between the reader and the reader antenna represented by $\Gamma_{rant}$ is caused by the testing environment represented by S parameters and $s_L$ as shown in Equation 53. As a result, $P_r^{chip}$ can be obtained. When $P_r^{chip}$ is less than the threshold power of the chip which is in the order of -10dBm, the reading fails and the maximum reading range can be read in the simulation model or measured directly in experiments. Here, the backward link is not considered since it is concluded (Nikitin, 2006) that the limitation of the reading range of a passive RFID systems mainly comes from the forward link not the backward link because usually the reader's sensitivity is, as mentioned before, low enough to detect the signal from the successfully excited tag.

## 8.2 Formula validation

In the last subsection, Equation 58 has been derived to calculate the power received by the chip. In this subsection, it is verified by simulation and experiments. However, as mentioned before, to implement Equation 58, the available source power of the reader generator should be adjusted according to $\Gamma_{rant}$ to keep the radiation power from the reader antenna as $P_{EIRP}/g^{reader}$. The implemented condition brings some obstacles in the experimental validation, since the available source power of most real reader generators cannot be adjusted arbitrarily. The available source power can only be set stage by stage and the gap between the adjacent stages is large (in our case the gap is 0.1W).

The approach we adopted to solve that problem is to keep the available source power unchanged as $P_{EIRP}/g^{reader}$ which is very easy to achieve by the real reader and leads to:

$$\frac{|V_1^+|^2}{2Z_0} = \frac{P_{EIRP}}{g^{reader}} \tag{59}$$

After substituting Equation 59 into Equation 56:

$$P_r^{chip} = \frac{P_{EIRP}}{g^{reader}}|s_{21}|^2 \frac{R_{chip}Z_0}{|Z_{chip}|^2} \frac{|1+s_L|^2}{|1-s_{22}s_L|^2} \tag{60}$$

Equation 60 is more convenient to be used in the form of dB, which is shown in Equation 61.

$$\begin{aligned} P_r^{chip}(\text{dBm}) \quad = \quad & P_{EIRP}(\text{dBm}) - G^{reader}(\text{dBi}) + |S_{21}|(\text{dB}) \\ & +10\log_{10}\frac{R_{chip}Z_0}{|Z_{chip}|^2} + 20\log_{10}|\frac{1+s_L}{1-s_{22}s_L}| \end{aligned} \tag{61}$$

In the following discussion, Equation 58 is verified indirectly by verifying Equation 61 by simulation and experiments. The experiments were conducted by testing the reading range of a self-made tag. The equipment used in the experiments is introduced first.

- *Self-made tag*

  The self-made tag shown in Fig. 6 is used. The chip is manufactured by Alien Technology which model is Higgs-2. The chip conforms to the EPCglobal Class 1 Gen 2 specifications. It is implemented in a CMOS process and uses EEPROM memory. The equivalent input impedance of the chip in parallel is shown in Fig. 7(a) in which the parallel resistance $R_p$ is 1500$\Omega$ and the parallel capacitance $C_p$ is 1.2pF. Usually, the input impedance of a tag antenna is presented in series. Hence, in order to simplify the analysis, the chip impedance is transformed into a series representation, so Fig. 7(a) becomes Fig. 7(b). At 923MHz which is the centre frequency of UHF RFID band in Australia, the input impedance in series is about 13.6-j142$\Omega$. Hence, $Z_{chip}$ in Equation 61 can be obtained. Typically the threshold power of this chip is -14dBm, but the threshold power is dependent on the manufacturing quality control, the worst could be -11dBm. More details of the chip can be found in the product data sheet (Alien Technology, 2008).

  The tag antenna is a meander line dipole antenna fabricated on FR4 board which thickness is 1.6mm and the dielectric constant is 4.4. The footprint of this antenna is 43.8×28.8 (unit mm). The output impedance of this antenna is designed to be approximately conjugate matched to the chip impedance.

  The chip is installed on the antenna by electrically conductive adhesive transfer tape

9703 manufactured by 3M (3M, 2007). Currents can pass perpendicularly through the sticky tape. The tape and adhesive material on it will bring losses and chip impedance changes. However, previous experiences with this tape reported by other colleagues in our laboratory indicated that these losses and impedance changes are negligible (NG, 2008).
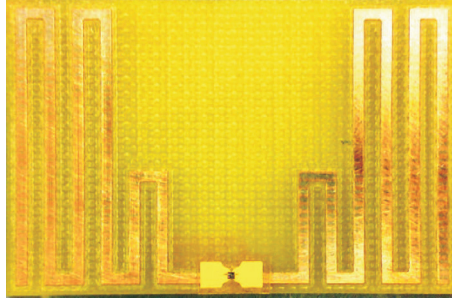


Fig. 6. A self-made tag used in experiment.



(a) In parallel                         (b) In series
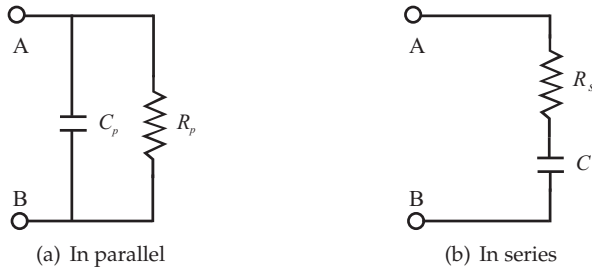
Fig. 7. The chip impedance illustration.

- *Reader*

  The RFID reader used in the experiment is manufactured by FEIG Electronics which model is ID ISC.LRU2000. The reader antenna is the linearly polarised patch antenna with 8dBi gain and manufactured by Cushcraft Corporation, model: S9028P. The reason why the linearly polarised reader antenna is used is to simplify the model building in the simulation discussed later.

- *Shielding tunnel*

  The reading range experiments were conducted by placing both the self-made tag and the reader antenna inside of a shielding tunnel. The size of the tunnel is $1826 \times 915 \times 690$ (unit mm), which is shown in Fig. 8. The shielding tunnel is surrounded by electromagnetic wave absorbing foam. The absorbing foam is manufactured by the Emerson & Cuming company for the frequency range from 600MHz to 4GHz. These absorbing foams can achieve maximum -22dB reflectivity around 1GHz. The inside space of the tunnel can thus be considered to be effectively free space.

As mentioned before, the reading range of the self-made tag were measured by placing the tag and the reader antenna in the shielding tunnel. Since the tunnel inside can be regarded as free space, it is not the complex environment as described in Subsection 7.3. In order to
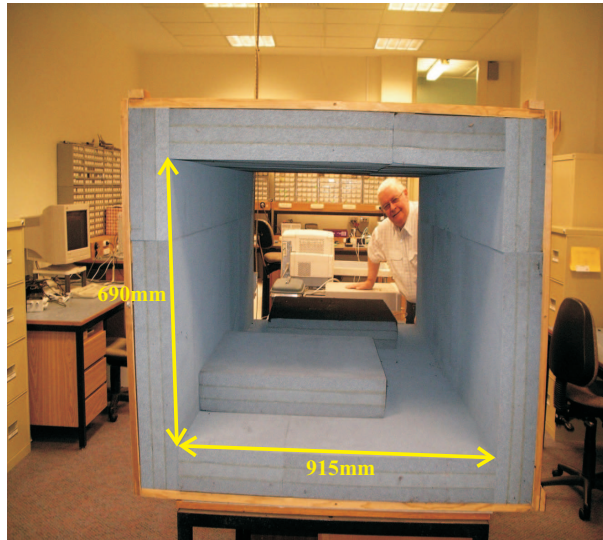
Fig. 8. A shielding tunnel.

make the environment complex, a square aluminium plate which length is 260mm is placed behind the tag. Various reading ranges of this tag were tested by varying the distance between the tag and the plate. The reading ranges are shown in Table 2. In Table 2, $d_t$ is the distance between the tag and the aluminium plate. In the experiments $d_t$ is formed by inserting one or two kinds of materials in slice between the tag and the plate. The materials are bubble wrap of which the thickness is 3mm and Teflon sheet of which the thickness is 0.97mm. It is believed that the effective permittivity of the bubble wrap is close to be 1. The relative permittivity of Teflon is usually about 2 with very low losses (Santra and Limaye, 2005; Plumb and MA, 1993). In order to minimise the effects of the Teflon, the Teflon sheet is cut into a much smaller footprint (6mm×8mm) than the tag. Given the low profile structure and small size, it is believed that the insertion of the Teflon sheet will not affect the results much either. The reading range tests were conducted by the equipment introduced before and under Australian UHF RFID regulations which frequency band is from 920MHz to 926MHz and the available source power of the reader generator is set to be 4W EIRP (36dBm). The reading range actually is the distance criterion after which the power received by the tag drops below its threshold power. In addition, the reading range of the tag in free space under the Australian regulations and tested by the equipment introduced before is about 5.2m.

| $d_t$ (mm) | 3 | 4 | 5 | 6 | 7 | 8 |
|---|---|---|---|---|---|---|
| Reading range (mm) | 230 | 350 | 470 | 890 | 1000 | 1140 |

Table 2. Reading ranges of the self-made tag in proximity to the aluminium plate by experiments.

As illustrated by Table 2, the further the tag is away from the aluminium plate, the longer the reading range that is obtained. This phenomenon is easily understood since the metal beside will degrade the performance of the tag antenna.

Then, the tag antenna, the aluminum plate behind the tag antenna and the reader antenna

were built in the simulation tool Ansoft HFSS. The two antennas' terminals are connected to two lumped ports separately. In HFSS, such ports possess implied transmission line characteristic impedances. These lines could be connected to the ports and those lines allow scattering parameters to be defined.

In terms of the characteristic impedance, it can be set in HFSS as an arbitrary complex impedance. But, in reality the characteristic impedance of the transmission line between the reader antenna and the reader is 50Ω. As for the characteristic impedance of the transmission line between the tag antenna and the chip, it can be assumed to be any value, since its length is nearly zero, its characteristic impedance does not really matter. But, in order to get the symmetrical scattering matrix, it is set to be 50Ω as well in the simulation. In terms of source, since in reality the reader antenna is active and the tag antenna is passive, the lumped ports connected to the two antennas are therefore set to be an active port and a passive port respectively. In addition, the reader antenna in the simulation is not exactly the same to the one used in the experiment, since the reader antenna used in the experiment is a commercial antenna which is enclosed, so that the inside structure cannot be seen. But it is known that this commercial antenna design is based on a patch antenna. Hence, in the simulation we designed a patch antenna as the reader antenna with geometrical and electrical parameters similar to the one in the experiments.

After building, setting and simulating the model, the S parameters are derived directly at the two lumped ports. Furthermore, we have already known that the Higgs-2 chip's impedance $Z_{chip}$ at 923MHz is about $13.6-j142\Omega$ and the characteristic impedance $Z_0$ of the transmission line is 50Ω. Hence, inserting the derived S parameters, $Z_{chip}$ and $Z_0$ into Equation 61, the power received by the chip at any relative distances among the aluminium plate, the tag and the reader antenna can be derived.

As mentioned before, as long as the communication between the reader and the tag is successful, the power received by the chip should be larger than the threshold power of the chip which is typically -14dBm. In other words, the longest reading range appears when the received power falls to -14dBm. Hence, in the simulation, the distance $d_t$ between the aluminium plate and the tag, and the distance between the tag and the reader antenna will not stop varying until the power calculated by Equation 61 reaches $-14$dBm to get the longest reading range. The results are shown in Table 3.

| $d_t$ (mm) | 3 | 4 | 5 | 6 | 7 | 8 |
|---|---|---|---|---|---|---|
| Reading range (mm) | 200 | 390 | 570 | 880 | 1040 | 1160 |

Table 3. Reading ranges of the self-made tag in proximity to the aluminium plate calculated by Equation 61 after deriving S parameters from the simulation.

In order to compare the data in Table 2 and Table 3, these results are plotted in Fig. 9. In Fig. 9, the $x$ axis represents the distance between the tag and the aluminium plate. The $y$ axis represents the reading range. The dashed curve comes from the experimental results which are given in Table 2 and the solid one comes from the calculated results by Equation 61 after deriving the S parameters from the simulation which are given in Table 3. The coincidence between the two curves validates Equation 61. It may be noticed that the differences between the two curves is relatively large when $d_t$ is less than 6mm. This is because when $d_t$ is small the reading range is very sensitive to the changes in $d_t$. In the simulation, $d_t$ is exactly as the number you give to the simulation, but in the experiments, as we mentioned before, the distance $d_t$ is formed by inserting the bubble wrap and Teflon sheet between the tag and the aluminum plate. The Teflon sheet is hard and its thickness at 0.97mm is very close to the 1mm
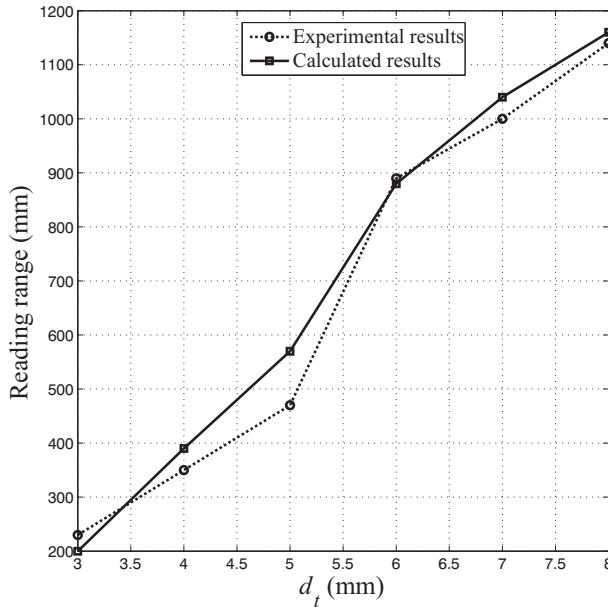
Fig. 9. Comparison between the reading range calculated by Equation 61 after deriving the S parameters from the simulation and the tested reading range.

assumed in the simulation. The thickness of the bubble wrap is about 3mm but it is soft and shape-flexible, hence the thickness may not be very accurately established. This may be the reason causing the error.

## 9. Conclusion

According to the discussion above, every aspect, e.g. the transponder IC design, the tag antenna design, the reader antenna design, and the deployed environment, in an RFID system affects the operating range of that system. Among all of them, there are a few factors which we believe play a significant role. (i) The selection of the parameter $\theta$, the magnitude squared of which establishes the fraction of the available tag antenna power that is not delivered to the tag chip is one of the keys to lengthening the operating range, since it governs how much power would be delivered to power the chip and how much will be backscattered to sense the reader. (ii) The rectifier design is critical since the enhancement of the rectifier efficiency can lower the threshold power of the chip. (iii) The environment in which the system is deployed could be an obstacle in obtaining long operating range, especially when the environment involves many electro-magnetically sensitive materials surrounding the tags or even very close to the tag. Those materials include metal and water etc.

In addition, in this chapter, a novel method for evaluating the reading range of a UHF RFID system deployed in an arbitrary environment is proposed by means of a scattering matrix. The method is verified by experiments.

## 10. References

[1] Alien Technology. Product overview of HiggsTM-2.
URL: http://www.alientechnology.com/docs/products/DS H2.pdf

[2] Balanis, C. A. (2005). *Antenna Theory*, 3rd ed., John Wiley, Hoboken, New Jersey.

[3] Che, W.; Yan, N.; Yang, Y. & Hao, M. (2008). A low voltage, low power RF/analog front-end circuit for passive UHF RFID tags. *Chinese Journal of Semiconductors*, Vol. 29, No. 3, pp. 433–437, Mar. 2008.

[4] Cole,P. H.; Turner, L.; Hu, Z. & Ranasinghe, D. (2010). The Future of RFID, In: *NUnique Radio Innovation for the 21st Century*, Ranasinghe, D.; Sheng, M. & Zeadally, S., (Ed.), Springer, 2010.

[5] De Vita, G. & Iannaccone, G. (2005). Design criteria for the RF section of UHF and microwave passive RFID transponders. *IEEE Transactions on Microwave Theory and Techniques*, Vol. 53, No. 9, pp. 2978–2990, Sept. 2005.

[6] Dobkin, D. & Weigand, S. (2005). Environmental effects on RFID tag antennas. *IEEE International Microwave Symposium Digest*, Vol. 5, No. 1, pp. 247–250, Jun. 2005.

[7] Finkenzeller, K. (2003). *RFID handbook: fundamentals and applications in contactless smart cards and identification*, 2nd ed., John Wiley and Sons, ISBN: 9780470844021.

[8] Fujitsu Microelectronics Limited. Ferroelectric RAM, *RFID Journal* Apr. 2006.
URL: www.fujitsu.com/downloads/EDG/binary/pdf/catalogs/a05000249e.pdf

[9] Fuschini, F.; Piersanti, C.; Paolazzi, F.; & Falciasecca, G. (2008). Electromagnetic and System Level Co-Simulation for RFID Radio Link Modeling in Real Environment. *The Second European Conference on Antennas and Propagation*, pp. 1–8, Nov. 2007.

[10] Fuschini, F.; Piersanti, C.; Paolazzi, F.; & Falciasecca, G. (2008). Analytical Approach to the Backscattering from UHF RFID Transponder. *IEEE Antennas and Wireless Propagation Letters*, Vol. 7, pp. 33–35, 2008.

[11] Griffin, J.; Durgin, G.; Haldi, A. & Kippelen, B. (2003). RF Tag Antenna Performance on Various Materials Using Radio Link Budgets. *IEEE Antennas and Wireless Propagation Letters*, Vol. 5, No. 1, pp. 247–250, Dec. 2006.

[12] Hodges, S.; Thorne, A.; Mallinson, H. & Floerkemeier, C. (2007). Assessing and optimizing the range of UHF RFID to enable real-world pervasive computing applications. *Proceedings of the 5th international conference on Pervasive computing*, 2007.

[13] Jiang, B.; Fishkin, K.; Roy, S. & Philipose, M. (2006). Unobtrusive long-range detection of passive RFID tag motion. *IEEE Transactions on Instrumentation and Measurement*, Vol. 55, No. 1, pp. 187–196, Feb. 2006.

[14] Karthaus, U. & Fischer, M. (2003). Fully integrated passive UHF RFID transponder IC with $16.7\mu$W minimum RF input power. *IEEE Journal of Solid-State Circuits*, Vol. 38, No. 10, pp. 1602–1608, Oct. 2003.

[15] Leong, K. S. (2008). Antenna position analysis and dual-frequency antenna design of high frequency ratio for advanced electronic code responding labels, Ph.D. dissertation, The University of Adelaide, Adelaide, Australia.

[16] Lung, H. L.; Lai, S.; Lee, H.; Wu, T. B.; Liu, R. & Lu, C. Y. (2004). Low-temperature capacitor-overinterconnect (COI) modular FeRAM for SOC application. *IEEE Transactions on Electron Devices*, Vol. 51, No. 6, pp. 920–926, Jun. 2004.

[17] Nakamoto, H.; Yamazaki, D.; Yamamoto, T.; Kurata, H.; Yamada, S.; Mukaida, K.; Ninomiya, T.; Ohkawa, T.; Masui, S. & Gotoh, K. (2007). A passive UHF RF identification CMOS tag IC using ferroelectric RAM in $0.35\mu$m technology. *IEEE Journal of Solid-State Circuits*, Vol. 42, No. 1, pp. 101–110, Jan. 2007.

[18] NG, M. L. (2008). Design of high performance RFID system for metallic item identification, Ph.D. dissertation, The University of Adelaide, Adelaide, Australia.

[19] Nikitin, P. & Rao, K. (2006). Performance limitations of passive UHF RFID systems. *IEEE Antennas and Propagation Society International Symposium*, pp. 1011–1014, Jul. 2006.

[20] Nikitin, P. & Rao, K. (2006). Theory and measurement of backscattering from RFID tags. *IEEE Antennas and Propagation Magazine*, Vol. 48, No. 6, pp. 212–218, Dec. 2006.

[21] No author stated. The Cost of RFID Equipment, *RFID Journal*.
     URL: www.rfidjournal.com/faq/20

[22] Plumb, R. & Ma, H. (1993). Swept frequency reflectometer design for in-situ permittivity measurements. *IEEE Transactions on Instrumentation and Measurement*, Vol. 42, No. 3, pp. 730–734, Jun. 1993.

[23] Prothro, J.; Durgin, G. & Griffin, J. (2005). The effects of a metal ground plane on RFID tag antennas. *IEEE Antennas and Propagation Society International Symposium*, pp. 3241–3244, Jul. 2006.

[24] Rappaport, T. (2002). *Wireless communications-principles and practie*, 2nd ed., Prentice Hall.

[25] Santra, M. & Limaye, K. (2005). Estimation of complex permittivity of arbitrary shape and size dielectric samples using cavity measurement technique at microwave frequencies. *IEEE Transactions on Microwave Theory and Techniques*, Vol. 53, No. 2, pp. 718–722, Feb. 2005.

[26] Young, P. H. (1994). *Electronic Communication Techniques*, 3rd ed., Merill, New York.

[27] 3M. Conductive Adhesive Transfer Tape 9703 (Data Sheet).
     URL: multimedia.3m.com/mws/mediawebserver?mwsId=66666UuZjcFSLXTtnxf VM xz 6E VuQEcuZgVs6EVs6E666666–

# Design and Fabrication of Miniaturized Fractal Antennas for Passive UHF RFID Tags

Ahmed M. A. Sabaawi and Kaydar M. Quboa

*University of Mosul, Mosul,*
*Iraq*

## 1. Introduction

Generally, passive RFID tags consist of an integrated circuit (RFID chip) and an antenna. Because the passive tags are batteryless, the power transfer between the RFID's chip and the antenna is an important factor in the design. The increasing of the available power at the tag will increase the read range of the tag which is a key factor in RFID tags.

The passive RFID tag antennas cannot be taken directly from traditional antennas designed for other applications since RFID chips input impedances differ significantly from traditional input impedances of 50 Ω and 75 Ω. The designer of RFID tag antennas will face some challenges like:

- The antenna should be miniaturized to reduce the tag size and cost.
- The impedance of the designed antenna should be matched with the RFID chip input impedance to ensure maximum power transfer.
- The gain of the antenna should be relatively high to obtain high read range.

Fractal antennas gained their importance because of having interesting features like: **miniaturization**, **wideband**, **multiple resonance**, **low cost** and **reliability**. The interaction of electromagnetic waves with fractal geometries has been studied. Most fractal objects have self-similar shapes, which mean that some of their parts have the same shape as the whole object but at a different scale. The construction of many ideal fractal shapes is usually carried out by applying an infinite number of times (iteration) an iterative algorithms such as Iterated Function System (IFS).

The main focus of this chapter is devoted to design fractal antennas for passive UHF RFID tags based on traditional and newly proposed fractal geometries. The designed antennas with their simulated results like input impedance, return loss and radiation pattern will be presented. Implementations and measurements of these antennas also included and discussed.

## 2. Link budget in RFID systems

To calculate the power available to the reader $P_r$, the polarization losses are neglected and line-of-sight (LOS) communication is assumed. As shown in Fig. 1, $P_r$ is equal to $G_r P'_r$ and can be expressed as given in equation (1) by considering the tag antenna gain $G_t$ and the tag-reader path loss (Salama, 2010):

$$P_r = G_r P_r' = G_r P_b' \left(\frac{\lambda}{4\pi d}\right)^2 \tag{1}$$

$$= G_r G_t P_b \left(\frac{\lambda}{4\pi d}\right)^2 \tag{2}$$
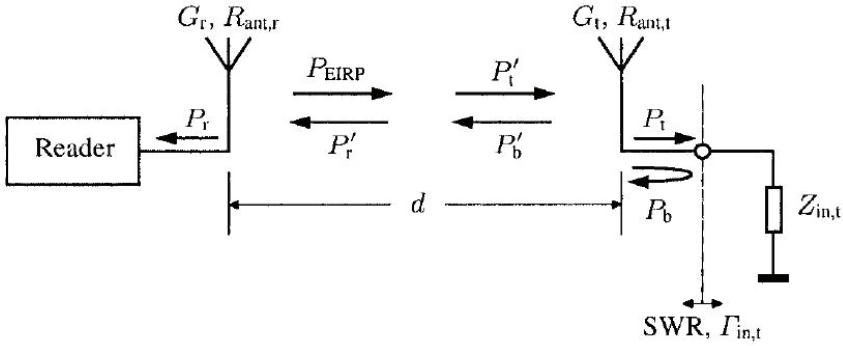


Fig. 1. Link budget calculation (Curty et al., 2007).

$P'_b$ can be calculated using SWR between the tag antenna and the tag input impedance:

$$P_b = P_t \left(\frac{SWR-1}{SWR+1}\right)^2 \tag{3}$$

or can be expressed using the reflection coefficient at the interface ($\Gamma_{in}$) as:

$$P_b = P_t |\Gamma_{in}|^2 \tag{4}$$

The transmitted power ($P_{EIRP}$) is attenuated by reader-tag distance, and the available power at the tag is:

$$P_t G_t = P_{EIRP} \left(\frac{\lambda}{4\pi d}\right)^2 \tag{5}$$

Substituting equations (3), (4) and (5) in equation (1) will result in the link power budget equation between reader and tag.

$$P_r = G_r G_t^2 \left(\frac{\lambda}{4\pi d}\right)^4 \left(\frac{SWR-1}{SWR+1}\right)^2 P_{EIRP} \tag{6}$$

or can be expressed in terms of ($\Gamma_{in}$) as:

$$P_r = G_r G_t^2 \left(\frac{\lambda}{4\pi d}\right)^4 |\Gamma_{in}|^2 P_{EIRP} \tag{7}$$

The received power by the reader is proportional to the $(1/d)^4$ and the gain of the reader and tag antennas. In other words, the *Read Range* of RFID system is proportional to the fourth root of the reader transmission power $P_{EIRP}$.

## 3. Operation modes of passive RFID tags

Passive RFID tags can work in receiving mode and transmitting mode. The goals are to design the antenna to receive the maximum power at the chip from the reader's antenna and to allow the RFID antenna to send out the strongest signal.

### 3.1 Receiving mode
The passive tag in receiving mode is shown in Fig. 2. The RFID tag antenna is receiving signal from a reader's antenna and the signal is powering the chip in the tag.
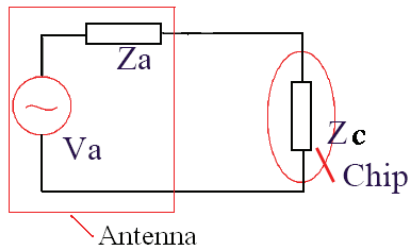


Fig. 2. Equivalent circuit of passive RFID tag at receiving mode (Salama, 2008).

where Za is antenna impedance, Zc is chip impedance and Va is the induced voltage due to receiving radiation from the reader. In this, maximum power is received when Za be the complex conjugate of Zc. In receiving mode, the chip impedance Zc is required to receive the maximum power from the equivalent voltage source Va. This received power is used to power the chip to send out radiation into the space

### 3.2 Transmitting mode
The passive RFID tag work in its transmitting mode as shown in Fig. 3. In transmitting mode, the chip is serving as a source and it is sending out signal thought the RFID antenna.
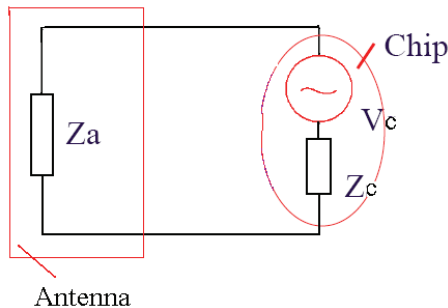


Fig. 3. Equivalent circuit of passive RFID tag in the transmitting mode (Salama, 2008).

## 4. Fractal antennas

A fractal is a recursively generated object having a fractional dimension. Many objects, including antennas, can be designed using the recursive nature of fractals. The term fractal, which means broken or irregular fragments, was originally coined by Mandelbrot to describe a family of complex shapes that possess an inherent self-similarity in their geometrical structure. Since the pioneering work of Mandelbrot and others, a wide variety of application for fractals continue to be found in many branches of science and engineering. One such area is fractal electrodynamics, in which fractal geometry is combined with electromagnetic theory for the purpose of investigating a new class of radiation, propagation and scatter problems. One of the most promising areas of fractal-electrodynamics research in its application to antenna theory and design (Werner et al, 1999). The interaction of electromagnetic waves with fractal geometries has been studied. Most fractal objects have self-similar shapes, which mean that some of their parts have the same shape as the whole object but at a different scale. The construction of many ideal fractal shapes is usually carried out by applying an infinite number of times (iterations) an iterative algorithms such as Iterated Function System (IFS). IFS procedure is applied to an initial structure called initiator to generate a structure called generator which replicated many times at different scales. Fractal antennas can take on various shapes and forms. For example, quarter wavelength monopole can be transformed into shorter antenna by Koch fractal. The Minkowski island fractal is used to model a loop antenna. The Sierpinski gasket can be used as a fractal monopole (Werner and Ganguly, 2003). The shape of the fractal antenna is formed by an iterative mathematical process which can be described by an (IFS) algorithm based upon a series of Affine transformations which can be described by equation (8) (Baliarda et al., 2000) (Werner and Ganguly, 2003):

$$\omega \begin{pmatrix} x \\ y \end{pmatrix} = \begin{bmatrix} r\cos\theta & -r\sin\theta \\ r\sin\theta & r\cos\theta \end{bmatrix} \begin{bmatrix} x \\ y \end{bmatrix} + \begin{bmatrix} e \\ f \end{bmatrix} \tag{8}$$

where $r$ is a scaling factor , $\theta$ is the rotation angle, $e$ and $f$ are translations involved in the transformation.

Fractal antennas provide a compact, low-cost solution for a multitude of RFID applications. Because fractal antennas are small and versatile, they are ideal for creating more compact RFID equipment — both tags and readers. The compact size ultimately leads to lower cost equipment, without compromising power or read range. In this section, some fractal antennas will be described with their simulated and measured results. They are classified into two categories: 1) Fractal Dipole Antennas; which include Koch fractal curve, Sierpinski Gasket and a proposed fractal curve. 2) Fractal Loop Antennas; which include Koch Loop and some proposed fractal loops.

### 4.1 Fractal dipole antennas

There are many fractal geometries that can be classified as fractal dipole antennas but in this section we will focus on just some of these published designs due to space limitation.

### 4.1.1 Koch fractal dipole and proposed fractal dipole

Firstly, Koch curve will be studied mathematically then we will use it as a fractal dipole antenna. A standard Koch curve (with indentation angle of 60°) has been investigated

previously (Salama and Quboa, 2008a), which has a scaling factor of r = 1/3 and rotation angles of θ = 0°, 60°, -60°, and 0°. There are four basic segments that form the basis of the Koch fractal antenna. The geometric construction of the standard Koch curve is fairly simple. One starts with a straight line as an initiator as shown in Fig. 4. The initiator is partitioned into three equal parts, and the segment at the middle is replaced with two others of the same length to form an equilateral triangle. This is the first iterated version of the geometry and is called the *generator*.

The fractal shape in Fig. 4 represents the first iteration of the Koch fractal curve. From there, additional iterations of the fractal can be performed by applying the IFS approach to each segment.

It is possible to design small antenna that has the same end-to-end length of it's Euclidean counterpart, but much longer. When the size of an antenna is made much smaller than the operating wavelength, it becomes highly inefficient, and its radiation resistance decreases. The challenge is to design small and efficient antennas that have a fractal shape.



(a) Initiator
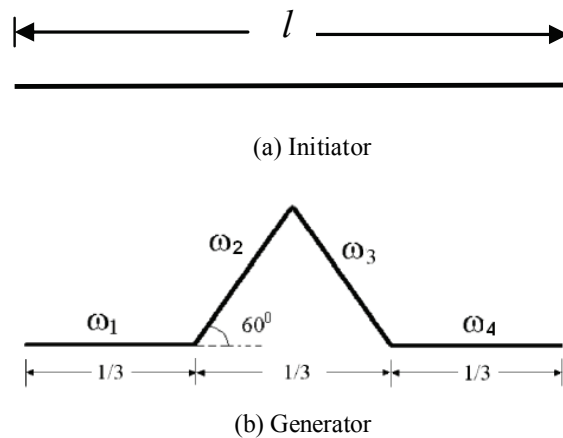


(b) Generator

Fig. 4. Initiator and generator of the standard Koch fractal curve.

Dipole antennas with arms consisting of Koch curves of different indentation angles and fractal iterations are investigated in this section. A standard Koch fractal dipole antenna using 3rd iteration curve with an indentation angle of 60° and with the feed located at the center of the geometry is shown in Fig. 5.



Fig. 5. Standard Koch fractal dipole antenna.

Table 1 summarizes the standard Koch fractal dipole antenna properties with different fractal iterations at reference port of impedance 50Ω. These dipoles are designed at resonant frequency of 900 MHz.

| Indent. Angle (Deg.) | $f_r$ (GHz) | RL (dB) | Impedance (Ω) | Gain (dBi) | Read Range (m) |
|---|---|---|---|---|---|
| 20 | 1.86 | -20 | 60.4-j2.6 | 1.25 | 6.08 |
| 30 | 1.02 | -22.53 | 46.5-j0.6 | 1.18 | 6.05 |
| 40 | 0.96 | -19.87 | 41-j0.7 | 1.126 | 6 |
| 50 | 0.876 | -14.37 | 35.68+j7 | 0.992 | 5.83 |
| 60 | 0.806 | -12.2 | 30.36+j0.5 | 0.732 | 5.6 |
| 70 | 0.727 | -8.99 | 23.83-j1.8 | 0.16 | 5.05 |

Table 1. Effect of fractal iterations on dipole parameters.

The indentation angle can be used as a variable for matching the RFID antenna with specified integrated circuit (IC) impedance. Table 2 summarizes the dipole parameters with different indentation angles at 50Ω port impedance.

| Iter. No. | Dim. (mm) | RL (dB) | Impedance (Ω) | Gain (dBi) | Read Range (m) |
|---|---|---|---|---|---|
| K0 | 127.988 | -27.24 | 54.4-j0.95 | 1.39 | 6.22 |
| K1 | 108.4 X 17 | -17.56 | 38.4+j2.5 | 1.16 | 6 |
| K2 | 96.82 X 16 | -12.5 | 32.9+j9.5 | 0.88 | 5.72 |
| K3 | 91.25 X 14 | -11.56 | 29.1-j1.4 | 0.72 | 5.55 |

Table 2. Effect of indentation angle on Koch fractal dipole parameters.

Another indentation angle search between 20° and 30° is carried out for better matching. The results showed that 3rd iteration Koch fractal dipole antenna with 27.5° indentation angle has almost 50Ω impedance. This modified Koch fractal dipole antenna is shown in Fig. 6. Table 3 compares the modified Koch fractal dipole (K3-27.5°) with the standard Koch fractal dipole (K3-60°) both have resonant frequency of 900 MHz at reference port 50Ω.
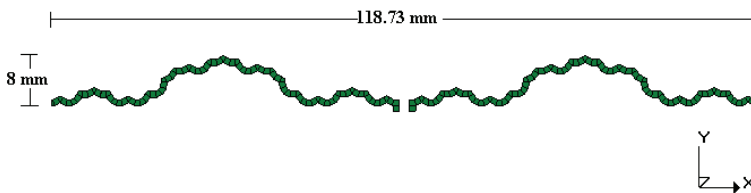


Fig. 6. The modified Koch fractal dipole antenna (K3-27.5°).

| Antenna type | Dim. (mm) | RL (dB) | Impedance (Ω) | Gain (dBi) | Read Range (m) |
|---|---|---|---|---|---|
| K3-60° | 91.2 X 14 | -11.56 | 29.14-j1.4 | 0.72 | 5.55 |
| K3-27.5° | 118.7 X 8 | -33.6 | 48+j0.48 | 1.28 | 6.14 |

Table 3. Comparison of (K3-27.5°) parameters with (K3-60°) at reference port 50Ω.

From Table 3, it is clear that the modified Koch dipole (K3-27.5°) has better characteristics than the standard Koch fractal dipole (K3-60°) and has longer read range.

Another fractal dipole will be investigated here which is the proposed fractal dipole (Salama and Quboa, 2008a). This fractal shape is shown in Fig. 7 which consists of five segments compared with standard Koch curve (60° indentation angle) which consists of four segments, but both have the same effective length.
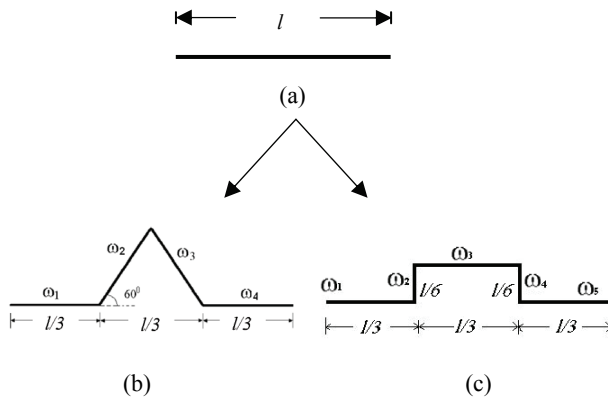


Fig. 7. First iteration of: (a) Initiator; (b) Standard Koch curve; (c) Proposed fractal curve generator .

Additional iterations are performed by applying the IFS to each segment to obtain the proposed fractal dipole antenna (P3) which is designed based on the 3rd iteration of the proposed fractal curve at a resonant frequency of 900 MHz and 50 Ω reference impedance port as shown in Fig. 8.
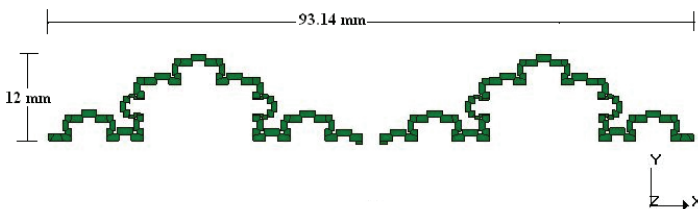


Fig. 8. The proposed fractal dipole antenna (P3) (Salama and Quboa, 2008a).

Table 4 summarizes the simulated results of P3 as well as those of the standard Koch fractal dipole antenna (K3-60°).

| Antenna type | Dim. (mm) | RL (dB) | impedance (Ω) | Gain (dBi) | Read Range (m) |
|---|---|---|---|---|---|
| K3-60° | 91.2 X 14 | -11.56 | 29.14-j1.4 | 0.72 | 5.55 |
| P3 | 93.1 X 12 | -14.07 | 33.7+j3 | 0.57 | 5.55 |

Table 4. The simulated results of P3 compared with (K3-60°)
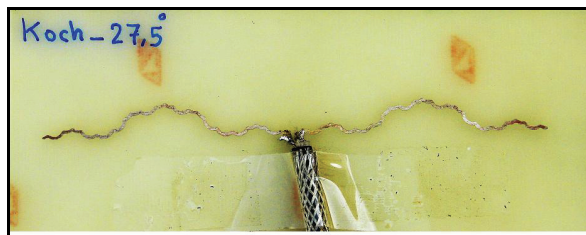


Fig. 9. Photograph of the fabricated K3-27.5° antenna.
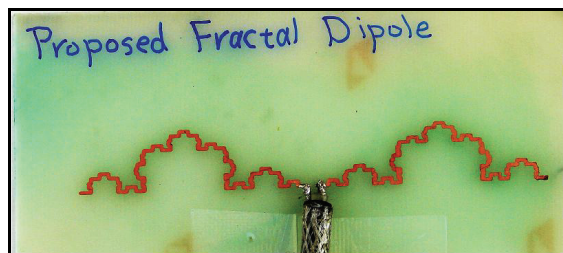


Fig. 10. Photograph of the fabricated (P3) antenna



(a)                                               (b)
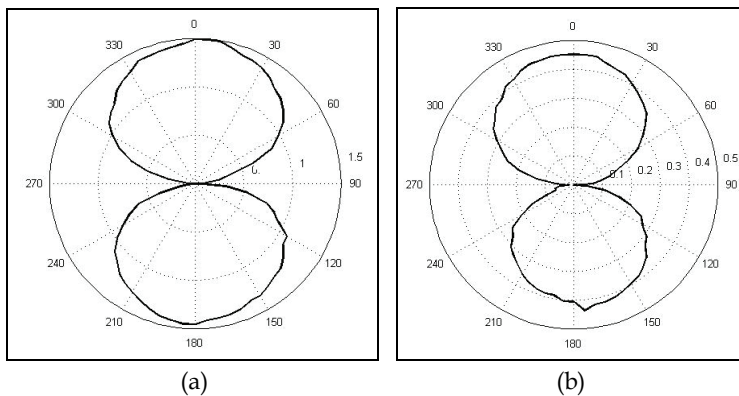
Fig. 11. Measured radiation pattern of (a) (K3-27.5°) antenna and (b) (P3) antenna

These fractal dipole antennas can be fabricated using printed circuit board (PCB) technology as shown in Fig. 9 and Fig. 10 respectively. A suitable 50 Ω coaxial cable and connector are connected to those fabricated antennas. In order to obtain balanced currents, Bazooka balun may be used (Balanis, 1997). The performance of the fabricated antennas are verified by measurements. Radiation pattern and gain can be measured in anechoic chamber to obtain accurate results. The measured radiation pattern for (K3-27.5°) and (P3) fractal dipole antennas are shown in Fig. 11 which are in good agreement with the simulated results.

### 4.1.2 Sierpinski gasket as fractal dipoles

In this section, a standard Sierpinski gasket (with apex angle of 60°) will be investigated (Sabaawi and Quboa, 2010), which has a scaling factor of r = 0.5 and rotation angle of θ = 0°. There are three basic parts that form the basis of the Sierpinski gasket, as shown in Fig. 12. The geometric construction of the Sierpinski gasket is simple. It starts with a triangle as an initiator. The initiator is partitioned into three equal parts, each one is a triangle with half size of the original triangle. This is done by removing a triangle from the middle of the original triangle which has vertices in the middle of the original triangle sides to form three equilateral triangles. This is the first iterated version of the geometry and is called the *generator* as shown in Fig. 12.
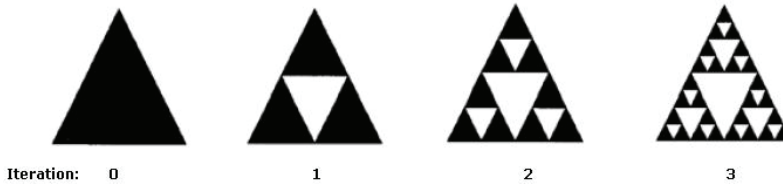


Fig. 12. The first three iterations of Sierpinski gasket.

From the IFS approach, the basis of the Sierpinski gasket can be written using equation (8).The fractal shape shown in Fig. 12 represents the first three iterations of the Sierpinski gasket. From there, additional iterations of the fractal can be performed by applying the IFS approach to each segment.

It is possible to design a small dipole antenna based on Sierpinski gasket that has the same end-to-end length than their Euclidean counterparts, but much longer. Again, when the size of an antenna is made much smaller than the operating wavelength, it becomes highly inefficient, and its radiation resistance decreases (Baliarda et al., 2000). The challenge is to design small and efficient antennas that have a fractal shape.

Dipole antennas with arms consisting of Sierpinski gasket of different apex angles and fractal iterations are simulated using IE3D full-wave electromagnetic simulator based on Methods of Moments (MoM). The dielectric substrate used in simulation has $\varepsilon_r$=4.1, tanδ=0.02 and thickness of (1.59) mm. A standard Sierpinski dipole antenna using 3rd iteration geometry with an apex angle of 60° and with the feed located at the center of the geometry is shown in Fig. 13.

Different standard fractal Sierpinski (apex angle 60°) dipole antennas with different fractal iterations at reference port impedance of 50 Ω are designed at resonant frequency of 900 MHz and simulated using IE3D software. The simulated results concerning Return Loss (RL), impedance, gain and read range (r) are tabulated in Table 5.
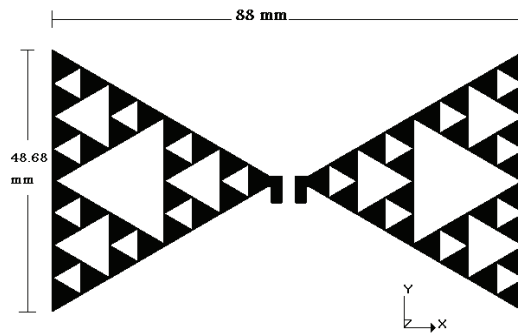
Fig. 13. The standard Sierpinski dipole antenna.

| Iter. No. | Dimension (mm) | RL (dB) | Impedance (Ω) | Gain (dBi) | r (m) |
|-----------|----------------|---------|---------------|------------|-------|
| 0 | 97.66X54.3 | -16.3 | 38.68+j7.8 | 1.38 | 6.14 |
| 1 | 93.6 X 51.5 | -15.4 | 37.17+j7.5 | 1.32 | 6.08 |
| 2 | 89.5 X 47.5 | -14 | 33.66+j3.22 | 1.25 | 6 |
| 3 | 88 X 48.68 | -12.6 | 32.55+j8.5 | 1.27 | 5.97 |

Table 5. Effect of fractal iterations on standard Sierpinski dipole parameters.

It can be seen from the results given in Table 5, that the dimensions of antenna are reduced by increasing the iteration number.

In this design, the apex angle is used as a variable for matching the RFID antenna with specified IC impedance. Table 6 summarizes the dipole parameters with different apex angles. Numerical simulations are carried out to 3rd iteration Sierpinski fractal dipole antenna at 50Ω port impedance. Each dipole has a resonant frequency of 900 MHz.

| Apex Angle (Deg.) | Dim. (mm) | RL (dB) | Impedance (Ω) | Gain (dBi) | r (m) |
|-------------------|-----------|---------|---------------|------------|-------|
| 40 | 94.1X32.5 | -15.77 | 36.17+j2.33 | 1.32 | 6.09 |
| 45 | 93.6 X 36 | -15.12 | 35.35+j3 | 1.39 | 6.12 |
| 50 | 91.8X40.7 | -15.34 | 36.61+j6.4 | 1.14 | 5.95 |
| 55 | 90.4X45.3 | -14.84 | 35.21+j4.5 | 1.149 | 5.95 |
| 60 | 88 X 48.6 | -12.6 | 32.55+j8.5 | 1.27 | 5.97 |
| 70 | 81.2X52.5 | -11.8 | 29.83+j3.8 | 0.86 | 5.66 |
| 80 | 78.44X61 | -9.94 | 26.75+j7.9 | 0.96 | 5.61 |

Table 6. Effect of apex angle on Sierpinski fractal dipole parameters.

From the results in Table 6, the best results (i.e. best gain and read range) are obtained at apex angle of 45°. From their, two fractal Sierpinski dipoles are designed for UHF RFID tags at 900 MHz . The first one has an apex angle of 45° (S3-45°), as shown in Fig. 14, while the other is the standard Sierpinski dipole of apex angle 60° (S3-60°).
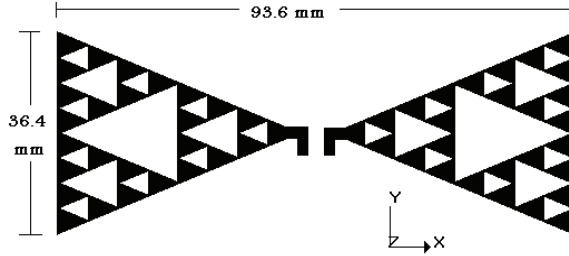


Fig. 14. The modified Seirpinski dipole antenna (S3-45°).

The effective parameters of (S3-45°) compared with the standard Sierpinski dipole (S3-60°) are given in Table 7.

| Antenna type | Dim. (mm) | RL (dB) | Impedance (Ω) | Gain (dBi) | r (m) |
|---|---|---|---|---|---|
| S3-45 º | 93.6 X 36 | -15.1 | 35.35+j3 | 1.39 | 6.12 |
| S3-60 º | 88 X 48.6 | -12.6 | 32.5+j8.5 | 1.27 | 5.97 |

Table 7. Comparison of (S3-45°) parameters with (S3-60°) at reference port impedance of 50Ω.

It is clear from Table 7 that the modified Sierpinski dipole antenna (S3-45°) has better gain and read range. Fig. 15 shows the simulated return loss of the modified Sierpinski dipole antenna (S3-45°).
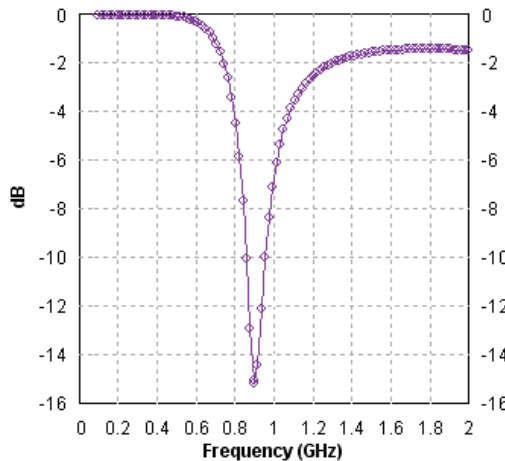


Fig. 15. The simulated return loss of (S3-45°).

The simulated radiation pattern with 2D and 3D views at φ=0 and 90° are shown in Fig. 16 for the modified Sierpinski dipole antenna (S3-45°).



(a) (b)
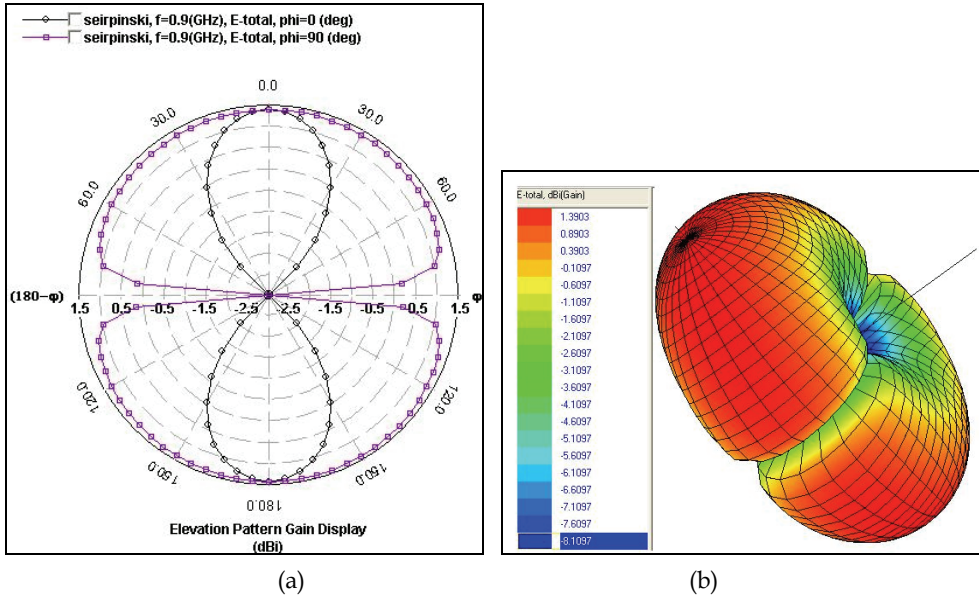
Fig. 16. The simulated radiation pattern of modified Sierpinski dipole antenna (S3-45°):
(a) 2D radiation pattern, (b) 3D radiation pattern.

The standard Sierpinski fractal dipole antenna (S3-60°) shown in Fig. 13 and the proposed Sierpinski fractal dipole (S3-45°) shown in Fig. 14 are fabricated using PCB technology as in Fig. 17 and Fig. 18 respectively. A 50Ω coaxial cable type RG58/U and BNC connector are connected to the fabricated antennas. In order to obtain balanced currents, Bazooka balun is used (Balanis, 1997).



Fig. 17. The fabricated S3-60° antenna.
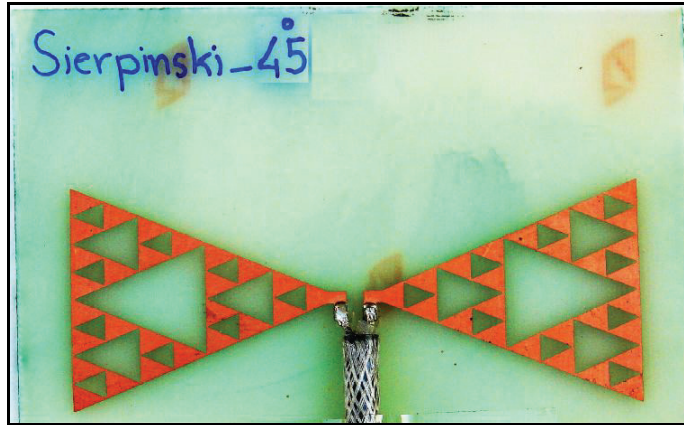
Fig. 18. The fabricated S3-45° antenna.

The performance of the fabricated antennas are verified by measurements. Radiation pattern and gain are measured in anechoic chamber. The measured radiation pattern for (S3-60°) and (S3-45°) fractal dipole antennas are shown in Fig. 19.



| (a) | (b) |
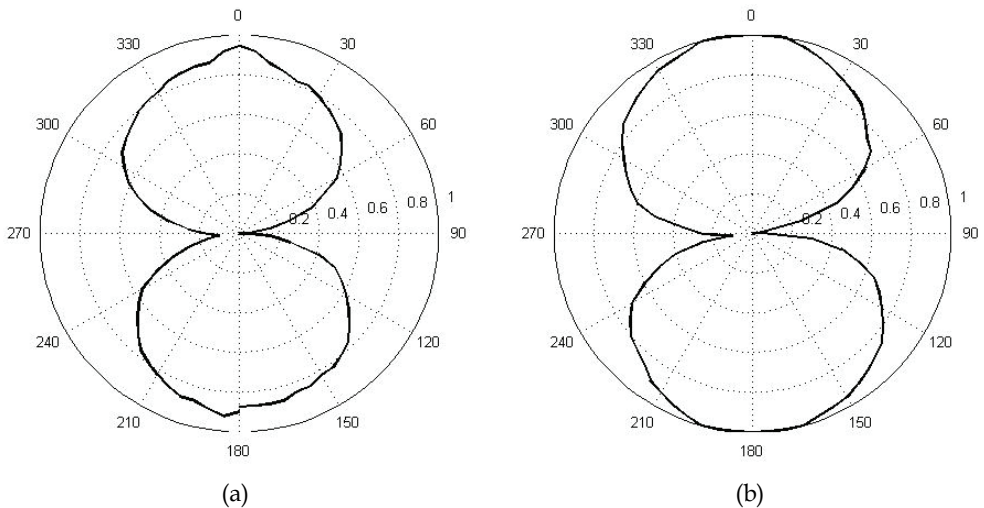
Fig. 19. Measured radiation pattern for the fabricated antennas, (a) (S3-45°) antenna and (b) (S3-60°) antenna.

From Fig. 19, maximum measured gain of (0.948) dBi is obtained for (S3-45°). The measured radiation pattern was carried out for φ=0. The Return Loss of the fabricated fractal dipoles is measured using (MOTECH RF-2000) and plotted as shown in Fig. 20.

From Fig. 20, a measured RL of (-27) dB could be compared with the simulated RL of (-15.12) dB given in Table 7 for (S3-45°) while measured RL of (-27) dB is compared with simulated RL of (-12.6) dB given in Table 7 for (S3-60°).
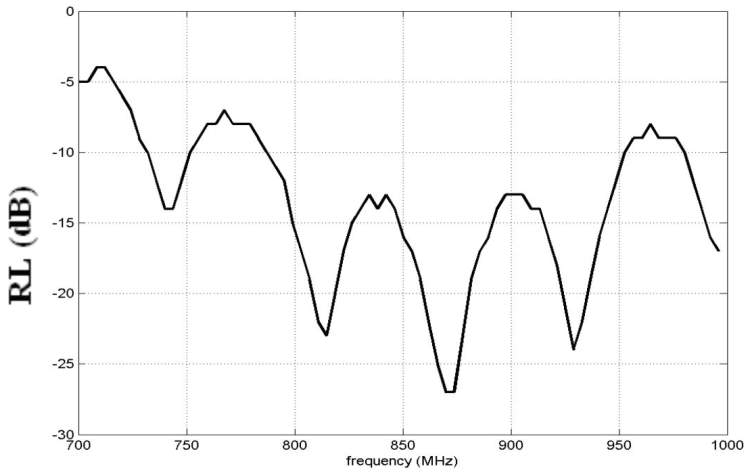
(a) Frequency (MHz)
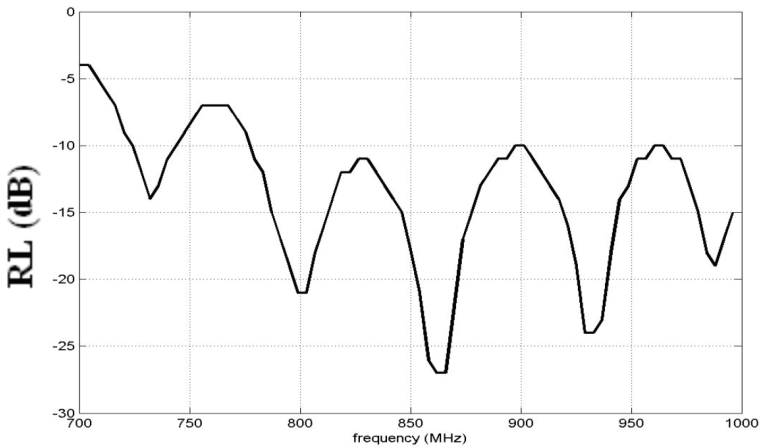


(b) Frequency (MHz)

Fig. 20. Measured RL for the fabricated antenna: (a) S3-45° antenna, (b) S3-60° antenna.

It is clear from Fig. 20 that the measured resonant frequency is around (873.86) MHz for (S3-45) and (862)MHz for (S3-60) when compared with the simulated resonant frequency at (900) MHz. The difference between measured and simulated values might be due to that the simulations are carried out using $\varepsilon_r$=4.1 while in practice it may be slightly different or matching was not perfect.

## 4.2 Fractal loop antennas

In this section, the design and performance of three fractal loop antennas for passive UHF RFID tags at 900 MHz will be investigated. The first one based on the 2nd iteration of the

Koch fractal curve and the other two loops are based on the 2nd iteration of the new proposed fractal curve with line width of (1mm) for both as shown in Fig. 21 (Salama and Quboa, 2008b).



(a)                                                (b)
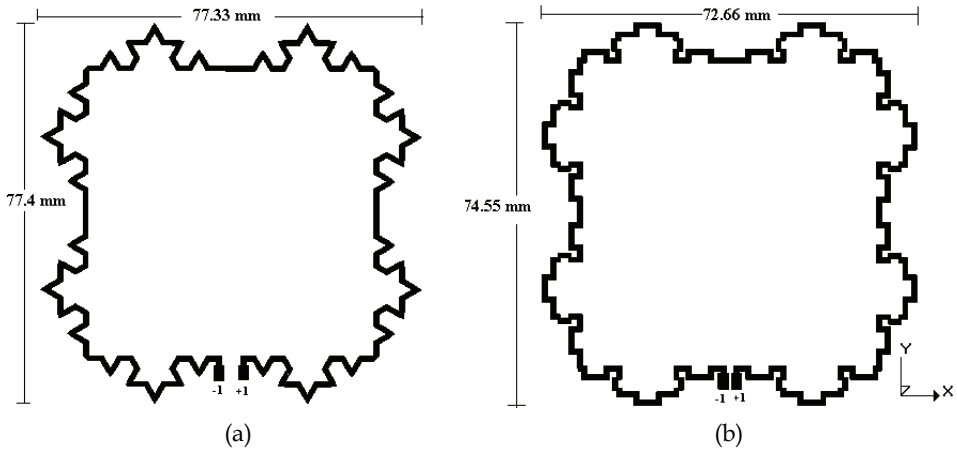
Fig. 21. The designed fractal loops: (a) Standard Koch fractal loop, (b) The new proposed fractal loop

A loop antenna responds mostly to the time varying magnetic flux density $\vec{B}$ of the incident EM wave. The induced voltage across the 2- terminal's loop is proportional to time change of the magnetic flux $\Phi$ through the loop, which in turns proportional to the area $S$ enclosed by the antenna. In simple form it can be expressed as (Andrenko, 2005):

$$V \propto \frac{\partial \Phi}{\partial t} \propto \omega \left| \vec{B} \right| S \tag{9}$$

The induced voltage can be increased by increasing the area (S) enclosed by the loop, and thus the read range of the tag will be increased. The proposed fractal curve has a greater area under curve than the standard Koch curve in second iteration. Starting with an initiator of length ($l$), the second iteration area is ($0.0766\ l^2\ cm^2$) for the proposed curve and ($0.0688\ l^2\ cm^2$) for the standard Koch curve. According to equation (9) one can except to obtain a better level of gain from proposed fractal loop higher than that from Koch fractal loop.

Fig. 22 shows the return loss (RL) of the designed loop antennas of 50Ω balanced feed port, and Table 8 summarizes the simulated results of the designed loop antennas.

| Antenna type | Return Loss (dB) | BW (MHz) | Impedance (Ω) | eff. (%) | Gain (dBi) | Read Range (m) |
|---|---|---|---|---|---|---|
| Standard Koch Loop | -12.35 | 31.4 | 80.73-j7.3 | 78.5 | 1.74 | 6.287 |
| Proposed Loop | -12.75 | 36 | 78.2-j8.9 | 81.8 | 1.97 | 6.477 |

Table 8. Simulated results of the designed loop antennas.
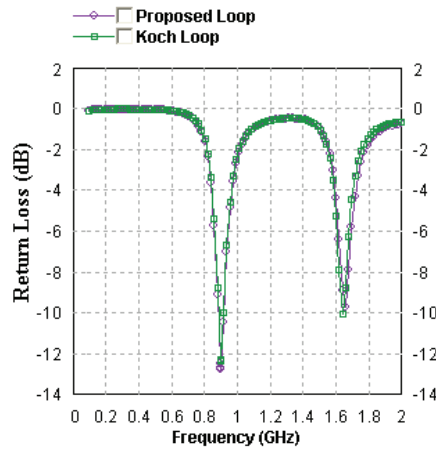
Fig. 22. Return loss of the two loop antennas.

From Table 8 it can be seen that the proposed fractal loop has better radiation characteristics than the standard Koch fractal loop. As a result, higher read range is obtained. The proposed fractal loop also is smaller in size than the standard Koch fractal loop. The measured radiation pattern is in good agreement with the simulated one for the proposed fractal loop antenna as shown in Fig. 23 .



(a)                                             (b)
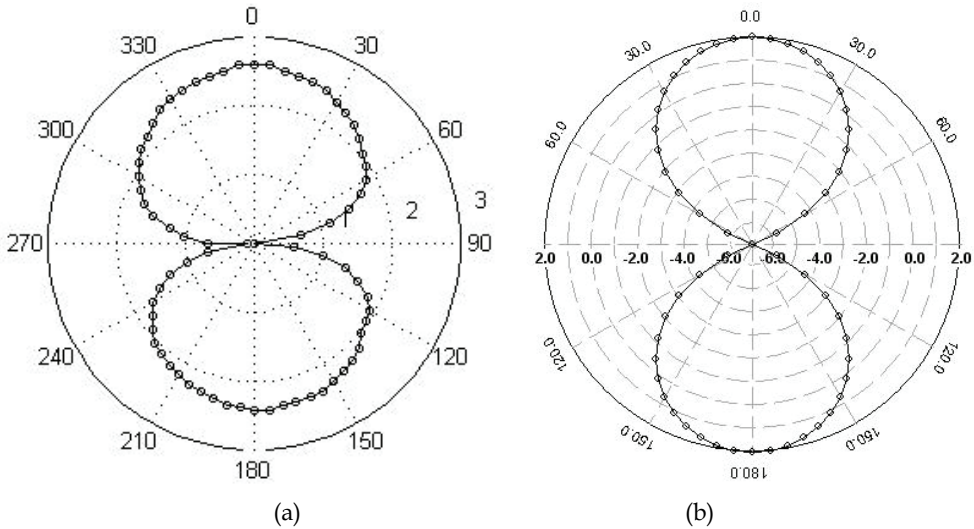
Fig. 23. The radiation pattern of the proposed fractal loop antenna:  (a) measured, (b) simulated (Salama& Quboa., 2008b).

Another new fractal curve is proposed as shown in Fig. 24 (Sabaawi et al, 2010) which consists of five segments compared with standard Koch curve (60° indentation angle) which consists of four segments, but has longer effective length ($l_{eff} = l . (3/2)^n$) compared with ($l_{eff} = l . (4/3)^n$) of standard Koch curve.

a-Initiator
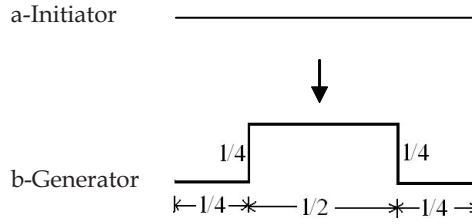
b-Generator

Fig. 24. First iteration of the proposed fractal curves: (a) initiator (n=0),(b) proposed fractal curve generator (n=1).

The Affine transformation of the proposed fractal curve in the $\omega$-plane can be described according to equation (1), where $\theta$ is a rotating angle and $r$ is a scaling factor, while $e$ and $f$ are translations involved in the transformation.

$$\omega = \left[ r\cos\theta, -r\sin\theta, r\sin\theta, r\cos\theta, e, f \right] \tag{10}$$

$$\omega_1 = \left[ \frac{1}{4}, 0, 0, \frac{1}{4}, 0, 0 \right]$$

$$\omega_2 = \left[ 0, -\frac{1}{4}, \frac{1}{4}, 0, \frac{1}{4}, 0 \right]$$

$$\omega_3 = \left[ \frac{1}{2}, 0, 0, \frac{1}{2}, \frac{1}{4}, \frac{1}{4} \right]$$

$$\omega_4 = \left[ 0, \frac{1}{4}, -\frac{1}{4}, 0, \frac{3}{4}, \frac{1}{4} \right]$$

$$\omega_5 = \left[ \frac{1}{4}, 0, 0, \frac{1}{4}, \frac{3}{4}, 0 \right]$$

$$\omega_t = \omega_1 \cup \omega_2 \cup \omega_3 \cup \omega_4 \cup \omega_5$$

Additional iterations can be performed by applying the Iterated Function System (IFS) to each segment. Fig. 25 shows the first iterations $P_0$, $P_1$, and $P_2$ of the proposed fractal curve.

$P_0$

$P_1$

$P_2$
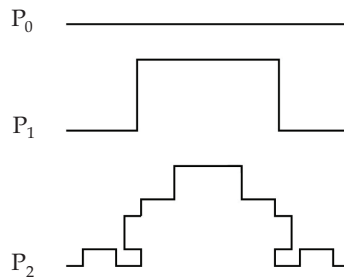
Fig. 25. First two iterations of the proposed fractal curves.

A new fractal loop antenna is designed for passive UHF RFID tags at 900 MHz based on 2nd iteration of the above proposed curve with line width of (1mm). The fractal loop is split into two halves (upper & lower halves) by making a horizontal cut at the centre of the loop as shown in Fig. 26. The central-cut is used to control the impedance of the antenna and hence increasing its matching.
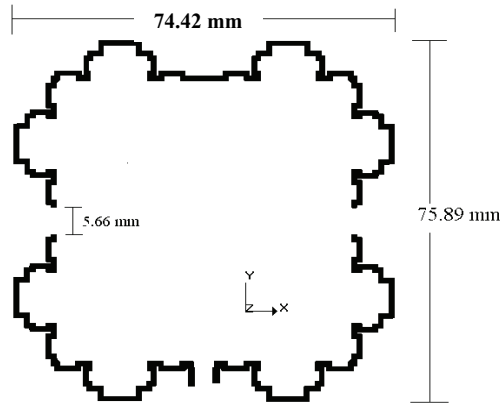


Fig. 26. The proposed fractal loop antenna.

As shown in Fig. 25, the proposed fractal curve has a greater area under curve than that of previous two loops in second iteration. Starting with an initiator of length ($l$), the second iterations area is ($0.1594\ l^2\ cm^2$) for the proposed curve in Fig. 26, and ($0.0766\ l^2\ cm^2$) for the fractal loop proposed in Fig. 21b (i.e more than twice the area).

The simulated results of the designed fractal loop include: input impedance ($Z_a$), return loss (RL) and radiation pattern will are shown in Figs. 27 & 28. These results will be useful in understanding the benefits of the designed antenna like its small size as well as its radiation properties.
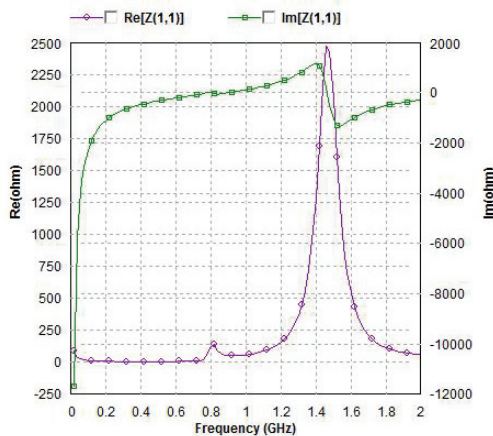


Fig. 27. The simulated input impedance of the fractal loop antenna
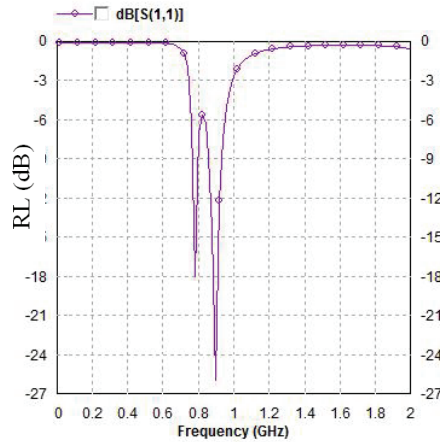
Fig. 28. The simulated return loss of the fractal loop antenna

As shown from Figs. 27 & 28, the impedance of the antenna is (65.88+j3.4) Ω at 900 MHz which is very close to the designing reference impedance of 50 Ω. It is also clear that the return loss is (-26 dB) at 900 MHz with simulated -10 dB operating bandwidth of (59 MHz). The simulated radiation pattern of the proposed fractal loop antenna is shown in Fig. 29.



(a)                                           (b)
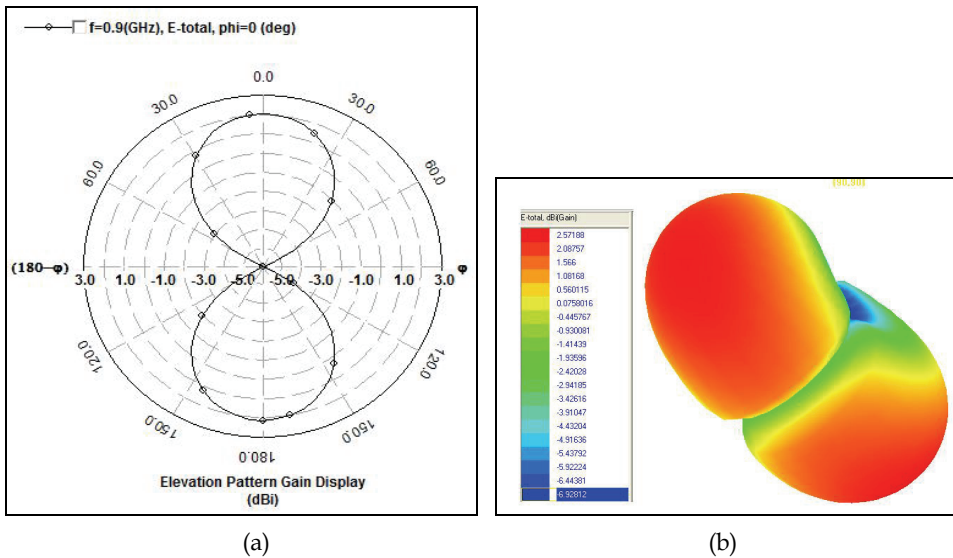
Fig. 29. The simulated Radiation Pattern. (a) 2D, (b) 3D.

One can see from the Fig. 29 that the radiation pattern at 900 MHz is almost omnidirectional with deep nulls, and it is almost the same radiation pattern of an ordinary dipole with simulated gain of (2.57 dBi). Table9 summarizes the simulated results of the proposed fractal loop antenna compared with the fractal loop antenna published in (Salama and Quboa, 2008b).

| Antenna type | Return Loss (dB) | BW (MHz) | Impedance (Ω) | eff. (%) | Gain (dBi) | Read Range (m) |
|---|---|---|---|---|---|---|
| Proposed loop | -26 | 59 | 65.8+j3.4 | 86.7 | 2.57 | 7.122 |

Table 9. Simulated characteristics of the designed fractal loop antenna.

It is clear from Table 9 that the new proposed fractal loop has better radiation characteristics from all those of the proposed fractal loop in (Salama and Quboa, 2008b) under the same design conditions and parameters (i.e. the same substrate parameters), and as a result longer read range is obtained which is the most important factor in designing RFID tags.

The proposed fractal loop antenna shown in Fig. 26 is fabricated using PCB technology as shown in Fig. 27. A 50Ω coaxial cable type RG58/U and BNC connector is connected to the fabricated antenna. In order to obtain balanced currents, Bazooka balun is used. The performance of the fabricated antennas is verified by measurements. Radiation pattern is measured in anechoic chamber. The return loss of the fabricated loop antenna is measured using MOTECH RF-2000 analyzer as shown in Fig. 28.
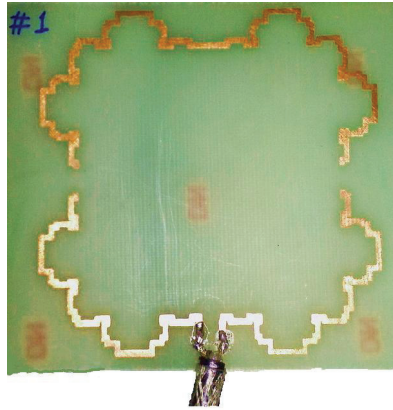


Fig. 27. The Fabricated Fractal Loop Antenna.
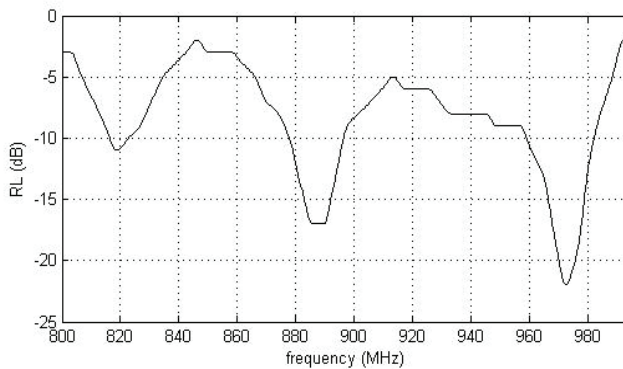


Fig. 28. Measured RL of the fabricated fractal loop antenna.

The measured return loss is (-17 dB) at a resonant frequency (889.62 MHz) compared with the simulated one of (-26 dB) at 900 MHz, and the bandwidth is (19.2 MHz) compared with the simulated bandwidth of (59 MHz). The disagreement between measured and simulated results of the fractal loop antenna is attributed to the fact that we lack sufficient information from the vendor of FR-4 material. This information would enable us to build accurate model for the dielectric material in the EM simulator, instead of working with single frequency point data.

The radiation pattern for the fractal dipole antenna is measured in anechoic chamber as shown in Fig. 29 which is in good agreement with the simulated results.
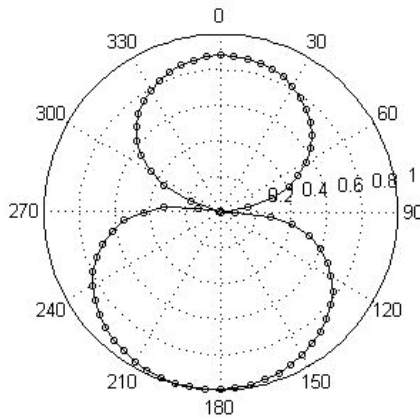


Fig. 29. Measured radiation pattern.

## 5. References

Andrenko A. S., (2005). Conformal Fractal Loop Antennas for RFID Tag Applications, *Proceedings of the IEEE International Conference on Applied Electromagnetics and Communications, ICECom.*, Pages:1-6, Oct. 2008.

Balanis C. A., (1997), Antenna Theory Analysis and Design, Jhon Whily, New York, (2nd Edition).

Baliarda C. P., Romeu J., & Cardama A., M. (2000), The Koch monopole: A small fractal antenna. *IEEE Trans. on Antennas and Propagation,* Vol.48, (2000) page numbers (1773-1781).

Curty J. P., Declerdq M., Dehollain C. & Joehl N. , (2007). *Design and Optimization of Passive UHF RFID Systems*, Springer, ISBN: 0-387-35274-0, New Jersey.

Sabaawi A. M. A., Abdulla A. I., Sultan Q. H., (2010), Design a New Fractal Loop Antenna For UHF RFID Tags Based On a Proposed Fractal Curve, Proceedings of The 2nd IEEE International Conference on Computer Technology and Development (ICCTD 2010) November 2-4, 2010, Cairo, Egypt.

Sabaawi A. M. A., Quboa K. M., (2010). Sierpinski Gasket as Fractal Dipole Antennas for Passive UHF RFID Tags. Proceedings of The Mosharaka International Conference on Communications, Electronics, Propagation (MIC-CPE2010), 3-5 March 2010, Amman, Jordan.

Salama A. M. A., (2010). Antennas of RFID Tags, Radio Frequency Identification Fundamentals and Applications Design Methods and Solutions, Cristina Turcu (Ed.), ISBN: 978-953-7619-72-5, INTECH, Available from: http://sciyo.com/articles/show/title/antennas-of-rfid-tags.

Salama A. M. A., Quboa K., (2008a). Fractal Dipoles As Meander Lines Antennas For Passive UHF RFID Tags, *Proceedings of The IEEE Fifth International Multi-Conference on Systems, Signals and Devices (IEEE SSD'08)*, Page: 128, Jordan, July 2008.

Salama A. M. A., Quboa K., (2008b). A New Fractal Loop Antenna for Passive UHF RFID Tags Applications, *Proceedings of the 3rd IEEE International Conference on Information & Communication Technologies: from Theory to Applications (ICTTA'08)*, Page: 477, Syria, April 2008, Damascus.

Werner D. H. & Ganguly S. (2003). An Overview of Fractal Antenna Engineering Research. *IEEE Antennas and Propagation Magazine,* Vol.45, No.1, (Feb. 2003), page numbers (38-56).

Werner D. H., Haupt R. L., Werner P. L., (1999). Fractal Antenna Engineering: The Theory and Design of Fractal Antenna Arrays. *IEEE Antennas and Propagation Magazine,* Vol.41, No.5, (1999) ,page numbers (37-58).

# Design of RFID Coplanar Antenna with Stubs over Dipoles

F. R. L e Silva and M. T. De Melo
*Universidade Federal de Pernambuco*
*Brasil*

## 1. Introduction

Radio Frequency Identification system, initially projected for objects identification in large scale – a counterpart of the well-known barcode, has been expanding its horizons and has been used for the automation of several services such as tracking goods, credit card charging, supply chain controlling, and others. RFID systems consist on a Reader that interrogates an identification Tag and this, in turn, sends an identification code back to the Reader. Specifically, the passive RFID Tags take advantage of being free of batteries. It converts part of the incoming RF signal from the reader into power supply. Because of its versatility, lots of researchers have been investing on RFID, which, despite the 35 years old of the first patent, is still considered new and somewhat obscure. This chapter covers topics including the system surveying and the working basics of the RFID, especially the physical air interface between the RFID tags (the mobile part) and the so-called Interrogators, which are fixed part of the network. This chapter focuses on the project of 2.45 GHz planar antennas, with a gain higher than the commercial ones, in such a way that, when these brand new antennas are used in RFID tags, they increase the system efficiency. More coverage area can be achieved with these higher gain antennas, as well as lower power requirements of the Interrogators. Most of the necessary theory topics to project this antenna are shown. As well as the theory, measured and simulated results are presented such as: input impedance, frequency response, radiation pattern and gain, which could certainly be the starting point for future works.

With respect to academic research over RFID, it is increasing year after year. The number of publications in important periodicals is increasing in recent years. This happens due to its great applicability in many areas like, health, commerce, safety, etc. In recent years, it is becoming one of the most attractive areas in wireless applications. Figure 1 presents the number of publications about RFID from 2003 to 2009 in the IEEE (Institute of Electric and Electronics Engineers). As one can see, there is a considerable increase in recent years. This Figure shows only the most relevant publications according to the algorithm of the IEEE research in a sample space of 100 publications. In reality, the number of publications is in the order of tens of hundreds.

In general the RFID system publications can achieve different focus. These can be about development of antenna, chips identification, software control, etc. As usual, in all engineer systems, there is something to improve. The system still is a bit expensive, as an Interrogator may cost U$ 2,000.00. Another point is behind intersystem and intra-system interference, as

it operates in the ISM bands (Industrial Scientific and Medical), free bands. Many others systems, operating in that band, can interfere with RFID systems.

**RFID Publications in the IEEE**
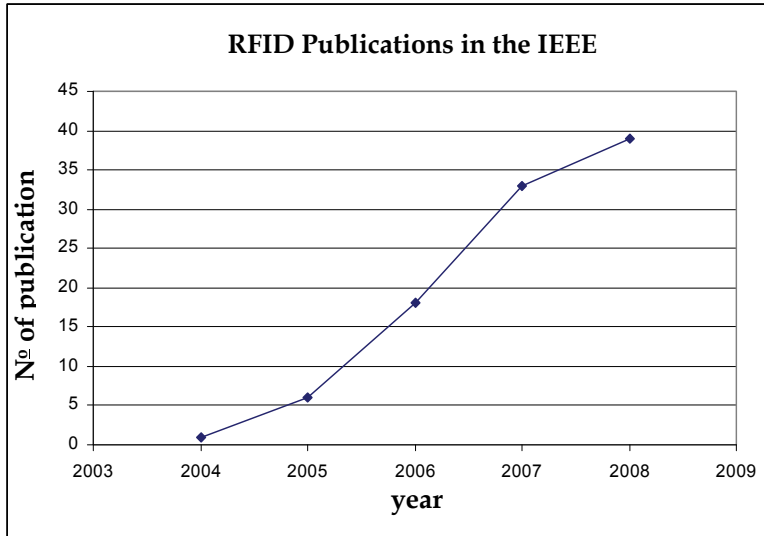
Fig. 1. RFID Publication in the IEEE. It is included publications over performance evaluation, development of news tools, new hardwares, etc.

**RFID antennas Publication in the IEEE**
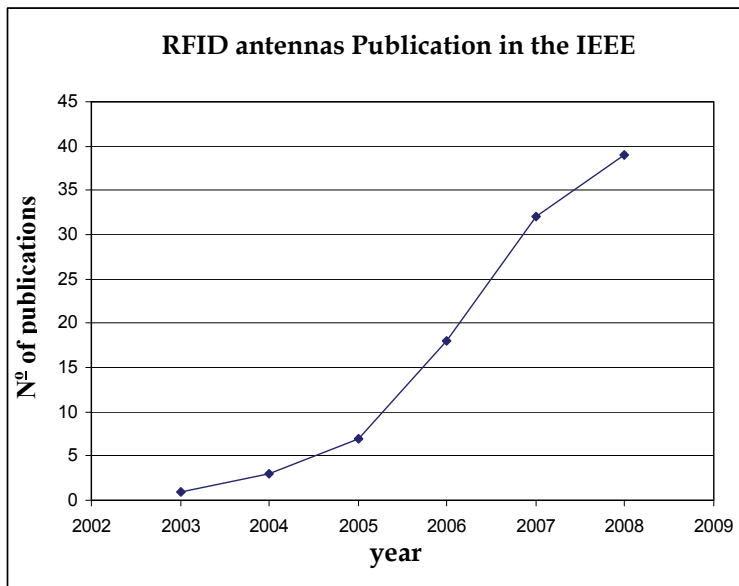
Fig. 2. Number of publications specifically for RFID antennas in the IEEE, in a sample space of 100 publications.

For a matter of power saving, design of high gain antenna can be necessary in the case of longer distance reading. On the other hand, some specific radiation patterns are suitable for grouped tags, avoiding the interfering effects. Besides, some Interrogators antenna arrays, can optimize the system power consume and/or optimize the number and position of the Interrogators, decreasing both the cost of implementation and the maintenance. It is clear that there is no any unique solution for whole problems, and perhaps, a particular solution for a particular problem. Figure 2 also shows an increase in the number of publications specifically for RFID antennas from 2002 to 2009 in the IEEE. These are only publications in the IEEE, there are other important periodicals, conferences, meeting, symposiums, etc. about RFID all over the world. Certainly, in this research area there is much work to do about optimization and cost reduction.

As the antenna design is one of the most important parts of RFID system development, it becomes necessary to see some basic concepts, analysis, and characterization of antennas used in RFID applications.

## 2. Important concepts

As predicted by Friis (Balanis, 1982) in (1), the reading range $r$ is a function of the following parameters: wavelength in the free space $\lambda$, EIRP power $P_t \cdot G_t$, tag antenna gain $G_r$ and the minimum required power for activating the RFIC chip $P_r$ (Karthaus & Fischer, 2003). RFIC operating with 16.7μW minimum power level (Karthaus & Fischer, 2003) and indoor Reader EIRP of 27dBm, gain improvements on the tag antenna could increase the reading range of the system. Figure 3 shows the system reading range as a function of the antenna gain. According to (Karthaus & Fischer, 2003), (Finkenzeller), passive RFIC tags have generally negative input reactance and may have low input resistance. The impedance of the RFIC and the antenna must be matched each other (Finkenzeller).

$$ r = \frac{\lambda}{4 \cdot \pi} \sqrt{\frac{P_t \cdot G_t \cdot G_r}{P_r}} \tag{1} $$
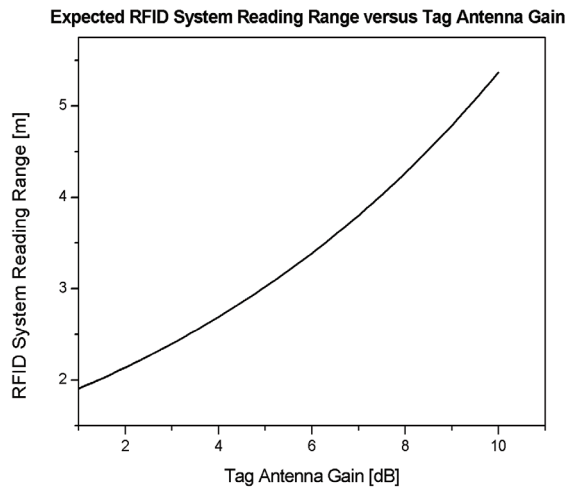


Fig. 3. Reading range versus tag antenna gain.

## 3. Tag antenna design

Let us see the design step by step. It consists of two $\lambda/2$ folded dipole array fed by $\lambda/4$ Transmission Line (TL) sections. Each folded dipole works like a load for a $\lambda/4$ transmission line (TL). As described in (de Melo et al., 1999), two loaded $\lambda/4$ TL are connected at the position A-A´. This yields to array of two planar dipoles. The transmission lines TL, as shown in Figure 4, of length $\lambda/4$ works like an impedance transformer for the required input impedance at the feeding points A-A'. From Figure 5, one can see the load in the shape of a planar folded dipole.
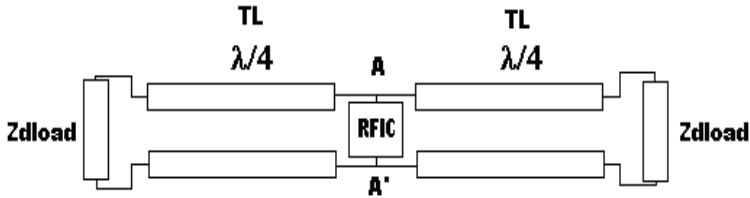


Fig. 4. Loaded CPS transmission lines.
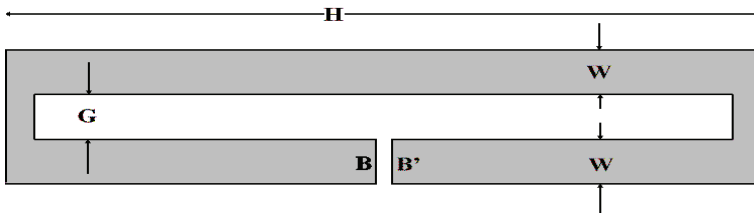


Fig. 5. Load in the shape of a dipole.

The transmission lines are connected together at the terminals A-A', as shown in Figure 4. Arrays of radiating elements produce higher gain than isolated elements (Balanis, 1982). This fact allows this antenna to be useful when farther reading ranges are required. Because its symmetry related to the central plane, only half the antenna is analyzed and the results are further corrected in order to represent the whole antenna. With the dimensions described in Table 1 (Condition 1), the input impedance of one dipole can be calculated using quasi-static equations of conformal mapping (Lampe, 1985), (Nguyen, 2001), (de Melo et al., 1999) and such impedance is referred to as $Z_{dipole}$. It is the load impedance for the transmission line.

In practice it is not simple to obtain the dipole impedance, taking into account the real values of the geometrical parameters. The known usual expressions are suitable for ideal conditions and do not take into account some parameters, like width D, shown in the Figure 6. Another example is the gap $G$ created in one of the strips for the signal feeding. Besides, the lower strip becomes smaller, comparing with the upper one. However, the expressions, published by (Lampe, 1985) still may be used to have an idea of the dipole behavior with variation of line width, space between strips, etc. To obtain the dipole impedance $Z_{dipole} = R_d + jX_d$ some simulations were carried out using the full wave simulator CST, varying the dipole geometric parameters.
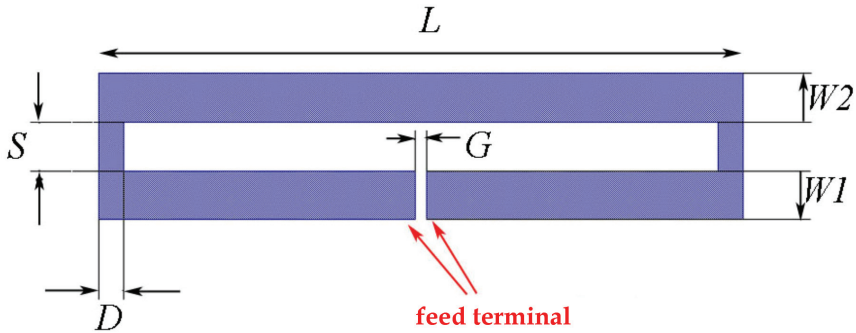
Fig. 6. Dimensions and parameters of the coplanar strip folded dipole.

Figures 7(a) and 7(b) present the real and imaginary part of the input impedance as a function of W1, respectively. Figures 8(a) and 8(b) present the real and imaginary part of the input impedance as a function of W2, respectively. Following the same idea, Figures 9 and 10 present the input impedance variations with S and D dimensions, respectively.
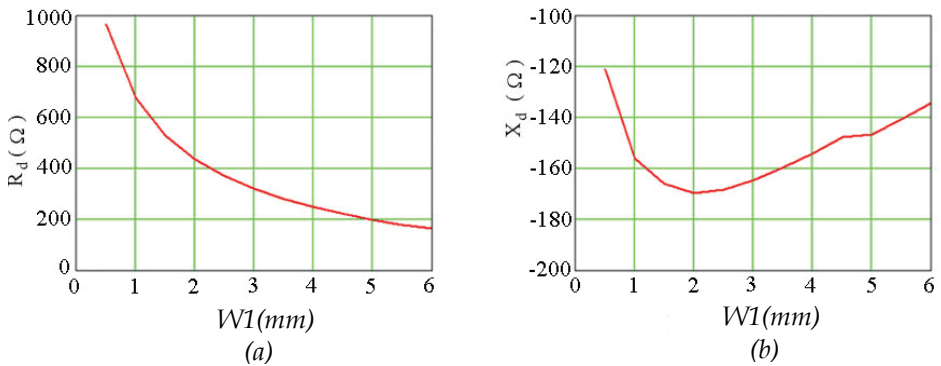


Fig. 7. Input impedance as a function of W1. (a) is the real part and (b) is the imaginary part.
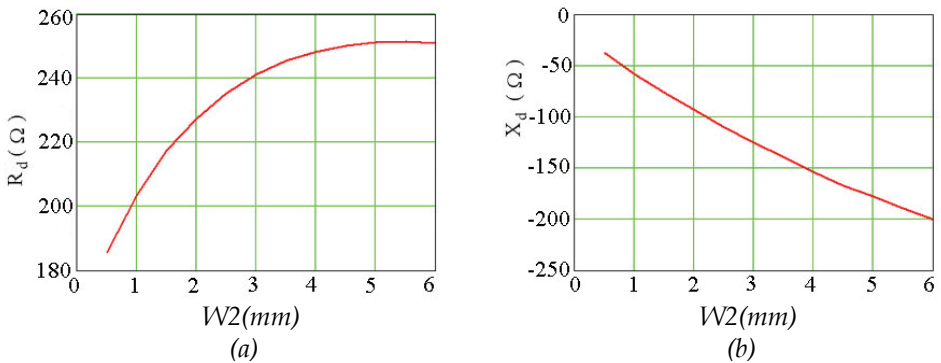


Fig. 8. Input impedance as a function of W2. (a) is the real part and (b) is the imaginary part.
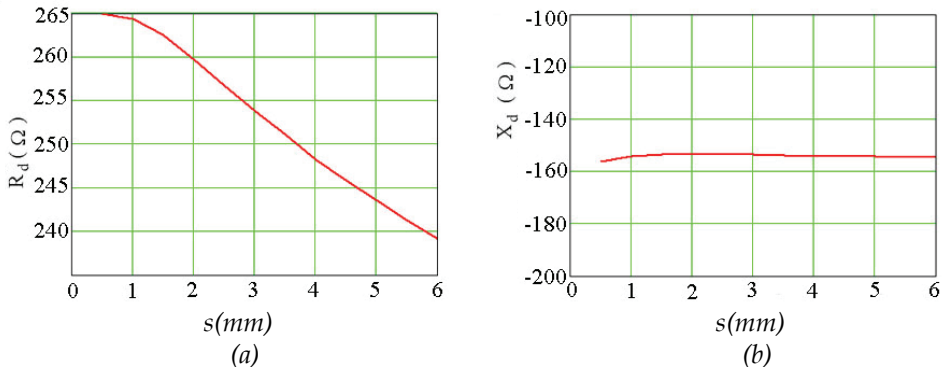
Fig. 9. Input impedance as a function of *s*. (a) is the real part and (b) is the imaginary part.
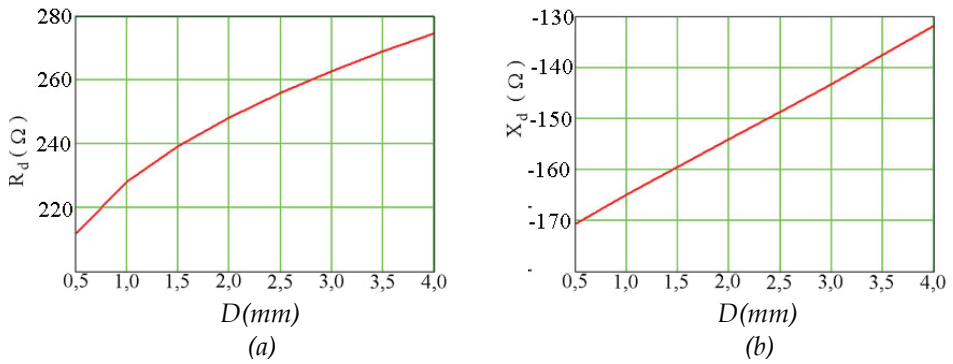


Fig. 10. Input impedance as a function of *D*. (a) is the real part and (b) is the imaginary part.

The half-antenna input impedance at the plane A-A′ (Figure 4) is given by the usual equation for transmission lines (Chang, 1992):

$$Z_{in} = Z_0 \frac{Z_{dipole} + Z_0 tanh(\gamma L)}{Z_0 + Z_{dipole} tanh(\gamma L)} \qquad (2)$$

where $\gamma$ is the propagation constant of the wave, L is the transmission line section length and $Z_0$ is the characteristic impedance of the transmission line. The value of $Z_0$ is also calculated by quasi-static conformal mapping equations.

Figure 11 shows a coplanar folded dipole design. This structure is more suitable for matching with only the real part of the input impedance. Figures 12(a) and 12(b) present the real and imaginary part of the input impedance as a function of the length of the stub *l*, respectively. The imaginary part goes from negative to positive values as the length *l* increases from 0(mm) to 20(mm). For a fixed value of *l*, Figures 12(a) and 12(b) can be used for impedance match between the antenna and the chip or between the antenna and the network analyzer. Note that the input impedance also can change with the spacing g, the width k and the distance H.
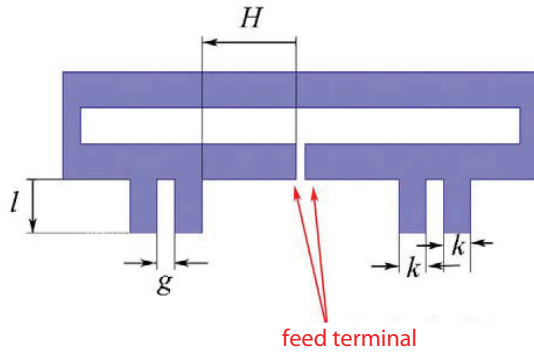
Fig. 11. Dimensions and parameters of the coplanar strip folded dipole.
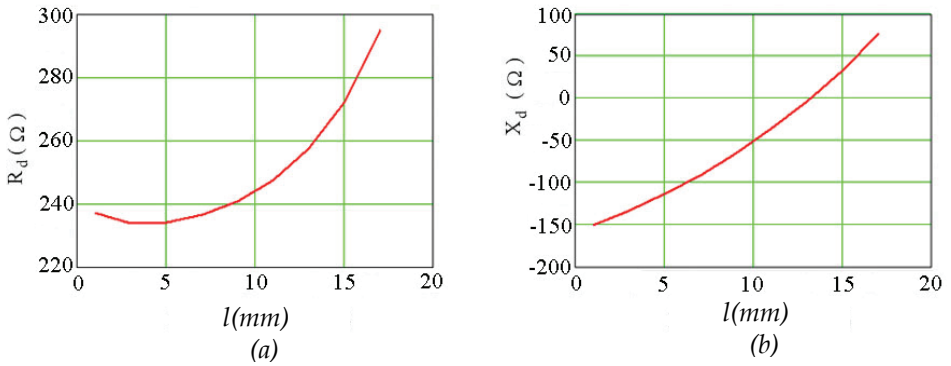


Fig. 12. Input impedance as a function of $l$. (a) is the real part and (b) is the imaginary part.
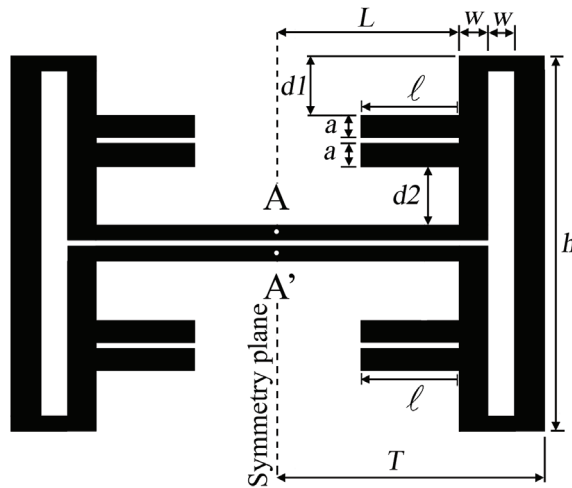


Fig. 13. Antenna layout. The stubs are placed over the dipoles.

| Dimensions | Condition 1 | Condition 2 |
|:---:|:---:|:---:|
| h | 53 mm | 53 mm |
| w | 4 mm | 4 mm |
| a | 3 mm | 3 mm |
| d1 | 8.5 mm | 8.5 mm |
| d2 | 8.5 mm | 8.5 mm |
| L | 26.5 mm | 26.5 mm |
| T | 38.5 mm | 38.5 mm |
| $\ell$ | **0 mm** | **14 mm** |

Table 1. Dimensions of the antenna

Note that all dimensions have the same value for condition 1 and 2, except for $\ell$. The $\ell$ = 0 mm means no stubs. For all dimensions described in Table 1 - condition 1, the input impedance of half the antenna is $Z_{in} = 100 + j100\Omega$. Because its symmetry, the impedance of whole antenna at the plane A-A´ is to be $Z_{ant} = \dfrac{Z_{in}}{2}$. In other words, $Z_{ant} = 50 + j50\Omega$.

The imaginary part of $Z_{ant}$ can be significantly decreased by placing planar stubs over the dipoles. On the other hand, the real part of $Z_{ant}$ is slightly altered. Those facts are important when purely real impedance is needed. That is the case when stubs of length $\ell$ = 14mm are added to the dipoles (Table 1 - Condition 2). At that length, the above described impedance becomes $Z_{ant} = 49\Omega$ and the imaginary part is no longer seen.

## 4. Fabrication measurement and simulation

The antenna described in the previous section was simulated with a full wave EM software. The fabricated antenna with stubs over the dipoles is shown in Figure 14. It was implemented on a RT6002 substrate of thickness 1.5mm, relative dielectric permittivity $\varepsilon_r$ = 2.94 and loss tangent $\delta$ = 0.0012. Simulations were taken in the 1.5 – 3 GHz range. Calculations of input impedance were taken at 2.45GHz, which is the central frequency of the free 2.4GHz part of the spectrum. Figure 15, 16 and 17 show the comparison between simulated and measured results and good agreement can be noticed. Figure 18 and 19 show the radiation pattern and the gain of this proposed antenna at 2.45GHz. The antenna lies in the plane $\theta$ = 90° and has its printed strips at the right-hand side. The maximum gain is increased over the direction perpendicular to the antenna plane. Still from Fig. 7, one sees that the highest simulated gain reaches 5.97dB over an isotropic radiator. The measured gain reaches 5.6dB, which is very close to the simulated one. These values are at least twice higher than the gain of an ordinary dipole (Finkenzeller). Simulated results show how the stub length can modify the $Z_{dipole}$ and the antenna input impedance $Z_{ant}$, as a consequence. Thus, it is possible to choose some suitable stub length for the desired antenna input impedance. For example, for $\ell$ = 14 mm, one finds the simulated antenna input impedance of $Z_{ant} = 50 + j7\Omega$. It is very close to that one of 49 $\Omega$, expected in the section before. On the other hand, the measured value of the new antenna is $Z_{ant} = 48 + j7\Omega$.
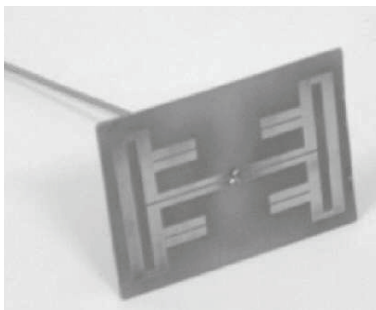
Fig. 14. The printed antenna.
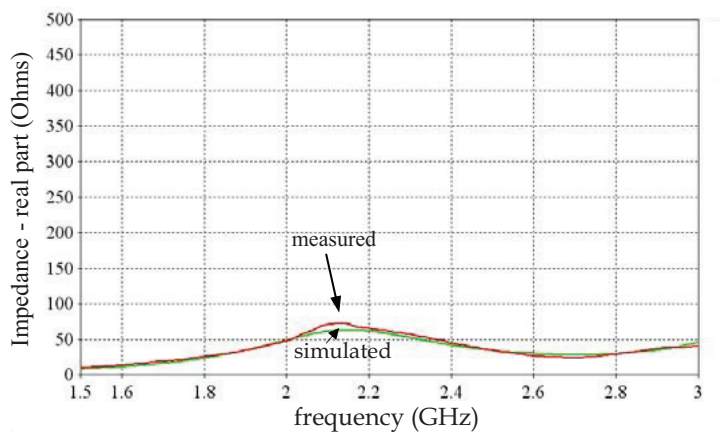


Fig. 15. Simulated and measured real part of the impedance.
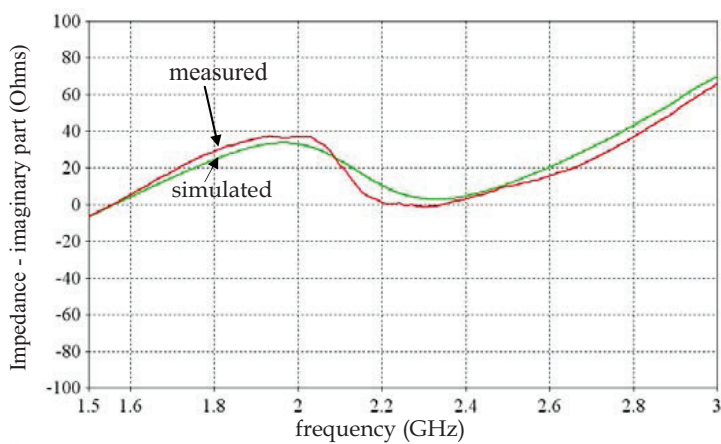


Fig. 16. Simulated and measured imaginary part of the impedance.

In the Figure 16 one notices a slight difference between the simulated and measured responses, at the central frequency. This may be explained due to a possible coupling between the two radiator elements.
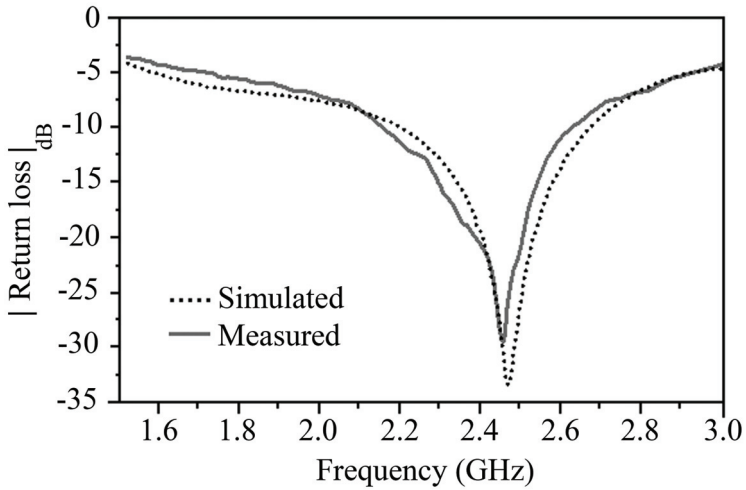


Fig. 17. Comparison of the simulated and measured return loss for the antenna shown in Figure 14.
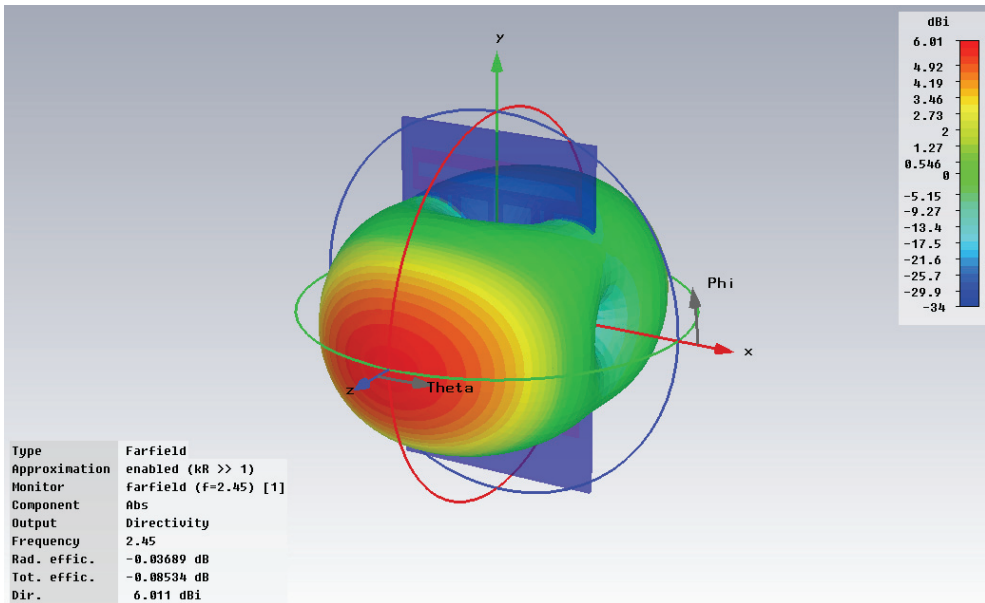


Fig. 18. Simulation results of radiation pattern, directivity, gain and radiation efficiency for the antenna in Figure 14.

For the gain calculation of the antenna in Figure 14, one takes the value from Figure 18. Directivity D = 6,011 dB and radiation efficiency η = 0,003689. Thus, one finds G = 6,011-0,003689 ≅ 5,97dB.
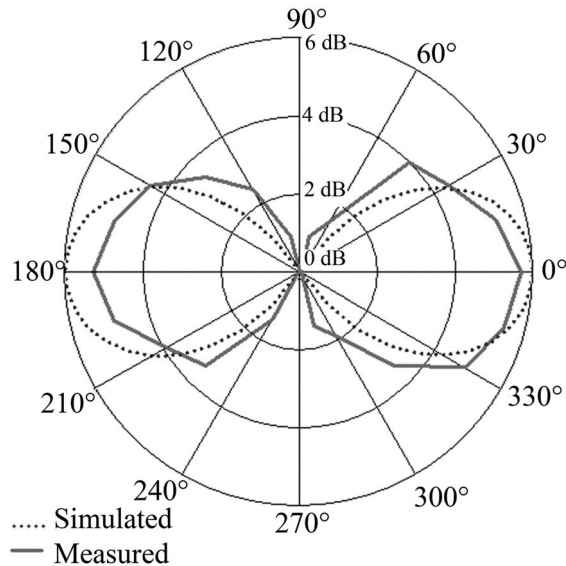


Fig. 19. Simulated and measured antenna gain over an isotropic antenna: 5.97dB and 5.6dB, respectively.

## 5. Conclusion

Good agreement between simulated and measured responses is seen. The reading range of RFID Tags can be increased by 41 % when this antenna is used. Stubs over the dipoles are a very useful tool when impedance adjustments are needed. This antenna has good performance comparing with the commercial versions available and seems to be promising as far as RFID applications are concerned. For the future some improvements can be carried out over the design. Decrease the whole size, modeling equation approach for the gaps, discrete elements equivalent circuit elaboration and insertion of this antenna into an active RFID system.

## 6. References

C. A., Balanis. (1982). "Fundamental Parameters of Antennas", Antenna Theory – Analysis and Design, 2nd ed., New York, NY, USA: John Wiley & Sons, Chapter 2, p. 88.
U. Karthaus and M. Fischer. (2003). "Fully Integrated Passive UHF RFID Transponder IC With 16.7µW Minimum RF Input Power", IEEE Journal of Solid State Circuits, vol. 38, no. 10, pp. 1602-1608, Oct.

K. Finkenzeller, RFID Handbook: Fundamentals and Applications in Contactless Smart Cards and Identification, 2nd edition, New York, NY, USA: John Wiley & Sons, pp.121, 133-136.

R.W. Lampe, (1985). "Design Formulas for an Asymmetric Coplanar Strip Folded Dipole", *IEEE Trans. Antennas and Propagat.*, vol. AP-33, no.9, pp. 1028-1031, Sep.

C. Nguyen, (2001). "Conformal Mapping", Analysis Methods for RF, Microwave and Millimeter-Wave Planar Transmission Line Structures, 1st ed., New York, NY, USA: John Wiley & Sons, Chapter 5, pp. 109-111.

M. T. de Melo, M. J. Lancaster, J. S. Hong, E. J. P. Santos and A. J. Belfort. (1999)."Coplanar Interdigital Delay Line Theory and Measurement". *Proceedings of the 29TH EUROPEAN MICROWAVE CONFERENCE, Munich, Miller Freeman*, v. 3, p. 227-230.

D. K. Cheng. (1992). "Theory and Applications of Transmission Lines", Field and Wave Electromagnetics, 2nd ed., New York, NY, USA: Addison-Wesley, Chapter 9, p. 451.

# 4

# An Inductive Self-complementary Hilbert-curve Antenna for UHF RFID Tags

Ji-Chyun Liu[1], Bing-Hao Zeng[1] and Dau-Chyrh Chang[2]
*[1]Ching Yun University Chung-Li City, Taoyuan County, Taiwan*
*[2]Oriental Institute of Technology Pan-Chiao City, Taipei County, Taiwan*
*R.O.C*

## 1. Introduction

Recently there has been a rapidly growing interest in RFID systems and its applications. Operating frequencies including 125 KHz–134 KHz and 140 KHz–148.5 KHz LF band, 13.56 MHz HF band and 868 MHz–960 MHz UHF band were applied to various supply chains. 433 MHz band was decided for active reader and 2.45 GHz band was applied for WiFi reader. Besides the reader antennas, the requirements of tag antennas are necessary for applications. In which, due to the benefit of long read range and low cost, the UHF tag will be used as the system of distribution and logistics around the world [1–13], [29–41].

Meander line antennas were commonly for UHF tags, due to the characteristics of high gain, omni-directionality, planarity and relatively small surface size [5]. However, the length-to-width ratio limited as 5:1 was proposed [2]. Recently, the half-Sierpinski fractal antenna was introduced with a small length-to-width ratio (<2:1) [11]. Meanwhile, the inductive impedance of tag antenna was necessary for matching the capacitive terminations of chip IC, thus the tuning apparatus was proposed [4], [8]–[10]. H-shaped meandered-slot antennas with the performance of broadband and conjugate impedance matching were developed for on-body applications [14], [15]. On the other hand, the self-complementary dipoles were introduced for the performance of wideband, high impedance and balun [16]–[23].

The Hilbert-curve, proposed by Hilbert and introduced by Peano [24], was known as the space-filling curves. The structure of this shape can be made of a long metallic wire compacted within a patch. As the iteration order of the curve increases, the Hilbert-curve can be space-filling the patch. It has been used in fractal antenna with size reduction [25–28], [44–52].

The main aim of this paper is to merge the meander line and meandered-slot structure of the RFID tag antenna in order to obtain a good performance of compact, broadband and conjugate impedance matching. Meantime, demonstrating the performance with a self-complementary Hilbert-curve tag antenna is proposed. The self-complementary Hilbert-curve tag antenna is constructed with substrate, Hilbert-curve, Hilbert-curve slot and tuning pad. For circular polarization analysis, the current distribution and electric field are exhibited. The inductive and broadband characteristics of frequency responses and directivity feature of radiation patterns and polarization are studied and presented.

## 2. Antenna configuration and basis

### 2.1 UFH RFID meander-line antenna

The typical dipole antenna consists of two parts, in Fig.1, one is the dipole resonators with half-wavelength for resonance and the other is the balun for the impedance transfer of balance to unbalance terminations. The standing voltage and current distribute among the dipole with maxima current and minimum voltage feeding in the center (0°) for linear polarization. For size reduction, in Fig.2, the meander-line configuration was applied in tag antenna. By tuning load-line structure, more wideband and inductive performance can be achieved.
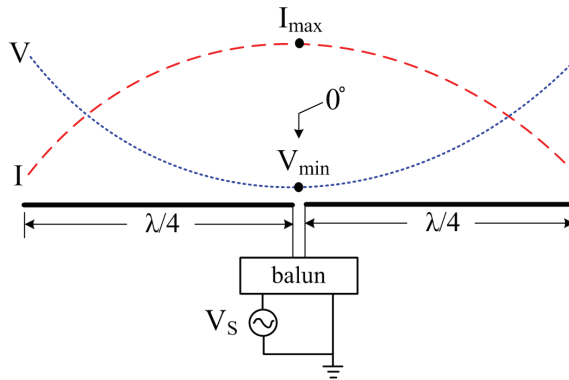
Fig. 1. Dipole antenna
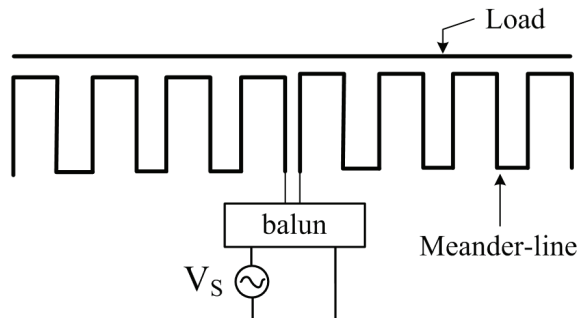
Fig. 2. Meander line antennas

### 2.2 Hilbert-curve and space filling

Hilbert-curve is a space filling curve with being self-similar and simple geometry. The configurations of Hilbert-curve for first four fractal iterations are shown in Figure 3. The original space has filling nature of these curves. This expresses that for a given area of a space, the total length of the line segments increase progressively as the iteration order increases. It can be interpreted as the cause for their relatively lower resonant frequency. It is evident that the fractal iteration order increases, the total length of the line segments

increases, even as the area it encompasses remain the same. Thus within a small area, a lower resonant frequency antenna with very large line length can be accommodated. In applications, the structure of this shape can be made of a long metallic wire compacted within a microstrip patch.

The topological dimension of the line segments is one, as it consists only of a line. The dimension of this original space is an integer value equated two. When we consider the length and number of line segments with 2nd, 3rd and 4th iterations, this dimension are 1.465, 1.694 and 1.834. These values point to the fact the geometry has fractional dimension. **As** the dimension approaches 2, the curve almost fills a space. In other words, for large iteration orders, the total length of the line segments tends to be extremely large. This could be a significant advantage in lower frequency antenna design since the overall effective length of the antenna is large. Thus the resonant frequency can be reduced considerably for a given area, by increasing the fractal iteration order. It may result in a larger reduction factor for the antenna size.
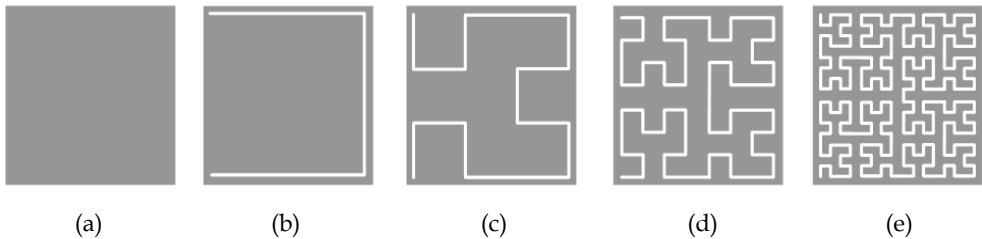


Fig. 3. First four fractal iterations for the Hilbert-curve configurations, (a) original space (b) 1st iterations (c) 2nd iterations (d) 3rd iterations (e) 4th iterations

### 2.3 Self- complementary antennas

Self-complementary antenna composed with electric and magnetic pair antennas is a potential antenna solution for multi-band and wide-band antenna system because of its excellent isolation performance at close proximity between antennas. The pair antennas can be configured with log-period, spiral and circular disk configuration depends on application shown in Fig. 4.

Antenna pair with self-complementary structure has a constant input impedance, independent of the source frequency and the antenna geometry. To achieve wideband CP performance, self-complementary structures were commonly used owing to their features of simple feeding and good axial ratio [17, 18, 23].

### 2.4 Self-complementary Hilbert-curve tag antenna

Complementary Hilbert-curve tag antenna is constructed with substrate, Hilbert-curve, Hilbert-curve slot and tuning pad ($L_t$) in Fig. 5. The Hilbert-curve is consisted of three series Hilbert-curve with the 3rd iteration. The dimensions are $L_1$ = 23.5 mm, $L_2$ = 24 mm, $L_t$ = 5mm, $W_1$ = 7.5 mm, $W_2$ = 8.5 mm, $W_3$ =0.75 mm, $W_4$ = 0.5 mm, and $g$ =0.35 mm. The thickness (h) of RT/duroid-6010 substrate is 6.35 mm (1.27mm×5) and the relative permittivity $\varepsilon_r$ is 10.2 shown in Fig. 6. The length-to-width ratio is 6.2:1 and the shortening ratio SR=0.69. The reduction is notable when the SR is more than 0.40 [2].

(a)



(b)



(c)
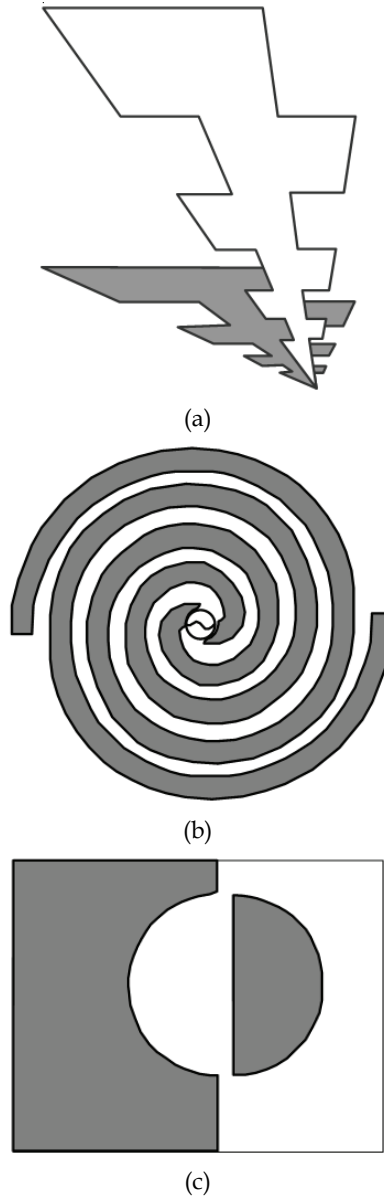
Fig. 4. Self-complementary antenna configurations, (a) log-period (b) spiral (c) circular disk

A typical circular polarization dipole cross-pair usually consist of two individuals with horizontal and vertical locations, and a two-phase signal with 90° difference. Fig. 7 illustrates the simulated current distributions and Fig. 6 depicts the simulated electric fields among the planar structures, which provide a clearly physical insight on understanding the circular polarization of the proposed antenna. Fig. 5 shows that the Hilbert-curve is excited

with concentrating current distributions at the 900 MHz resonance while the maximum amplitude located at –11.3° with deviation from central feed-line (0°). The Hilbert-curve slot is expressed with lower current distributions. Fig. 8 presents both Hilbert-curve line and Hilbert-curve slot are excited with intensive electric fields at the 900 MHz resonance while the minimum amplitude presented at –22.5°.
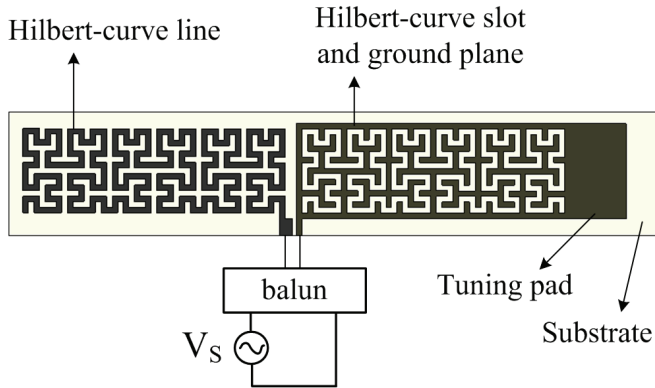
Fig. 5. Complementary Hilbert-curve antenna
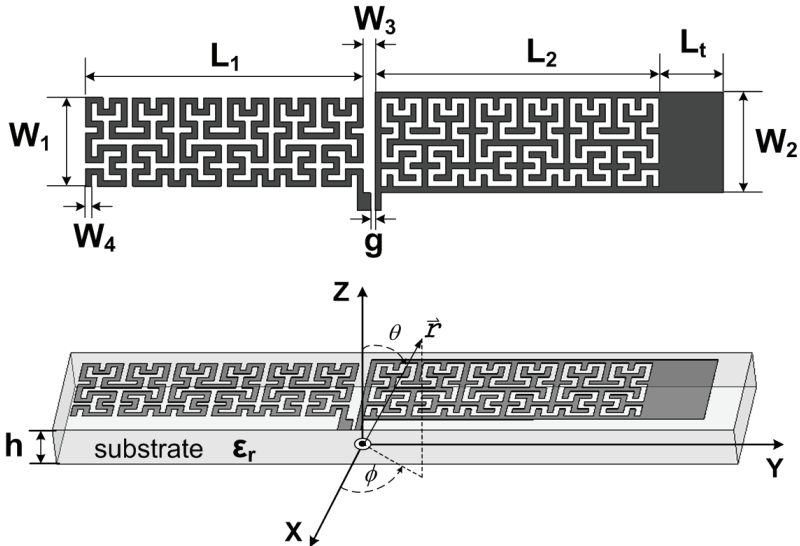
Fig. 6. Dimensions of complementary Hilbert-curve tag antenna

Since the phase difference with 33.8° among maximum current amplitude and minimum electric field existed, in company with the different locations of the left Hilbert-curve line and the right Hilbert-curve slot, the elliptic polarization will be obtained. Thus, the circular polarization can be observed along a certain direction.
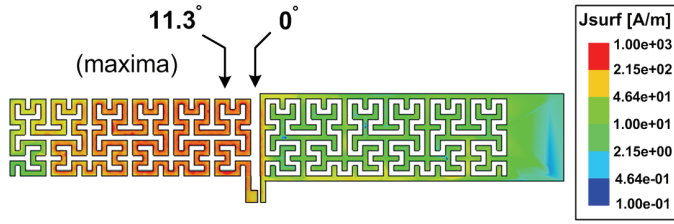
Fig. 7. Current distributions
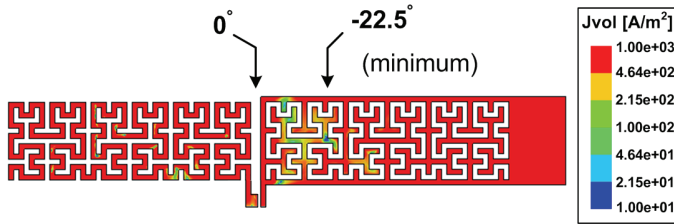


Fig. 8. Electric fields

## 2.5 Applications

The maximum activation distance of the tag for the given frequency is given [14]–[15] by

$$d_{max} = \frac{c}{4\pi f} \sqrt{\frac{EIRP_R}{P_{chip}} \tau G} \tag{1}$$

Where $EIRP_R$ is the effective transmitted power of reader, $P_{chip}$ is the sensitivity of tag microchip, $G$ is the maximum tag antenna gain, and the power transmission factor

$$\tau = \frac{4R_{chip}R_A}{\left|X_{chip} + X_A\right|^2} \leq 1 \tag{2}$$

with tag antenna impedance ( $Z_A = R_A + jX_A$ ) and microchip impedance ( $Z_{chip} = R_{chip} + jX_{chip}$ ).

## 3. Simulations and experiments

By using the commercial software of HFSS tool [42], the simulation results included return loss spectrums, impedance spectrum, circular polarization and two-cut radiation patterns are presented and analyzed. For comparison, the return loss spectrums of the proposed antenna with UHF-bands of 900 MHz are measured and simulated shown in Fig. 9.

The simulated and measured results of frequency responses are in agreement. In measurement, while the return loss is smaller than -10dB, the frequency responses cover both Europe 865.6–867.6 MHz band and USA 902–928 MHz band, ranging from 820 to 935 MHz (bandwidth = 115 MHz). For applications, the frequency responses are fully applied in the operation bands of the RFID UHF-band. For impedance spectrum analysis in Fig. 10, it shows the real parts of impedance become maximum value (178.7 Ω) at 970 MHz frequency,

the real parts of impedance value (102.5 Ω) and the imaginary parts of impedance present inductive characteristic (+41.3 Ω) at 900 MHz frequency. The inductive impedance can be available for matching the capacitive RFID chip.
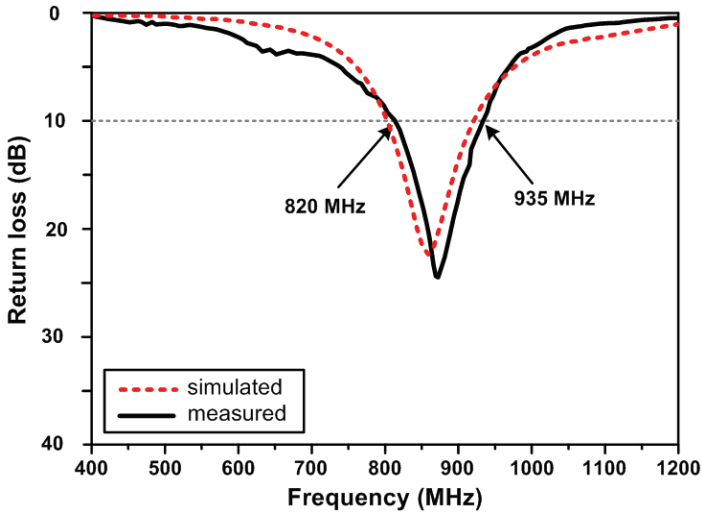
Fig. 9. Simulated and measured results of return loss spectrum
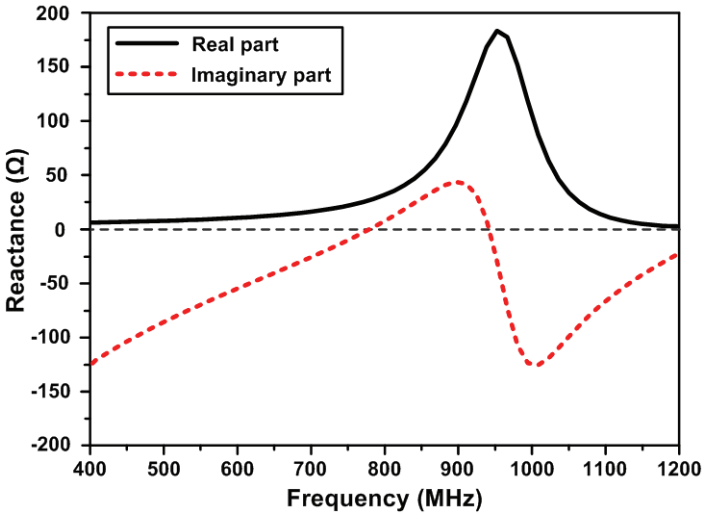
Fig. 10. Simulated results of impedance spectrum

The radiation patterns are obtained by an automatic measurement system in an anechoic chamber. The under-tested antenna is located on the X-Y plane shown in Fig. 4, and the feeding line is located along the X-axis. Thus, two radiation patterns with Y-Z cut and X-Z cut are obtained.

The two cut patterns with resonant 900 MHz are represented in Fig. 11 respectively. Broadside patterns are observed in the Y-Z cut and quasi-omnidirectional patterns are obtained in the X-Z cut. The measured maximum gain was 1.68 dBi for 900 MHz. For polarizations, the AR spectrum is presented in Fig. 12. The minimum AR with 0.16 at $\phi$ = 0°, $\theta$ = 90°and the right-hand circular polarizations (–3dB AR BW = 383 MHz) are observed along the direction of the $\phi$ and $\theta$ , thus the proposed antenna can be applied to circular polarization applications which represents one of the availabilty and usefulness in contrast to the conventional meander-line and meander-slot tags.
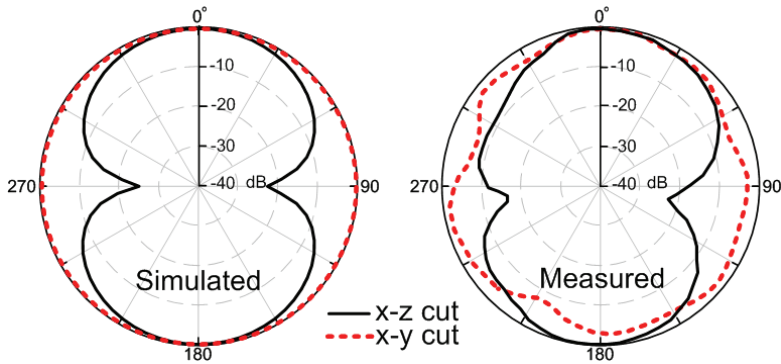


Fig. 11. Radiation patterns for 900 MHz
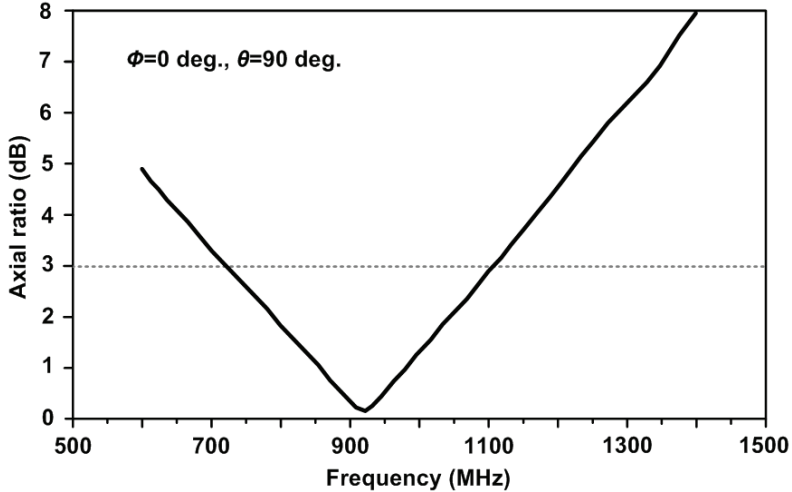


Fig. 12. AR spectrum

## 4. Conjugate matching performance

For example, the effective transmitted power $EIRP_R$ of reader is 1W, the sensitivity $P_{chip}$ of tag microchip is -10dBm, the maximum tag antenna gain $G$ = 1.62dBi, and the activation

distance $d_{min/max}$ = 2.5/3 m, the power transmission factor can be obtained $\tau$ = 0.73/0.87 by using (2). Then, from (3) and tag antenna impedance ($Z_A$ = 102.5+j41.3 $\Omega$ ), the microchip impedance ($Z_{chip}$ = 14.7-j45.2 $\Omega$ ) is calculated. For 900 MHz signal, the capacitance (757 pf) of the chip microchip is presented.

For applications, the variation in antenna impedance, microchip impedance and tuning pad ($L_t$ = 1.0, 2.0, 3.0, 4.0 and 5.0 mm) is shown in Table I. The varied inductive impedance can be available for matching the related capacitive RFID chip (564–787 pf) by tuning the pad length.

| $L_t$ (mm) | $Z_A$ ($\Omega$) | $G_{max}$ (dB) | $d_{min/max}$ (m) | $\tau_{min/max}$ | $Z_{chip}$ ($\Omega$) |
|---|---|---|---|---|---|
| 1 | 97.8+j46.3 | 0.98 | 2.5/3 | 0.71/0.96 | 15.6- j46.4 |
| 2 | 98.7+j45.6 | 1.12 | 2.5/3 | 0.68/0.99 | 14.3- j45.5 |
| 3 | 97.3+j44.2 | 1.21 | 2.5/3 | 0.78/0.98 | 15.7- j44.3 |
| 4 | 99.6+j43.4 | 1.38 | 2.5/3 | 0.76/0.93 | 14.2- j45.8 |
| 5 | 102.5+j41.3 | 1.62 | 2.5/3 | 0.73/0.87 | 14.7- j45.2 |

Table 1. Variation results

A microchip, RI-UHF-STRAP-08 of TI, is used for applications [43]. The data sheet is presented in Table 2. The diagram of complex plane $Z(\omega)$ is presented in Fig. 13. The microchip impedance locus $Z_{chip}(\omega)$ is firstly plotted in the complex plane. The arrowhead attached to the locus indicates the direction of increasing $\omega$ from 860 to 960 MHz. Then, tuning the length, as g=0.45 mm, $L_f$ = 5.8 mm and $L_t$ = 6.3 mm, the antenna impedance locus $Z_a(\omega)$ is obtained. The intersection of these two loci corresponds to the operating point. Due to the operating point $Z_{chip}$ = 287+j55 $\Omega$ and $Z_a$ = 287-j55 $\Omega$ , $\tau$ =0.54 is calculated by (2). As $EIRP_R$ =1W, $P_{chip}$= -13dBm and G = 1.62dBi, $d_{max}$ =33 m is obtained by (1).
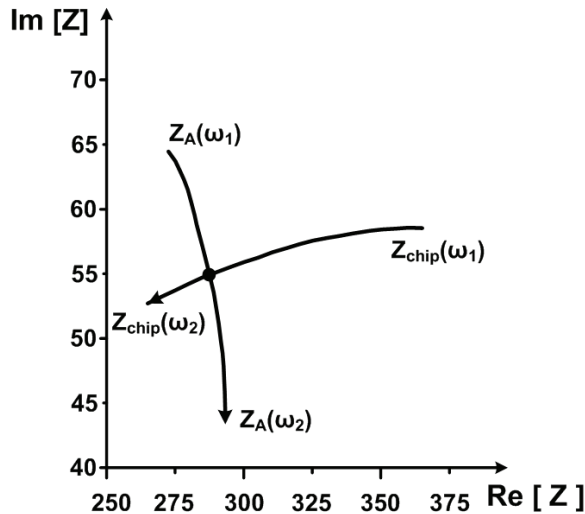


Fig. 13. Impedance locus

| PART NUMBER | RI-UHF-STRAP-08 | | | | |
|---|---|---|---|---|---|
| **Absolute Maximum Ratings** | | | | | |
| | NOTES | Min | Max | Unit | |
| Input current, pad to pad | | | 1 | mA | |
| Input voltage to any pad (sustained) | | | 1.5 | V | |
| Power dissipation | TA = 25°C | | 1.5 | mW | |
| Storage temperature range | Single Strap | -40 | 85 | °C | |
| | On Reel | -40 | 45 | | |
| Operating temperature | Read | -40 | 65 | °C | |
| | Write | -25 | 65 | | |
| Assembly survival temperature | 1 minute maximum | | 150 | °C | |
| RF Exposure | 800 ~ 1000 MHz | | 10 | dBm | |
| ESD immunity | Charged-Device Model (CDM) | 0.5 | | kv | |
| | Human-Body Model (HBM) | 2 | | kv | |
| **Recommended Operating Conditions** | | | | | |
| | | Min | Max | Unit | |
| $T_A$ Operating temperature | | -40 | 65 | °C | |
| $f_{res}$ Carrier frequency | | 860 | 960 | MHz | |
| **Electrical Characteristics** | | | | | |
| PARAMETER | TEST CONDITIONS | Min/ Max | Typ | Unit | |
| Sensitivity | Reading | -9/ - | -13 | dBm | |
| | Programming | -6/ - | -19 | | |
| $\Delta\Gamma$ Change in modulator reflection coefficient | | | >0.2 | | |
| $t_{DRET}$ Data retention | | 10/ - | | Years | |
| W&E Write and erase endurance | | 100000/ - | | Cycles | |
| Strap Parallel Impedance | Typical Read (–13 dB) | | 380 | Ω | |
| | | | 2.8 | pF | |

Table 2. Specification of microchip RI-UHF-STRAP-08

For deterministic design, the design procedure is stated as: The guided wavelength ( $\lambda_g / 2$ ) of the central frequency determines the total length of series Hilbert-curve. The desired response and impedance are then tuned by $L_t$. The final tuning is with $g$. Using (1) and (2) with the specifications and boundary condition $d_{1/2}$, the $Z_{chip}$ is obtained. If it is not satisfied, retuning $L_t$ and $g$ till the desired value is achieved.

## 5. Conclusion

The self-complementary antenna with Hilbert-curve configuration for RFID UHF-band tags is presented in this paper. The good performance of compact, broadband (BW=150 MHz), circular polarization and conjugate impedance matching are achieved for applications. The

structure is smaller in size and easy to fabricate in tag circuits. Its operations cover UHF-bands 820 to 935 MHz for return loss < -10dB. Both simulation and measurement results are agreed with the verified frequency responses. The inductive impedance is achieved and be available for matching the capacitive RFID chip.

In field analysis, broadside patterns are observed in the Y-Z cut and quasi-omnidirectional patterns are obtained in the X-Z cut. The measured maximum gain was 1.68 dBi for 900 MHz. The circular polarization (–3dB AR BW = 383 MHz) feature of radiation patterns for 900 MHz are presented. It is a compact and available tag antenna for UHF RFID applications.

## 6. References

[1] Marrocco, G. (2003). Gain-optimized self-resonant meander line antennas for RFID applications. *IEEE Antennas Wireless Propag. Lett.*, Vol. 2, pp. 302–305, ISSN: 1536-1225.

[2] Keskilammi, M. & Kivikoski, M. (2004). Using text as a meander line for RFID transponder antennas. *IEEE Antennas Wireless Propag. Lett.*, Vol. 3, pp. 372–374, ISSN: 1536-1225.

[3] Ukkonen, L.; Sydanheimo, L. & Kivikoski, M. (2005) Effects of metallic plate size on the performance of microstrip patch-type tag antennas for passive RFID. *IEEE Antennas Wireless Propag. Lett.*, Vol. 4, pp. 410–413, ISSN: 1536-1225.

[4] Son, H.W. & Pyo, C.S. (2005). Design of RFID tag antennas using an inductively coupled feed," *Electron. Lett.*, Vol. 41, No. 18, pp. 994–996, ISSN: 0013-5194.

[5] Rao, K.V.S.; Nikitin, P.V. & Lam, S.F. (2005). Antenna design for UHF RFID tags: a review and a practical application. *IEEE Trans. Antennas Propag.*, Vol. 53, No. 12, pp. 3870–3876, ISSN: 0018-926X.

[6] Ukkonen, L.; Schaffrath, M.; Engels, D.W.; Sydanheimo, L. & Kivikoski, M. (2006). Operability of folded microstrip patch-type tag antenna in the UHF RFID bands within 865-928 MHz. *IEEE Antennas Wireless Propag. Lett.*, vol. 5, pp. 414–417, ISSN: 1536-1225.

[7] Chang, C.C. & Lo, Y.C. (2006). Broadband RFID tag antenna with capacitively coupled structure," *Electron. Lett.*, Vol. 42, No. 23, pp. 1322–1323, ISSN: 0013-5194.

[8] Son, H.W.; Choi, G.Y. & Pyo, C.S. (2006). Design of wideband RFID tag antenna for metallic surfaces. *Electron. Lett.*, Vol. 42, No. 5, pp. 263–265, ISSN: 0013-5194.

[9] Ahn, J.; Jang, H.; Moon, H. Lee, J.W. & Lee, B. (2007). Inductively coupled compact RFID tag antenna at 910 MHz with near-isotopic radar cross-section (RCS) patterns. *IEEE Antennas Wireless Propag. Lett.*, Vol. 6, pp. 518–520, ISSN: 1536-1225.

[10] Hu, S.; Law, C.L. & Dou, W. (2007). Petaloid antenna for passive UWB-RFID tags. *Electron. Lett.*, Vol. 43, No. 22, pp. 1174–1176, ISSN: 0013-5194.

[11] Vemagiri, J.; Balachandran, M.; Agarwal, M. & Varahramyan, K. (2007). Development of compact half-sierpinski fractal antenna for RFID applications. *Electron. Lett.*, Vol. 43, No. 22, pp. 1168–1169, ISSN: 0013-5194.

[12] Kim, K.H.; Song, J.G.; Kim, D.H.; Hu, H.S. & Park, J.H. (2007). Fork-shaped RFID tag antenna mountable on metallic surfaces. *Electron. Lett.*, Vol. 43, No. 23, pp. 1400–1402, ISSN: 0013-5194.

[13] Olsson, T.; Hjelm, M.; Siden, J. & Nilsson, H.E. (2007). Comparative robustness study of planar antenna. *IET Microw. Antennas Propag.*, Vol. 1, No. 3, pp. 674–680, ISSN: 1751-8725.

[14] Marrocco, G. (2007). RFID antennas for the UHF remote monitoring of human subjects. *IEEE Trans. Antennas Propag.*, Vol. 55, No. 6, pp. 1862–1870, ISSN: 0018-926X.

[15] Calabrese, C. & Marrocco, G. (2008). Meandered-slot antennas for sensor-RFID tags. *IEEE Antennas Wireless Propag. Lett.,* Vol.7, pp. 5–8, ISSN: 1536-1225.

[16] Mushiake, Y. (1992). Self-complementary antennas. *IEEE Antennas Propag. Mag.,* Vol. 34, No. 6, pp. 23–29, ISSN: 1045-9243.

[17] Mushiake Y. (2004). A report on Japanese developments of antennas from yagi-uda antenna to self-complementary antennas,"*IEEE Antennas Propag. Mag.*, Vol. 46, No. 4, pp. 47–60, ISSN: 1045-9243.

[18] Xu, P.; Fujimoto, K. & Lin, S. (2002). Performance of quasi-self-complementary antenna Using a monopole and a slot, *Proceeding of IEEE Int. Symp. Antennas and Propag.*, pp. 464–477, ISBN: 0-7803-7330-8, San Antonio, Texas, June 2002, USA.

[19] Xu, P. & Fujimoto, K. (2003). L-shape self-complementary antenna, *Proceeding of IEEE Int. Symp. Antennas and Propag.*, pp. 95–98, ISBN: 0-7803-7846-6, Columbus, Ohio, June 2003, USA.

[20] Mosallaei, H. & Sarabandi, K. (2004). A Compact Ultra-wideband Self-complementary Antennas with Optimal Topology and Substrate, *Proceeding of IEEE Int. Symp. Antennas and Propag.*, pp. 1859–1862, ISBN: 0-7803-8302-8, Monterey, California June 2004, USA.

[21] Saitou, A.; Iwaki, T.; Honjo, K.; Sato, K.; Koyama, T. & Watnabe, K. (2004). Practical realization of self-complementary broadband antenna on low-loss resin substrate for UWB applications, *Proceeding of Int. IEEE MTT-S, Microw. Symp. Digest,* pp. 1265–1268, ISBN: 0-7803-8331-1, YKC Corp., October 2004, Tokyo, Japan.

[22] Wong, K.L.; Wu, T.Y.; Su, S.W. & Lai, J.W. (2003). Broadband printed quasi-self-complementary antenna for 5.2/5.8 GHz operation. *Microwave Opt. Technol. Lett.*, Vol. 39. No. 6, pp. 495-496, ISSN: 1098-2760.

[23] Chen, W.S.; Chang, C.T. & Ku, K.Y. (2007). Printed triangular quasi-self-complementary antennas for broadband operation, *Proceeding of Int. Symp. Antennas and Propag.*, pp. 262–265, Niigata University, August 2007, Niigata, Japan.

[24] Sagan, H. (1994). Space-filling curves, Springer-Verlag, ISBN: 3-540-94265-3, New York.

[25] Anguera, J.; Puente, C. & Soler, J. (2002). Miniature monopole antenna based on the fractal Hilbert curve, *Proceeding of IEEE Int. Symp. Antennas and Propag.*, Vol. 4, pp. 546–549, ISBN: 0-7803-7330-8, San Antonio, Texas, June 2002, USA.

[26] Best, S.R. & Morrow, J.D. (2002). The effectiveness of space-filling fractal geometry in lowering resonant frequency. *IEEE Antennas Wireless Propag. Lett.*, Vol. 1, pp. 112–115, ISSN: 1536-1225.

[27] Gonzalez-Arbesu, J.M.; Blanck, S. & Romeu, J. (2003). The Hilbert curve as a small self-resonant monopole from a practical point of view. *Microwave Opt. Technol. Lett.*, Vol.39, No. 1, pp. 45–49, ISSN: 1098-2760.

[28] Yang, X.S.; Wang, B.Z. & Zhang, Y. (2006). Two-port reconfigurable Hilbert curve patch antenna. *Microwave Opt. Technol. Lett.*, Vol. 48, No. 1, pp. 91–93, Jan. 2006. ISSN: 1098-2760.

[29] Rathod, J.M. & Kosta, Y.P. (2009). Low cost development of RFID antenna, *Proceeding of Asia Pacific. Microwave Conference,* Vol. 7, NO. 10, pp. 1060-1063, ISBN: 978-1-4244-2801-4. Dec. 2009, Singapore.

[30] Toccafondi, A. & Braconi, P. (2007). Compact meander line antenna for HF-UHF tag integration. *Proceeding of IEEE Int. Symp. Antennas and Propag.*, Vol. 9, NO. 15, pp. 5483-5486 , ISBN: 978-1-4244-0877-1, June 2007, Hawaii.

[31] Kin, S.L.; Mun, L.N. & Cole, P.H. (2007). Miniaturization of Dual Frequency RFID Antenna with High Frequency Ratio. *Proceeding of IEEE Int. Symp. Antennas and Propag.*, Vol. 9, No. 15, pp. 5475-5478 , ISBN: 978-1-4244-0877-1, June 2007, Hawaii.

[32] Roudet, F.; Vuong, T.P. & Tedjini, S. (2007). Metal effects over 13.56 MHz RFID reader antenna in an electrical switchboard. *Proceeding of IEEE Int. Symp. Antennas and Propag.*, Vol. 9, NO. 15, pp. 2777-2780, ISBN: 978-1-4244-0877-1. June 2007, Hawaii.

[33] Pengcheng, L.; Yu, J.R. & Chieh, P.L. (2008). A experiment study of RFID antennas for RF detection in liquid solutions. *Proceeding of IEEE Int. Symp. Antennas and Propag.*, Vol. 5, NO. 11, pp. 1-4, ISBN: 978-1-4244-2041-4. July 2008, San Diego, CA.

[34] Toccafondi, A.; Giovampaola. C.D.; Mariottini, F. & Cucini, A. (2009). UHF-HF RFID integrated tag for moving vehicle identification. *Proceeding of IEEE Int. Symp. Antennas and Propag.*, Vol. 1, NO. 5, pp. 1-4, ISBN: 978-1-4244-3647-7. June 2009, Charleston, SC.

[35] Iliev, P.; Le Thuc, P.; Luxey, C. & Staraj, R. (2009). Dual-band HF-UHF RFID tag antenna. *Electron. Lett.,* Vol. 45, NO. 9, pp. 439-441, ISBN: 0013-5194.

[36] Hirvonen, M.; Pesonen, N.; Vermesan, O.; Rusu, C. & Enoksson, P. (2008). Multi-system, multi-band RFID antenna: Bridging the gap between HF- and UHF-based RFID applications. *Proceeding of European Microwave Conference on Wireless Technol.,* Vol. 27, No. 28, pp. 346-349, ISBN: 978-2-87487-008-8. Oct. 2008, Amsterdam.

[37] Wang, D.; Xu, L.; Huang, H. & Sun, D. (2009). Optimization of Tag Antenna for RFID System. *Proceeding of Information Technology and Computer Science on International Conference,* Vol. 2, No. 26, pp. 36-39, ISBN: 978-0-7695-3688-0. July 2009, Kiev.

[38] Bassen, H.; Seidman, S.; Rogul, J.; Desta, A. & Wolfgang, S. (2007). An Exposure System for Evaluating Possible Effects of RFID on Various Formulations of Drug Products. *Proceeding of IEEE Int. Conference on RFID,* Vol. 26, NO 28, pp. 191-198, ISBN: 1-4244-1013-4. March 2007, Grapevine, TX.

[39] Allen, M.L.; Jaakkola, K.; Nummila, K. & Seppa, H. (2009). Applicability of Metallic Nanoparticle Inks in RFID Applications. *IEEE Trans. Components and Packaging Technologies,* Vol. 32, No. 2, pp. 325-332, ISBN: 1521-3331.

[40] Mayer, L.W. & Scholtz, A.L. (2008). A Dual-Band HF / UHF Antenna for RFID Tags. *Proceeding of IEEE 68th Vehicular Technology Conference,* Vol. 21, No. 24, pp. 1-5, ISBN: 1090-3038. Sept. 2008, Calgary, BC.

[41] Kariyapperuma, A.V. & Dayawansa, I.J. (2009). Bi-loop' RFID reader antenna for tracking fast moving tags. *Proceeding of IEEE Radio and Wireless Symposium,* Vol. 18, No. 22, pp. 449-452, ISBN: 978-1-4244-2698-0. Jan. 2009, San Diego, CA. HFSS version 11.0, Ansoft Software Inc., 2007. Texas Instruments Incorporated, http://www.ti.com/.

[42] Vinoy, K.J.; Jose, K.A.; Varadan, V.K. & Varadan, V.V. (2001). Resonant Frequency of Hilbert Curve Fractal Antennas. *Proceeding of IEEE Int. Symp. Antennas and Propag.*, Vol. 3, pp. 648–4651, ISBN: 0-7803-7070-8. July 2001Boston, MA.

[43] Vinoy, K.J.; Jose, K.A.; Varadan, V.K. & Varadan, V.V. (2001) Hilbert Curve Fractal Antennas with Reconfigurable Characteristics. *Inte. Microwave Symposium Digest, IEEE MTT-S l.* Vol.1, pp.381-384, ISBN: 0-7803-6538-0. 2001, Phoenix, AZ.

[44] Yang, X.S.; Wang, B.Z. & Zhang, Y. (2005). A Reconfigurable Hilbert Curve Patch Antenna. *Proceeding of IEEE Int. Symp. Antennas and Propag.*, Vol.2B, pp.613-616, ISBN: 0-7803-8883-6. July 2005.

[45] Murad, N.A.; Esa, M.; Yusoff, M.F.M.; & Ali, S.H.A. (2006). Hilbert Curve Fractal Antenna for RFID Application. *Inte. RF and Microwave Conference,* pp.182-186, ISBN: 0-7803-9745-2. Sept. 2006, Putra Jaya.

[46] Takemura, N. (2009). Inverted-FL antenna with self-complementary structure. *IEEE Trans. Antennas Propag.*, Vol. 57, No.10 , pp. 3029–3034, ISSN : 0018-926X.

[47] Suh, S.Y.; Nair, V.K.; Souza, D. & Gupta, S. (2007). High isolation antenna for multi-radio antenna system using a complementary antenna pair. *Proceeding of IEEE Int. Symp. Antennas and Propag.*, pp.1229-1232, ISBN: 978-1-4244-0877-1. June 2007, Honolulu, HI.

[48] Guo, L.; Chen, X. & Parini, C.G. (2008). A Printed Quasi-Self-Complementary Antenna for UWB Applications. *Proceeding of IEEE Int. Symp. Antennas and Propag.*, pp.1-4, ISBN: 978-1-4244-2041-4. July 2008, San Diego, CA.

[49] Guo, L.; Wang, S.; Chen, X. & Parini, C. (2009). A Small Printed Quasi-Self-Complementary Antenna for Ultrawideband Systems. *IEEE Antennas Wireless Propag.* Vol.8, 2009, pp.554-557, ISSN : 1536-1225.

[50] Xu, P.; Kyohei F. & Shiming L. (2002). Performance of Quasi-Selfcomplementary Antenna Using a Monopole and a Slot. *Proceeding of IEEE Int. Symp. Antennas and Propag.*, pp.464-467, ISBN: 0-7803-7330-8. 2002.

# Design of a Very Small Antenna for Metal-Proximity Applications

Yoshihide Yamada

*National Defence Academy, Dept. of Electronic Engineering*
*Japan*

## 1. Introduction

A radio frequency identification (RFID) system consists of a reader, a writer, and a tag. Film-type half-wavelength dipole antennas (shown in Fig. 1.1) have been used as tag antennas in many applications [1]. The antenna performance is governed by the electric current in the tag. When the abovementioned antenna is mounted on the surface of a metallic object, the radiation characteristics are seriously degraded because of the image current induced in the object. Therefore, studies have been carried out to construct tag antennas that are suitable for use with metallic objects, and some promising antenna types have been proposed.

In this chapter, design approaches for metal-proximity antennas (antennas placed in close proximity to a metal plate) are discussed. In Section 2, typical metal-proximity antennas are described. An example of the aforementioned type of antenna is a normal-mode helical antenna (NMHA), which can show high efficiency despite its small size. We focus on the design of this antenna. In Section 3, the fundamental equations used in the NMHA design are summarized. In particular, we propose an important equation for determining the self-resonant structure of the antenna. We fabricate an antenna to show that its electrical characteristics are realistic. In Section 4, we explain the impedance-matching method necessary for the NMHA and provide a detailed description of the tap feed. In Section 5, we discuss the use of NMHA as a tag antenna and provide the read ranges achieved.
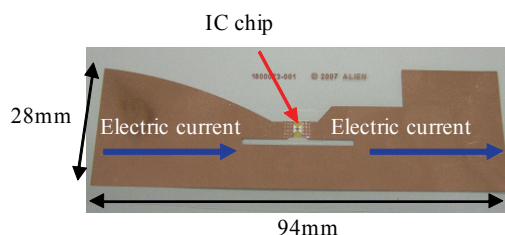


Fig. 1.1 A typical tag antenna

## 2. Tag antennas for metal-proximity use

Typical examples of metal-proximity tag antennas are given in Table 2.1. Some examples of metal-proximity antennas are patch antennas [2] and slot antennas [3], which can be

mounted on a metal plate. Since these antennas comprise flat plates, the antenna thickness decreases but the size does not small. Another example of a metal-proximity antenna is the normal-mode helical antenna (NMHA) [4]. The wire length of this antenna is approximately one-half of the wavelength, and hence, the antenna is small-sized. Moreover, because this antenna has a magnetic current source, it can be mounted on a metallic plate. The antenna gain increases when the antenna is placed in the vicinity of a metal plate. Because the antenna input resistance is small, a tap-feed structure is necessary to increase the resistance.

|  |  |  |
|---|---|---|
| ·Frequency　953MHz<br>·Thickness : 4mm<br>·Read range : 13m<br>·Commercial products | ·Frequency　915MHz<br>·Thickness : 0.25mm<br>·Read range : 5m<br>·Researching | ·Frequency　953MHz<br>·Thickness : 16mm<br>·Read range : 8m<br>·Researching |
| [2] Patch antenna | [3] Slot antenna | [4] Normal mode helical antenna |

Table 2.1 Metal-proximity tag antennas
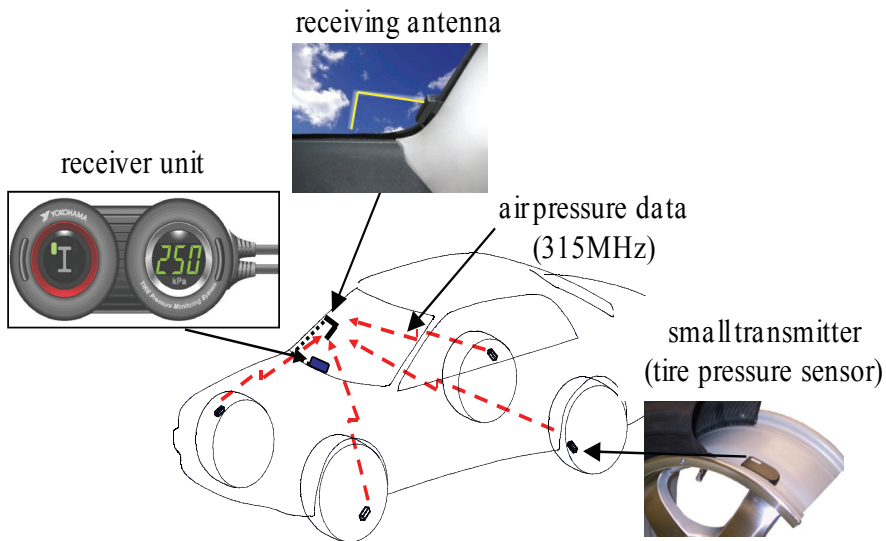


Fig. 2.1 Application of NMHA to tire-pressure monitoring system

The feasibility of using very small NMHAs in a tire-pressure monitoring system (TPMS) [5] and metal-proximity RFID tags [6] has been studied. The RFID applications are explained in

detail in Section 5. Figure 2.1 shows the TPMS system (called AIRwatch) developed by The Yokohama Rubber Co., Ltd. Transmitters connected to tire-pressure sensors are mounted on the wheels, and a receiver unit is placed on the dashboard. A receiving antenna (a film antenna) is attached to the windshield. Each sensor uses the FSK scheme to modulate 315-MHz continuous waves with air pressure data. The modulated waves are transmitted from a small loop antenna in the sensor. The receiving antenna collects all the transmitted waves, and the pressure levels are indicated on the receiver unit. To apply this system to trucks and buses, it is necessary to replace the small-loop antenna with an NMHA [7] since the gain and effectiveness of the latter are high under metal-proximity conditions.

## 3. Design and electrical characteristics of normal-mode helical antenna

### 3.1 Features of NMHA

The structural parameters of the NMHA are shown in Fig. 3.1. The length, diameter, and number of turns of the antenna are denoted by $H$, $D$, and $N$, respectively. The diameter of the antenna wire is denoted by $d$. A comprehensive treatment of this antenna has been given by Kraus [8]. In Kraus's study, the antenna current was divided across the straight part and circular parts of the antenna. Conceptual expressions for the two current sources are shown in Fig. 3.1. The straight part acts like a small dipole antenna, and the circular parts act like small loop antennas. The radiation characteristics of these small loops are equivalent to those of a small magnetic current source. Therefore, the radiated electric fields are composed of two orthogonal electrical components produced by electric and magnetic current sources. Hence, the radiated electric field polarization becomes circular or elliptical depending on the $H$-to-$D$ ratio. Because the radiated fields are produced by small electrical and magnetic current sources, the radiation patterns are almost constant for various small antennas. The directional gain is almost 1.5 (1.8 dBi).
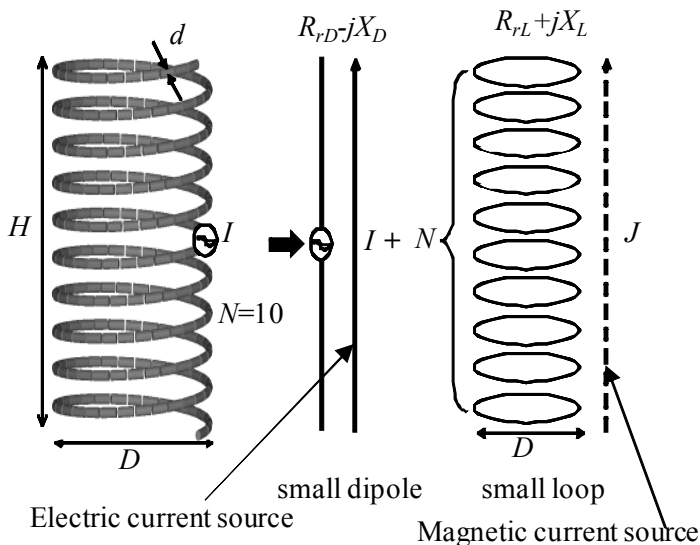


Fig. 3.1 Conceptual equivalence of normal-mode helical antenna

The existence of a magnetic current source is advantageous for using an antenna in the proximity of a metal plate. The electrical image theory indicates that radiation from a magnetic current source is increased by the existence of a metal plate. Another important feature of an NMHA is its impedance. A small dipole has capacitive reactance, and the small loops have inductive reactance. By appropriate choice of the $H, D,$ and $N$ values, the capacitive and inductive reactances can be made to cancel out each other. This condition is called the self-resonant condition, and it is important for efficient radiation production. In this case, the input impedance becomes a pure resistance. It should be noted that this pure resistance is small, and therefore, an impedance-matching structure is necessary. Moreover, the ohmic resistance of the antenna wire must be reduced to a considerable extent.

Important aspects of the NMHA design are summarized in Table 3.1. Simple equations for $R_r, R_l, E_\theta,$ and $E_\phi$, which are related to radiation production, have been presented by Kraus [8]. A useful expression for the inductive reactance ($X_L$) has been developed by Wheeler [9]. However, a correct expression for the capacitive reactance ($X_C$) has not yet been presented; we plan to develop the appropriate equation for this value. We also compare the theoretical values of the antenna quality factor (Q) with the experimental results. We then consider an important design equation that can be used to determine the self-resonant structures. This equation is derived from the equations for $X_L$ and $X_C$, and its accuracy is confirmed by comparison of the calculated and simulated results. Using these equations, we can design small antennas with high gain. Because the radiation patterns are almost constant, the antenna efficiency is important for achieving high gain. Finally, the impedance-matching method is important, and three methods are usually considered. However, in the first method among these, the circuit method, the antenna gain is greatly reduced because of the accompanying ohmic resistances of the circuit elements.

| Aspect | Features | Comments |
|---|---|---|
| Equations of electrical characteristics | Input resistance: $R_r$, $R_l$<br>Radiation fields: $E_\theta$, $E_\phi$<br>Input reactance: $X_L$, $X_C$<br>Q factor | Antenna efficiency<br>Polarization<br>Self-resonance<br>Bandwidth |
| Self-resonant structure | Determine relation between N, H, D: Using $X_L = X_C$ condition | Design equation must be developed |
| Design data for high antenna performance | Antenna efficiency | Low ohmic resistance is necessary |
| Impedance matching | Circuit method<br>Off-center feed<br>Tap feed | Not suitable<br>Limited application<br>Most useful |

Table 3.1 Important aspects of NMHA design

To estimate the electrical characteristics of the NMHA, we perform electromagnetic simulations based on the method of moments (MoM) using a commercial simulator, FEKO.

We compare the simulated results with the experimental results. By appropriate choice of the simulation parameters, we can obtain reliable results.

## 3.2 Equations for main electrical characteristics
### 3.2.1 Equations of electrical constants for radiation
The radiation characteristics of small antennas are estimated from the antenna input impedance, which is given by

$$Zin = R_{rD} + R_{rL} + R_l + j(X_L - X_C) \tag{3.1}$$

Here, $R_{rD}$ is the radiation resistance of the small dipole; $R_{rL}$, the radiation resistance of the small loops; and $R_l$, the ohmic resistance of the antenna wire. $X_L$ and $X_C$ are the inductive and capacitive reactances, respectively. The exact expressions for $X_L$ and $X_C$ will be discussed in the later sections.

We now summarize the expressions for the radiation characteristics.

a. Small dipole [10]

The radiation characteristics of the small dipole are given by the following expressions, in which the structural parameters shown in Fig. 3.1 are used:

$$Rr_D = 20\pi^2 \left( \frac{H}{\lambda} \right)^2 \tag{3.2}$$

Here, $\lambda$ is the wavelength.

$$E_\theta = \frac{IHe^{-j\kappa R}}{j\ 4\pi\omega\varepsilon} \left( \frac{1}{R^3} + \frac{j\kappa}{R^2} - \frac{\kappa^2}{R} \right) \sin\theta \tag{3.3}$$

Here, I is the antenna current, R is the distance from the antenna, and k is the wave number. The terms $1/R^2$ and $1/R^3$ represent the static electric field and the inductive electric field, respectively. The values of $1/R^2$ and $1/R^3$ decrease rapidly as R increases. The $1/R$ term indicates the far electric field and corresponds to the radiated electric field.

b. Small loop [11]

The radiation characteristics of the small loops are given by the following expressions, in which the structural parameters shown in Fig. 3.1 are used:

$$R_{rL} = 320\pi^6 (a/\lambda)^4\ n^2 \tag{3.4}$$

Here, $a$ and $n$ indicate the radius of the loop and the number of turns, respectively.

$$E_\phi = \frac{\omega\mu ISe^{-j\kappa R}}{4\pi} \left( -\frac{j}{R^2} + \frac{\kappa}{R} \right) \sin\theta \tag{3.5}$$

The $1/R$ term represents the radiated electric field. Here, I is the loop antenna current, and S is the area of a loop.

## 3.2.2 Equations for input reactance of NMHA [12]
The equivalent model of the small dipole and small loops (shown in Fig. 3.1) cannot be used for the expressions for $X_L$ and $X_C$. For the stored electromagnetic power of the NMHA, highly precise electromagnetic models must be developed.

a. Self-resonant structure

The self-resonant structures of an NMHA are important when designing reactance equations. These structures can be obtained from the structural parameters that satisfy the condition $X_L = X_C$. The aforesaid parameters can be easily identified by electromagnetic simulations, but such simulations are tedious and time-consuming.. An alternative method would involve the use of design equations. However, a convenient equation for determining the resonant structure has not yet been developed; we plan to develop such an equation.

The self-resonant structures calculated from simulations are shown in Fig. 3.2. Here, the 315-MHz data used for the TPMS are shown. For a given $N$ value, a strict relationship between $H$ and $D$ is determined. As $N$ increases, $D$ decreases rapidly, indicating that the total wire length ($L_0$) of the antenna changes only to a slight extent. The calculated wire lengths are shown in Fig. 3.3. The values of $L_0/\lambda$ range from 0.35 to 0.72. These data are important for choosing the appropriate wire length when fabricating an actual antenna.[61.38]
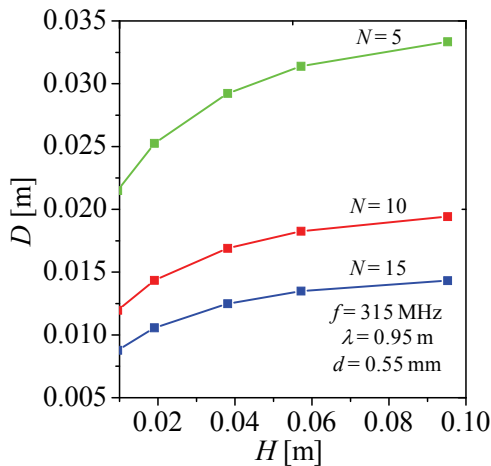


Fig. 3.2 NMHA resonant structures
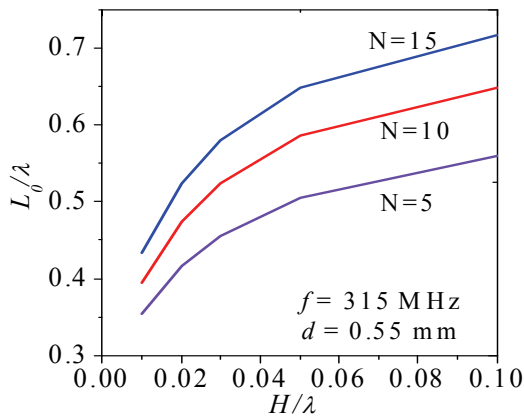


Fig. 3.3 NMHA wire lengths ($L_0$)

The typical electrical performance of the self-resonant structure is the excited current in the antenna. The peak electrical currents of the resonance are shown in Fig. 3.4. To illustrate the physical phenomena in detail, sequential $N$ values of 4, 5, and 6 are selected. In the calculation, the feed voltage $V$ is set to 1 V. The current values show a peak near the resonant structures. The current decreases rapidly with an increase in the distance between the resonant structure and the measurement point. The condition $X_L = X_C$ is important for the production of strong radiation currents. Another important point to be noted is that the peak current values are almost inversely proportional to $H$. Since $V = R_{in}I_M$, an increase in $I_M$ implies a decrease $R_{in}$. As exepected, $R_{in}$ decreases as $H$ decreases.
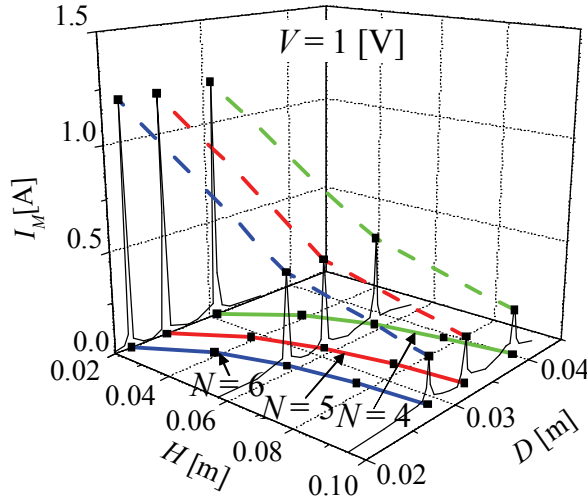


Fig. 3.4 Maximum currents near the resonances

b.    Equation for inductive reactance

The calculated magnetic field distributions are shown in Fig. 3.5. It can be seen that the magnetic field vectors constantly pass through the coil. The field distributions around the anntena are similar to those in the case of a conventional coil. No unique distributions are observed.

The equation for the antenna inductance ($L_W$) was established by Wheeler [9]. By applying Wheeler's equation to the center-feed antenna, we obtain

$$L_W = \frac{19.7ND^2}{9D + 20H} \times 10^{-6} \quad [\text{H}] \tag{3.6}$$

Here, the unit [H] stands for Henry.

The inductive reactance ($X_L$) is given by

$$X_L = \omega L_W \quad [\Omega] \tag{3.7}$$

The calculated inductive reactance $X_L$ (Fig. 3.6) is rather large: it ranges from 59 Ω to 205 Ω. In this figure, the dependence of $X_L$ on the structural parameters ($N$, $D$, and $H$) is explained by taking into account Eq. (3.6). The relation between $X_L$ and $H$ is determined on the basis of

the denominator in Eq. (3.6). The change in $X_L$ with $N$ is rather slow and is determined by the term $ND^2$ in this equation.
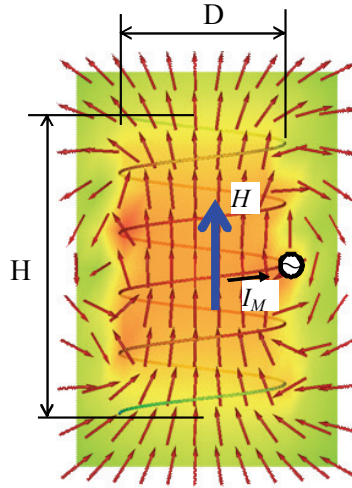


Fig. 3.5 Magnetic field distribution
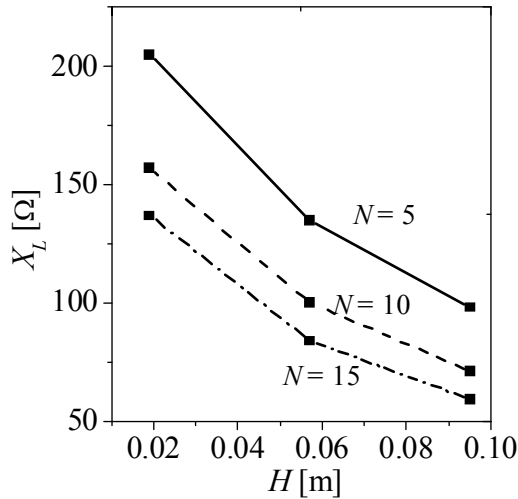


Fig. 3.6 Inductive reactance

c.    Equation for capacitive reactance

In this chapter, we discuss the development of a useful expression for capacitive reactance. The calculated electric field distributions are shown in Fig. 3.7. The directions of the electric field vectors appear to be unique. At the edges of the antenna, the vectors appear to converge or diverge in specific areas. These areas form short cylinders of height αH, as shown by the dashed lines.
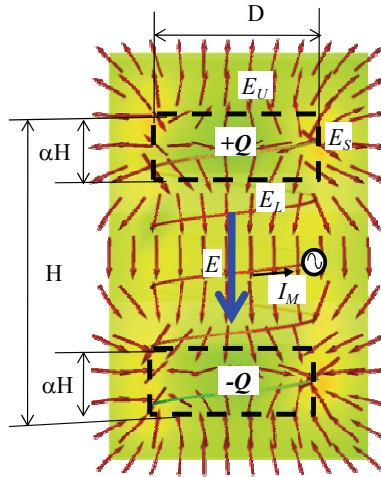
Fig. 3.7 Electric field distributions
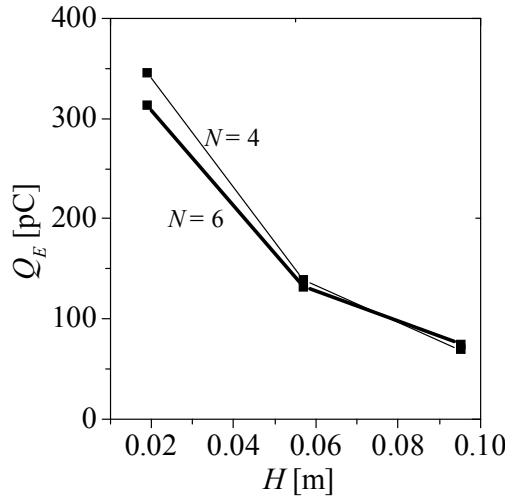


Fig. 3.8 Stored charge

By applying the divergence theorem of Maxwell's equation, we calculate the charge stored in a cylinder from the following equation:

$$Q = \varepsilon \iint E dS = \varepsilon \left\{ \iint E_S dS + \iint E_L dS + \iint E_U dS \right\} \quad [C] \tag{3.8}$$

Here, the unit [C] stands for Coulomb. Surface integrals over the side wall, lower disc, and upper disc of the cylinder are evaluated.

The calculated $Q$ values are shown in Fig. 3.8. By comparing the cylinder height coefficients ($\alpha$) of many resonant structures, we estimated the value of $\alpha$ in the present study to be 0.21.

The $Q$ values are inversely proportional to $H$; this trend agrees well with the relationship between $I_M$ and H shown in Fig. 3.4. This agreement corresponds to the relation $Q = I_M / \omega$. The magnitude of $\omega$ (= $2\pi f$) is $2 \times 10^9$. If we set $I_M$ and $H$ to 1.2 A and 0.02 m, respectively, in Fig. 3.4, we have

$$I_M / \omega = 1.2/(2 \times 10^9) = 600 \times 10^{-12} \tag{3.9}$$

The value derived using Eq. (3.9) corresponds well with the Q and H values (400 pC and 0.02 m, respectively) determined from Fig. 3.8. Thus, the use of Eq. (3.8) is justified.

The next step is to derive an expression for the capacitance (C) on the basis of Eq. (3.8). The relationship between Q and C depends on the electric power (We). Two expressions for We are given as follows.

$$W_e = \frac{Q^2}{2C} \tag{3.10}$$

This expression gives the total electric power stored in the +Q and –Q capacitor.

$$W_e = \zeta \iiint \varepsilon E_L^2 dv / 2 \tag{3.11}$$

The volume integral gives the electric power in the NMHA. The coefficient $\zeta$ is introduced to express the total power.

By equating Eqs. (3.10) and (3.11), we obtain an expression for $C$:

$$C = \frac{\left\{ \varepsilon \iint E dS \right\}^2}{\zeta \varepsilon \iiint E_L^2 dv} \tag{3.12}$$

Eq. (3.12) can be converted into an expression based on the structural parameters:

$$C = \frac{\varepsilon^2 N \left\{ \pi DaHE_S + \pi(\frac{D}{2})^2 (E_U + E_L) \right\}^2}{\zeta \varepsilon E_L^2 \pi(\frac{D}{2})^2 (1 - 2\alpha)H} = \frac{3.82 \varepsilon \pi N (4.4\alpha H + D)^2}{4\zeta(1 - 2\alpha)H} \tag{3.13}$$

Here, we use the conditions $E_S = 1.1(E_L + E_U)$ and $E_S = 2.15E_L$, on the basis of the simulation results; $\alpha$ is the cylinder height shown in Fig. 3.7. For the $N$ dependence, we recall the $ND^2$ term in Eq. (3.6). To model the gradual change of $C$ with $N$ we multiply $N$ by $(4.4aH+D)^2$.

The expression for $X_C$ is obtained from Eq. (3.13):

$$X_C = \frac{1}{\omega C} = \frac{4\zeta(1 - 2\alpha)H}{3.82\omega \varepsilon \pi N (4.4\alpha H + D)^2} = \frac{279\lambda H}{\pi N (0.92H + D)^2} \tag{3.14}$$

Here, we use $\omega \varepsilon = 1/(60\lambda)$ and $\alpha = 0.21$. Moreover, we set $\zeta$ to 7.66 for equating $X_C$ with $X_L$ at $N = 10$; see Fig. 3.6.

The calculated $X_C$ values are shown in Fig. 3.9. At $N = 10$, the $X_C = X_L$ condition is achieved (Figs. 3.9 and 3.6). At $N = 5$ and $N = 15$, $X_C$ and $X_L$ are in good agreement with each other. As a fall, agreement of $X_C$ and $X_L$ are well. Thus, Eq. (3.14) is confirmed to be useful.
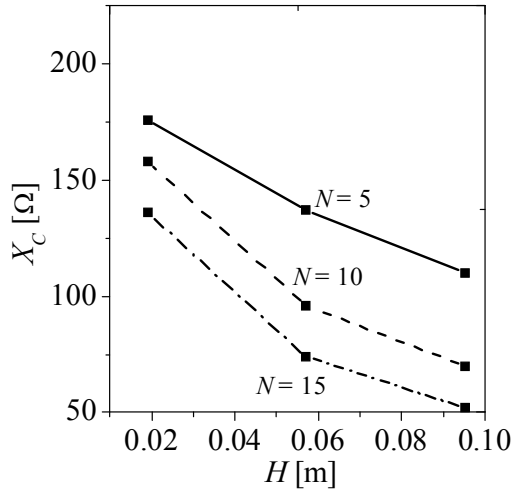
Fig. 3.9 Capacitive reactance
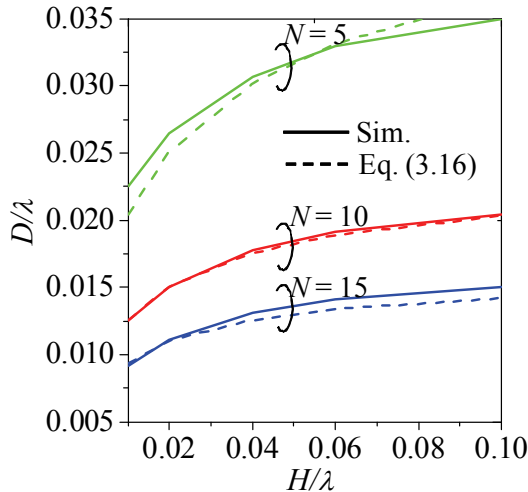


Fig. 3.10 Calculated and simulated self-resonant structures

### 3.2.3 Design equation for self-resonant structures [12]

The deterministic equation is given by equating Eqs. (3.7) and (3.14). The resulting equation is

$$\omega \frac{19.7ND^2}{9D+20H} \times 10^{-6} = \frac{279\lambda H}{N\pi(0.92H+D)^2} \tag{3.15}$$

To clarify the frequency dependence, we divide the numerator and denominator of Eq. (3.15) by $\lambda^2$ and obtain

$$600\pi \frac{19.7N(\frac{D}{\lambda})^2}{9\frac{D}{\lambda}+20\frac{H}{\lambda}} = \frac{279\frac{H}{\lambda}}{N\pi(0.92\frac{H}{\lambda}+\frac{D}{\lambda})^2} \tag{3.16}$$

An important feature of this design equation is that it becomes frequency-independent when the structural parameters are normalized by the wavelength.

To ensure the accuracy of this equation, the calculated results are compared with the curves in Fig. 3.2. Figure 3.10 shows this comparison. At $N = 10$, the curve obtained on the basis of Eq. (3.16) agrees well with that obtained on the basis of the simulation results. At $N = 5$ and $N = 15$, small differences are observed between the two curves; however, the maximum difference is less than 9.4%. Thus, Eq. (3.16) is confirmed to be useful.

### 3.2.4 Ohmic resistance
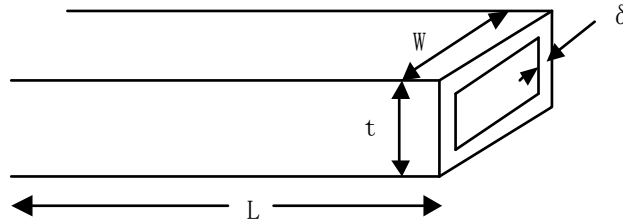


Fig. 3.11 Cross-sectional view of antenna wire

Figure 3.11 shows a cross-sectional view of the antenna wire. The parameters $W$, $t$, and $L$ represent the width, thickness, and total length of the wire, respectively, and $\delta$ is the skin depth:

$$\delta = \sqrt{\frac{2}{\omega\mu\sigma}} \tag{3.17}$$

Here, $\sigma$ is the conductance of the wire metal.

If the current is concentrated within the skin depth $\delta$, the ohmic resistance is

$$R_l = \alpha \frac{L}{2(t+W)\delta} \cdot \frac{1}{\sigma} = \alpha \frac{L}{d\delta\pi} \cdot \frac{1}{\sigma} \tag{3.18}$$

Here, $\alpha$ is the coefficient of the tapered current distribution, and $d$ is the wire diameter.

By applying Eq. (3.17) to Eq. (3.18), we obtain the following expression for the ohmic resistance:

$$R_l = \alpha \frac{L}{2(t+W)}\sqrt{\frac{240\pi^2}{2\lambda\sigma}} = \alpha \frac{L\pi}{(t+W)}\sqrt{\frac{30}{\lambda\sigma}} = \alpha \frac{L}{d}\sqrt{\frac{120}{\lambda\sigma}} \tag{3.19}$$

In small NMHAs, because the current distribution becomes sinusoidal, Eq. (3.19) agrees well with the simulation result at $\alpha = 0.6$.

The $\delta$ values are shown in Fig. 3.12. Here, a copper wire is considered, and the $\sigma$ value is set to $5.8 \times 10^7$ [1/$\Omega$m]. The $t$ value should be more than four times the $\delta$ value. The calculated results, i.e., the results obtained using Eq. (3.19), are shown in Fig. 3.13; an important point to be noted is that the values of $R_l$ are not sufficiently small. By substituting the $L_0$ value determined from Fig. 3.3 in Eq. (3.19), we can calculate the $R_l$ values for NMHAs. In Fig. 3.3, $L_0$ is about 0.48 m (0.95 $\times$ 0.5) at 315 MHz, and hence, $R_l$ is approximately 0.7 $\Omega$. If the frequency changes and $L$ and $d$ are changed analogously, $R_l$ becomes inversely proportional to $\sqrt{\lambda}$. The most effective way to reduce $R_l$ is to increase $W$ or $d$.
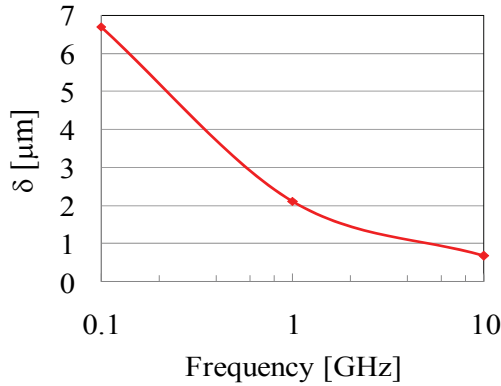


Fig. 3.12 Skin depth ($\delta$)
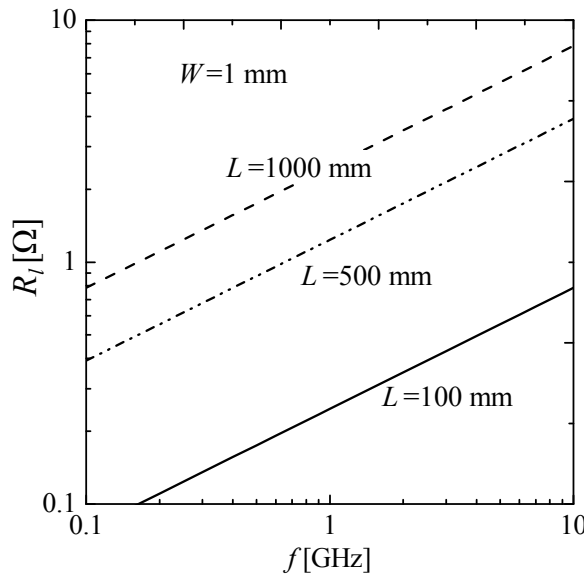


Fig. 3.13 Ohmic resistance

### 3.2.5 Input resistances

The simulated input resistances ($R_{in}$) of the self-resonant structures are shown in Fig. 3.14. Here, $R_{in}$ is expressed as follows:

$$R_{in} = R_r + R_l = R_{rD} + R_{rL} + R_l \qquad (3.20)$$

For an $R_l$ value of approximately 0.7 Ω, $R_l$ shares the dominant part of $R_{in}$ at $H$ = 0.02 m in Fig. 3.14 In these small antennas, most of the input power is dissipated as ohmic resistance, and only a small component of the input power is used for radiation.
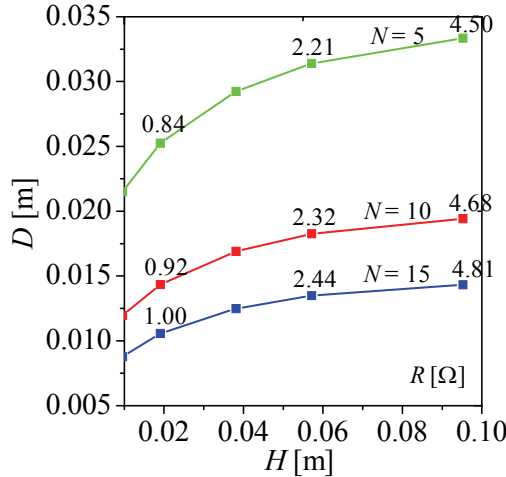


Fig. 3.14 Input resistances

Table 3.2 gives the details of the input resistances. The calculated results, i.e., the results obtained using Eqs. (3.2), (3.4), and (3.17), are compared with the simulated results. The $R_{rD}+R_{rL}$ values determined from the aforementioned equations agree well with the simulated results. The calculated and simulated $R_l$ values also agree well with each other; in the equation, an α value of 0.6 is used. Finally, the $R_{in}$ values are compared, and the antenna efficiencies ($\eta = (R_{rD}+R_{rL})/R_{in}$) are obtained. The calculated and simulated results agree well, and thus, the equations are confirmed to be accurate. Moreover, $R_l$ has a large negative effect on the antenna efficiency.

| Structure | | $R_{rD}[\Omega]$ | $R_{rL}[\Omega]$ | $R_l[\Omega]$ | $R_{in}[\Omega]$ | η[dB] |
|---|---|---|---|---|---|---|
| $N$ = 5 $H$ = 0.02λ | Eq. | 0.0790 | 0.2378 | 0.6380 | 0.9548 | -4.7911 |
| | Sim. | 0.2537 | | 0.5862 | 0.8399 | -5.1988 |
| $N$ = 15 $H$ = 0.02λ | Eq. | 0.0790 | 0.0656 | 0.8008 | 0.9453 | -8.1554 |
| | Sim. | 0.1987 | | 0.7988 | 0.9975 | -7.0067 |

Table 3.2 Resistances determined by calculation and simulation

### 3.2.6 Q factor

The Q factor is important for estimating the antenna bandwidth. The radiation Q factor ($Q_R$) for electrically small antennas is defined as

$$Q_R = \text{stored energy } (E_{sto}) / \text{radiating energy } (E_{dis}) \tag{3.21}$$

For antennas, these energies are expressed by the input impedance:

$$E_{sto} = X\,I^2 \tag{3.22}$$

$$E_{dis} = R_r \tag{3.23}$$

Therefore, $Q_{imp}$ can be expressed as follows:

$$Q_{imp} = X / R_r \tag{3.24}$$

Another expression for the Q factor is based on the frequency characteristics; in this case, the Q factor is referred to as $Q_A$:

$$Q_A = f_c / \Delta f \tag{3.25}$$

Here, $f_c$ is the center frequency and $\Delta f$ is the bandwidth. In this expression, a small $Q_A$ value indicates a large bandwidth.

McLean [13] gave the lower bound for the Q factor ($Q_M$):

$$Q_M = \frac{1}{ka} + \frac{1}{(ka)^3} \tag{3.26}$$

Figure 3.15 shows examples of $Q_A$ and $Q_M$ for NMHAs; Ds is the diameter of the sphere enclosing an NMHA. The antenna structures labeled A and B are those shown in Fig. 3.16. The $Q_A$ values of A and B are based on the measured voltage standing wave ratio (VSWR) characteristics shown in Fig. 3.19. We can see that $Q_A$ is smaller than $Q_M$, because of the ohmic resistance of the antenna.
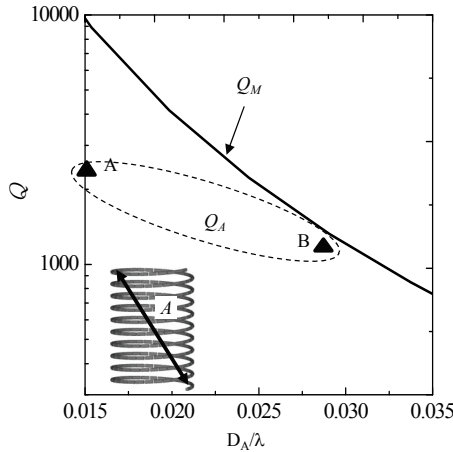


Fig. 3.15 Q factors for NMHA

## 3.3 Achieving a high antenna gain

The efficiency ($\eta$) of a small antenna is defined as

$$\eta = (R_{rD} + R_{rL})/(R_{rD} + R_{rL} + R_l) \tag{3.27}$$

Since (see Table 3.2) $R_l$ is greater than $R_r$ ($=R_{rD} + R_{rL}$), $R_l$ must be decreased in order to achieve high antenna efficiency. From Eq. (3.19), it is clear that increasing the antenna wire width ($W$) or diameter ($d$) is the most effective way to reduce $R_l$. If $W$ is increased, it would be necessary to ensure that neighboring wires are well separated from each other.

By substituting Eqs. (3.2), (3.4), and (3.19) in Eq. (3.27), we can calculate $\eta$; the result is shown in Fig. 3.16.

It can be seen that $\eta$ decreases with a decrease in $H$ and $D$. In this case, we use a very narrow antenna wire ($d$ = 0.05 mm). At points A and B, $\eta$ is 10% (-10 dB) and 25% (-6 dB), respectively. The relationship between the antenna gain ($G_A$) and $\eta$ is given by

$$G_A = G_D \, \eta \qquad [\text{dBi}] \tag{3.28}$$

Here, $G_D$ is the directional gain of the antenna. In electrically small antennas, $G_D$ remains almost constant at 1.8 dBi. The antenna gains at points B and A are $G_A$ = -4.2 dBi and -8.2 dBi, respectively. Given the small antenna size, these gains are large. Moreover, the gains can be increased if a thicker wire is used. In conclusion, it is possible to achieve a high gain when using small antennas.
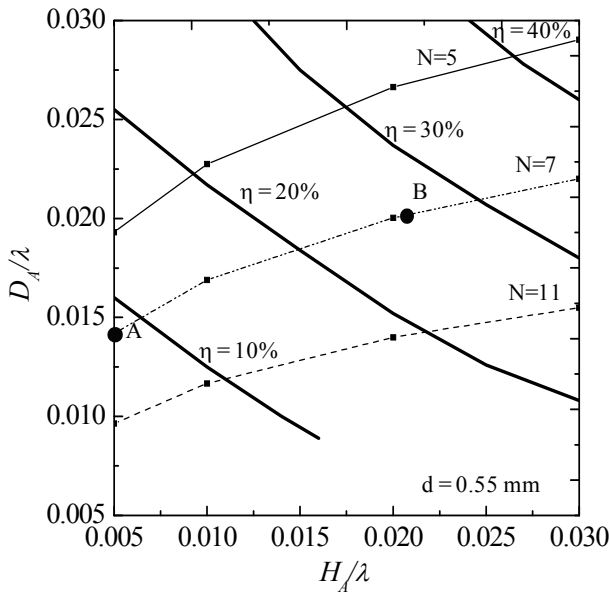


Fig. 3.16 Efficiency of NMHA

## 3.4 Examples of electrical performance

In order to investigate the realistic characteristics, we fabricated a 0.02$\lambda$ antenna (point B in Fig. 3.16), as shown in Fig. 3.17. The antenna impedances are measured with and without a

tap feed. The tap structure is designed according to the procedure given in Section 4.2.4. Excitation is achieved with the help of a coaxial cable. The coaxial cable is covered with a Sperrtopf balun to suppress the leak current. The measured and calculated impedances are shown in Fig. 3.18. The results agree well both with and without the tap feed, thereby confirming that the measurement method is accurate. The tap feed helps in bringing about an effective increase in the antenna input resistance. The bandwidth characteristics are shown in Fig. 3.19; the measured and simulated results agree well. The bandwidth at VSWR < 2 is estimated to be 0.095%.



(a) w/o tap                    (a) With tap
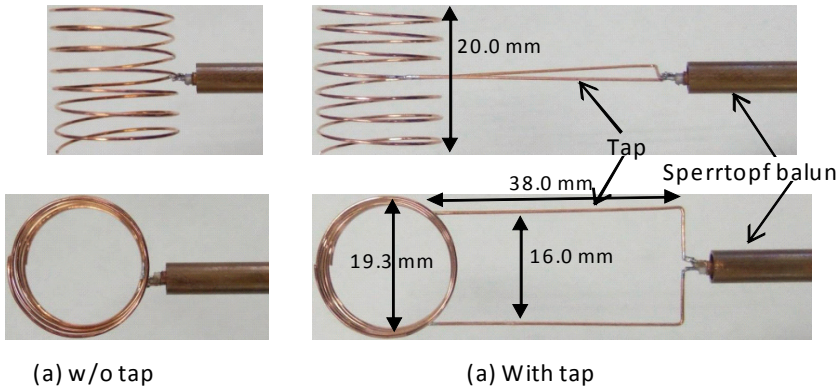
Fig. 3.17 Fabricated antenna ($H$ = 0.021λ, $D$ = 0.020λ)
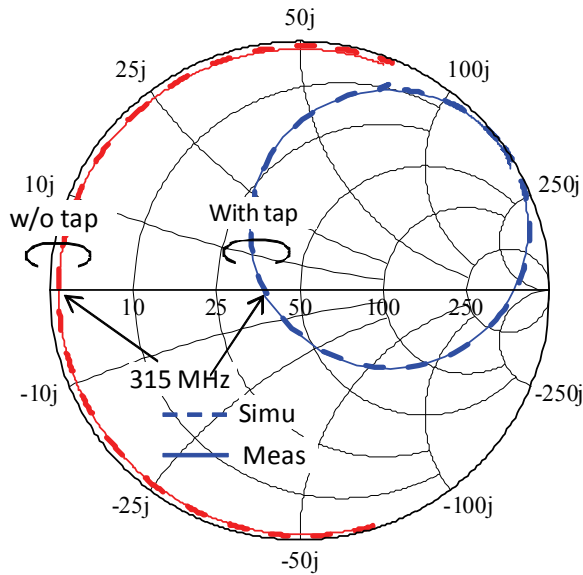


Fig. 3.18 Antenna input impedance
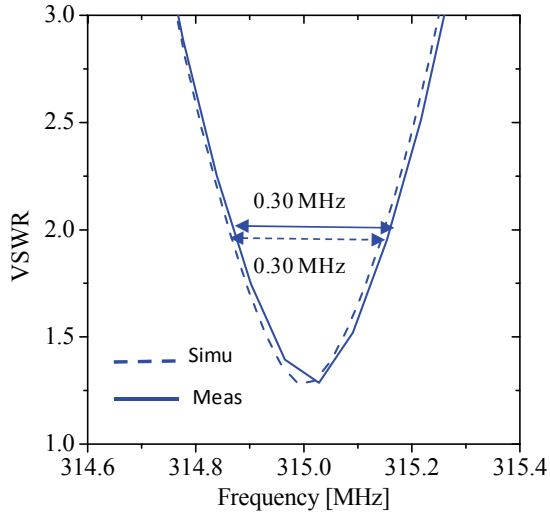
Fig. 3.19 VSWR characteristics
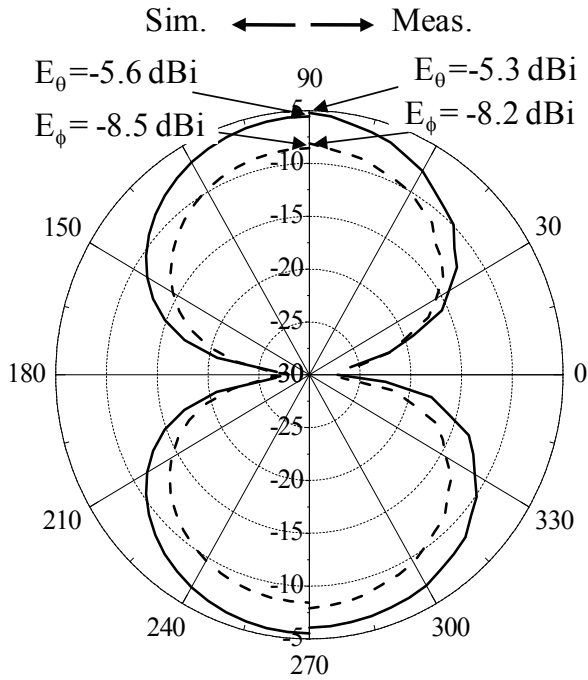


Fig. 3.20 Radiation patterns

As can be seen from Fig. 3.20, the measured and simulated radiation characteristics are in good agreement. The $E_\theta$ component corresponds to the radiation from the electric current

source shown in Fig. 3.1, and the $E_\phi$ component corresponds to the radiation from the magnetic current source shown in Fig. 3.1. There is a 90° phase difference between the $E_\theta$ and $E_\phi$ components. Therefore, the radiated electric field is elliptically polarized. Because the magnitude difference between the $E_\theta$ and $E_\phi$ components is only 3 dB, the radiation field is approximately circularly polarized. The magnitude of the $E_\theta$ and $E_\phi$ components correspond to $R_{rD}$ in Eq. (3.2) and $R_{rL}$ in Eq. (3.4). The antenna gains of the $E_\theta$ and $E_\phi$ components can be estimated by the η value shown in Fig. 3.16. The value η × $G_D$ ($G_D$ indicates the directional gain of 1.5) of structure B becomes -4 dBi. This value agrees well with the total power of the $E_\theta$ and $E_\phi$ components.

## 4. NMHA impedance-matching methods

### 4.1 Comparison of impedance-matching methods

For the self-resonant structures of very small NMHAs, effective impedance-matching methods are necessary because the input resistances are small. There are three well-known impedance-matching methods: the circuit method, the displaced feed method, and the tap feed method as shown in Fig. 4.1. In the circuit method, an additional electrical circuit composed of capacitive and inductive circuit elements is used. In the displaced feed method, an off-center feed is used. The amplitude of the resonant current ($I_{dis}$) is lower at the off-center point than at the center point ($I_M$), and hence, the input impedance given by $Z_{in} = V/I_{dis}$ is increased. As the feed point approaches the end of the antenna, the input resistance approaches infinity. This method is useful only for objects with pure resistance. Since the RFID chip impedance has a reactance component, this method is not applicable to RFID systems. In the tap feed method, an additional wire structure is used. By appropriate choice of the width and length of the wire, we can achieve the desired step-up ratio for the input resistance. Moreover, the loop configuration can help produce an inductance component, and therefore, conjugate matching for the RFID chip is possible. This feed is applicable to various impedance objects.
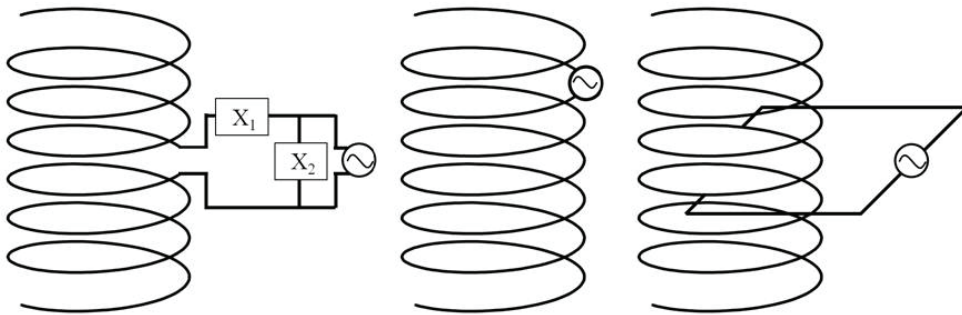


(a) Circuit method                (b) Displaced feed          (c) Tap feed

Fig. 4.1 Configurations of impedance matching methods

The features of the three methods are summarized in Table 4.1. For the circuit method, the capacitive and inductive elements are commercialized as small circuit units. These units have appreciable ohmic resistances.

If the NMHA input resistances are around 1 Ω, the ohmic resistance values become significant. This method is not suitable for small antennas with small input resistances. For the displaced feed method, the matching object must have pure resistance. The tap feed method can be applied to any impedance object, but it is not clear how the tap parameters can be determined when using this method.

| Method | Advantages | Disadvantages | Design |
|--------|-----------|---------------|--------|
| Circuit method [8] | With capacitance and inductance chips, matching is easily achieved | Severe reduction in antenna gain by chip losses | Theoretical method has been established |
| Displaced feed [9] | Simple method of shifting a feed point No reduction in antenna gain | Limited to pure resistance objects | Displacement position is easily found empirically |
| Tap feed [10] | Uses additional structure No reduction in antenna gain Applicable to any object | Additional structure increases antenna volume | Design method has not been established |

Table 4.1 Comparison of impedance-matching methods

## 4.2 Design of tap feed structure [14]
### 4.2.1 Derivation of equation for input impedance
The tap feed method has been used for the impedance matching of a small loop antenna [15]. The tap is designed using the equivalent electric circuit. The tap configuration for the NMHA is shown in Fig. 4.2. The antenna parameters $D$ and $H$ are selected such that self-resonance occurs at 315 MHz. The tap is attached across the center of the NMHA, and the tap width and tap length are denoted as $a$ and $b$, respectively. The equivalent electric circuit is shown in Fig. 4.3. Here, $L$, $C$, and $R$ are the inductance, capacitance, and input resistance, respectively. The tap is excited by the application of a voltage $V$; $M_A$ is the mutual inductance between the NMHA and the tap.

In the network circuit shown in Fig. 4.3, the circuit equations for the NMHA and the tap are as follows:

$$\left\{\frac{1}{j\omega C}+R+j\omega(L-M_A)\right\}I_A+j\omega M_A(I_A-I_T)=0 \tag{4.1}$$

$$j\omega(L_T-M_A)I_T+j\omega M_A(I_T-I_A)=V \tag{4.2}$$

From the above equations, the input impedance ($Z_{in} = V/I_T$) of the NMHA can be deduced:

$$Z_{in} = \frac{R(\omega M_A)^2}{R^2 + (\omega L - \frac{1}{\omega C})^2} + j\frac{R^2(\omega L_T) - (\omega M_A)^2(\omega L - \frac{1}{\omega C}) + \omega L_T(\omega L - \frac{1}{\omega C})^2}{R^2 + (\omega L - \frac{1}{\omega C})^2} \quad (4.3)$$

Here, the tap inductance ($L_T$) is given by [16]:

$$L_T = \frac{\mu}{\pi}\left[ b\ln(\frac{4ab}{d(b + \sqrt{a^2 + b^2})}) + a\ln(\frac{4ab}{d(a + \sqrt{a^2 + b^2})}) + 2(d/2 + \sqrt{a^2 + b^2} - b - a) \right] \quad (4.4)$$
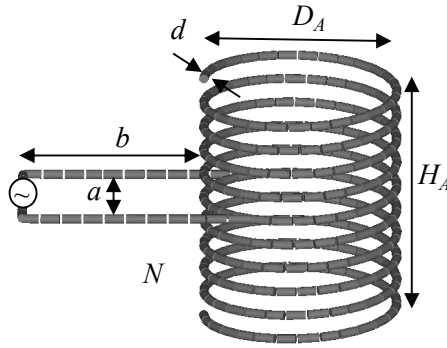


Fig. 4.2 Tap configuration for NMHA
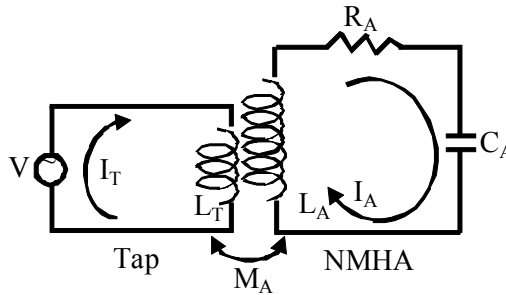


Fig. 4.3 Equivalent circuit for tap feed

### 4.2.2 Simple equation for step-up ratio

At the self-resonant frequency ($\omega_r = 2\pi f_r$), the imaginary part of Eq. (4.3) becomes zero. Therefore, we have

$$R^2(\omega_r L_T) - (\omega_r M_A)^2(\omega_r L - \frac{1}{\omega_r C}) + (\omega_r L - \frac{1}{\omega_r C})^2 = 0 \quad (4.5)$$

If the variable of the above equation is replaced by ($\omega_r L - 1/\omega_r C) = \alpha$, this expression becomes second-order in $\alpha$. The two solutions are

$$\alpha(\pm) = \frac{\omega_r M_A{}^2 \pm \sqrt{\omega_r{}^2 M_A{}^4 - 4R^2 L_T{}^2}}{2L_T} \qquad (4.6)$$

We label these two solutions $\alpha(+)$ and $\alpha(-)$. For these $\alpha$ values, the resonant points are shown in Fig. 4.4.
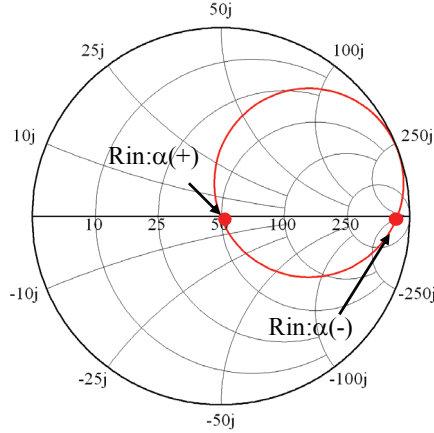


Fig. 4.4 Resonant points

In the root of Eq. (4.6), the following assumption is applicable. This assumption is valid when the tap width ($a$) is nearly equal to the antenna diameter ($D$):

$$\omega_r{}^2 M_A{}^4 \rangle\rangle 4R^2 L_T{}^2 \qquad (4.7)$$

Then, the expression for $\alpha$ becomes simple:

$$\alpha(+) = \frac{\omega_r M_A{}^2}{L_T} \qquad (4.8)$$

By using $\alpha(+)$ in Eq. (4.3), we can derive an expression for the input resistance ($R_{in}$):

$$R_{in} = R(L_T / M_A)^2 \qquad (4.9)$$

Finally, the step-up ratio ($\gamma$) of the input resistance can be simply expressed as

$$\gamma = (L_T / M_A)^2 \qquad (4.10)$$

The important point to be noted in this equation is that $M_A$ has a strong effect on the step-up ratio. In the following section, the calculation method and $M_A$ results are presented.

### 4.2.3 Calculation method and results for mutual inductance
The calculation structure is shown in Fig. 4.5. $B_A$ is the magnetic flux density in the NMHA, and $I_T$ is the tap current.
$M_A$ can be calculated using the following equation [17]:
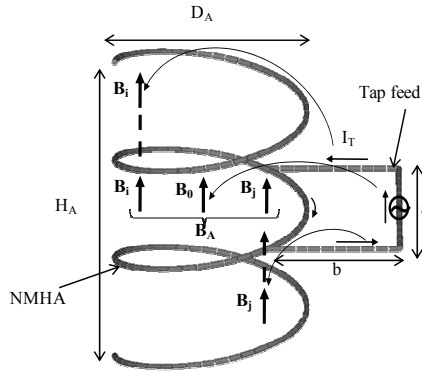
Fig. 4.5 Calculation structure

$$M_A = \frac{\int_S \mathbf{B}_A \cdot d\mathbf{S}}{I_T} = \frac{\mu \int_S \mathbf{H}_A \cdot d\mathbf{S}}{I_T} \tag{4.11}$$

Here, $B_A$ is the sum of the $B_i$ values of each loop in Fig. 4.5. The magnetic field ($H_i$) in each loop is given by

$$H_{0i} = \int_l \frac{I_T}{4\pi r^2} \sin\theta dl \tag{4.12}$$

Here, $r$ represents the distance between a point on the tap and a point inside a loop. In this calculation, a current $I_T$ exists at the center of the tap wire. Therefore, even if the the magnetic field is applied at point close to the tap wire.
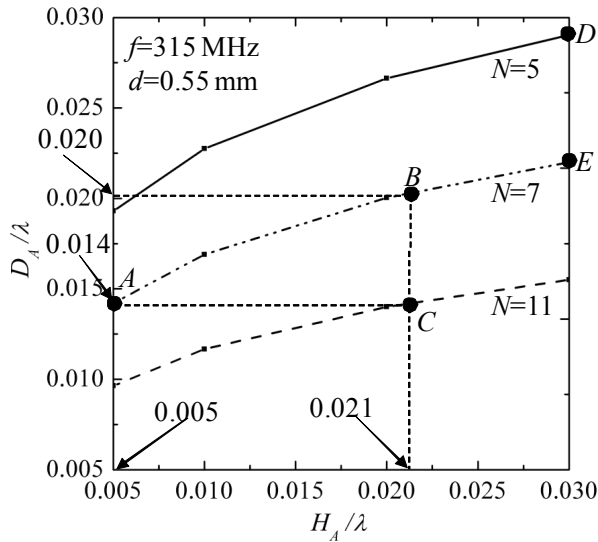


Fig. 4.6 Study structures of NMHA

To establish the design of the tap feed, the $L_T/M_A$ values in Eq. (4.10) must be represented by the structural parameters. Calculations are performed for the structures shown in Fig. 4.6. Points A, B, and C are used to investigate the dependence of $M_A$ on the structural parameters.
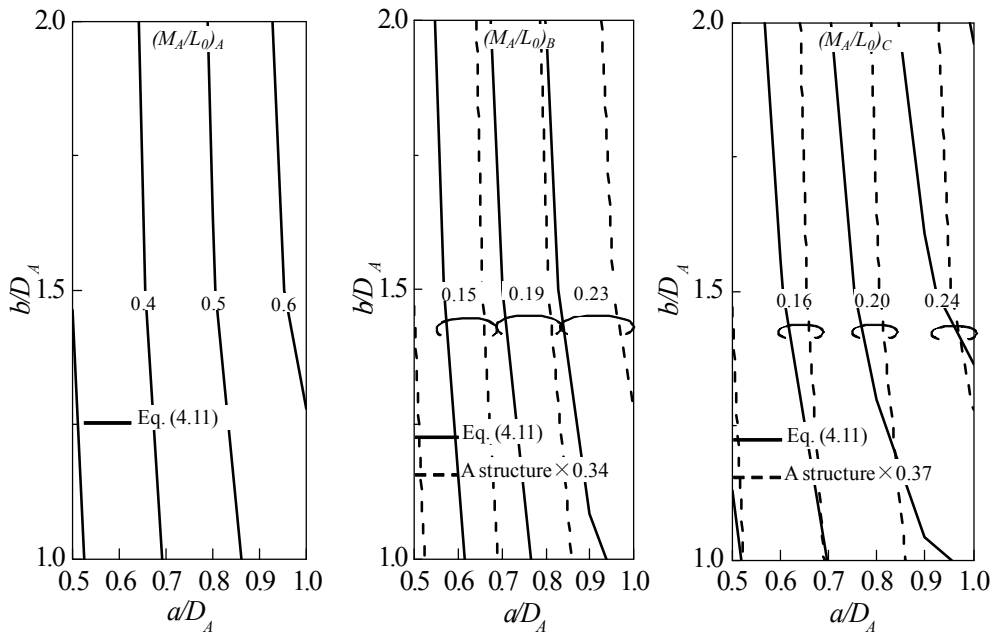


Fig. 4.7 Calculated results: $M_A/L_0$

The calculated $M_A$ values are shown in Figs. 4.7(a), (b), and (c). The $M_A$ value is normalized by the $L_0$ value, which is the self-inductance of a small loop with diameter D. $L_0$ is given by [18]

$$L_0 = \frac{\mu D}{2}\left\{\ln(\frac{8D}{d}) - 1.75\right\} \tag{4.13}$$

Structure A in Fig. 4.7(a) is used as a reference to determine the dependence of $M_A$ on the structural parameters. Comparison of structures A and B reveals the dependence of $M_A/L_0$ on $H_A$ and $D_A$. Taking into account Eq. (4.11), we show that $M_A$ is proportional to $D_A/H_A$. The $D_A/H_A$ value for structure B becomes 0.34 times that for structure A. In Fig. 4.7(b), the solid lines indicate the calculated results obtained using Eq. (4.11). The dotted lines indicate the transformed values, i.e., the product of the values in Fig. 4.7(a) and 0.34. The data corresponding to the solid and dotted lines are in good agreement, thus confirming that the $M_A/L_0$ values are proportional to the $D_A/H_A$ value. We now compare structures A and C. Eq. (4.11) shows that $M_A$ is proportional to $N/H_A$. The $N/H_A$ value for structure C is 0.37 times that for structure A. In Fig. 4.7(c), the solid lines indicate the calculated results obtained using Eq. (4.11). The dotted lines indicate the transformed values, i.e., the product of the values shown in Fig. 4.7(a) and 0.37. The solid and dotted lines agree well, confirming the proportional relationship between $M_A/L_0$ and $N/H_A$ value. We thus have

$$\frac{M_A}{L_0} \propto \frac{D_A N}{H_A} \tag{4.14}$$

### 4.2.4 Universal expression for $M_A$

The design equation becomes universal if the $M_A/L_0$ value is expressed in terms of $M_0/L_0$. Here, $M_0$ is the mutual inductance between the one-turn loop and a tap. If we introduce a coefficient $\alpha_A$, $M_A/L_0$ can be given by

$$\frac{M_A}{L_0} = \alpha_A \frac{D_A N}{H_A} \frac{M_0}{L_0} \tag{4.15}$$

The $M_0/L_0$ values calculated using from Eq. (4.11) (assuming $N = 1$) are shown in Fig. 4.8. The $M_0/L_0$ values show small deviations with the $D_A$ values. If all the structural deviations depending on $D_A$, $H_A$, and $N$ are contained in the coefficient term, $\alpha_A$ can be expressed as follows:

$$\alpha = 0.05 + 0.0075N + 4.5(\frac{H}{N^2 D}) \tag{4.16}$$

We use $D_A = 0.020\lambda$ (see Fig. 4.8) for the $M_0/L_0$ values.
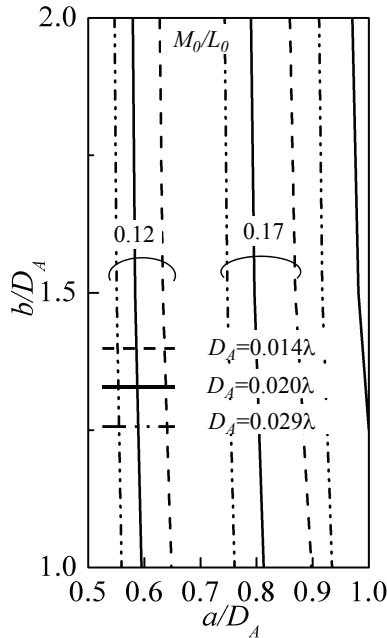


Fig. 4.8 Calculated results: $M_0/L_0$

### 4.2.5 Design equation for step-up ratio in NMHA tap feed

By applying Eq. (4.15) to Eq. (4.10), we can express the step-up ratio ($\gamma$) as follows:

$$\gamma = (\frac{L_T}{M_A})^2 = (\frac{H_A}{\alpha_A D_A N})^2 (\frac{L_T}{M_0})^2 = (\frac{H_A}{\alpha_A D_A N})^2 \gamma_0 \qquad (4.17)$$

This equation is the objective design equation for a tap feed. Here, $\gamma_0$ is given by

$$\gamma_0 = (\frac{L_T}{M_0})^2 \qquad (4.18)$$

The calculated $\gamma_0$ values are shown in Fig. 4.9. For each $\gamma_0$, the tap structural parameters $a/D_A$ and $b/D_A$ are given.
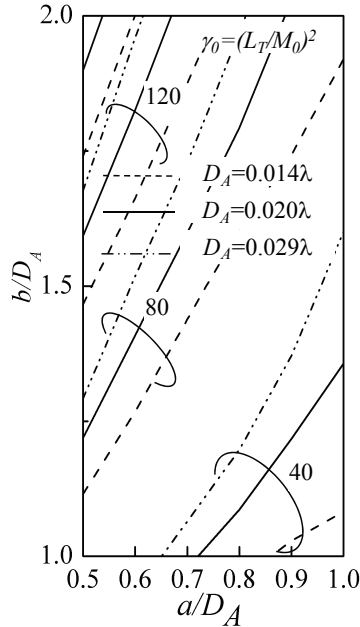


Fig. 4.9 Calculated results: $\gamma_0$

### 4.2.6 Design procedure for tap feed

We now summarize the design procedure. First, the self-resonant NMHA structure is determined on the basis of Fig. 3.2 or Eq. (3.16). Then, the antenna input resistance is estimated using Eqs. (3.2), (3.4), and (3.19). The requested $\gamma$ value is determined by taking into account the feeder line impedance. Then, Eq. (4.17) is used to determine the tap structure. The $\gamma_0$ value is determined by substituting the antenna parameters and $\gamma$ value in Eq. (4.17). The final step involves the use of the data provided in Fig. 4.9. The objective $\gamma_0$ curve in Fig. 4.9 is identified Then, the relation between $a/D_A$ and $b/D_A$ is elucidated, and a suitable combination of $a/D_A$ and $b/D_A$ is selected.

## 5. Antenna design for RFID tag

In this section, the proximity effect of a metal plate on the self-resonant structures and radiation characteristics of the antenna is clarified through simulation and measurement. An

operating frequency of 953 MHz is selected, and antenna sizes of 0.03λ–0.05λ are considered. We discuss the fabrication of tag antennas for Mighty Card Corporation [19].

## 5.1 Design of low-profile NMHA [20]

The projection length of the NMHA is reduced by adopting a rectangular cross section, so that the antenna can be used in an RFID tag. The simulation configuration is shown in Fig. 5.1. The antenna thickness is $T$, and the size of the metal plate is $M$. The spacing between the antenna and the metal plate is $S$. The equivalent electric and magnetic currents are I and J, respectively. $E_\theta$ and $E_\phi$ correspond to the radiation from the electric and magnetic currents, respectively.
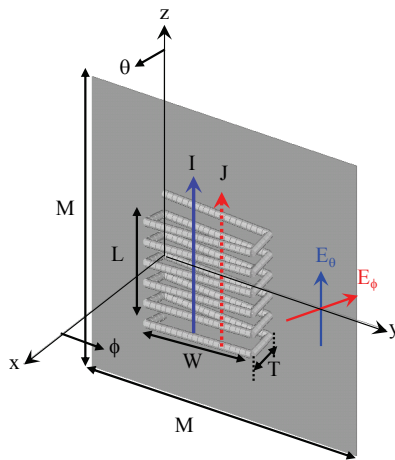


Fig. 5.1 Simulation configuration

The most important aspect of the antenna design is the self-resonant structure. The self-resonant structure without a metal plate is shown in Fig. 3.10. The design equation (Eq. (3.16)) is not effective when a metal plate is present in the vicinity of the antenna. Therefore, the self-resonant structure is determined by electromagnetic simulations. The calculated self-resonant structures are shown in Fig. 5.2; $T$ and $N$ are variable parameters. Other parameters, such as $d$, $S$, and $M$ are shown in the figure. For small values of $T$, large $W$ values are required so that the cross-sectional area is maintained at a given value. For smaller values of $N$, too, large $W$ values are required so that the individual inductances of the cross-sectional areas are increased.

An example of the input impedance in the structure indicated by the triangular mark at $T = 3$ mm is shown in Fig. 5.3. At 953 MHz, the input impedance becomes a pure resistance of 0.49 Ω. Because the antenna has a small length of 0.04λ, the input resistance is small. The radiation characteristics are shown in Fig. 5.4. To simplify the estimation of the radiation level, the input impedance mismatch is ignored by assuming a "no mismatch" condition in the simulator. The dominant radiation component is $E_\phi$, which corresponds to the magnetic current source. Surprisingly, an antenna gain of –0.5 dBd is obtained under these conditions. Here, the unit dBd represents the antenna gain normalized by that of the 0.5λ dipole antenna. The high gain is a result of the appropriate choice of the ohmic resistance ($R_l$) on

the basis of the radiation resistance ($R_r$). $R_l$ is determined from the antenna wire length and $d$ given by Eq. (3.19). Here, because $R_r$ is 0.24 Ω, $R_l$ should be smaller than this value. To achieve a small ohmic resistance, $d$ should be made as large as possible. When $d$ is 0.8 mm, $R_l$ is 0.25 Ω, and hence, a radiation efficiency of about 50% is achieved. This antenna gain confirms that a small rectangular NMHA in close proximity to a metal can be used in several practical applications.
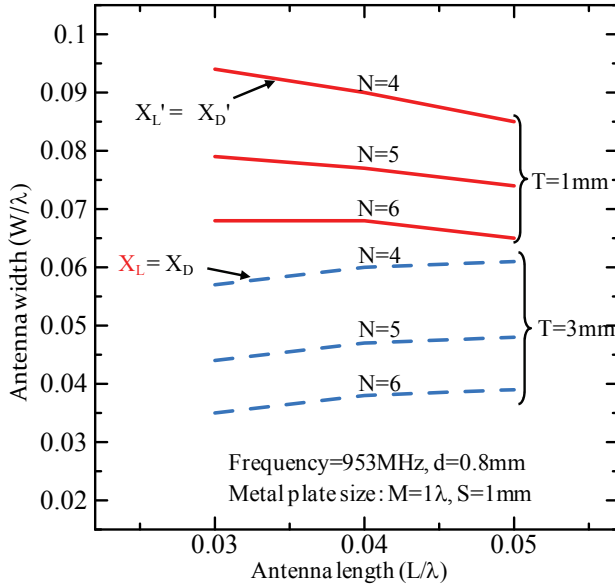


Fig. 5.2 Self-resonant structures
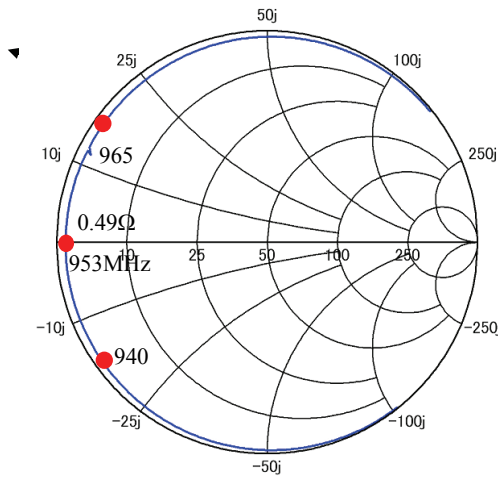


Fig. 5.3 Input impedance
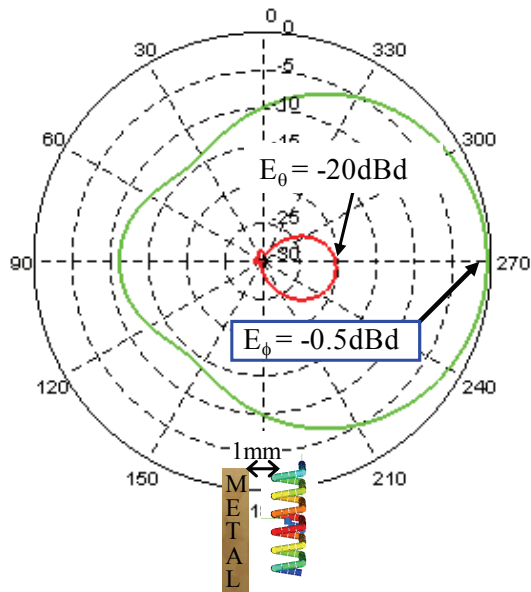
Fig. 5.4 Radiation characteristics
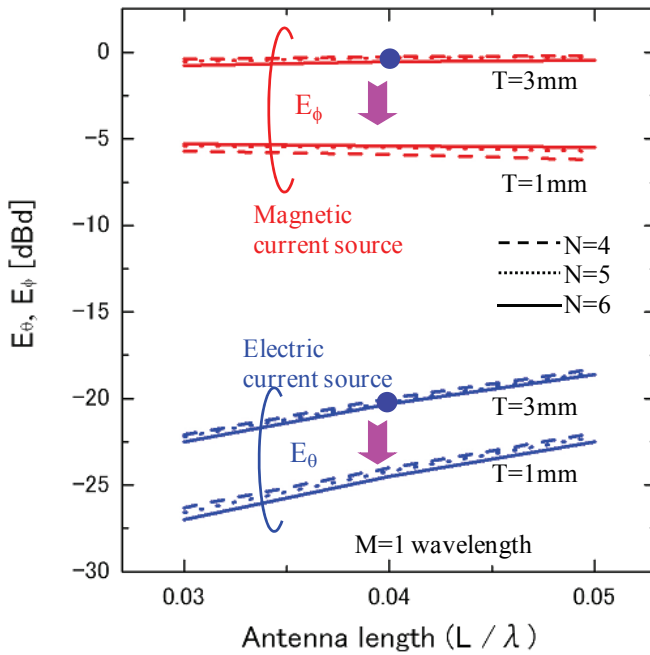


Fig. 5.5 Radiated field components

The important antenna gain characteristics for the self-resonant structures are shown in Fig. 5.5. It is noteworthy that the $E_\phi$ components are dominant, while the $E_\theta$ components are less than –20 dBd. There is no difference in the antenna gain even when $N$ is changed. For large $T$ values, a high antenna gain is achieved. When $T$ is 3 mm, the gain is expected to be comparable to that of a $0.5\lambda$ dipole antenna. Moreover, the antenna gain remains constant for different values of $L$. Hence, excellent antenna gains may be obtained for small antenna sizes such as $0.03\lambda$.

## 5.2 Practical antenna characteristics

A high gain can be expected for a small NMHA. However, because the input resistance of such an antenna is small, an impedance-matching structure is required for practical applications. A tap-matching structure is used for a 50-$\Omega$ coaxial cable, as shown in Figs. 5.6(a) and (b). The tap structure is rather simple. Wire diameters of 0.8 mm and 0.5 mm are selected for the antenna and the tap, respectively. Because the spacing between the antenna and the metal plate is small (1 mm), appropriate arrangement of the tap arms is important.



(a) Perspective view



(b) Cross-sectional view
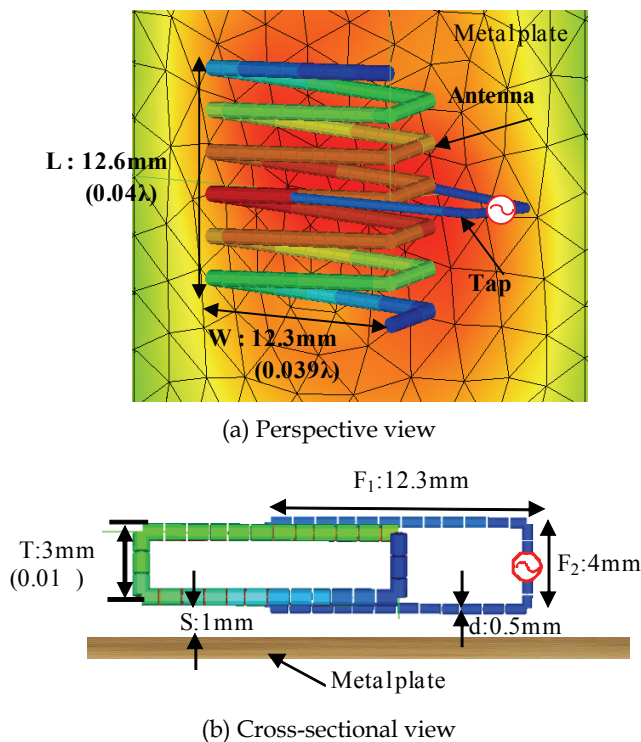
Fig. 5.6 Experimental NMHA structure

The fabricated antenna and feed cable are shown in Fig. 5.7. The tap arms are soldered to the antenna wire, and a coaxial cable is used as a feed line. A Sperrtopf balun is attached to the coaxial cable to suppress leak currents. Figure 5.8 shows the measured and calculated antenna impedances. The measured and calculated values are in good agreement, both in

the presence and absence of the tap feed. When the tap feed is used, the antenna impedance is exactly 50 Ω, and this confirms the effectiveness of the tap feed. The bandwidth characteristics are shown in Fig. 5.9. A 3.5-MHz bandwidth is obtained when VSWR < 2. This bandwidth corresponds to 0.4% of the center frequency.
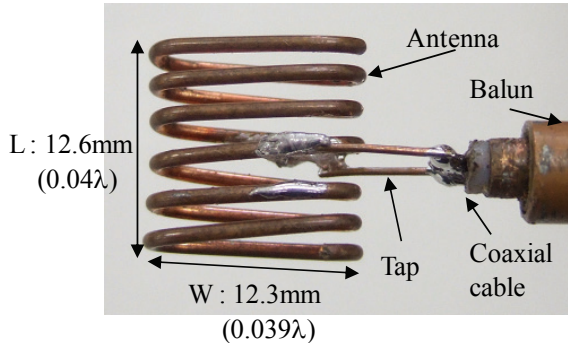


Fig. 5.7 Fabricated NMHA structure
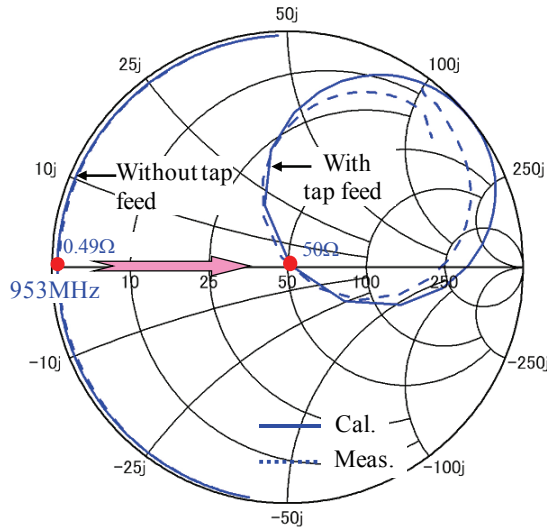


Fig. 5.8 Input impedance

The important radiation characteristics observed when the antenna is placed near a metal plate are shown in Fig. 5.10. The separation $S$ in this case is 1 mm. A square metal plate with a size of $0.5\lambda$ is used. The $E_\phi$ component is dominant when the antenna is in close proximity to the metal plate. A high antenna gain of –0.5 dBd is achieved. The $E_\phi$ level in the presence of the metal plate exceeds that in the absence of the metal plate by about 10 dB. The usefulness of the NMHA in a metal-proximity application is verified. At the same time, the intensity of the $E_\theta$ component decreases to –11 dBd. This shows that the electrical current source does not work well under metal-proximity conditions.

Fig. 5.9 VSWR characteristics



$E_\theta = -10.1$

$E_\phi = -0.53\mathrm{dBd}$

$E_\theta = -10.4$

$E_\phi = -0.53\mathrm{dBd}$

Cal.(dotted)                        Meas.(solid)
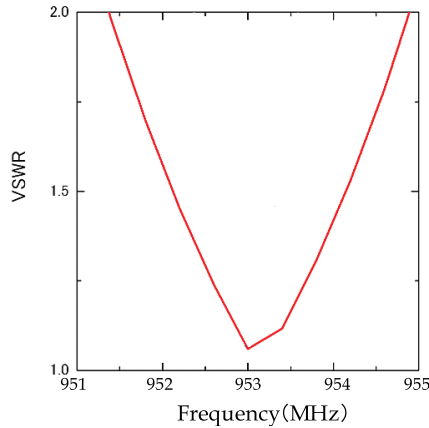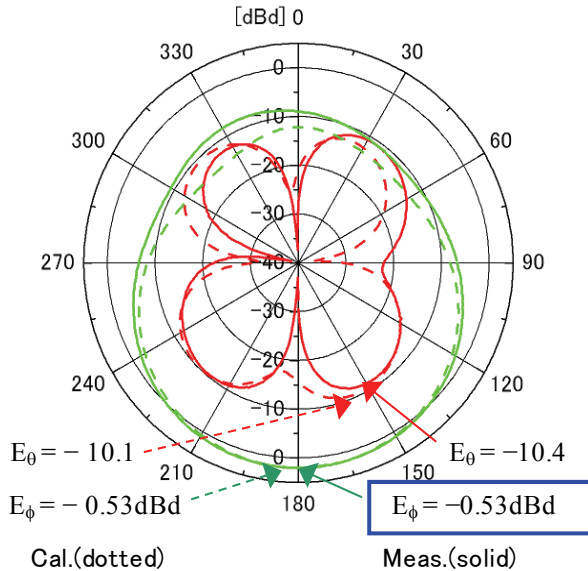
Fig. 5.10 Radiation characteristics

### 5.3 RFID tag antenna

In order to use the rectangular NMHA as a tag antenna, the input impedance must be matched to the IC impedance of $Z_{IC} = 25 - j95\ \Omega$. Therefore, the antenna size and tap size are modified as shown in Fig. 5.11. The tap length is increased to obtain the necessary inductance for achieving conjugate matching with the IC capacitance. The spacing between the antenna and the metal plate is set to 1.5 mm. A $0.5\lambda$ square metal plate is used. The impedance-matching process is shown in Fig. 5.12. The tap length (T3) is important for matching the impedance to the IC. Almost complete conjugate matching can be achieved at T3 = 17 mm.

(a) Perspective view



(b) Cross-sectional view
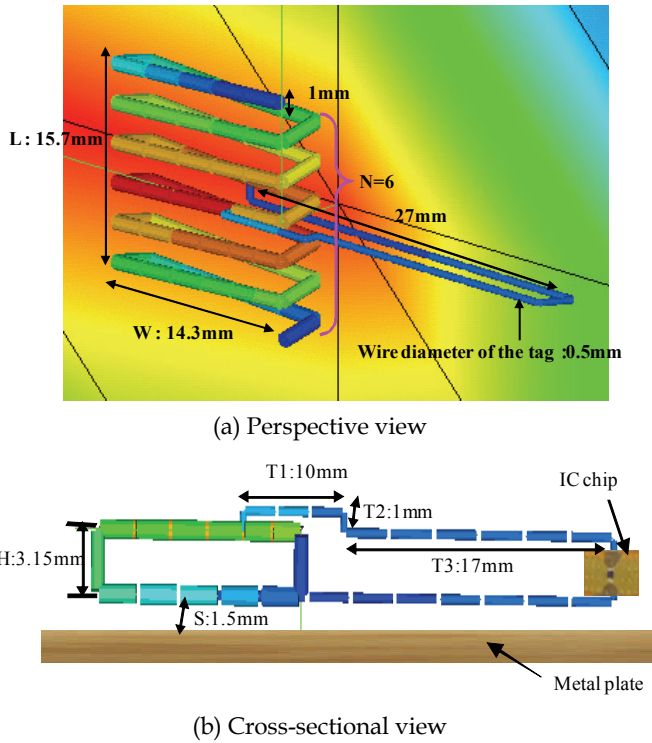
Fig. 5.11 Configuration of RFID tag antenna
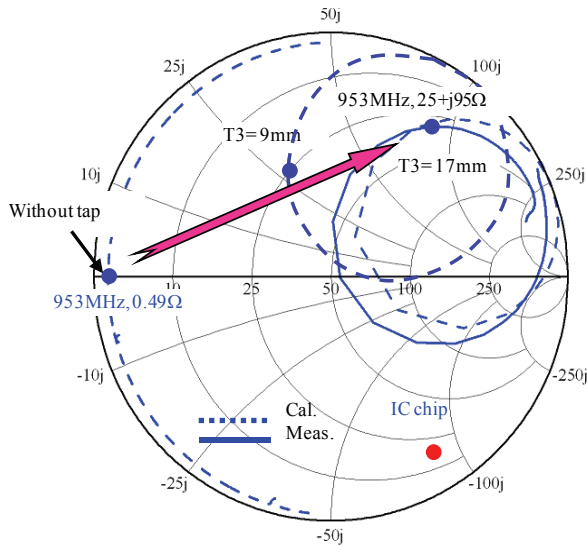


Fig. 5.12 Input impedance
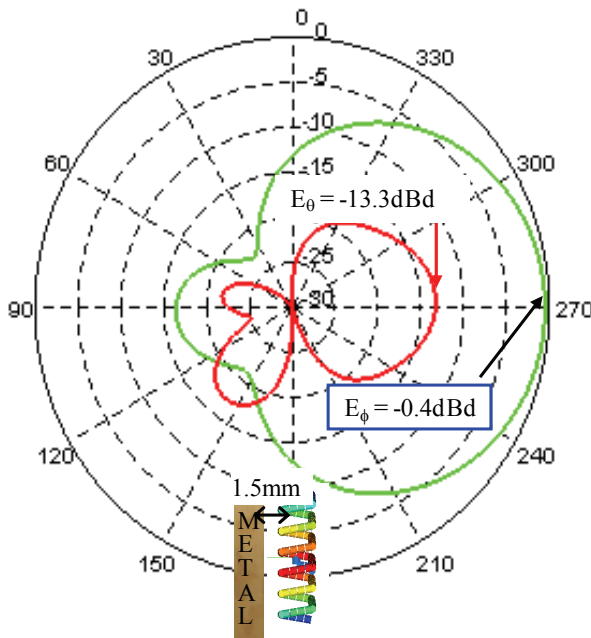
Fig. 5.13 Radiation characteristics
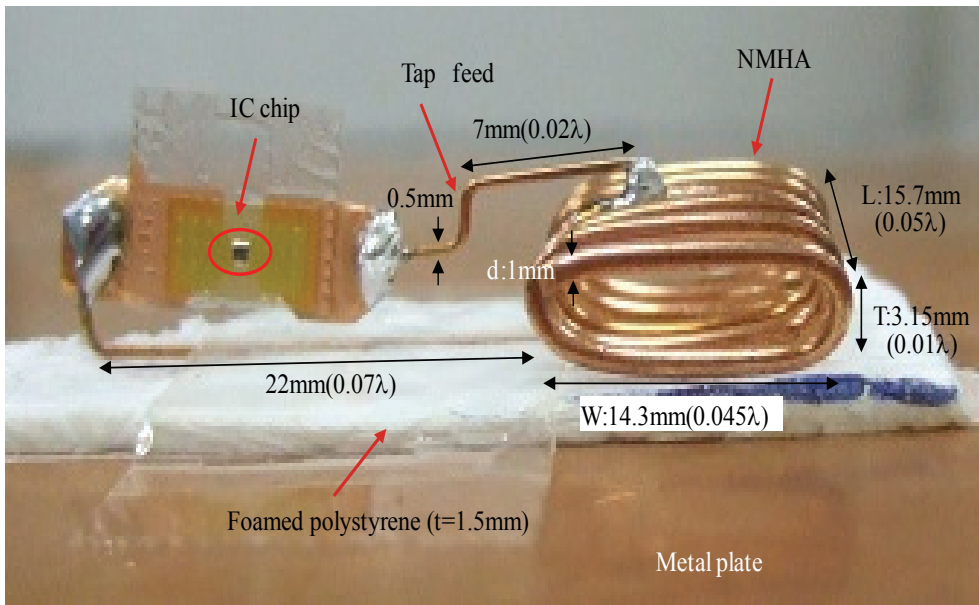


Fig. 5.14 Fabricated antenna

To estimate the antenna gain of this structure, we evaluate the radiation characteristics; the results are shown in Fig. 5.13. The antenna input impedance is designed to be $Z_{ANT} = 25 + j95\ \Omega$. To simplify the radiation intensity calculation, the input-impedance mismatch is ignored by adopting the "no mismatch" condition. An antenna gain of –0.4 dBd is obtained in this case. Therefore, the electrical performance is expected to be comparable to that of conventional tags.

On the basis of these results, we fabricate an actual antenna with a help of Mighty Card Corporation, as shown in Fig. 5.14. This antenna is composed of a copper wire with a diameter of 1 mm. The IC is inserted into the tap arm. The antenna and IC are placed on a piece of polystyrene foam attached to the metal plate. The thickness of the foam is 1.5 mm, and the size of the square metal plate is $0.5\lambda$.

## 5.4 Read-range measurement

The read range is measured using the set-up shown in Fig. 5.15. A commercial reader antenna is used for transmitting and receiving. This reader antenna is connected to a reader unit and a computer. When the tag information is read, the tag number is shown on the computer screen. Read-range measurements are conducted by changing the distance between the reader antenna and the tag. The distance at which the tag number disappears is considered to be the read range. These read ranges might be affected by the height pattern at the measurement site, and hence, the height of the tag is so chosen that the highest possible electrical strength is obtained.
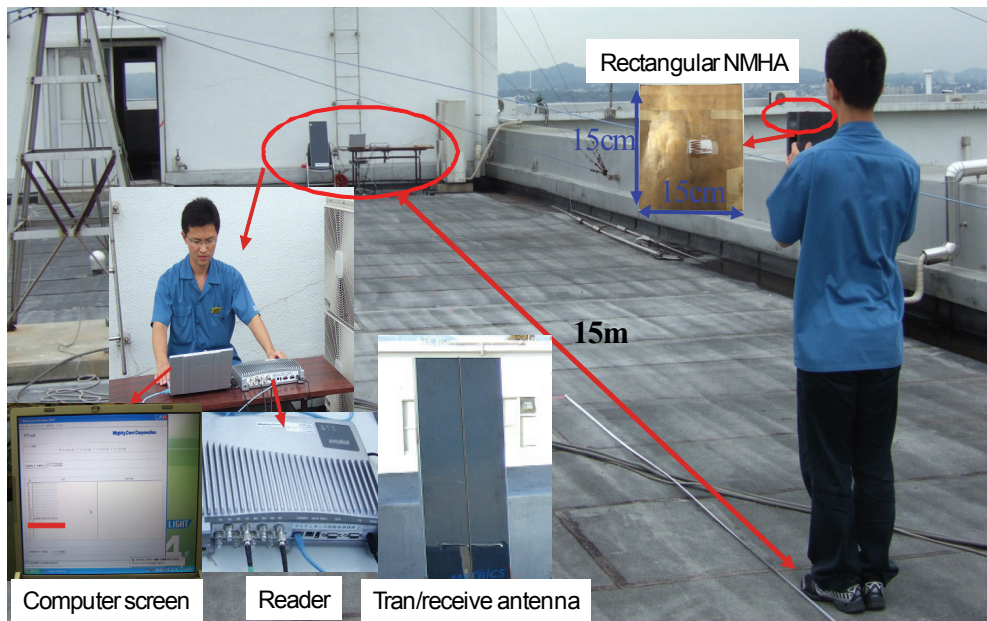


Fig. 5.15 Read-range measurement set-up

The measured read ranges are summarized in Table 5.1. For conventional antennas placed in a free space, read ranges of 9 m are obtained. In the case of a metal proximity use, read ranges become very small. For the NMHA, read ranges of 6 m and 15 m are obtained without and with the metal plate, respectively. The reason of this read range increase is attributed to the antenna gain of Fig. 5.13. The effectiveness of the tag is confirmed by the aforementioned read-range measurement.

| | Antenna in free space | Read range | Antenna in free space | Read range |
|---|---|---|---|---|
| Conventional Antenna | 16mm ... 95mm | 9m | 42mm ... 47mm | 9m |
| | Without a metal plate | Read range | With a metal plate | Read range |
| Low profile NMHA | 15mm ... 15mm | 6m | 150mm ... 150mm | 15m |
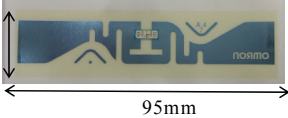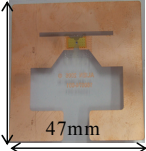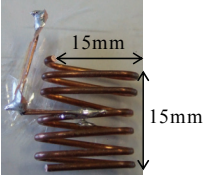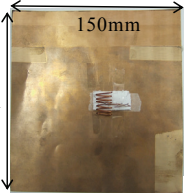
Table 5.1 Results of read-range measurement

## 6. Conclusions

A normal-mode helical antenna (NMHA) with a small size and high gain is proposed for use as an RFID tag antenna under metal-plate proximity conditions. The important features of the design are as follows:

1.  Fundamental equations for important electrical characteristics have been summarized, and useful databases have been shown.
2.  The antenna efficiency, which is related to the structural parameters, is important for achieving high antenna gain.
3.  A simple design equation for determining the self-resonant structures has been developed.
4.  For the fabrication of an actual antenna, the tap feed has been carefully designed so that a small input resistance is obtained.
5.  A simple design equation for determining the tap-feed structures has been developed.
6.  A small RFID tag antenna that can be used under metal-plate proximity conditions has been designed.
7.  A read range superior to that of conventional tags has been achieved.

## 7. References

[1] http://www.alientechnology.com/tags/index.php

[2] http://www.omni-id.com/products/omni-id-max.php

[3] Xuezhi Zeng, et al, "Slots in Metallic Label as RFID Tag Antenna," APS 2007, pp.1749-1752, Hawaii, June.2007.

[4] W.G. Hong, W.H. Jung and Y. Yamada, "High Performance Normal Mode Helical Antenna for RFID Tags", IEEE AP-S'07, pp.6023-6026, Hawaii, June 2007

[5] K. Tanoshita, K. Nakatani and Y. Yamada, "Electric Field Simulations around a Car of the Tire Pressure Monitoring System", IEICE Trans. Commu., Vol.E90-B, No.9, 2416-2422, 2007

[6] W. G. Hong, Y. Yamada and N. Michishita, Low profile small normal mode helical antenna achieving long communication distance ", Proceedings of iWAT2008, pp.167-170, March 2008

[7] Q.D. Nguyen, N. Michishita, Y. Yamada and K. Nakatani, "Electrical Characteristics of a Very Small Normal Mode Helical Antenna Mounted on a Wheel in the TPMS Application", IEEE AP-S'09, Session 426, No.4, June 2009

[8] J. D. Kraus, "ANTENNAS, second edition", McGraw-Hill Book Company, pp. 333-338, 1988

[9] H.A. Wheeler, "Simple Inductance formulas for Radio Coils," Proc.IRE, Vol.16, pp.1398-1400, 1928.

[10] W. L. Stutzman and G. A. Thiele, "Antenna Theory and Design, second edition", John Wiley & Sons, Inc., pp. 43-47 and p.71, 1998

[11] W. L. Stutzman and G. A. Thiele, "Antenna Theory and Design, second edition", John Wiley & Sons, Inc., pp.71-75, 1998

[12] Q.D. Nguyen, N. Michishita, Y. Yamada and K. Nakatani, "Deterministic Equation for Self-Resonant Structures of Very Small Normal-Mode Helical Antennas", IEICE Trans. Communications., to be published in May, 2011

[13] J. S. McLean, "A re-examination of the fundamental limits on the radiation Q of electrically small antenna", IEEE Trans. Antennas Propag., Vol.44, No.5, pp.672-676, May 1996

[14] Q.D. Nguyen, N. Michishita, Y.Yamada and K. Nakatani, "Design method of a tap feed for a very small no-mal mode helical antenna", IEICE Trans. Communications., to be published in Feb., 2011

[15] K. Fujimoto, A. Henderson, K. Hirasawa and J.R. James, "SMALL ANTENNAS", Research Studies Press Ltd., pp.86-92,1987

[16] K. Fujimoto, A. Henderson, K. Hirasawa and J.R. James, "SMALL ANTENNAS", Research Studies Press Ltd., pp.78,1987

[17] Simon Ramo, John R. Whinnery and Theodore Van Duzer, FIELDS AND WAVES IN COMMUNICATION ELECTRONICS – Third Edition, JOHN WILEY&SONS, INC., pp.189-193, 1993

[18] W. L. Stutzman and G. A. Thiele, "Antenna Theory and Design, second edition", John Wiley & Sons, Inc., p.75, 1998

[19] http://www.mightycard.co.jp/

[20] W.G. Hong, N. Michishita and Y. Yamada, "Low-profile Normal-Mode Helical Antenna for Use in Proximity to Metal", ACES Journal, Vol.25, No.3, pp.190-198, March 2010

# Using Metamaterial-Based Coplanar Waveguide Structures for the Design of Antennas on Passive UHF RFID Tags

Benjamin D. Braaten and Masud A. Aziz
*North Dakota State University*
*United States*

## 1. Introduction

Radio Frequency Identification (RFID) is becoming a very affordable and reliable way of to track inventory items. Because of this, RFID systems have received considerable attention from researchers, engineers and industry personnel. Particularly, researchers involved with RFID systems have developed smaller antennas for tags deployed in these systems. Several of these designs have involved meander-line antennas (Finkenzeller, 2003), metamaterial-based designs (Dacuna & Pous, 2007) and various materials (Griffin et. al., 2006). This chapter will describe the main parameters of interest in a RFID system using Friis's transmission equation. This will then be followed by a section on recent work on applying RFID systems to smart shelves, metallic plates and livestock tracking. Then a section on coplanar-waveguides (CPW) is presented followed by the design of metamaterial-based CPW antennas for passive UHF RFID tags.

## 2. An introduction to passive RFID systems

RFID technology is an automatic means of object identification with minimal human intervention or error (Qing & Chen, 2007). Recently, RFID technology has been extensively used to improve automation, inventory control, tracking of grocery products in the retail supply chain and management of large volumes of books in libraries (Jefflindsay, 2010; Teco, 2010). RFID tags have functions similar to a bar code; however they can be detected even when they are blocked by obstacles. RFID tags also carry more information than a bar code (Finkenzeller, 2003).

A RFID system consists of a reader (or interrogator) and several tags (or transponders). A typical RFID system is shown in Fig 1. The reader consists of a transmitting and receiving antenna and it is typically connected to a PC or any other monitoring device. The tag has a single antenna for both transmitting and receiving. Digital circuitry (or IC) that communicates with the reader is attached to the antenna on the tag. The reader sends out an electromagnetic field that contains power and timing information into the space around itself (sometimes called the interrogation zone (Finkenzeller, 2003)). If there is a tag in the interrogation zone, then the tag receives the electromagnetic field using its receiving antenna. The tag then utilizes its IC to communicate with the reader. The IC collects power

and timing information from the electromagnetic field and sends proper backscattered messages to the reader using the transmitting antenna of the tag. The maximum distance that a reader can interrogate a tag is termed as the max read range of the tag.
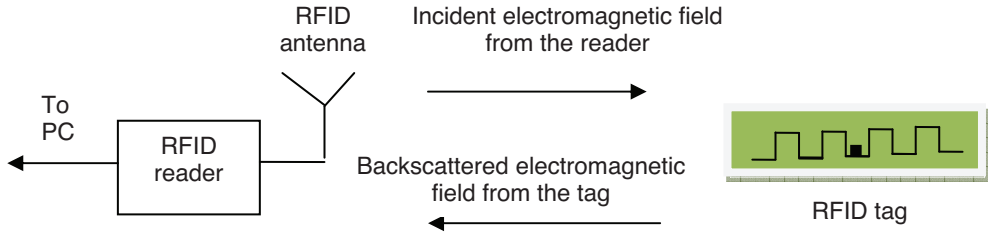


Fig. 1. Overview of a RFID system.

Depending upon the power source of the tag, a RFID system can be classified into three major categories: active, semi-passive, and passive (Finkenzeller, 2003). An active tag uses its own power from the battery attached to it to communicate with the reader. A semi-passive tag also has its own battery but it is only awakened by the incident electromagnetic field from the reader. This greatly enhances the read range of the tag (Finkenzeller, 2003). A passive tag uses the power from the incident electromagnetic field. The incoming electromagnetic field from the reader induces a port voltage on the tag antenna and the IC uses its power harvesting circuit to provide power to the digital portion of the circuit. The power is then used by the IC to communicate with the reader.

The RFID system can be described by the Friis transmission equation (Stutzman & Thiele, 1998):

$$P_r = P_t \frac{G_r G_t \lambda^2}{\left(4\pi R\right)^2} q \tag{1}$$

where $P_t$ is the power transmitted by the reader, $P_r$ is the power received by the passive tag, $G_t$ is the gain of the antenna on the reader, $G_r$ is the gain of the antenna on the tag, $\lambda$ is the free-space wavelength of the transmitting frequency by the reader, $R$ is the distance between the antenna on the reader and the antenna on the tag and $q$ is the impedance mismatch factor ($0 \le q \le 1$) between the passive IC and the antenna.

Equation (1) assumes a polarization match between the antenna used by the reader and the antenna on the passive tag. Therefore, a good match between the passive IC and the antenna on the tag is essential. It is also assumed that the tag is in the far-field of the reader. Therefore, a larger gain of the antenna on the tag will mean more power for the passive IC on the tag. Moreover, using a longer wavelength will also improve the power at the tag. However, the power available to the tag reduces by the distance squared as the tag and reader antenna are moved apart. Equation (1) can also be expressed as follows (Braaten et al., 2008; Rao et al., 2005):

$$R = \frac{\lambda}{4\pi} \sqrt{\frac{q G_t G_r P_t}{P_r}} \ . \tag{2}$$

If the threshold power required to activate the IC on the tag is $P_{th}$, then maximum read range $r_{max}$ can be derived from Equation (2)

$$r_{max} = \frac{\lambda}{4\pi} \sqrt{\frac{qG_tG_rP_t}{P_{th}}} \; .$$ (3)

Equation (3) is very useful for predicting the max read range of a passive RFID tag. Generally, $P_{th}$ of a RFID tag is known. Moreover, $P_t$ and $G_t$ are fixed. This leaves the two variables $q$ and $G_r$ to the designer. Typically, a tag is designed to have the highest $r_{max}$. One way of achieving this is to have a good match between the antenna and the IC on the tag with a large $G_r$.

## 3. Summary of previous work

### 3.1 RFID shelves
Recently, the RFID smart-shelf system has received considerable attention. This is due to the increasing demands for large-scale management of such items as grocery products in the retail supply chain, large volume of books in libraries, bottles in the pharmaceutical industry, and important documentation in offices (Landt, 2005; Want, 2006). The RFID smart shelf is a regular shelf with a reader antenna embedded in the shelf. This ideally allows for only detecting the tagged items located on that shelf. Extending this concept to every shelf in a store makes it possible to automatically locate and inventory every item.

There have been many different smart-shelves proposed by different authors. Design of a smart-shelf can be found in both the High Frequency (HF) and Ultra-High Frequency (UHF) range. The main difference is that at HF the energy coupling between the reader antenna and the tag is essentially made through the magnetic field (Medeiros et al., 2008). A very common reader antenna configuration is a loop antenna (Qing & Chen, 2007; Cai et. al., 2007). Good coupling requires close proximity between the reader antenna and the tag. At UHF, readers are equipped with antennas such as patch antennas (Lee et. al., 2005) and energy coupling to the tag antenna is made through propagating waves.

At UHF, it is difficult to limit the antenna radiation exactly to the shelf boundary without resorting to costly metal or absorbing shields. One solution can be to incorporate a leaking microstrip line with an extended ground plane in the shelf. This shelf design exploits the leaking fields from a microstrip line (undesirable in microwave circuits) for applications of RFID systems in small areas (Medeiros et al., 2008).

### 3.2 Tags on metallic objects
There is a strong interest from many industries (aeronautics, automotive, construction, etc.) in tagging metal items (airplane or automotive parts, metal containers, etc.) using both active and passive RFID tags (Rao et. al., 2008). Unfortunately, tag performance is affected by the electrical properties of metal objects that are in contact or close proximity to the tag antenna. A series of measurements were used to measure the far-field gain pattern and gain penalty of several tag antennas when connected to different objects (Griffin et. al., 2006). The Antenna Gain Penalty (AGP) is defined to be the loss in gain of the antenna due to metal attachment. The measured gain showed sufficient distortion due to permittivity, loss tangent of the material, surface waves and diffraction (Griffin et. al., 2006).

The presence of the metal plate shifts up the resonant frequency of the HF reader loop antenna and weakens the intensity of the magnetic field (Qing & Chen, 2007). When a metal plate is positioned close to a loop antenna, the magnetic field generated by the loop antenna reaches the surface of the metal plate. In order to satisfy the boundary conditions on the

metal surface, the magnetic field normal to the surface must be zero. For this to occur, an additional current, known as the eddy current, is induced within the metal plate. The induced current opposes the magnetic flux generated by the antenna, which may significantly dampen the magnetic flux in the vicinity of the metal surface. The damping of magnetic flux leads to a reduction of the inductance of the loop antenna. Therefore, the resonant frequency of the antenna is increased (Finkenzeller, 2003). The resonant frequency of the antenna also depends on the position of the metal objects. The back-placed metal (metal positioned at the back of the antenna) has the most significant impact on the resonant frequency of the antenna as opposed to the side or bottom placed metal (Qing & Chen, 2007).

Several antennas have been proposed to overcome the abovementioned constraints. An RFID tag with a thin foam backing material that is capable of operating efficiently both as a dipole antenna and as a microstrip antenna has been proposed (Mohammed et. al., 2009). The antenna behaves as a dipole antenna in free space and acts as a patch antenna when it is attached to metal objects. A wideband metal mount RFID tag that works on a variety of metals also was proposed (Rao et. al., 2008). Reduction in the size of the antenna also has been achieved by introducing a quasi-Yagi antenna on a RFID tag (Zhu et. al., 2008). The impact of a wooden and metallic surface together on the antenna has also been studied (Kanan & Azizi, 2009).

### 3.3 Cattle tag research

RFID technology has many applications. One use of this technology is for livestock identification. Animals such as cattle and sheep are tagged for purposes, such as disease control, breeding management, and stock management (Ng et. al., 2005). Loop antennas have been proposed as the RFID tag antenna in the cattle tags (Braaten et. al., 2006). One of the reasons that loop antennas are widely used is that they are not required to be very large. Loops are used as receiving antennas because the output of the loop is proportional to the number of turns and the permeability of the material the loop is wound on. Therefore, weak signals can be detected by using a loop with a large number of turns and wound on a material with significant permeability. Antennas with dielectric superstrates have also been proposed (Braaten et. al., 2008). It has been shown that a passive tag with a meander-line antenna and dielectric superstrate can significantly augment the read range of the tag.

## 4. Coplanar-waveguide structures

Coplanar-waveguide (CPW) transmission lines are used extensively in wireless communications (Pozar, 2005; Collin, 2001). A CPW transmission line is shown in Fig. 2. The reference planes and signal plane are printed on the same conducting layer. Each plane is usually made of a conducting material such as copper. The dielectric is typically isotropic and ungrounded. The signal propagating down the CPW transmission line is symmetrically guided between the signal plane and the outer reference planes. The advantages of a CPW transmission line are that it only requires a single conducting layer and components can be easily connected between the signal plane and the reference plane. This is very useful for printed circuit boards with many different layers because only a single layer dedicated to microwave signals is needed. The disadvantage of a CPW transmission line is the need to keep both reference planes at the same potential all along the signal trace. This can be difficult to do on a single conducting layer.

Many advances have been made on the CPW transmission line. For example novel filters have been developed (Velez et al., 2009) and right/left-handed propagation has been demonstrated (Eleftheriates and Balmain, 2005) on CPW transmission lines. Many of the new techniques and structures that have been developed can also be used for the design of new antennas. The following section uses a new structure developed for CPW filters to reduce the overall size of printed dipoles.
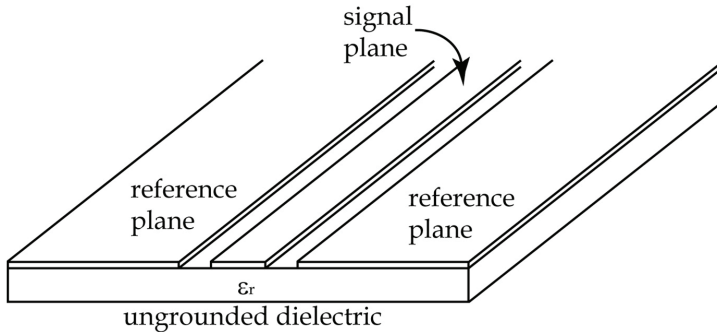


Fig. 2. A CPW transmission line on a dielectric substrate.

## 5. Metamaterial-based antenna design using OCSRR and MOCSRR particles.

Antennas on a passive UHF RFID tag are typically printed on the top side of a thin flexible substrate while adhesive is applied to the bottom side to attach the tag to a desired object. Because of this, all the conducting material (i.e., copper) used for the antenna is constrained to a single layer.  This restriction requires the entire topology of the antenna to be printed on the same plane.  Many different types of meander-line antennas for passive UHF RFID tags printed on a single conducting layer have been proposed (Marrocco, 2003; Calabrese et al., 2008).  Many of these meander-line antennas have proven to be useful, however recently a special type of printed dipole (Braaten, 2010a; Braaten et al., 2010b) based on the meander-line structure has recently been developed. Particularly, these newly developed printed antennas use open complementary split ring resonator (OCSRR) and meander open complementary split ring resonator (MOCSRR) particles connected in series to form electrically small resonant dipoles (Velez et al., 2009).

### 5.1 The OCSRR particle
First, the OCSRR particle is introduced. The layout of each individual OCSRR particle is show in Fig. 3 (a). Each particle is a coplanar-waveguide (CPW) structure with various concentric ring gaps etched from the copper. A port is defined on each side of the particle and the equivalent circuit in Fig. 3 (b) is used to model the OCSRR particle in Fig. 3 (a). The equivalent inductance $L_{eq,o}$ represents the inductance between ports a and b caused by the ring between the ring slots connecting the two ports and the equivalent capacitance $C_{eq,o}$ represents the distributed capacitance between ports a and b caused by the ring slots. Each section of the meander-line antenna in Fig. 4 has the same equivalent circuit as the OCSRR particle in Fig. 3 (b). Therefore, by connecting several OCSRR particles in series, an alternate electrically small resonant antenna can be designed.

## 5.2 Equivalent circuit and the dimensional relation of the OCSRR particle

To illustrate the behaviour of the OCSRR particle in Fig. 3, the equivalent circuit is extracted and discussed in this section for various values of $r_d$ (i.e., inner disc radius values) of the OCSRR particle. The CPW structure shown in Fig. 5 can be used to extract the equivalent circuit of the OCSRR particle (Velez et al., 2009). A convenient method of extracting the equivalent circuit is to use a commercially available full wave electromagnetic solver such as Momentum (Advanced Design System 2009a) to simulate the CPW structure in Fig. 5. When the particles resonate, the impedance on the 50 Ω CPW transmission line caused by the particles is infinity. This will result in an optimum match (i.e., lowest $S_{11}$ values) between the 50 Ω ports and 50 Ω CPW transmission line to occur at resonance. Then, from the simulated $S_{11}$ values, an equivalent circuit can be extracted using a curve fitting technique. This equivalent circuit can then be placed in the location of the OCSRR particle in Fig. 3 and be used to represent the physical OCSRR particle. The equivalent circuit loads the 50 Ω CPW transmission line in a manner similar to the actual OCSRR particles. With a technique to extract the equivalent circuit of the OCSRR particle, a designer is able to determine how various dimensions of the OCSRR particle ultimately affect the equivalent circuit of that particular particle. Particularly, how the dimensions affect the individual capacitance and inductance values of the equivalent circuit of the OCSRR particle can be shown.

Using the method described in the previous paragraph, the equivalent circuit of the OCSRR particle in Fig. 3 (a) was extracted for various dimensions of the inner disc (i.e., for various values of $r_d$) and scale factors (i.e., for various values of S). For the various values of $r_d$ the dimensions of the OCSRR particle were w = 8.3 mm, h = 8.1 mm, s = 0.51 mm, m = 0.47 mm, n = 0.39 mm, $r_i$ = 0.45 mm and t = 0.39 mm. The substrate was defined to be 1.36 mm thick and had a permittivity of 4.2. The values of M and N in Fig. 5 are 0.4 mm and 3.1 mm, respectively. The results from these computations are shown in Table 1. The results in Table 1 can be used to design an OCSRR particle with a specific resonant frequency.
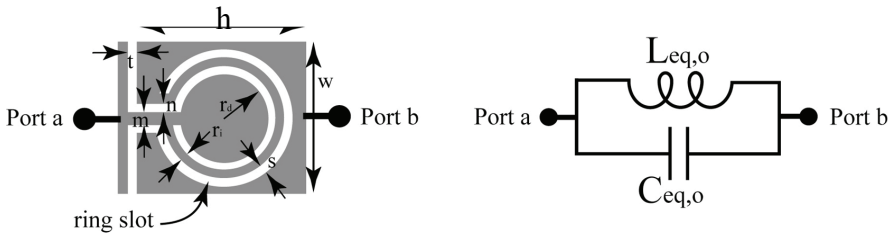


Fig. 3. (a) Layout of the OCSRR particle (the gray area is the copper) and (b) the equivalent circuit of the OCSRR particle.
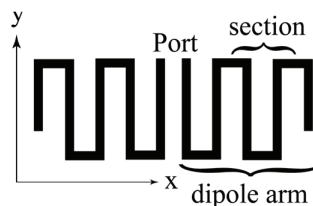


Fig. 4. Layout of a meander-line dipole.
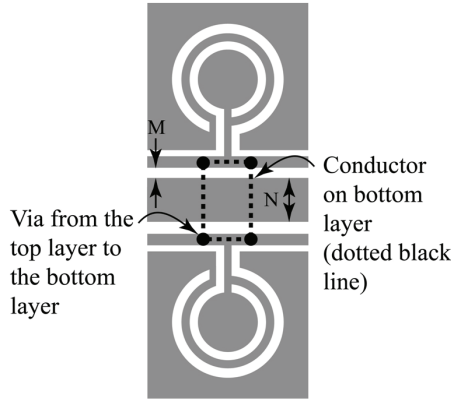
Fig. 5. CPW structure used to extract the equivalent circuit of the OCSRR particle (the gray area is the copper).

| $r_d$ (mm) | $L_{eq}$ (nH) | $C_{eq}$ (pF) | $f_0$ (GHz) |
|:---:|:---:|:---:|:---:|
| 1.0 | 1.5 | 2.95 | 2.39 |
| 1.2 | 1.5 | 2.95 | 2.39 |
| 1.4 | 1.5 | 3.0 | 2.37 |
| 1.6 | 1.5 | 3.0 | 2.37 |
| 1.8 | 1.4 | 3.25 | 2.35 |
| 2.0 | 1.7 | 3.05 | 2.2 |
| 2.2 | 1.7 | 3.05 | 2.2 |

Table 1. Equivalent circuit design table for the OCSRR particle for various values of $r_d$.

| S | $L_{eq}$ (nH) | $C_{eq}$ (pF) | $f_0$ (GHz) |
|:---:|:---:|:---:|:---:|
| 0.7 | 1.0 | 2.85 | 2.98 |
| 0.75 | 1.1 | 2.9 | 2.81 |
| 0.8 | 1.3 | 2.85 | 2.61 |
| 0.85 | 1.2 | 3.2 | 2.56 |
| 0.9 | 1.4 | 3.15 | 2.39 |
| 0.95 | 1.4 | 3.25 | 2.35 |
| 1.0 | 1.7 | 3.05 | 2.2 |

Table 2. Equivalent circuit design table for the OCSRR particle for various scale factors S.

Next, the dimensions of OCSRR particle were fixed at w = 8.3 mm, h = 8.1 mm, s = 0.51 mm, m = 0.47 mm, n = 0.39 mm, $r_i$ = 0.45 mm, $r_d$ = 2.0 mm and t = 0.39 mm. Starting from these dimensions the particles were scaled by several factors symmetrically in both the x- and y-directions. For example, for a scaling factor of S = 1.0, the dimensions of the particle are unchanged. Then by scaling the particle by 0.8, every dimension of the particle is reduced by

20%. A scaling factor of 0.7 then reduces the size of the particle by 30% and so on. The equivalent circuit and resonant frequency was computed for each scaling factor using the CPW structure in Fig. 5. The results from these computations are shown in Table 2.

### 5.3 Discussion

The results in Table 1 show how the resonant frequency of the OCSRR particle can be reduced by increasing the radius value of the inner disc. This is expected, because the equivalent capacitance of the particle is larger for larger radius values. The increased capacitance is a result of the smaller ring gap. As the distance between the conducting inner disk and the conducting ring (in the ring gap) reduces, the capacitance between the two conductors increase which results in a lower resonant frequency.

The results in Table 2 show how the resonant frequency is related to different scaling factors of the OCSRR particle. The resonant frequency of the particle was increased by approximately 6 – 7% for a 5% change in the scaling factor. This is very useful for designing an OCSRR particle for a specific resonant frequency.

### 5.4 Antenna designs using the OCSRR particle

OCSRR particles can be connected in series in a manner shown in Fig. 6 to form an electrically small resonant dipole. In fact, a dipole consisting of series connected OCSRR particles have characteristics similar to the meander-line dipole in Fig. 4. The equivalent circuit of each meander-line section is a capacitor connected in parallel with an inductor. The vertical traces in each meander-line section contribute to the equivalent capacitance and the current travelling on each horizontal segment contributes to the equivalent inductance. The equivalent circuit of an OCSRR particle is the same as the equivalent circuit of each meander-line section. Therefore, by connected OCSRR particles in series, an alternate to the meander-line dipole can be designed. Furthermore, it turns out that the overall size of a dipole with series connected OCSRR particles is much smaller than a meander-line dipole with the same resonant frequency.
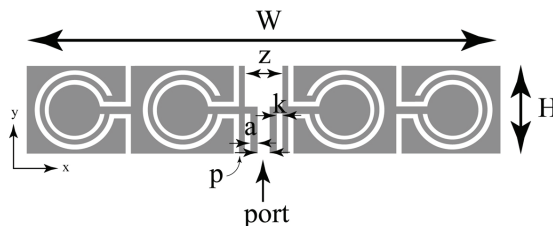


Fig. 6. Layout of the printed dipole using series connected OCSRR particles (the gray area is the copper).

The characteristics of the OCSRR dipole in Fig. 6 have been previously studied (Braaten, 2010a) and the results are summarized here in Tables 3 and 4. Table 3 shows how the input impedance of the OCSRR antenna in Fig. 6 changes for various values of $\varepsilon$ at a frequency of 920 MHz. The results in Table 4 show how the input impedance changes for various values of $d$ (i.e., substrate thickness) at a frequency of 920 MHz. Using the results in Tables 3 and 4, a designer will be able to predict how the input impedance of the antenna on the tag may change by being attached to a particular item. Knowing this information is useful for

designing a successful antenna on a passive UHF RFID tag. Notice that the gain is mostly unaffected except for thicker substrates.

A prototype passive UHF RFID tag using the OCSRR antenna in Fig. 6 has also been presented and tested (Braaten, 2010a). The read range of the prototype tag was > 5 m with overall dimensions of W = 55.54 mm and H = 11.91 mm. These overall dimensions are much smaller than many commercially available tags.

| ε | $f_0$ (MHz) | $Z_{in}$ (Ω) | G (dB) |
|---|---|---|---|
| 1.0 | 920 | 6.6-j94.7 | 1.82 |
| 2.2 | 920 | 7.9-j27 | 1.89 |
| 4.25 | 920 | 13.8+j110 | 1.89 |
| 5.8 | 920 | 36.5+j375 | 1.76 |

Table 3. Input impedance and gain of the OCSRR antenna at 920 MHz for various values of ε.

| d (mm) | $f_0$ (MHz) | $Z_{in}$ (Ω) | G (dB) |
|---|---|---|---|
| 0.127 | 920 | 7.4-j49 | 1.87 |
| 0.787 | 920 | 13.8+j110 | 1.88 |
| 1.57 | 920 | 28.1+j288 | 1.70 |
| 3.14 | 920 | 93+j677 | 1.35 |

Table 4. Input impedance and gain of the OCSRR antenna at 920 MHz for various values of d.

### 5.5 The MOCSRR particle

Next, the characteristics of the MOCSRR particle are investigated. The layout of an individual MOCSRR particle is shown in Fig. 7 (a). This particle is similar to the OCSRR particle except the ring slots take a meander route between ports a and b and not a circular route as in the OCSRR particle. This meander route results in a much lower resonant frequency for over all dimensions similar to an OCSRR particle. This lower resonant frequency is very useful for designing small resonant dipoles which is important for designing small efficient passive RFID tags.

### 5.6 Equivalent circuit and the dimensional relation of the MOCSRR particle

Using the CPW structure in Fig. 8 and the method discussed in section 5.2, the equivalent circuit is extracted for the MOCSRR particle for various values of δ and scaling factors. The dimensions of the MOCSRR particle in Fig. 7 are y = 8.2 mm, x = 8.05 mm, c = 0.42 mm, v = 0.22 mm, d = 2.92 mm, h = 5.17 mm, t = 0.33 mm, g = 0.31 mm and q = 0.43 mm. The substrate was defined to have a thickness of 1.36 mm and a permittivity of 4.2. The values of M and N in Fig. 8 were 0.4 mm and 3.1 mm, respectively. The overall dimensions of the MOCSRR particle and the OCSRR particle are similar to show the differences between the equivalent circuits of each particle.

The results of these computations are shown in Tables 5 and 6. Table 5 shows how the resonant frequency can be reduced by increasing the value of δ while the results in Table 6 show how the resonant frequency of the MOCSRR particle is related to the scaling factor

and δ = 1.54 mm. For a 5% reduction in the overall size of the particle, a 100 MHz increase in resonant frequency has been observed (i.e., the resonant frequency is approximately reduced 5 – 6% for each scale step).
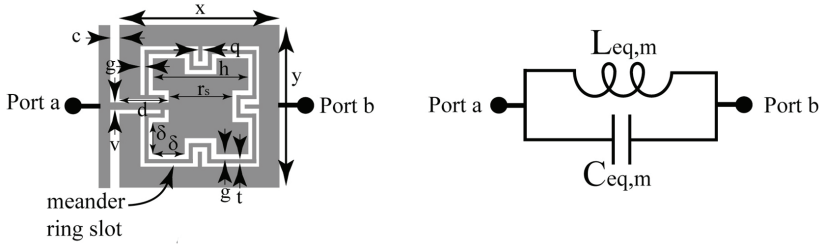


Fig. 7. (a) Layout of the MOCSRR particle (the gray area is the copper) and (b) the equivalent circuit of the MOCSRR particle.
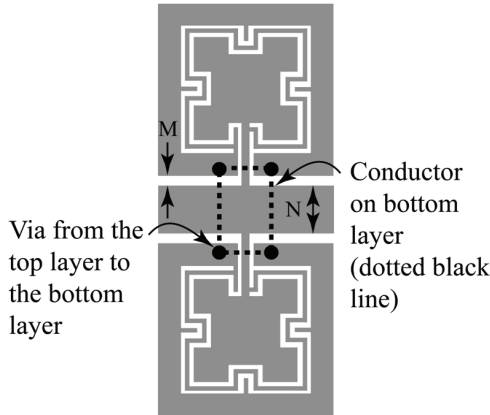


Fig. 8. CPW structure used to extract the equivalent circuit of the OCSRR particle (the gray area is the copper).

| δ (mm) | $r_s$ (mm) | $L_{eq}$ (nH) | $C_{eq}$ (pF) | $f_0$ (GHz) |
|--------|--------|--------|--------|--------|
| 0.9 | 1.6 | 3.6 | 2.9 | 1.55 |
| 1.0 | 1.7 | 3.8 | 2.75 | 1.55 |
| 1.1 | 1.8 | 3.7 | 2.85 | 1.55 |
| 1.2 | 1.9 | 3.4 | 3.1 | 1.55 |
| 1.3 | 2.0 | 3.4 | 3.15 | 1.53 |
| 1.4 | 2.1 | 3.5 | 3.1 | 1.52 |
| 1.5 | 2.2 | 3.7 | 3.25 | 1.45 |

Table 5. Equivalent circuit design table for the MOCSRR particle for various values of dimension $r_s$ and δ.

| S | $L_{eq}$ (nH) | $C_{eq}$ (pF) | $f_0$ (GHz) |
|-----|-----|-----|-----|
| 0.7 | 2.4 | 2.25 | 2.16 |
| 0.75 | 2.7 | 2.45 | 1.95 |
| 0.8 | 2.9 | 2.6 | 1.83 |
| 0.85 | 2.9 | 2.9 | 1.73 |
| 0.9 | 3.2 | 2.95 | 1.63 |
| 0.95 | 3.4 | 3.1 | 1.55 |
| 1.0 | 3.7 | 3.25 | 1.45 |

Table 6. Equivalent circuit design table for the MOCSRR particle for various scale factors S.

## 5.7 Discussion

Comparing the results in Table 1 to the results in Table 5 shows how much the resonant frequency of the particle is reduced by using a meander ring slot instead of a circular ring slot. This is because the results in Tables 1, 2, 5 and 6 show that the MOCSRR particle has approximately twice the inductance as the OCSRR particle while the capacitance is comparable. This is very useful for antenna miniaturization because the impedance of the particles is inductive. This inductive property can be used for matching transmission lines to the capacitive input impedance of electrically small antennas.

## 5.8 Antenna designs using the MOCSRR particle

MOCSRR particles can be connected in a similar manner to the series connected OCSRR particles shown in Fig. 6 in section 5.4. This will result in the layout show in Fig. 9. Since the equivalent circuit of each MOCSRR particle has the same equivalent circuit of each meander-line section in Fig. 4, an electrically small resonant dipole can be designed.

To understand the behaviour of the antenna in Fig. 9, the input impedance was computed for various substrate values of permittivity and thicknesses. The results for a = 0.4 mm and z = 1.09 mm are shown in Figs. 10 – 13 (particle dimensions are defined in section 5.6 with δ = 1.54 mm).
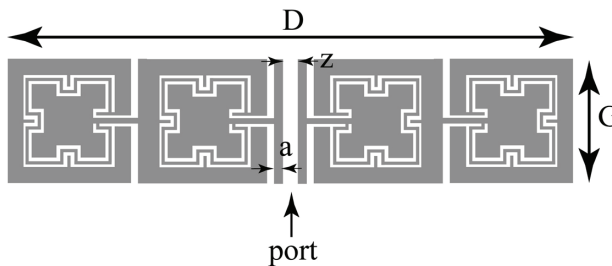


Fig. 9. Layout of the printed dipole using series connected MOCSRR particles (the gray area is the copper).

The results Figs. 10 and 11 show how the input impedance of the antenna is related to the permittivity of the substrate. For these computations the substrate thickness was fixed at d = 1.36 mm. For example, at 920 MHz the antenna is most appropriately matched to the input impedance of the passive IC for a substrate permittivity of 4.2. This makes the antenna

in Fig. 9 desirable for printing on FR4 substrates. Figs. 10 and 11 also show how the input impedance can change dramatically for slightly lower and higher values of substrate permittivity. This information is useful for a designer when a tag is placed on various items. By understanding how the impedance of the antenna changes for various substrates, the maximum read range of a tag used on multiple items could be predicted.
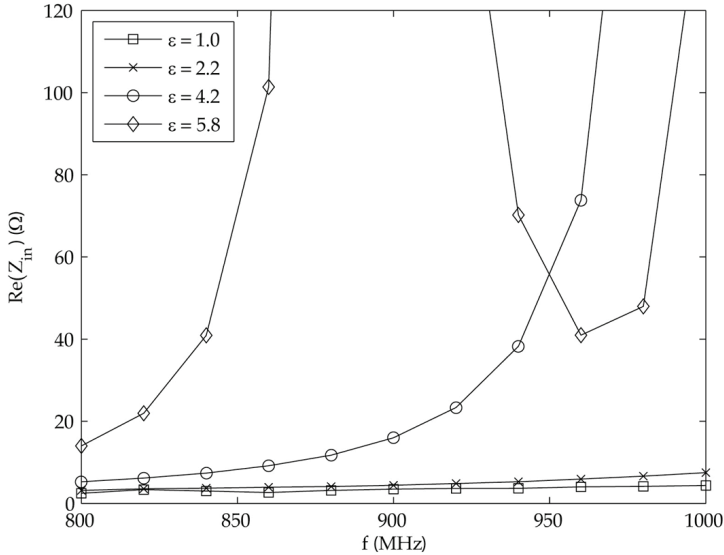


Fig. 10. Real part of the input impedance of the MOCSRR antenna for various values of ε.
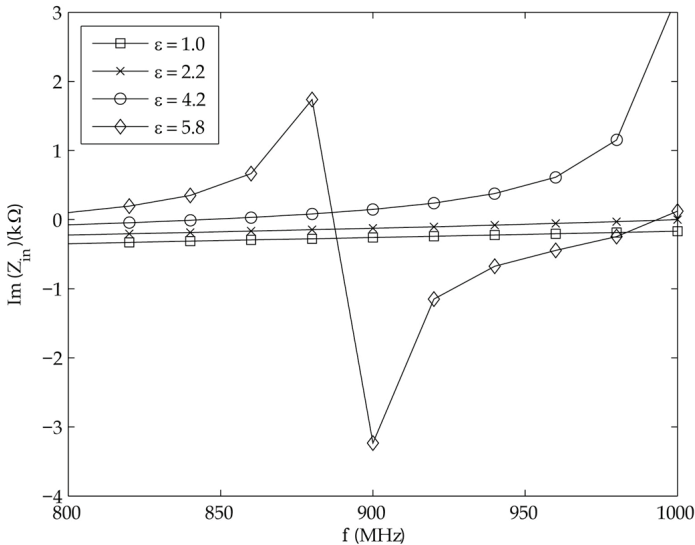


Fig. 11. Imaginary part of the input impedance of the MOCSRR antenna for various values of ε.

The results in Figs. 12 and 13 provide further information on the behaviour of the MOCSRR antenna. These results show how the input impedance changes with substrates of different thicknesses. At 920 MHz the antenna in Fig. 9 has the optimum match at d = 1.36 mm.
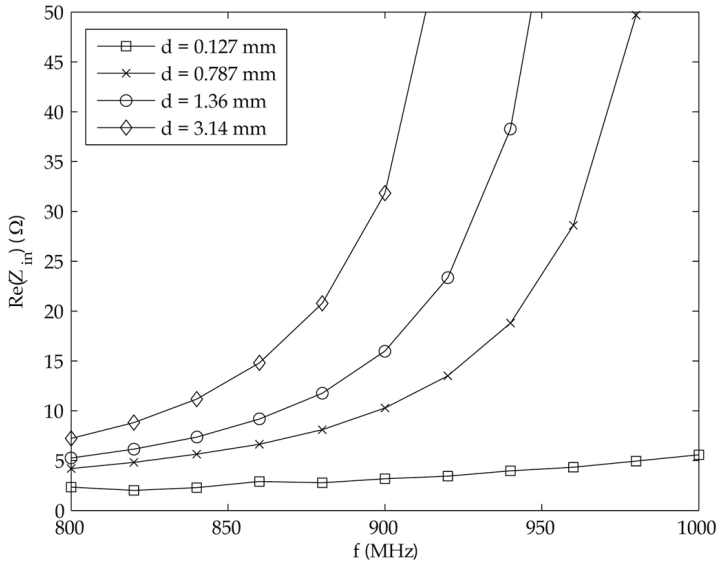


Fig. 12. Real part of the input impedance of the MOCSRR antenna for various values of d.
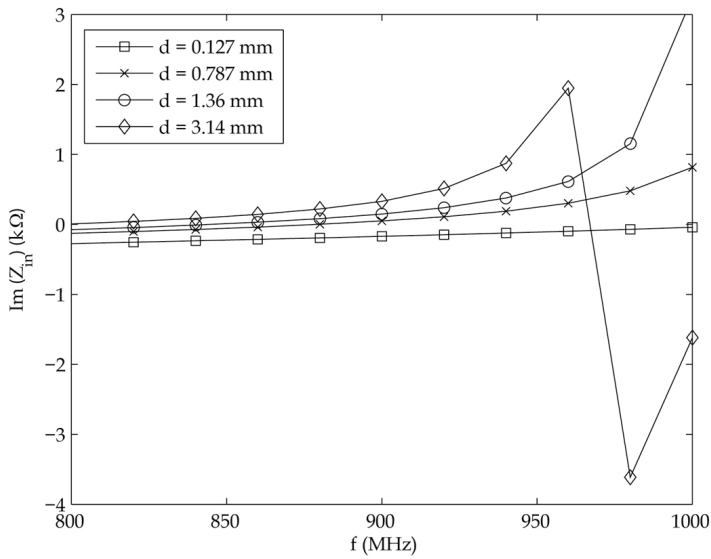


Fig. 13. Imaginary part of the input impedance of the MOCSRR antenna for various values of d.

## 6. Future work

Many different future topics of research could be explored as a result of this work. Several of these topics could involve work on a different type of CPW particle, left-handed propagation using the MOCSRR particles or analytical relations between the resonant frequencies of the particle to various geometrical values. Studying these topics could further reduce the size of the resonant antennas presented here or significantly shorten the design time for an engineer using these particular antennas on a passive RFID tag.

## 7. Conclusion

Initially in this work a RFID system has been introduced using the Friis transmission equation. This introduction was then followed by recent applications of RFID systems and an introduction of the CPW structure. This then lead to sections outlining the design of small resonant dipoles with OCSRR and MOCSRR particles. Particularly, the results in these sections showed how the resonant frequencies of the particles were extracted and related to various geometrical dimensions and how the input impedance of the small resonant dipoles was related to various substrates.

## 8. References

Advanced Design System 2009a, Agilent Technologies, www.agilent.com.

Braaten, B.D.; Feng, Y.; & Nelson, R.M., "High-frequency RFID tags: an analytical and numerical approach for determining the induced currents and scattered fields," *IEEE International Symposium on Electromagnetic Compatibility,* pp. 58-62, August 2006, Portland, OR.

Braaten, B. D.; Owen, G. J.; Vaselaar, D.; Nelson, R. M.; Bauer-Reich, C.; Glower, J.; Morlock, B; Reich, M.; & Reinholz, A., "A printed Rampart-line antenna with a dielectric superstrate for UHF RFID applications," in *Proceedings of the IEEE Interntational Conference on RFID,* pp. 74-80, April, 2008, Las Vegas, NV.

Braaten, B. D., "A novel compact UHF RFID tag antenna designed with series connected open complementary split ring resonator (OCSRR) particles," *IEEE Transactions on Antennas and Propagation*, vol. 58, no. 11, November, 2010a, pp. 3728 – 3733 2010a.

Braaten, B. D.; Aziz, M. A.; Schroeder, M. J.; and Li, H., "Meander open complementary split ring resonator (MOCSRR) particles implemented using coplanar waveguides," *IEEE International Conference on Wireless Information Technology and Systems,* Honolulu, Hawai, Aug. 28 - Sep. 3, 2010b.

Cai, A.; Qing, X.; & Chen, Z.N., "High frequency RFID smart table antenna," *Microwave Optical Technological Letters*, vol. 49, no. 9, September 2007, pp. 2074-2076.

Calabrese, C. & Marrocco, G., "Meander-slot antennas for sensor-RFID tags," *IEEE Antennas and Wireless Propagation Letters.,* vol. 7, pp. 5-8, 2008.

Collin, R. E. (2001). *Foundations for Microwave Engineering,* 2nd ed., John Wiley and Sons, Inc. Hoboken, New Jersey.

Dacuna, J. & Pous, R. "Miniaturized UHF tags based on metamaterials geometries," *Building Radio Frequency Identification for the Global Environment*, July 2007, [Online], www.bridge-project.eu.

Eleftheriates, G. V. & Balmain, K. G. (2005) *Negative-Refraction Metamaterials: Fundamentals Principles and Applications,* John Wiley and Sons, Hoboken, New Jersey.

Finkenzeller, K. (2003). *RFID Handbook:Fundamentals and Applications in Contactless Smart Cards and Identification*, John Wiley and Sons, West Sussex, England.

Griffin, J.D.; Durgin, G.D.; Haldi, A.; & Kippelen, B., "RF tag antenna performance on various materials using radio link budgets," *IEEE Antennas and Propagation Letters*, vol. 5, no. 1, 2006, pp. 247-250.

Jefflindsay, 2010, "RFID Systems for Enhanced Shopping Experiences,"Experiences,"http://www.jefflindsay.com/rfid4. s html Kanan, R.; & Azizi, A., "UHF RFID transponders antenna design for metal and wood surfaces," *IEEE International Conference on RFID*, pp. 270-277, April, 2009, Orlando, FL.

Landt, J., "The history of RFID," *IEEE potentials*, vol. 24, no. 4, 2005, pp. 8-11.

Lee, J.M.; Kim, N.S.; & Pyo, C.S., "A circular polarized metallic patch antenna for RFID reader," in *Asia-Pacific Conference on Communication*, pp. 116-118, October 2005, Australia.

Marrocco, G., "Gain-optimized self-resonant meander line antennas for RFID applications," *IEEE Antennas and Wireless Propagation Letters.,* vol. 2, pp. 302-305, 2003.

Medeiros, C.R.; Costa, J.R.; & Fernandes, C.A., "RFID smart shelf with confined detection volume at UHF," *IEEE Antennas and Wireless Propagation Letters*, vol. 7, 2008, pp. 773-776.

Mohammed, N.A.; Sivakumar, M.; & Deavours, D.D., "An RFID tag capable of free-space and on-metal operation," *IEEE Radio and Wireless Symposium*, pp. 63-66, 2009, San Diego, CA.

Ng, M. L.; Leong, K. S.; Hall, D.M.; & Cole, P.H., "A small passive UHF RFID tag for livestock identification," *IEEE International Symposium on Microwave, Antenna, Propagation and EMC Technologies for Wireless communications,* vol. 1, 2005, pp. 67-70.

Pozar, D. M. (2005). *Microwave Engineering,* 3rd ed., John Wiley and Sons, Inc., Hoboken, New Jersey.

Qing, X. & Chen, Z.N., "Proximity effects of metallic environments on high frequency RFID reader antenna: Study and Applications," *IEEE Transactions on Antennas and Propagation,* vol. 55, no. 11, November, 2007, pp. 3105-3111.

Rao, K. V. S.; Nikitin, P.V.; & Lam, S.F., "Antenna Design for UHF RFID Tags: A Review and a Practical Application," *IEEE Transactions on Antennas and Propagation,* vol. 53, no. 12, December, 2005, pp. 3870-3876.

Rao, K. V. S.; Nikitin, P.V.; & Lam, S.F., "Wideband metal mount UHF RFID tag," *IEEE Antenna and Propagation Society International Symposium*, pp. 1-4, 2008, San Diego, CA.

Stutzman, W.L. & Thiele, G.A. (1998). *Antenna Theory and Design*, 2nd ed., John Wiley and Sons, Inc., New York.

Teco, 2010, "RFID Smart Shelf," http://www.teco.edu/research/projects/smartshelf/.

Velez, A.; Aznar, F.; Bonache, J.; Valazquez-Ahumada, M. C.; Martel, J.; and Martin, F., "Open complementary split ring resonators (OCSRRs) and their application to

wideband CPW band pass filter," *IEEE Microwave and Wireless Components Letters,* vol. 19, no. 4, pp. 197-199, Apr. 2009.

Want, R., "An introduction to RFID technology," *IEEE Pervasive Computing*, vol. 5, no. 1, 2006, pp. 25-33.

Zhu, W.; Yuan, B.; Zhang, Z.; Wang, J.; & Huang, J., "A novel 2.4 GHz Quasi-Yagi tag antenna for RFID of metallic object," *Asia Pacific Microwave Conference*, pp. 1-4, 2008, Macau.

# Fully Printable Chipless RFID Tag

Stevan Preradovic and Nemai Karmakar
*Monash University*
*Australia*

## 1. Introduction

### 1.1 Radio frequency identification

Radio frequency identification (RFID) is a wireless data capturing technique which utilizes radio frequency (RF) waves for automatic identification of objects. RFID relies on RF waves for data transmission between the data carrying device, called the RFID tag, and the interrogator (Finkenzeller, 2003; Kraiser & Steinhagen, 1995)

A typical RFID system is shown in Fig. 1. An RFID system consists of three major components: a **reader** or **interrogator**, which sends the interrogation signals to an RFID tag, which is to be identified; an RFID **tag** or **transponder**, which contains the identification code; and **middleware software**, which maintains the interface and the software protocol to encode and decode the identification data from the reader into a mainframe or personal computer. The RFID reader can read tags only within the reader's interrogation zone. The reader is most commonly connected to a host computer which performs additional signal processing and has a display of the tag's identity (Preradovic & Karmakar, 2007). The host computer can also be connected via internet for global connectivity/networking.
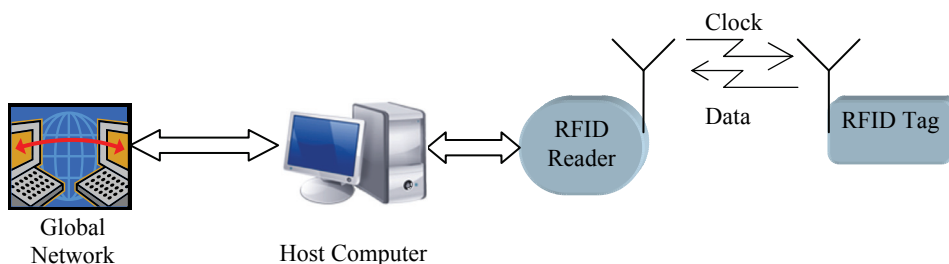


Fig. 1. Block diagram of a typical RFID system.

RFID was first proposed by Stockman (Stockman, 1948) in his landmark paper "Communication by Means of Reflected Power" in 1948. Stockman advocates that by alternating the load of the tag antenna it is possible to vary the amount of reflected power (also called "antenna load modulation") and therefore perform modulation. This new form of wireless technology is now known as RFID. Since then researchers and engineers have been working on developing low cost RFID systems.

## 1.2 Difficulties of achieving low cost RFID

The use of RFID instead of optical barcodes has not yet been achieved due to the greater price of the RFID tag (10 cents) compared to the price of the optical barcode (less than 0.1 cents). The arguments for not having a cheap RFID tag are comprehensively presented in (Fletcher, 2002). Fletcher advocates that Application Specific Integrated Circuit (ASIC) design and testing along with the tag antenna and ASIC assembly result in a costly manufacturing process. This is why it is not possible to further lower the price of the chipped RFID tag. The basic steps for manufacturing a chipped RFID tag are shown in Fig 2.
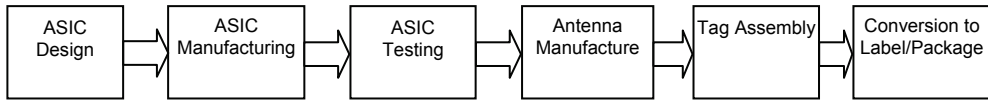


Fig. 2. RFID label/tag manufacturing process.

The design of silicon chips has been standardized for over 30 years and the cost of building a silicon fabrication plant is in the billions of US dollars (Hodges & Jackson, 1988; Baker et al, 1998). Since silicon chips are fabricated on a wafer-by-wafer basis there is a fixed cost per wafer (around US $1000). As the cost of the wafer is independent of the IC design, the cost of the RFID chip can be estimated based on the required silicon area for the RFID chip. Significant achievements have been made in reducing the size of the transistors allowing more transistors per wafer area (Natarajan, 2008). Decreasing the amount of transistors needed results in an even smaller silicon area, hence a lower RFID chip price. As a result, great efforts have been made by the Massachusetts Institute of Technology (MIT) to design a RFID ASIC with less than 8000 transistors. Although this will reduce the price of the silicon chip, its miniature size imposes limitations and further handling costs.

The cost of dividing the wafer, handling the die and placing them onto a label remains significant, even if the cost of the RFID chip were next-to-nothing. The cost of handling the die increases with the use of smaller than standard chips, simply because the electronics industry is not standardized for them. Hence, with highly-optimized low transistor count ASICs, implemented assembly processes and extremely large quantities (over 1 billion) of RFID chips sold per annum, a minimum cost of 5 cents is the reality for chipped RFID tags.

## 1.3 Chipless RFID tags

Given the inevitable high cost of silicon chip RFID tags (when compared to optical barcodes), efforts to design low cost RFID tags without the use of traditional silicon ASICs have emerged. These tags, and therefore systems, are known as **chipless** RFID systems. Most chipless RFID systems use the electromagnetic properties of materials and/or design various conductor layouts/shapes to achieve particular electromagnetic properties/behaviour. The main focus of this thesis will be on chipless RFID systems.

There have been some reported chipless RFID tag developments in recent years. However, most are still reported as prototypes and only a handful are considered to be commercially viable or available. The challenge for researchers when designing chipless RFID tags is how to perform data encoding without the presence of a chip. In response to this problem two general types of RFID tags can be identified: time domain reflectometry (TDR)-based and spectral (frequency) signature-based chipless RFID tags. Fig. 3 shows the classification of reported chipless RFID tags.
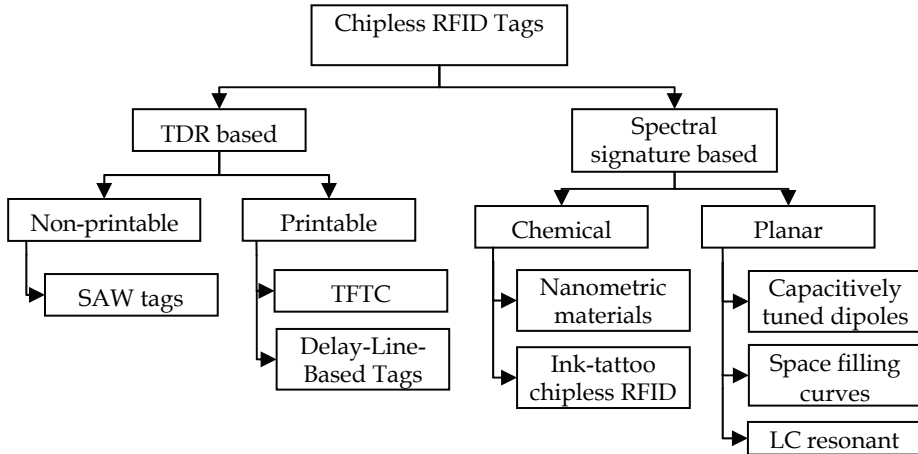
Fig. 3. Classification of chipless RFID tags.

**TDR-based chipless RFID tags** are interrogated by sending a signal from the reader in the form of a pulse and listening to the echoes of the pulse sent by the tag. A train of pulses is thereby created which can be used to encode data. Various RFID tags have been reported using TDR-based technology for data encoding. We can distinguish between non-printable and printable TDR-based tags.

An example of a **non-printable** TDR-based chipless RFID tag is the surface acoustic wave (SAW) tag developed by RFSAW Inc (Harma et al, 2006) which is also the commercially most successful. **SAW tags** are excited by a chirped Gaussian pulse sent by the reader centred around 2.45 GHz. The interrogation pulse is converted to a surface acoustic wave using an interdigital transducer (IDT). The surface acoustic wave propagates across the piezoelectric crystal and is reflected by a number of reflectors which create a train of pulses with phase shifts. The train of pulses is converted back to an EM wave using the IDT and detected at the reader end where the tag's ID is decoded (Hartmann, 2002).

**Printable TDR-based** chipless tags can be found either as Thin-Film-Transistor-Circuits (TFTC) or microstrip-based tags with discontinuities. **TFTC tags** are printed at high speed on low cost plastic film (Das & Harrop, 2006). TFTC tags offer advantages over active and passive chip-based tags due to their small size and low power consumption. They require more power than other chipless tags but offer more functionality. However low cost manufacturing processes for TFTC tags have not yet been developed. Another issue is the low electron mobility which limits the frequency of operation up to several MHz.

**Delay-line-based** chipless RFID tags operate by introducing a microstrip discontinuity after a section of delay-line as reported in (Shretha et al, 2007). The tag is excited by a short pulse (1ns) EM signal. The interrogation pulse is received by the tag and reflected at various points along the microstrip line creating multiple echoes of the interrogation pulse. The time delay between the echoes is determined by the length of the delay-line between the discontinuities. This type of tag is a replica of the SAW tag using microstrip technology which makes it printable. Although initial trials of and experiments on this chipless technology have been reported, only 4 bits of data have been successfully encoded, which shows the limited potential of this technology.

**Spectral signature-based chipless tags** encode data into the spectrum using resonant structures. Each data bit is usually associated with the presence or absence of a resonant peak at a predetermined frequency in the spectrum. So far, five types of spectral signature-based tags have been reported and all five are considered to be fully printable. We can distinguish two types of spectral signature tags based on the nature of the tag: chemical and planar circuit.

**Chemical tags** are designed from a deposition of resonating fibres or special electronic ink. Two companies from Israel use **nanometric materials** to design chipless tags. These tags consist of tiny particles of chemicals which exhibit varying degrees of magnetism and when electromagnetic waves impinge on them they resonate with distinct frequencies, which are picked up by the reader. They are very cheap and can easily be used inside banknotes and important documents for anti-counterfeiting and authentication. CrossID, an Israeli paper company, claims to have 70 distinct chemicals which would provide unique identification in the order of $2^{70}$ (over $10^{21}$) when resonated and detected suitably (Glickstein, 2004). Tapemark also claims to have "nanometric" resonant fibres which are 5 microns in diameter and 1mm in length (Collins, 2004). These tags are potentially low cost and can work on low grade paper and plastic packaging material. Unfortunately, they only operate at frequencies up to a few KHz, although this gives them very good tolerances to metal and water.

**Ink-tattoo chipless tags** use electronic ink patterns embedded into or printed onto the surface of the object being tagged. Developed by Somark Innovations (Jones, 2007), the electronic ink is deposited in a unique barcode pattern which is different for every item. The system operates by interrogating the ink-tattoo tag by a high frequency microwave signal (>10 GHz) and is reflected by areas of the tattoo which have ink creating a unique pattern which can be detected by the reader. The reading range is claimed to be up to 1.2 m (4 feet). In the case of animal ID, the ink is placed in a one-time-use disposable cartridge. For non-animal applications the ink can be printed on plastic/paper or within the material. Based on the limited information available for this technology (which is still in the experimental phase) the author assumes that it is spectral signature based.

**Planar circuit chipless RFID tags** are designed using standard planar microstrip/co-planar waveguide/stripline resonant structures such as antennas, filters, and fractals. They are printed on thick, thin and flexible laminates and polymer substrates. **Capacitively tuned dipoles** were first reported by *Jalaly* (Jalaly & Robertson, 2005). The chipless tag consists of a number of dipole antennas which resonate at different frequencies. When the tag is interrogated by a frequency sweep signal the reader looks for magnitude dips in the spectrum as a result of the dipoles. Each dipole has a 1:1 correspondence to a data bit. Issues regarding this technology include: tag size (lower frequency longer dipole – half wavelength) and mutual coupling effects between dipole elements.

**Space-filling curves** used as spectral signature encoding RFID tags were first reported by *McVay* (McVay et al, 2006). The tags are designed as Peano and Hilbert curves with resonances centred around 900 MHz. The tags represent a frequency selective surface (FSS) which is manipulated with the use of space-filling curves (such as the Hilbert curve). The tag was successfully interrogated in an anechoic chamber. Only 3 bits of data have been reported to date. However, the tag requires significant layout modifications in order to encode data.

**LC Resonant** chipless tags comprise of a simple coil which is resonant at a particular frequency. These tags are considered 1-bit RFID tags. The operating principle is based on the magnetic coupling between the reader antenna and the LC resonant tag. The reader

constantly performs a frequency sweep searching for tags. Whenever the swept frequency corresponds to the tag's resonant frequency, the tag will start to oscillate, producing a voltage dip across the reader's antenna ports. The advantage of these tags is their price and simple structure (single resonant coil), but they are very restricted in operating range, information storage (1 bit), operating bandwidth and multiple-tag collision. These tags are mainly used for electronic article surveillance (EAS) in many supermarkets and retail stores (Tagsense, 2006).

## 2. Chipless RFID tag operating principle

In this book chapter we present a fully printable chipless RFID system based on multiresonators and cross-polarized ultra-wide band (UWB) monopole antennas. The tag's unique ID is encoded as the spectral signatures of the resonators. The main differences between the chipless RFID system presented here and others reported by McVay *et al* (McVay et al, 2006) and Jalaly *et al* (Jalaly & Robertson, 2005) are that we encode data in both amplitude and phase and the operation is not based on radar cross section (RCS) back-scattering. The chipless RFID system works on retransmission of the interrogation signal with the encoded unique spectral ID. The received and transmitted signals are cross-polarized in order to achieve good isolation between the two. Due to the robust design based on microwave engineering (multiresonators) and antenna technology (cross-polarized Tx/Rx antennas), we believe to have achieved less mutual coupling effects, greater number of possible bits and easier encoding than that reported by McVay *et al* and Jalaly *et al*.
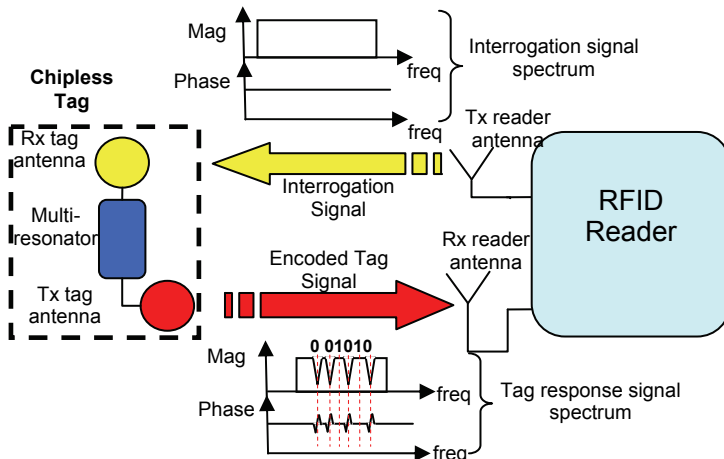


Fig. 4. Principal block diagram of chipless RFID system.

As the chipless RFID system uses spectral signatures for data encoding and is fully passive, the tags do not need any power supply in order to operate (Preradovic et al, 2009). The main application for this chipless RFID system is mainly short range (up to 40 cm) tagging of extremely low cost items. Hence, power limitation restrictions (transmitted EIRP maximum of -45 dBm outdoors and -55 dBm indoors), does not present a major concern for the presented system. The principal block diagram of the chipless RFID system is shown in Fig. 4. As can be seen in Fig. 4, the chipless tag encodes data in the frequency spectrum and thus

has a unique ID of spectral signatures. The spectral signature is obtained by interrogating the tag by a continuous wave (CW) multi-frequency signal of uniform amplitude and phase. The tag then receives the interrogation signal and encodes the data into the frequency spectrum in both magnitude and phase. The encoded signal is then retransmitted back to the reader. This allows the reader to use two criteria for data decoding – amplitude and phase.
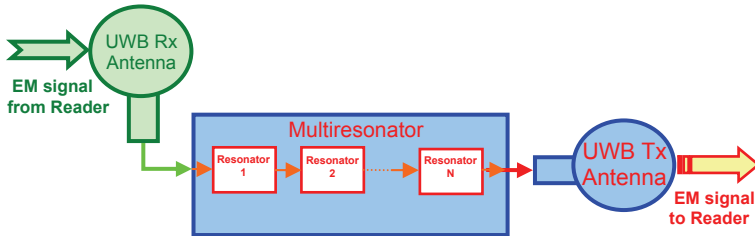


Fig. 5. Block diagram of chipless RFID tag.

The chipless RFID tag consists of UWB antennas and a multiresonating circuit operating in the UWB frequency spectrum as shown in Fig. 5. The UWB antennas are used to receive the interrogation signal sent from the reader and transmit the signal back to the reader after performing spectral signal modulation by the multiresonator. The multiresonator is a combination of multiple filtering sections which are used to modulate the spectrum of the interrogation signal sent by the reader. Modulation is performed in both magnitude and phase of the spectrum.

The chipless RFID reader is an electronic device which can detect the ID of the chipless tag when it is within the reader's interrogation zone. The block diagram of the chipless RFID reader is shown in Fig. 6. The RFID reader has transmitting and receiving antennas to send the interrogation signal to the chipless tags and receive the encoded signal from the chipless tags. The RFID reader transmitter comprises a voltage controlled oscillator (VCO), low noise amplifier (LNA) and power amplifier (PA). Tuning of the VCO's output frequency is done by the microcontroller through the digital-to-analog (ADC) converter. The reader transmitter generates the interrogation signal which is sent to the chipless tag. The chipless tranponder encodes its spectral signature into the reader's interrogation signal and sends the signal back to the reader. The signal flow diagram of the chipless RFID system is shown in Fig. 7.
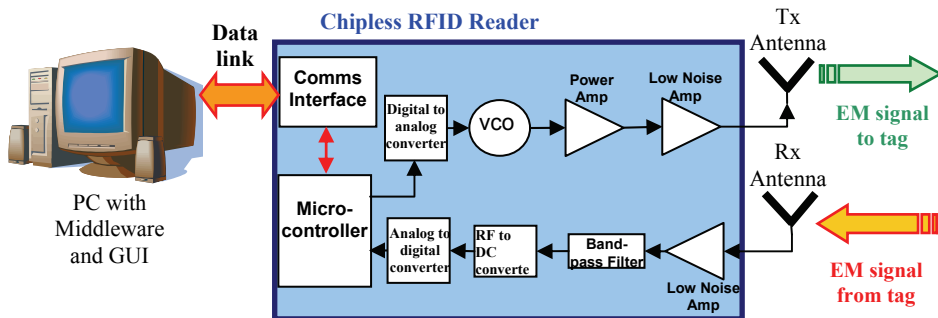


Fig. 6. Block diagram of proposed chipless RFID reader.
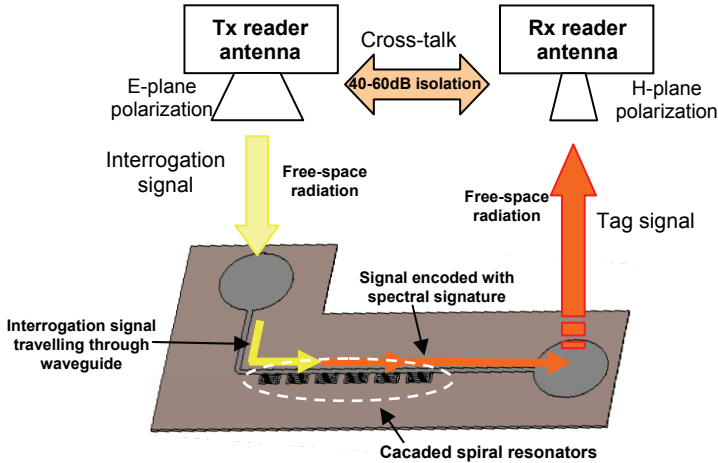
Fig. 7. Chipless RFID system signal flow diagram.

The chipless tag encodes data in the frequency spectrum thus encoding the spectrum with its unique spectral signature. The spectral signature is obtained by the RFID reader by interrogating the tag by a multi-frequency signal. The tag encodes its spectral signature into the interrogation signal spectrum using a multiresonating circuit which is a multi-stop band filter. The multiresonator is a set of cascaded spiral resonators designed to resonate at particular frequencies and create stop bands. The stop band resonances introduce magnitude attenuation and phase jumps to the transmitted interrogation signal at their resonant frequencies which are detected as abrupt amplitude attenuations and phase jumps by the RFID reader. In order to provide isolation between the transmitting and receiving signal, the reader and tag antennas are cross-polarized. As a result, cross-talk between the transmitting and receiving antennas is minimized at the cost of introducing restrictions in tag positioning and orientation.

The chipless RFID system is designed for a short range conveyor belt system where the tagged items are tracked moving through the interrogation zone of a fixed reader antenna system as shown in Fig. 8.
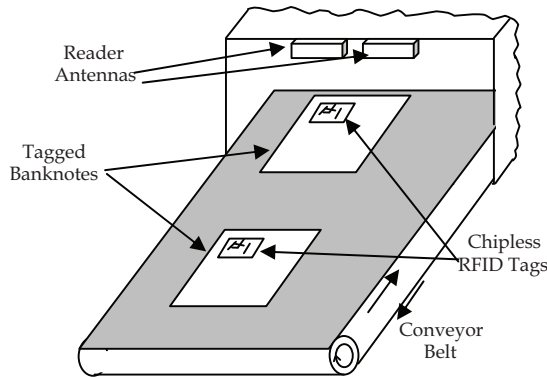


Fig. 8. Potential conveyor belt application for chipless RFID system.

## 3. Chipless RFID tag development

In this section the chipless tag development is presened. The tag design steps are shown in Fig. 9. The tag design was begun by designing the tag monopole antennas and achieving the necessary return loss bandwidth and radiation pattern. Following the tag antenna design, design and optimization of the spiral resonators (multiresonating circuit) were carried out. When the tag antenna and multiresonating circuit were optimized they are integrated to form a complete chipless RFID tag which were then tested in a wireless experimental setup inside an anechoic chamber (for theoretical verification) and in a laboratory (for investigations of robustness). In the following sections, the design of the tag antenna, multiresonator and integrated tag are presented

| Monopole Antenna Parametric Study & Optimization | Multi-resonator Parametric Study & Optimization | Antenna & Multi-resonator Integration to Form Chipless Tag | Chipless Tag Testing |
|---|---|---|---|
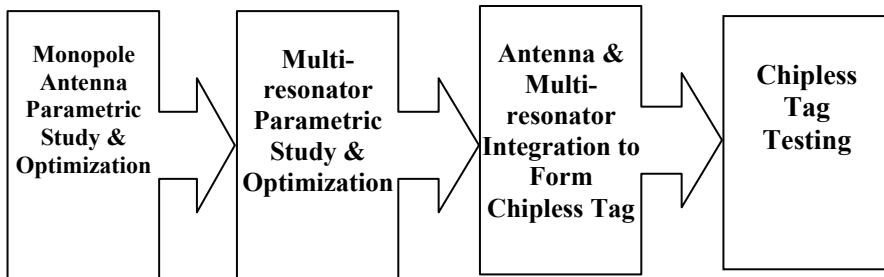
Fig. 9. Chipless Tag design process.

### 3.1 Chipless tag antenna - UWB monopole

Circular UWB monopole antennas have a simple layout and exhibit extremely large bandwidth and a figure-of-eight radiation pattern (Chen et al, 2007; Alipour & Hassani, 2008; Wu et al, 2008). UWB dipole antennas have been reported by researchers with similar radiation properties and bandwidth as those found using UWB monopoles (Quintero & Skrivervik, 2008; Mudroch et al, 2009; Whyte et al, 2008). Both types of antennas are fully printable and initially appear suitable for deployment as the chipless RFID tag antenna. The main disadvantage of UWB dipoles when compared to UWB monopoles is that they require an impedance matching circuit and/or balun which can increase the size and complexity of design of the tag. As UWB monopole antennas need no impedance matching circuit or balun for their successful operation, they are a preferred solution for the chipless RFID tag antenna. The UWB characteristic of the monopole antenna is attributed to the overlapping of the antenna modes (resonances) which are closely distributed over the spectrum (Angelopoulos et al, 2006). The operational principle of the UWB disc monopole is shown in Fig. 10. The use of the higher order modes influences the monopole's radiation pattern in the E-plane which becomes distorted from a figure-of-eight radiation pattern in the fundamental mode. At the antenna's fundamental mode of operation the wavelength of the transmitting/receiving signal is greater than the antenna's dimensions and because the antenna operates in an oscillating mode a standing wave is formed. As the frequency of the signal (and therefore operation) increases, the antenna starts operating in a hybrid mode of standing and travelling waves. At higher frequencies the travelling waves are dominant since the wavelengths at these frequencies are smaller than the antenna structure. Therefore, due to the hybrid modes of antenna operation it is possible to create an extremely wide-

band operating antenna at the expense of radiation pattern distortion at higher operating modes. These distortions are due to the surface current distribution in higher order modes. The H plane radiation pattern remains constant throughout the operating band. This is due to the symmetry of the antenna's configuration along its axis of rotation.
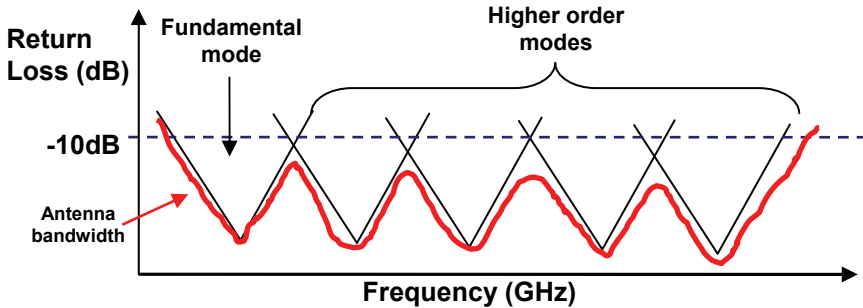


Fig. 10. UWB monopole operational principle.
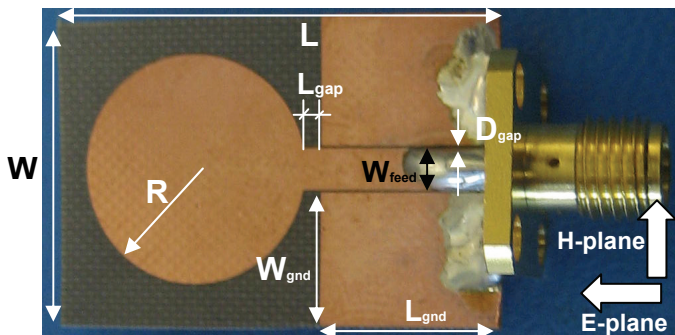


Fig. 11. Photograph of CPW fed UWB monopole (L = 27 mm, W = 18.8 mm, Lgnd = 12 mm, Wgnd = 8mm, Dgap = 0.15 mm, Lgap = 2 mm, Wfeed = 2.5 mm and R =7 mm, substrate Taconic TF-290 $\varepsilon_r$ = 2.9, h = 0.09 mm, tan$\delta$ = 0.0028).

The CPW disc monopole antenna is a single layer-metallic structure comprised of a copper disc with radius $R$ and a 50$\Omega$ CPW printed on the same side of the dielectric substrate Taconic TF-290 ($\varepsilon r$=2.9, h=90µm, tan$\delta$=0.0028). The manufactured CPW monopole antenna with design parameters is shown in Fig. 11.

### 3.2 Chipless tag multiresonator

In this section the design of the chipless tag multiresonator is presented. The chipless tag encodes data by using spectral signature encoding. Each tag has a different spectral signature by filtering out a predefined set of frequencies. The multiresonator circuit comprises a set of cascaded spiral resonators which resonate at different frequencies.

Coplanar waveguide (CPW) technology was used for designing high Q spiral resonators. The CPW was first proposed by C. P. Wen in 1969 (Wen, 1969). Wen proposed the novel waveguide as a dielectric substrate coated with a single layer of copper. It consists of a conductor centre strip with conductive ground plane sheets on both sides of the strip. The

impedance of the strip is determined by the width of the strip, the gap, the permittivity and thickness of the dielectric. In practice this means that we can have multiple widths of the CPW strip on the same dielectric which would have, for example, a 50 ohm impedance at the cost of modification of the gap between the strip and ground planes. This property of CPW makes it a very flexible transmission line technology. CPW technology uses spiral shapes etched out in the stripline to create stop bands. The layout of a spiral resonator designed on 90 µm thin Taconic TF-290 laminate is shown in Fig. 12.
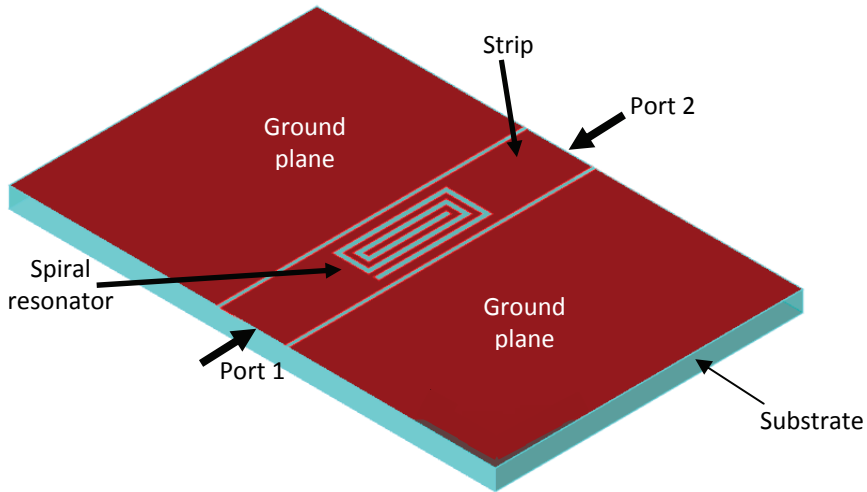
Fig. 12. Layout of spiral resonator etched out in a CPW strip line.
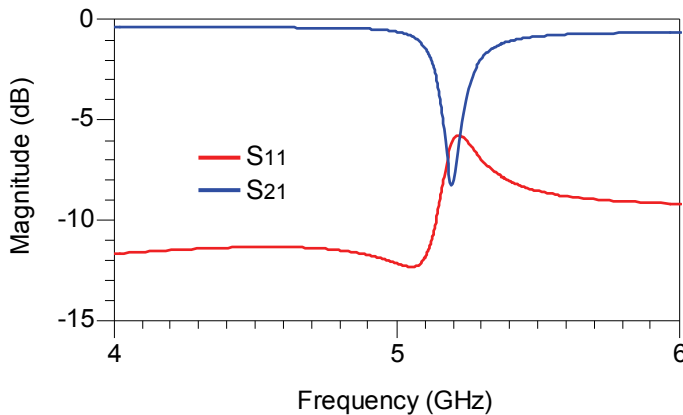
Fig. 13. Simulated frequency response of spiral resonator etched out in a CPW strip line on TF-290  ($\varepsilon r$ = 2.9, h = 90 µm, tan$\delta$ = 0.0028).

The CPW the ground plane and the spiral resonator are on the same plane (top layer). The strip line is separated from the continuous metallic ground planes by a gap. At its resonant frequency, the spiral resonator creates a stop band as can be seen in Fig. 13. The 2-port s-

parameters of the CPW spiral resonator were obtained from ADS Momentum 2008. The CPW spiral resonator was designed on Taconic TF-290 (εr = 2.9, h = 90 µm , tanδ = 0.0028). Each spiral resonator introduces a different stop-band resonance. By varying the dimensions of the spiral resonator we can vary the resonance. Fig. 14 shows the variation of the spiral's resonant frequency and attenuation with the spiral's resonator length $L_{spiral}$ as obtained from ADS 2008 Momentum simulation.
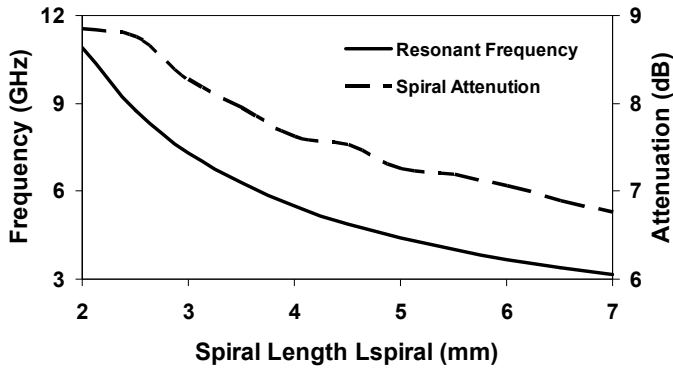


Fig. 14. CPW spiral resonant frequency and attenuation vs spiral length $L_{spiral}$.

The advantages of the CPW spiral resonator in comparison to the microstrip spiral resonator are higher attenuation at resonant frequency and the single sided layout. The disadvantages are in terms of compact layout, since CPW spiral resonators can be cascaded only by placing them in series. Fig. 15 shows a photograph of the fabricated 3-bit multiresonator on TF-290 substrate. The 3-bit multiresonator consists of 3 spiral resonators cascaded within a 50 ohm CPW strip line. The spirals are etched in the CPW strip line. The CPW multiresonator provides 3 distinguishable resonances between 2 and 2.5 GHz. Each resonance is separated by approximately 200 MHz from each other. In order to design the spirals at different frequencies, the length of each spiral has been varied so that the spiral's resonant frequency is tuned.
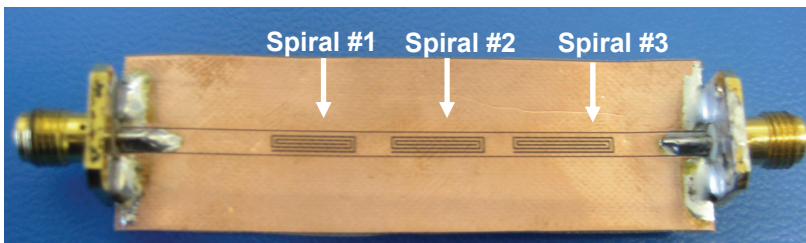


Fig. 15. Photograph of manufactured CPW 3-bit multiresonator on 90 µm Taconic TF-290 substrate.

Fig. 16 shows the simulated frequency response in both magnitude and phase of the 3-bit multiresonator. From Fig. 16 it is clear that at the resonant frequencies of each spiral of the multiresonator there is a magnitude null and phase jump in the magnitude and phase of the spectrum of the CPW multiresonator. These distinct nulls and jumps in magnitude and

phase respectively are interpreted as logic "0" while their absences at the resonant frequencies are interpreted as logic "1".
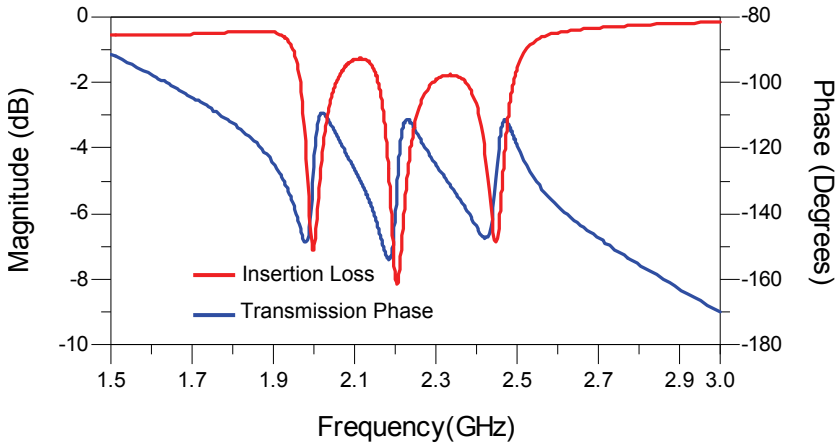


Fig. 16. Measured insertion loss and transmission phase of CPW 3-bit multiresonator.

### 3.3 Encoding data using spiral shorting

It is necessary to encode data into the tag in order for the tag to have a unique ID. The short ing of the turns of the spiral as shown in Figs 17 creates shifting of the resonance frequency of the spiral up where it will be of no significance. The shift of the resonant frequency with the shorting of the turns is shown in Fig. 18. The advantage of shorting turns over to removing the entire spiral from the layout is that it enables future printing techniques to preserve the layout with all of the spirals shorted and when encoding data the shorting can be removed via a laser or other etching technique. The frequency signatures of tags with different IDs are shown in Figs 19 and 20.
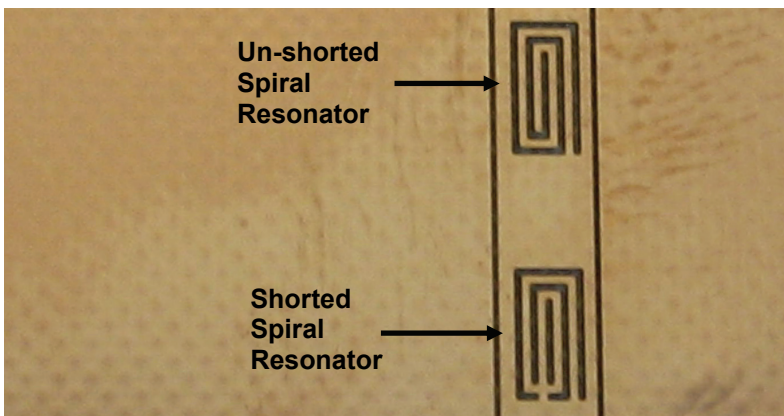


Fig. 17. Photograph of removing spiral resonances via spiral shorting for CPW multiresonator.
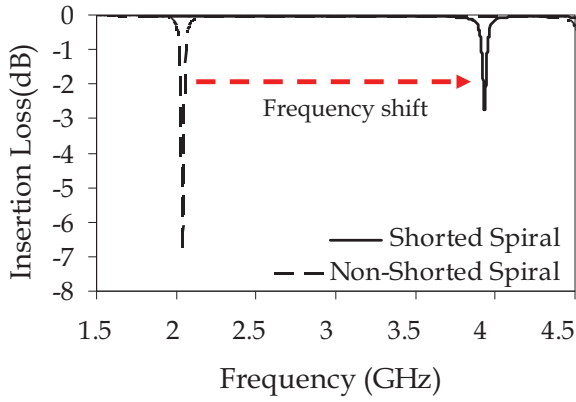
Fig. 18. Frequency shift of resonant frequency with short-circuited spiral.
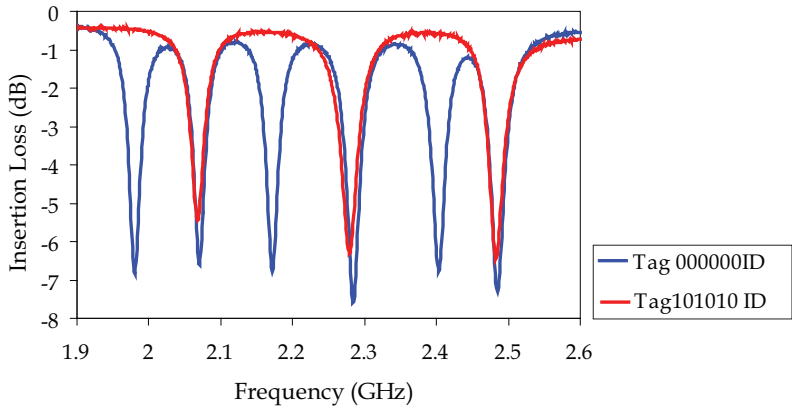


Fig. 19. Measured insertion losses of chipless tags with different spectral signatures.
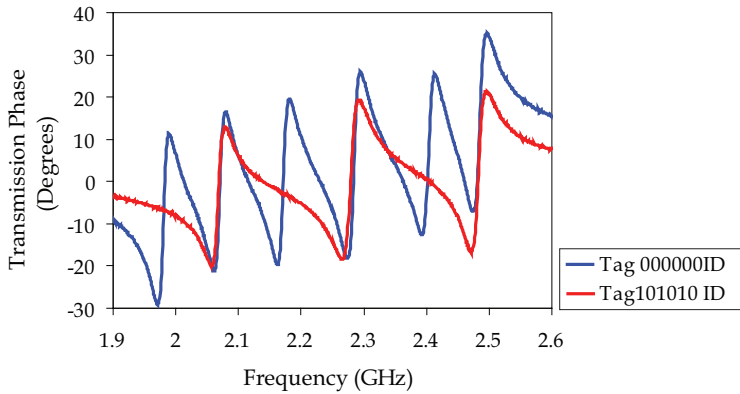


Fig. 20. Measured transmission phases of chipless tags with different spectral signatures.

### 3.4 Chipless RFID tag

The flexible chipless tag was designed on laminate Taconic TF-290 (εr = 2.9, h = 90 µm, tanδ = 0.0028) using ADS Momentum 2008. For this purpose, the antenna and multiresonators were designed individually. The layout of the chipless RFID tag with design parameters printed on flexible TF-290 laminates is shown in Fig. 21. The tag was designed on CPW, making it single-sided.
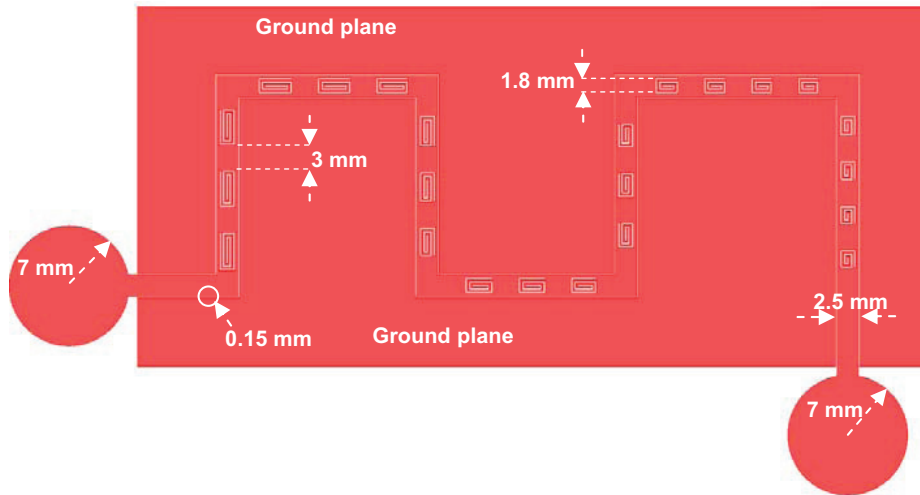


Fig. 21. Layout of integrated flexible CPW 23-bit chipless tag with design parameters on Taconic TF-290 laminate (εr = 2.9, h = 0.09 mm, tanδ = 0.0028).
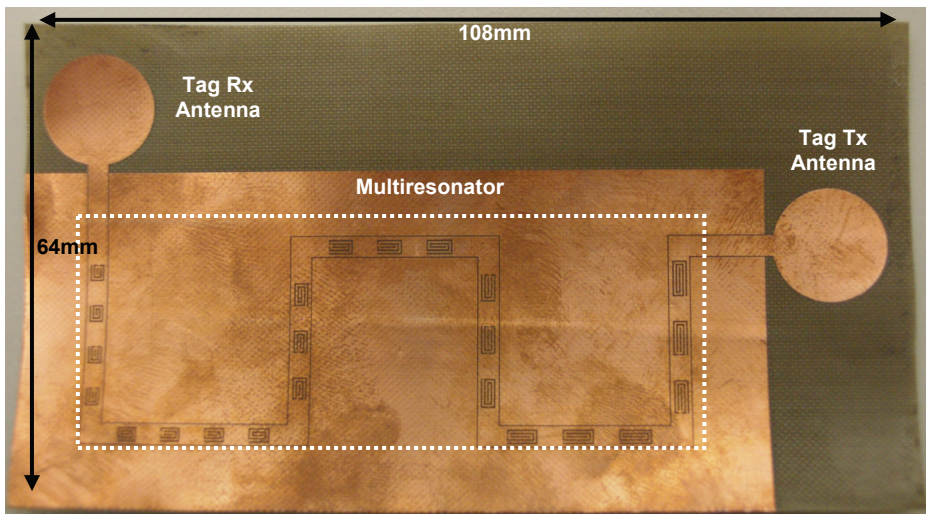


Fig. 22. Photograph of 23-bit chipless RFID tag on Taconic TF-290 (εr = 2.9, h = 90 µm, tanδ = 0.0028).

A photograph of the tag is shown in Fig. 22. The tag encodes 23 bits of data between 5 and 10.7 GHz. The chipless tag is comprised of a vertically- polarized UWB disc-loaded monopole receiving tag antenna, a multiresonating circuit and a horizontally-polarized UWB transmitting tag antenna designed using CPW technology. The chipless tag is designed to fit the Australian banknote and its dimensions are 108mm by 64mm. The spirals were etched out with the spiral trace and separation between spiral traces being 0.2 mm. The 50 ohm CPW strip line was designed to be 2.5 mm with the gap separation from the ground plane being 0.15 mm. The spirals were etched in the strip line with a 3 mm separation between adjacent cascaded spirals.

## 4. Results

### 4.1 UWB monopole

The measured antenna return loss vs frequency is shown in Fig. 23. The antenna yields UWB operation with greater than 10 dB return loss from 5 to 11 GHz.
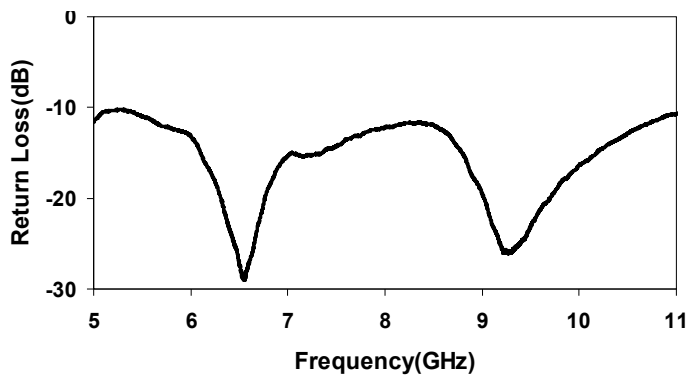


Fig. 23. Measured return loss of chipless RFID tag UWB monopole antenna.
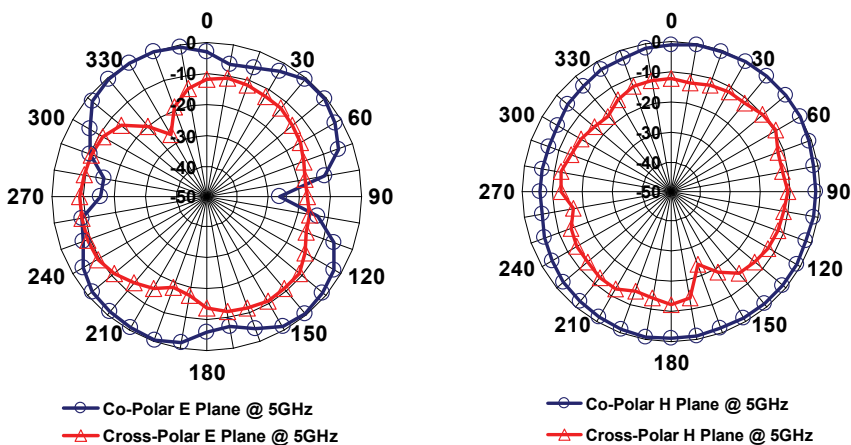


Fig. 24. Measured co-polar and cross-polar radiation patterns of UWB monopole at 5 GHz.
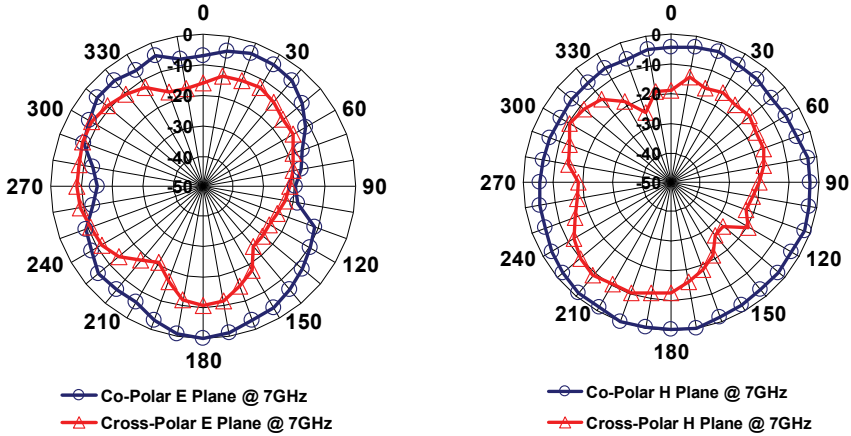
Fig. 25. Measured co-polar and cross-polar radiation patterns of UWB monopole at 7 GHz.
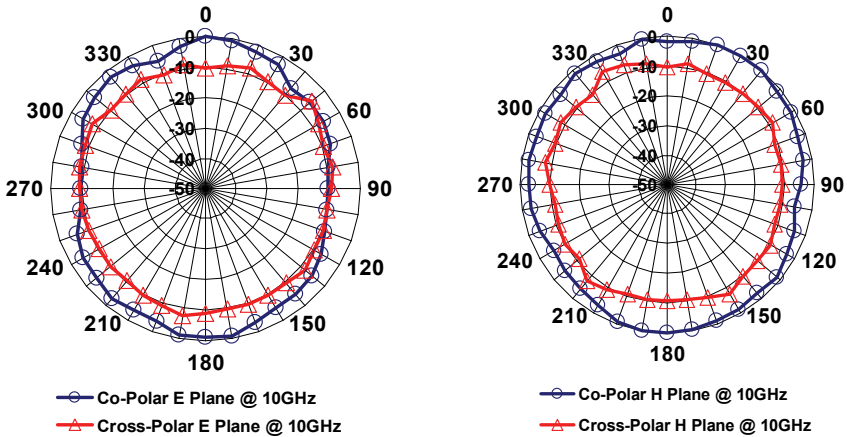


Fig. 26. Measured co-polar and cross-polar radiation patterns of UWB monopole at 10 GHz.

Fig. 23 shows multiple operating modes of the UWB monopole antenna. In order to achieve extremely large bandwidth, UWB monopole antennas rely on the overlapping of their modes. Hence, changes in radiation patterns are expected with frequencies outside the monopole's fundamental mode of operation of around 4.2 GHz. The antenna co-polar and cross-polar radiation patterns from 5-10 GHz in both E and H planes (as shown in Fig. 11) are presented in Figs 24, 25 and 26.

The tag antennas show good cross-polar component suppression (at least in the order of 10 dB average) which is essential for robust readings and isolation between the interrogation signal and encoded signal.

## 4.2 Multiresonator

The CPW-based UWB 23-bit chipless RFID tag encodes 23 bits of data from 5 to 10.7 GHz. The tag is printed on thin flexible laminate Taconic TF-290. The 23 bits of data are encoded
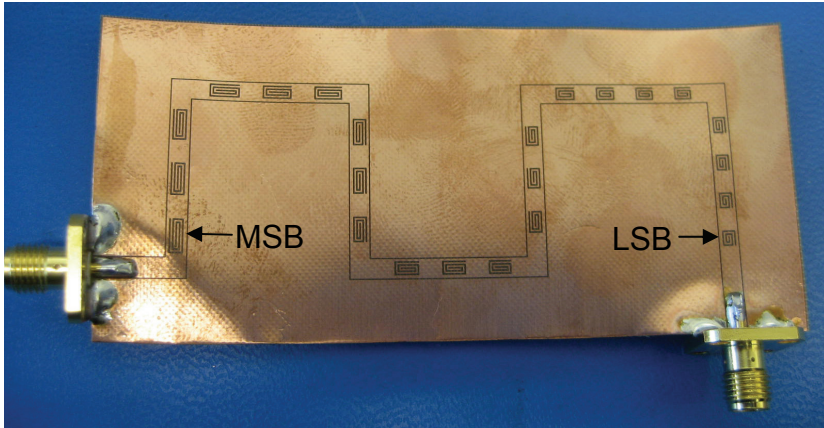
Fig. 27. Photograph of the 23 spiral multiresonating circuit on TF-290.
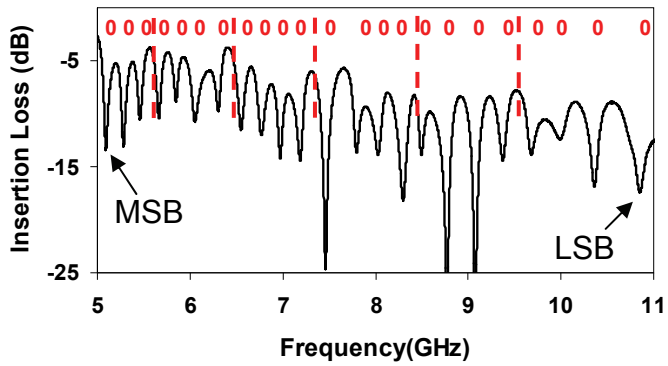


Fig. 28. Measured tag insertion loss of 23 bit tag ID "0x000000".
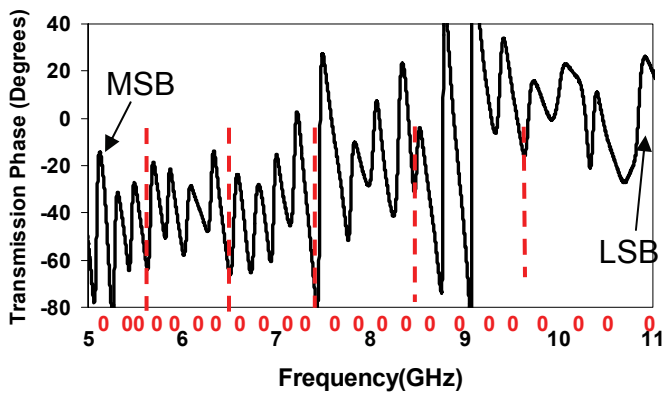


Fig. 29. Measured tag transmission phase of 23 bit tag ID "0x000000".

using a 23 spiral multiresonating circuit shown in Fig. 27. The measured spectral signatures in both insertion loss vs frequency and transmission phase vs frequency of the 23-bit tag are shown in Figs 28 and 29 respectively. From Figs 28 and 29 it is clear that the 23 logic '0' bits are detected in the magnitude as magnitude nulls (or dips) while their phase signature is represented by 23 phase jumps. These measurements confirm the successful operation of the multiresonator.

## 4.3 Field trials

The experimental setup in the anechoic chamber consists of the chipless tag, the vector network analyzer (VNA) PNA E8361A as the reader electronics and horn antennas as the reader antennas. Horn antennas were used to increase the reading range of the tag since they have high gain (~11 dBi). The experiment was conducted in the Monash University Anechoic Chamber in order to validate the successful encoding of the tag and its detection at the reader end using the network analyzer. The chipless tag and the reader antennas were mounted on plastic stands and placed into the anechoic chamber. A block diagram of the experimental setup is shown in Fig. 30.
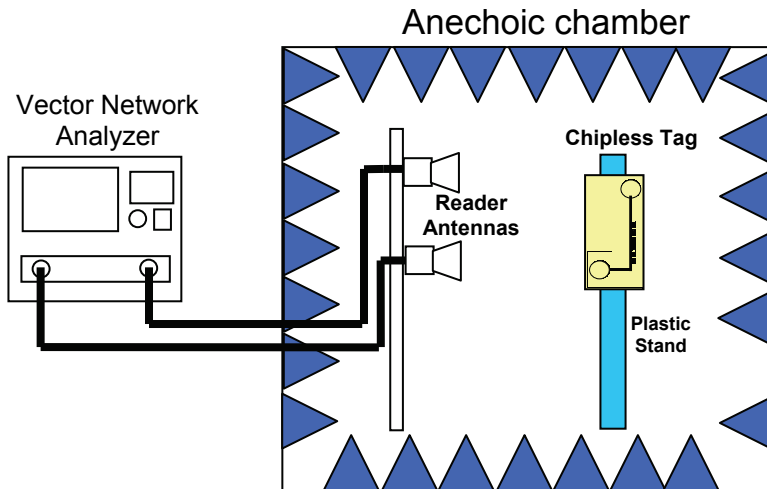


Fig. 30. Block diagram of the anechoic chamber setup.

As the horn antennas covered the frequency range from 7 - 12 GHz, the tag was interrogated starting from 7 GHz. This resulted in reading 13 bits of the entire 23-bit data encoded by the tag. However, this was sufficient to prove the successful operation of the tag and provide a read range estimation using horn antennas. A photograph of the experimental setup is shown in Fig. 31.

The use of horn antennas as reader antennas in this experimental setup greatly increased the reading range of the tag. We attribute this to the greater isolation of the cross-polarized reader antennas, and their higher directivity and higher gain than those of the log periodic arrays (presented in Chapter 4). The cross-polar reader antennas are shown in Fig. 32. As can be seen from Fig. 33, the isolation between the reader antennas is well above 65 dB.
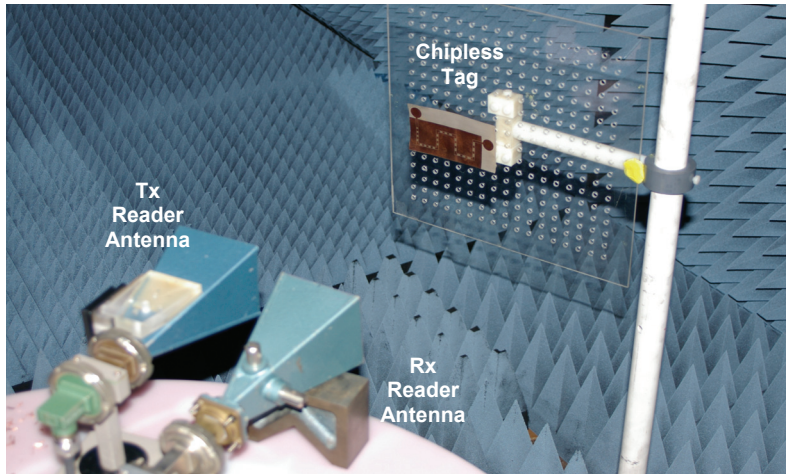
Fig. 31. Photograph of the experimental setup in the anechoic chamber of UWB RFID system.
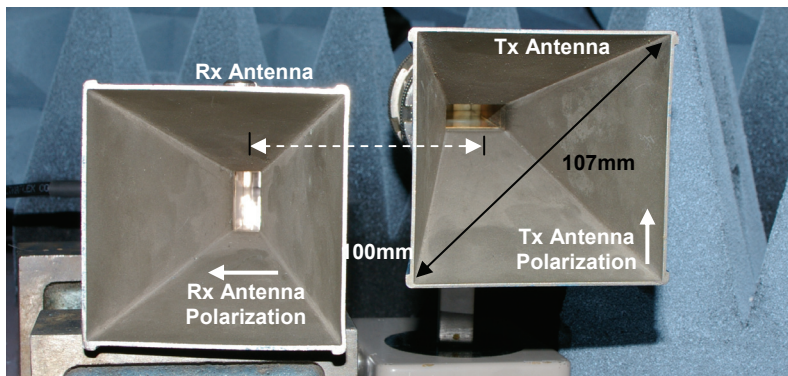


Fig. 32. Photograph of cross-polarized horn antennas used at reader end with 10cm separation.
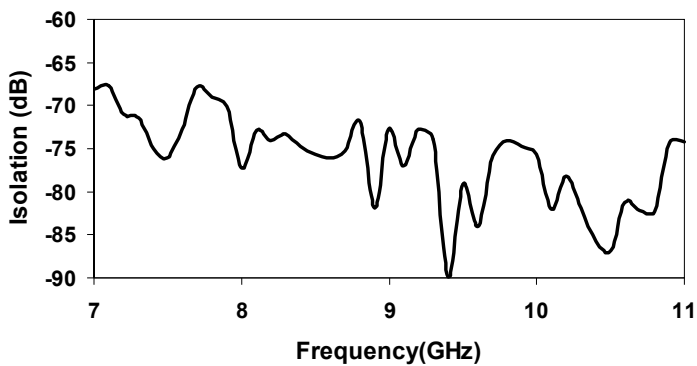


Fig. 33. Measured isolation between cross-polarized reader horn antennas.

We encoded the tag with ID '0x000000'and placed it from 5 cm to 70 cm (in steps of 5 cm) away from the horn reader antennas as shown in Fig. 31. The PNA was calibrated with the output power at the ports being -28 dBm. Both amplitude and phase data were retrieved when interrogating the tag. The chipless RFID tag was detected using a reference tag "0x111111" which carried no resonances. Hence, when the two results were compared the encoded resonances from tag ID '0x000000' were successfully detected. The normalized magnitude and phase of tag ID"0x000000" at 10 cm are presented in Figs 34 and 35 respectively. The measured results vs distance of tag from reader antennas are shown in Fig. 36.
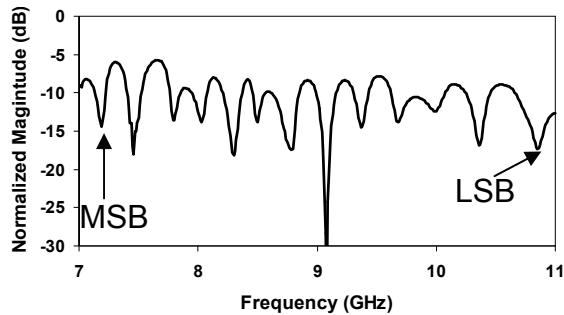


Fig. 34. Normalized magnitude variation vs frequency of chipless RFID tag with ID"0000000000000" from 7 – 10.7 GHz.
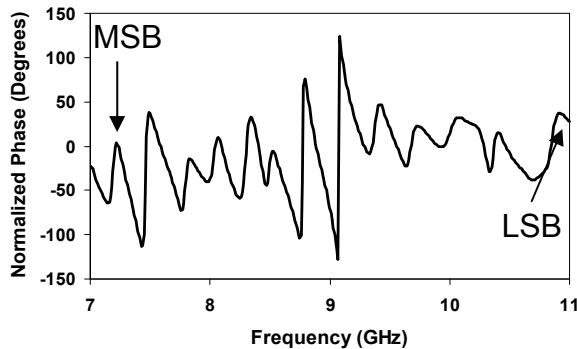


Fig. 35. Normalized phase variation vs frequency of chipless RFID tag with ID"0000000000000" from 7 – 10.7 GHz.

From Fig. 36 it is clear that in the anechoic chamber the tag can be detected further away (up to 70 cm) when using phase data detection than when using amplitude data detection. This is attributed to the greater robustness of phase when compared to amplitude. The successful interrogation of the tag in both amplitude and phase was conducted up to 50 cm. This result shows an improvement in the reading range detection of 300% in amplitude data and 75% in phase data (up to 70 cm) compared with the results reported in the previous section. The increased reading range in amplitude was greatly influenced by the increase of the cross-polar isolation of the tag antennas, increased isolation between the reader horn antennas and higher gain of the reader antennas (~11dBi over the entire band).
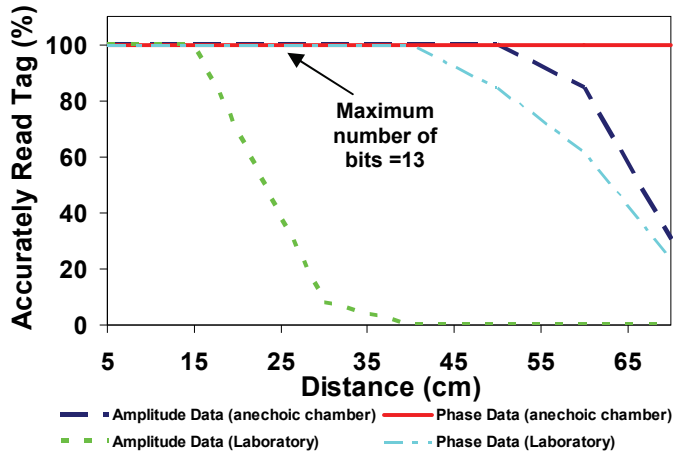
Fig. 36. Number of successfully detected bits vs distance of tag from reader antennas from 7 – 10.7 GHz (maximum of 13 detectible bits).

The chipless tag was placed in a laboratory setup (outside the anechoic chamber Fig. 37) in order to measure the detection range of this particular setup when exposed to environmental influences.
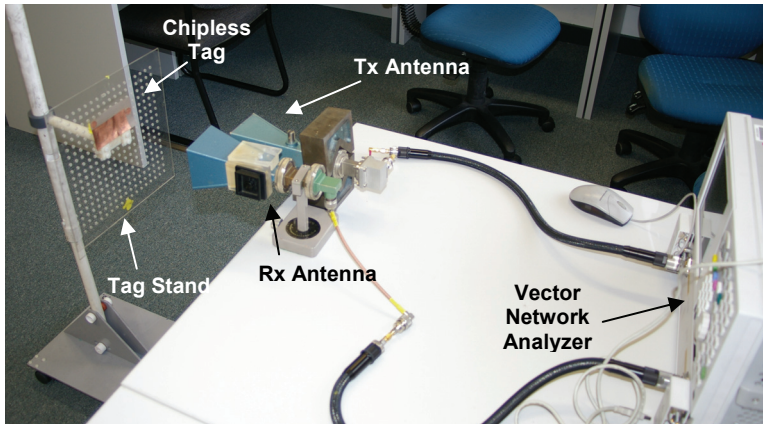


Fig. 37. Photograph of the experimental setup in the laboratory.

Fig. 36 shows that the tag was read accurately in both amplitude and phase up to 15 cm when placed in a laboratory as shown in Fig. 37. The phase data were detectable at greater reading ranges (up to 35 cm) than the amplitude data due to robustness of the phase data. Fig 36 clearly shows that the reading range dropped by 50% outside the anechoic chamber due to interference from the environment. However, it should be mentioned that the detection procedure was a simple comparison of tag data with no resonances and tag data with all resonances. The reading range could be improved by using signal processing techniques (such as matched filtering) to isolate the tag signal from the noise and interference and thus increase the reading range (Hartmann et al, 2004).

## 5. Conclusion

In this chapter we have presented the development and testing of a chipless RFID tag based on multiresonators. The development and successful testing of the chipless RFID tag meets the demand for a fully-printable ultra-low cost tag used for tagging items on conveyor belts. The salient feature of the novel chipless RFID tag is its fully-printable single-layered design in a compact and low cost format. It has significant amount of data encoding capability (up to 23 bits were designed).

Prior to the design and development of the chipless RFID tag a comprehensive literature review of RFID tags was conducted. The goal of the literature review was to identify the niche areas of design and development in RFID in which novel research could be carried out. The comprehensive literature review of chipless RFID tags revealed that chipless tags which are fully printable, multi-bit with ease of data encoding were not currently available. Some work had been carried out on capacitively tuned dipoles and fractal Hilbert curve-based tags but without the ability of data encoding.

The chipless RFID tag presented in this chapter comprises two main components: UWB antenna and multiresonator. The multiresonating circuit consisted of cascaded spiral resonators which operate at different resonant frequencies. Each resonant frequency corresponded to a single data bit. The spiral resonator was chosen as the main encoding element since it exhibits compact size, high Q and small bandwidth in comparison to other planar resonators which exhibited stop-band performance.

Spectral signature encoding is used to encode data by the tag. Spectral signature requires a one to one (1:1) correspondence of the frequency spectrum behaviour to the tag's multiresonator layout. In particular, each spiral resonator had a 1:1 correspondence with a data bit, which meant that each data bit had a predetermined spiral resonant frequency. To the best of the author's knowledge, spectral signature encoding utilizing both amplitude and phase of the spectral signature is the first of its kind and has not been reported previously. The spiral resonance was represented by a null in the amplitude and abrupt jump in the phase which encoded logic "0". Encoding logic "1" was represented by the absence of an amplitude null and phase jump.

A fully novel "spiral shorting" concept of data encoding is presented in this thesis. The spiral resonator is shorted by shorting the spiral turns with a single trace. When shorted, the spiral resonator has a resonant frequency which is outside the operating band of the chipless RFID tag, hence resulting in the absence of the resonance. This is characterized as a logic "1" bit in the spectral signature. The removal of the shorting between the spiral turns introduces the resonance of the spiral resonator which is a representation of logic "0". This novel data encoding technique provides a new manufacturing advantage of the chipless RFID technology over other reported chipless RFID tags in terms of minimum layout modifications and the use of laser etching for mass tag encoding.

The design of the UWB monopole antennas for the chipless RFID tags was carried out. UWB disc-loaded monopole antennas exhibit omni-directional radiation patterns over their operating band and have an efficient and compact layout. The monopoles was designed using CPW technology as well.

The UWB chipless RFID system which utilizes a fully printable chipless CPW RFID tag which can be used for tracking low cost items such as banknotes, envelopes and other paper/plastic products, items and documents has been tested successfully. The chipless RFID tag operates between 5 and 10.7 GHz of the UWB spectrum. By exciting the tag with a wideband signal it was possible to detect variations in the magnitude and phase of the

received tag signal and decode the tag's ID at distances up to 70 cm in a noise-free environment and up to 35 cm in a laboratory (noisy) environment. It was necessary to calibrate the reader with a reference signature ID with no resonances when performing amplitude and phase data decoding.

Given the potential high demand on RFID technology in terms of reading range and applications some open issues and further areas of interest remain to be addressed in future projects. So far, the RFID tag has been designed to operate in predefined alignment situations and applications since the polarization of the antennas is crucial for successful reading. Further studies could focus on developing planar circularly-polarized tag antennas which would remove the present stringent alignment requirements. Another improvement which could be considered is making the tag operate with a single antenna instead of two which would dramatically reduce the size of the chipless tag. Further size reduction of the chipless tag can be achieved by using sub-millimetre-wave and millimetre-wave frequency bands. New applications for chipless tags (such as tram and train ticketing) could be established by extending the capacity of the chipless tags to 124 bits.

## 6. References

K. Finkenzeller (2003), "RFID Handbook - 2nd Edition", John Wiley & Sons, Ltd., 2003.

U. Kraiser, W. Steinhagen (1995), "A low-power transponder IC for high-performance identification systems", *IEEE Journal of Solid-State Circuits*, vol. 30, no. 3, pp:306-310, March 1995.

S. Preradovic, N. Karmakar (2009), "Modern RFID readers", *Microwave Magazine,* internet article, Available:<http://www.mwjournal.com/article.asp?HH_ID=AR_4830> (Accessed August 2009)

H. Stockman (2009), "Communication by Means of Reflected Power", Proceedings of the IRE, pp: 1196-1204, October 1948.

R. R. Fletcher (2002), "Low-cost electromagnetic tagging: design and implementation", PhD Thesis, September 2002. Available<www.media.mit.edu/physics/publications/theses/97.02.fletcher.pdf>

D. A. Hodges, H. G. Jackson (1998), "Analysis and design of digital integrated circuits – 2nd Edition", McGraw-Hill, New York, USA, 1988.

J. R. Baker, H. W. Li, D. E. Boyce, "CMOS circuit design, layout and simulation", IEEE Press, New York, USA, 1998.

S. Natarajan (2008), "A 32nm logic technology featuring 2nd –generation high-k + metal-gate transistors, enhanced channel strain and $0.171\mu m^2$ SRAM cell size in a 291Mb Array", *IEEE International Electron Devices Meeting 2008 IEDM 2008*, pp:1-3, San Francisco, USA, 15-17 Dec. 2008.

S. Harma, V. P. Plessky, C. S. Hartmann, W. Steichen (2006), "SAW RFID tag with reduced size", *IEEE Ultrasonics Symposium 2006*, pp:2389-2392, Vancouver, Canada, Oct. 2006.

C. S. Hartmann (2002), "A global SAW ID tag with large data capacity", Reprint form *Proceedings of 2002 IEEE Ultrasonics Symposium*, vol. 1, pp:65-69, Munich, Germany, October, 2002, Available:http://www.rfsaw.com/pdfs/Global_SAW_ID_Tag_lg.pdf

R. Das, P. Harrop, Chip-less RFID forecasts, technologies & players 2006 – 2016, IDTechEx internet article, Feb.2006. <http://www.idtechex.com/products/en/view.asp?productcategoryid=96> (accessed March 2006)

S. Shretha, J. Vemagiri, M. Agarwal and K. Varahramyan (2007), "Transmission line reflection and delay-based ID generation scheme for RFID and other applications", *Int. J. Radio Freq. Identification Technol. Appl.*, vol. 1, no. 4, pp:401-416, 2007.

M. Glickstein (2006), Firewall protection for paper documents, RFID Journal internet article, Feb. 2004, <http://www.rfidjournal.com/article/articleprint/790/-1/1/>(accessed February 2006)

J. Collins (2004), RFID fibers for secure applications, RFID Journal internet article, March 2004. <http://www.rfidjournal.com/article/articleprint/845/-1/1/>(accessed April 2006)

K. C. Jones (2007), "Invisible tattoo ink for chipless RFID safe, company says", EE Times white paper, October 2007 <http://eetimes.eu/industrial/196900063> (accessed June 2009)

Jalaly, I. D. Robertson (2005), "RF barcodes using multiple frequency bands", *IEEE MTT-S International Microwave Symposium Digest 2005*, pp:4-7, Long beach, USA, June 2005.

J. McVay, A. Hoorfar, N. Engheta (2006), "Theory and experiments on Peano and Hilbert curve RFID tags", *Proceedings of the Wireless Sensing and Processing*, vol. 6248, pp:624808, San Diego, USA, Aug. 2006

Tagsense, Inc. (2006), "Chipless RFID products", data sheet, <http://www.tagsense.com/ingles/products/product_chipless.html> (accessed October 2006).

J. McVay, A. Hoorfar, N. Engheta (2006), "Space-filling curve RFID tags", *2006 IEEE Radio and Wireless Symposium*, pp: 199-202, San Diego, USA, 17-19 Jan. 2006.

Jalaly, D. Robertson (2005), "Capacitively-tuned split microstrip resonators for RFID barcodes", *2005 European Microwave Conference*, vol. 2 pp:4, Paris, France, 4-6 Oct. 2005.

S. Preradovic, I. Balbin, N. C. Karmakar, G. F. Swiegers (2009), "Multiresonator-based chipless RFID system for low-cost item tracking", *IEEE Transactions on Microwave Theory and Techniques,* vol. 57, no. 5, pp: 1411-1419, May 2009.

X. Chen, L. Guo, J. Liang, C. Parini (2007), "On the performance of UWB monopole antennas", *IEEE International Conference on Ultra-Wideband ICUWB 2007*, pp:210-213, Singapore, Sep. 2007.

A. Alipour, H. R. Hassani (2008), "A novel omni-directional UWB monopole antenna", *IEEE Transactions on Antennas and Propagation*, vol. 56, no. 12, pp: 3854-3857, Dec. 2008.

Q. Wu, J. Ronghong, J. Geng, M. Ding (2008), "Printed omni-directional UWB monopole antenna with very compact size", *IEEE Transactions on Antennas and Propagation*, vol. 56, no. 3, pp:896-899, March 2008.

G. Quintero, A. K. Skrivervik (2008), "Analysis of planar UWB elliptical dipoles fed by a coplanar stripline", *IEEE International Conference on Ultra-Wideband ICUWB 2008*, vol. 1, pp: 113-116, Hannover, Germany, Sep. 2008.

M. Mudroch, P. Cerny, P. Hazdra, M. Mazanek (2009), "UWB dipole antenna optimization with neural network tuned algorithm", *3rd European Conference on Antennas and Propagation EUCAP 2009,* pp:1491-1494, Berlin, Germany, March 2009.

G. Whyte, F. Darbari, I. McGregor, I. Glover, I. Thayne (2008), "Different feeding geometries for planar elliptical UWB dipoles, and the excitation of leakage current", *38th European Microwave Conference EuMC 2008*, pp:1382-1385, Amsterdam, Netherlands, Oct. 2008.

E.E. Angelopoulos, A. Z. Anastopoulos, D. I. Kaklamani, A. A. Alexandridis, F. Lazarakis, K. Dangakis (2006), "Circular and elliptical CPW-Fed slot and microstri-fed antennas for ultrawideband applications", *IEEE Antennas and Wireless Propagation Letters*, vol. 5, no. 1, pp:294-297, December 2006.

B.P. Wen (1969), "Coplanar waveguide: a surface strip transmission line suitable for nonreciprocal gyromagnetic device applications", *IEEE Transactions on Microwave Theory and Techniques*, vol. 17, no.12, pp:1087-1090, December 1969.

C. Hartmann, P. Hartmann, P. Brown, J. Bellamy, L. Claiborne, W. Bonner (2004), "Anti-collision methods for global SAW RFID tag system", *IEEE Ultrasonics Symposium*, vol. 2, pp:805-808, Montreal, Canada, August 2004.

# The Interaction of Electrostatic Discharge and RFID

Cherish Bauer-Reich[1], Michael Reich[2] and Robert Nelson[3]
[1,2]*North Dakota State University, Center for Nanoscale Science and Engineering*
[3]*University of Wisconsin - Stout, Department of Engineering and Technology*
*USA*

## 1. Introduction

Electrostatic discharge, or ESD, is a common hazard in the electronics industry. Despite the fact that RFID has been in use for nearly forty years, there has been little to no discussion in the scholarly literature on how ESD interacts with RFID tags as a system. The intent of this chapter is to give the reader an overview of ESD and the aspects of RFID with which it interacts. Next, a view of ESD protections incorporated into RFID ICs is presented. A statistical examination of RFID tag susceptibility is summarized, and the chapter ends with a discussion of ESD issues that affect the RFID manufacturing environment. This document should, therefore, provide the reader with a comprehensive view of the interaction of RFID with ESD as well as a starting point for studying related areas.

## 2. Introduction to ESD

Electrostatic discharge (ESD) is the phenomena where a current passes from an object of high potential to one of low potential. For electronics, ESD is often an event which can be quickly but imperceptibly destructive. A device exposed to ESD can often be permanently damaged or destroyed with no obvious evidence as to the cause.

ESD is a multi-stage process that begins with the accumulation of charge on an object. Charge is often accumulated on a surface through a process called *triboelectric charging*. This process occurs when two materials come in contact. Materials have different affinity for electrons, so some materials may easily release electrons to the other material while others will take them. As the material is separated, the transferred electrons may or may not move back to the original material depending on, among other things, the rate of separation. Materials separated quickly will often leave a higher residual charge than those that are separated relatively slowly. Other factors which may impact charge accumulation are rubbing, surface cleanliness and smoothness as well as contact pressure and surface area.

The amount and rate of charge accumulation depends strongly on the types of materials involved. Charge accumulates when one insulator comes in contact with another. Two conductors will not leave residual charge because of the high electron mobility in both materials. When a charged insulator comes in contact with another insulator or conductor, it can transfer some or all of its charge. Beyond that, one must consider the material's affinity for triboelectric charging. A guide to estimate the likelihood of charge buildup in a fairly qualitative manner is the *triboelectric series*, shown in 1. The triboelectric series lists many common materials and their affinity for accumulating or rejecting electrical charge. The

materials in the center of the chart are almost electrically neutral. Materials at one end (i.e., the 'negative' end) will have a strong affinity for gathering negative charge, while those at the other end (i.e., the 'positive' end) will easily release electrons, leaving a positive residual charge. When a material with a strong affinity for negative charge comes into contact with a material which prefers positive charge, charge accumulation on the material with a negative charge affinity is very likely. For example, human skin easily gives up electrons and teflon attracts electrons. When these come in contact, electrons will tend to move from human skin to the teflon, leaving the skin positively charged and the teflon negatively charged.

| POSITIVE |
|:---:|
| Air |
| Human Skin |
| Asbestos |
| Glass |
| Mica |
| Human Hair |
| Nylon |
| Wool |
| Fur |
| Lead |
| Silk |
| Aluminum |
| Paper |
| Cotton |
| Wood |
| Steel |
| Sealing wax |
| Hard rubber |
| Mylar |
| Epoxy-glass |
| Nickel, copper |
| Brass, Silver |
| Gold, platinum |
| Polystyrene foam |
| Acrylic |
| Polyester |
| Celluloid |
| Orion |
| Polyurethane foam |
| Polyethylene |
| Polypopylene |
| Polyvinylchloride (PVC) |
| Silicon |
| Teflon |
| NEGATIVE |

Table 1. Triboelectric Series Chart (Ott, 1988)

The second step in an ESD event involves transfer of charge from the insulator surface to a conductor. This can happen via direct conduction or induction. The conduction process occurs when a conducting body comes in direct contact with the charged insulator. The induction process occurs when the charge on the insulating material induces a charge redistribution in a nearby conductor. As an example, a negatively charged insulator will cause the side nearest the insulator to develop a positive charge resulting in a negative charge on the opposite side of the conductor. The net charge of the conducting object, however, is zero as there has not been a direct transfer of electrons. If the object comes in contact with ground, however, a net charge may result on the conductor as some of the charge from one side may be removed during contact.

The third step in the ESD process is discharge. Once charge has accumulated, it will generally be held on the object until it has dissipated or been discharged onto an object of lower potential. Dissipation is usually a preferable process: the static charge is released from the region slowly enough that the current is not harmful to electronics. This is the mechanism employed by several types of ESD mitigation techniques, such as wrist straps and ESD jackets. The material has a resistance that is low enough for current to flow and prevent electrostatic buildup. However, it is sufficiently high to prevent a large current should there be enough buildup. Discharge, however, usually is the result of a process where current flows relatively quickly from one object to another relatively unimpeded. The higher the speed, the larger the current and the more likely that damage to a device will occur.

An example of voltage levels for various ESD-generating events is given in 2. The current from a discharge event is calculated using

$$I = C \frac{dV}{dt}. \tag{1}$$

Discharge events are usually on the order of a nanosecond, and the capacitance will vary based on the type of discharge. The value used in the human body model, which will be discussed later, is 150 pF. Using these values, it is easy to see how even a small potential difference can result in currents on the order of 1A or more.

ESD damages electronics in two ways. First, the current can directly cause damage. Second, the discharge event creates strong localized fields that induce current on an object. High currents can damage electronics directly by heating or dielectric breakdown. The fields can cause damage such as overstress or an interruption in device function. When large enough, fields can also cause induced currents in nearby devices. These induced currents can cause damage in the same manner as an arc discharge current.

One common misconception is that ESD only occurs when there is a path to ground. In reality, a path to ground potential is not necessary for current to flow. If there is any buildup of charge on an object and it comes in contact with a second object at a different potential, charge will flow from one object to another until the potential has been equalized. It is important to keep in mind that RFID tags, despite lacking a path to a ground potential, can still experience a discharge current if they come into contact with an object at a significantly different potential. Electronics should be handled in such a way that they are exposed to minimal amounts of static charge and are not put into contact with conducting surfaces. However, the level of static discharge that can be tolerated is device dependent. Electronics are generally classified into groups based on their tolerance to charge potentials. The class is determined by the model used to test the equipment. The models each have a different discharge current waveform which is supposed to incorporate representative impedance values for different scenarios.

|                                              | Electrostatic Voltage | |
| --- | --- | --- |
| Means of Static Generation | 10 to 20% Relative Humidity | 65 to 90% Relative Humidity |
| Walking across carpet | 35,000 | 1,500 |
| Walking on vinyl floor | 12,000 | 250 |
| Worker moving at bench | 6,000 | 100 |
| Opening a vinyl envelope | 7,000 | 600 |
| Picking up a common polyethylene bag | 20,000 | 1,200 |
| Sitting on chair, padded with polyurethane foam | 18,000 | 1,500 |

Table 2. Common Electrostatic Voltages (Ott, 1988)

More specifically, the human body model (HBM) and charged device model (CDM) use current waveforms which are representative of discharge currents from a human or to a metallic object by a charged device, respectively. There are other models, and thus corresponding waveforms, which can be used to test a device. Choice of the model is somewhat dependent on the circumstances which may confront the device during manufacture and use. The classification scheme is dependent on the testing model. HBM is generally the least stressful testing environment, so the voltage levels for each class are higher than for other models. Examples of the classifications for HBM and CDM models are shown in 3.

| Human Body Model Sensitivity Classification | |
| --- | --- |
| Class | Voltage Range (V) |
| Class 0 | $< 250$ |
| Class 1A | 250 to $< 500$ |
| Class 1B | 500 to $< 1000$ |
| Class 1C | 1000 to $< 2000$ |
| Class 2 | 2000 to $< 4000$ |
| Class 3A | 4000 to $< 8000$ |
| Class 3B | $\geq 8000$ |
| Charged Device Model Classification | |
| Class | Voltage Range (V) |
| Class C1 | $< 125$ |
| Class C2 | 125 to $< 250$ |
| Class C3 | 250 to $< 500$ |
| Class C4 | 500 to $< 1000$ |
| Class C5 | 1000 to $< 1500$ |
| Class C6 | 1500 to $< 2000$ |
| Class C7 | $\geq 2000$ |

Table 3. HBM and CDM Classification

## 3. Introduction to RFID

Radio Frequency Identification (RFID) has become an the primary solution to most item tracking. RFID tags are used to track library books, livestock, and shipments of commercial goods. Recently, Walmart laid plans to use item-level tracking; that is, it plans to track individual items using RFID (Bustillo, 2010). Further, RFID is now being embedded in most countries' passports (Evers, 2006) and the US military has required all items from suppliers to be tagged (Ames, 2005). Because use of RFID is becoming pervasive, it is important to examine the reliability of such devices.

We will assume that the reader has a basic knowledge of most RFID systems. More comprehensive reviews can be found in (Dobkin, 2008; Finkenzeller, 2003; Glover & Bhatt, 2006). In this section, we intend to give an overview of how RFID systems work from an electromagnetics viewpoint. This overview is meant to be sufficient for the reader to understand the issue of ESD interaction with RFID and is by no means comprehensive. There are two components to most RFID systems: the reader and the tag (sometimes referred to as a transponder). The reader can be broken down further into a data storage device, a reader module, and an antenna. The tag is far more simple than the reader; we will regard it as an antenna and an integrated circuit (IC) or chip.

The reader antenna emits a radio-frequency (RF) signal which induces a current on the tag antenna. In a passive tag, i.e., one without batteries, the current must be large enough to power both circuitry and return communications. The IC will typically modulate its impedance, creating a change in the current on the antenna which generates a return signal. This return signal will couple with the reader antenna via magnetic induction or electrical field backscatter. Systems which operate in the LF (128 kHz) and HF (13.56 MHz) frequency ranges are more likely to use magnetic induction, while those in the UHF (860 - 960 MHz) and microwave (2.4 and 5.8 GHz) frequencies typically operate using backscatter (Finkenzeller, 2003; Glover & Bhatt, 2006).

The ESD research on RFID performed by the authors focused on passive tags, i.e., tags that have no battery to power either communications or circuitry. Thus, the presence of batteries may affect tag susceptibility but because there are no other scholarly studies of which the authors are aware, the extent is yet unknown. Additionally, this research has focused on UHF tags where backscatter is the primary means of information transfer.

## 4. Susceptibility of RFID integrated circuits

RFID ICs are designed to be low in cost and consequently must be manufactured in high volumes in order to be cost-effective (Dobkin, 2008). As mentioned in the previous section, a passive UHF tag is designed to be powered solely by the RF signal received from the RFID reader. In order to communicate with an RFID reader, the RFID IC must decode any commands sent by the reader and transmit responses back to the reader when required. Therefore, the RFID IC must contain at least three main components: i) a power supply circuit that takes incoming RF energy and converts it to a DC voltage which is suitable for powering the IC, ii) a logic section that interprets any received commands and generates appropriate responses, and iii) a method of transmitting information back to the RFID reader. Since most RFID ICs only have external pads or connections that are designed to mate with the antenna, only the power supply and the transmitting section of the RFID IC is exposed to the outside world and potential ESD damage.

Explicit details on the inner workings of commercial RFID ICs are not provided by manufacturers, though some information may be found on specific RFID ICs that have been reverse-engineered, c.f. (Torrance, 2009). However, there has been a fairly substantial body of work published in the literature on RFID IC designs, some of which will be highlighted below. Details provided in publications such as these allow us to make reasonable conclusions about the internal workings of commercial RFID ICs.

Since the RFID IC is powered by the RF signal transmitted by the reader, any RFID IC must have a way to convert the transmitted RFID signal to a DC voltage level high enough to power the digital state machine within the rest of the IC. This implies that two functions must be performed: *rectification* of the incoming signal, and a *potential step-up* to an acceptable level. Both of these functions are commonly implemented using a charge pump circuit. A charge pump consists of a bank of capacitors connected by diodes arranged in a fashion designed to facilitate flow of charge in one direction only. The simplest kind of charge pump, a voltage doubler, is shown in 1. The function of the circuit is to 'pump' charge from capacitor C1 on the left to capacitor C2 on the right, where it can be used to power any electronics connected across capacitor C2.
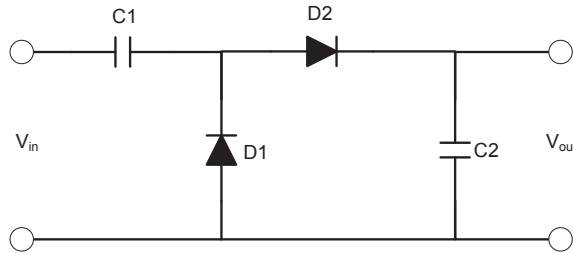


Fig. 1. Example Charge Pump

The operation of this circuit is fairly straighforward. When interrogating or waiting for a response from an RFID tag, the RFID reader will transmit an RF signal. When this signal is negative with respect to the input terminals, diode D1 will be forward biased, and capacitor C1 will begin to charge. If we represent the maximum peak voltage of the input as $V_{pk}$ and the turn-on voltage of the diodes as $V_{on}$, when $V_{in} = -V_{pk}$, the voltage across capacitor C1 will be $-V_{pk} + V_{on}$, where we have assumed the positive terminal of the capacitor to be on the left side of the capacitor. As the input signal goes from negative to positive, diode D1 will turn off. Once the input voltage is positive enough, diode D2 will turn on, and the charge stored in capacitor C1 is transferred to C2. When $V_{in} = V_{pk}$, the voltage at the output will be

$$V_{out} = V_{pk} - V_{C1} - V_{D2} \tag{2}$$
$$= V_{pk} + V_{pk} - V_{on} - V_{on}$$
$$= 2\left(V_{pk} - V_{on}\right)$$

The input voltage available at $V_{out}$ is roughly double that of $V_{in}$. Multiple diode-capacitor stages may be cascaded to produce higher input voltages, though there is a practical limit to the number of stages that can be added. This is due to the increasing voltage required

to forward bias all the diodes in the circuit. The designs presented in (Barnett et al., 2006; Bergeret et al., 2006; Bo et al., 2009; Curty et al., 2005; Facen & Boni, 2006; Karthaus & Fischer, 2003) provide details on specific implementations of this type of circuit. It is worth noting that the designs in (Barnett et al., 2006; Facen & Boni, 2006) contain additional rectification circuitry in front of the charge pump circuitry.

As mentioned in the previous section, an RFID tag communicates with an RFID reader by modulating the RF signal transmitted by the RFID reader. In order to modulate the signal from the RFID reader, the RFID IC must have some method to change the input impedance presented to the antenna. Only two states are required in order to transmit data back to the RFID reader. One state is typically a matched state where the RFID IC is able to absorb the maximum amount of energy from the RF signal (Nikitin et al., 2005). There are several choices available for the second impedance state. In general, the second impedance state may be resistive, reactive, or both. As shown in (Dobkin, 2008), the choice of impedance has implications for the amount of energy scattered from the RFID tag antenna, the amount of power available to the RFID IC, and the modulation scheme (amplitude-shift-keying or phase-shift-keying). In the simple case where the input of the RFID IC is set to either an open or a short for one impedance state, no power can be absorbed by the RFID IC. Therefore, the RFID IC must be able to store enough energy during the matched impedance state to operate through the duration of the mismatched state. This is the approach taken in (Curty et al., 2005), where a simple two-transistor MOS switch is used to present either a matched impedance or a short-circuit to the antenna. This results in an amplitude-shift-key modulation of the RF signal transmitted by the RFID reader. In contrast, the design presented in (Karthaus & Fischer, 2003) implements a phase-shift-key modulation scheme by switching the input capacitance of the RFID IC using a MOS varactor. Using a reactive match allows this design to absorb some RF energy from the transmitted signal in both impedance states.

Both the power supply and modulation circuitry contain ESD-sensitive PN junction devices, and therefore must be protected from damage by ESD events. ESD protection of RFID ICs includes additional challenges beyond those encountered in traditional ICs. Standard ESD protection techniques, such as those given in texts including (Amerasekera & Duvvury, 2002), can result in the addition of relatively high parasitic capacitances. As noted in (Glidden et al., 2004), these high capacitances can have a negative impact on the recifier conversion efficiency. This is of critical importance when the only power source for the RFID IC is the RF energy that can be received by the RFID tag antenna.

Also, the input impedance of the RFID IC will have an impact on the design of the tag antenna. A highly capacitive RFID IC will drive a requirement for the tag antenna to have an equally high inductance. This inductance is required to create an equal but opposite reactance in the operating frequency band compared to the reactance generated by the RFID IC input capacitance. Typical input impedances for commerical RFID ICs are on the order of 1500 ohms in parallel with 0.8 picofarads (AlienTech, 2008; Impinj, 2010), which results in an input impedance of $30.9 - 213j$ ohms at a frequency of 915 MHz.

The input capacitance of the RFID IC has implications on the overall Q of the circuit and the final operating bandwidth of the RFID tag, as noted in (Bo et al., 2009). Because of these issues, there has been at least one proposed RFID IC design that dispenses with ESD protection altogether (Curty et al., 2005). However, this practice not standard, and most RFID ICs will have ESD protection circuitry similar to that shown in (Facen & Boni, 2006).

## 5. Susceptibility of RFID tags

In theory, tag susceptibility to ESD events would be similar to that of individual IC chips. However, because tags are not simply composed of ICs, there are other factors which will affect susceptibility. There is little publicly available data on the interplay between these factors and ESD events. In 2004, an article in a paper industry publication claimed damage during use destroyed 1-30% of tags with typical rates being 5-6%. (Shaw, 2004) This data was provided by Appleton, a company which had developed dissipative coatings for RFID. As this data was fairly limited, giving no information on the types of tags tested and what factors altered the failure rate, the authors of this chapter tested and analyzed several commercially available tags and published the result in (Bauer-Reich et al., 2007). The results of that testing will also be summarized here. A further study performed accelerated stress testing on RFID tags (Sood et al., 2008). In that study, ESD was mentioned as a potential stress, but its effects on RFID tags were not explicitly examined.

There are several types of tags which are commercially available. It is reasonable to assume that some tags will be less susceptible than others, such as those encapsulated in plastics. However, many industries and government entities which ship or warehouse products, from clothing to pharmaceuticals to military supplies, are using variations on the passive, paper-label tags. These tags are used because they can have printing on the front, making it easier to visually identify the contents of crates and boxes. These tags are also the most likely to be physically touched by people. Because the IEC standard governing ESD testing (IEC61000-4-2, 2005) utilizes the human body model in its testing apparatus, this was the most appropriate choice of test.

Several factors were examined to see how they affected tag susceptibility: environment, potential difference, proximity to IC, IC type, antenna type, and covering material. Six different types of tags were chosen for testing. The characteristics of the tags are summarized in 4.

Two testing environments were utilized. The first environment was similar to IEC 61000-4-2 for ungrounded devices (IEC61000-4-2, 2005), while the other used a wooden table-top to more closely match similar to a warehouse environment. The discharge was created by a Schaffner NSG 432 Manual Discharge Device using the positive charge generator with the rounded-tip finger. Two hundred sixteen tags were tested in the presence of a ground plane. One hundred sixty-two tags were tested without a ground plane.

To measure the effects of the discharge, the change in minimum power required to activate the tag was measured using the procedure described in Bauer-Reich et al. (2007). The minimum power was measured before and after application of the discharge The discharge was applied when the tag was not operating. The normalized increase in minimum activation power was then calculated from the initial activation power $P_{initial}$ and the final activation power $P_{final}$ using the following equation:

$$P_{normalized} = \frac{P_{initial} - P_{final}}{P_{Initial}} \tag{3}$$

This formula implies that a tag that was unaffected and had the same activation power after the discharge would have a normalized increase in minimum activation power equal to zero. In the case where a tag completely failed and was unable to be read after discharge, $P_{normalized}$ would be equal to one.

It should be noted that in several of the tests, the normalized power of the tag is negative. It was hypothesized that this resulted from residual charge residing in the charge pump

apparatus. Although no verification was performed, many of the tags were checked singificantly later and found to be functioning much closer to their original value. It appears that residual charge may reduce the amount of energy required to power the tag, thus making it easier for the tag to operate with less input from the reader antenna.

| Tag Type | Tag Characteristics | | |
|---|---|---|---|
| | Antenna | Label Covering Resistance (GΩ/mm) | IC |
| 1 | Patch-like | 8 | Gen 2 |
| 2 | Dipole-like | 17 | Gen 2 |
| 3 | Dipole-like | 17 | Gen 2 |
| 4 | Dipole-like | 17 | Gen 2 |
| 5 | Dipole-like | 7 | Gen 1 |
| 6 | Patch-like | 7 | Gen 1 |

Table 4. Summary of Tag Characteristics (©2007 IEEE (Bauer-Reich et al., 2007))

Of primary concern was how the presence of a ground plane, such as the one designated in the IEC standard, would change susceptibility. It has been suggested by (Greason, 1989) that the presence of a ground plane can increase the susceptibility of some devices. The overall results as shown in 2 indicate that a ground plane increases damage to tags. A larger percentage of tags were damaged when the ground plane was present than when not. However, the ground plane seemed to alter results when testing other factors. Therefore, the remainder of the results will be presented in the context of whether or not a ground plane was present.



(a) Testing with a ground plane.          (b) Testing without a ground plane.
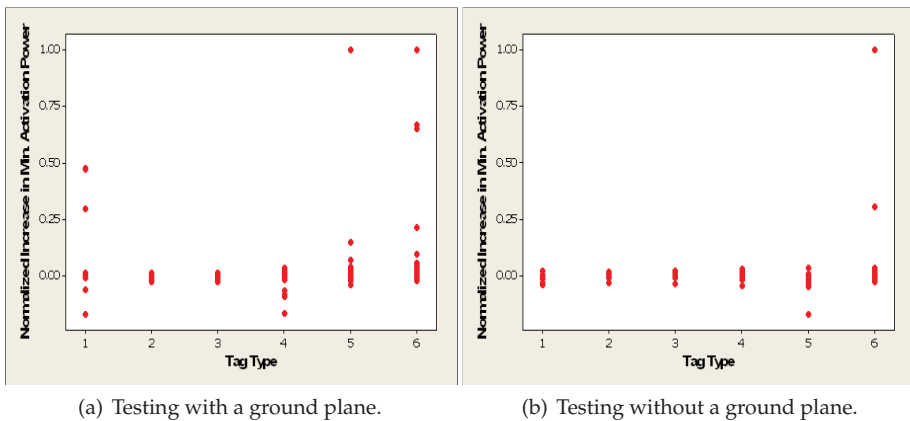
Fig. 2. The change in minimum activation power based on tag type. Two hundred sixteen tags were tested in the presence of a ground plane. One hundred sixty-two tags were tested without a ground plane. (©2007 IEEE (Bauer-Reich et al., 2007))

The next issue examined was the proximity of the discharge to the IC. The relationship was tested by placing discharges at distances of 1 cm, 3 cm, and 5 cm from the IC (3). When a ground plane was not present, there was a clear inverse relationship between the distance to the discharge and damage rates. The highest damage rates therefore corresponded to

the closest distance. The lower damage rate at farther distances is likely due to additional inductance in the path to the IC with increasing distance. When the ground plane was present, the relationship was not as obvious. The farthest discharge point had the highest rate of failure, with the closest being slightly less. The intermediate point resulted in the lowest rate of damage.



(a) Testing with a ground plane.        (b) Testing without a ground plane.
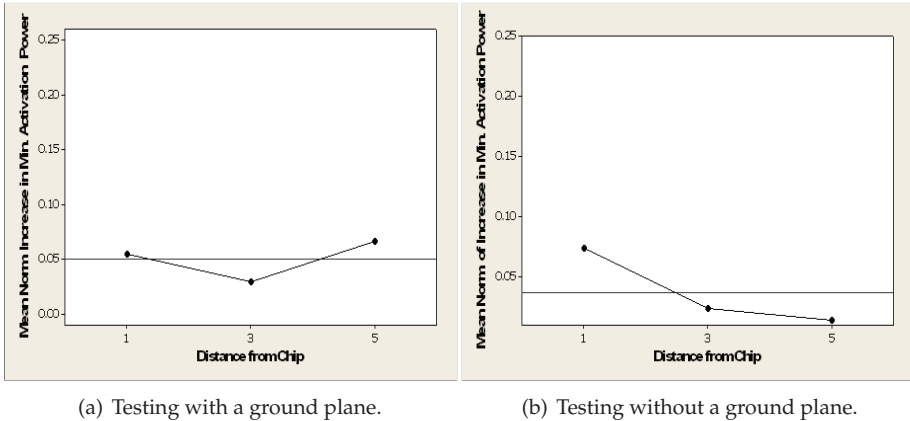
Fig. 3. The effect of discharge distance from the RFID tag IC on minimum activation power. (©2007 IEEE (Bauer-Reich et al., 2007))

It was postulated that the potential level would have a direct relationship with tag damage. The potential levels tested were 8 kV, 15 kV, 20 kV, and 25 kV (4). When the ground plane was present, it appeared that the larger discharges caused greater damage until one reached the 25 kV level. At 25 kV, the damage caused appeared to be less than the other three levels. Possible explanations are that there was sufficient arcing that the tag was bypassed (an event which was observed), there may have been multiple smaller discharges, or that the current waveform changed with the larger potential value. When the ground plane was removed, tag damage had an inverse relationship with charge level, decreasing with higher potentials.

When producing RFID tags, there are several factors affecting susceptibility which are under the direct control of the manufacturer. There were three such issues examined in the study: antenna type, IC, and tag covering or label material. The resistance of the label material seemed to play an important role: materials with higher resistivities covered tags that had lower damage levels. Proper selection of label material, therefore, seems to be an important way to decrease the likelihood of damage.

A second factor was the tag antenna. The antennas were grouped into two types: a dipole and a "patch-like" antenna. The patch-like antenna would be more accurately described as a fat dipole. The dipole antennas fared better in testing, indicating that a fat dipole may not be an ideal choice 5. However, testing did not illuminate what factors caused higher susceptibility for fat dipoles. It was also noted that, because an electromagnetic analysis of each antenna was not performed, it is likely that antenna type may have also played a role in some of the unexpected results for other factors.

Finally, the IC was examined. Four of the six tags utilized ICs that conformed to the EPCglobal Class 1 Generation 2 standard (EPCglobalGen2, 2008), while the remaining two tags utilized ICs that conformed to the EPCglobal Class 1 Generation 1 standard (EPCglobalGen1, 2002).

(a) Testing with a ground plane.                    (b) Testing without a ground plane.
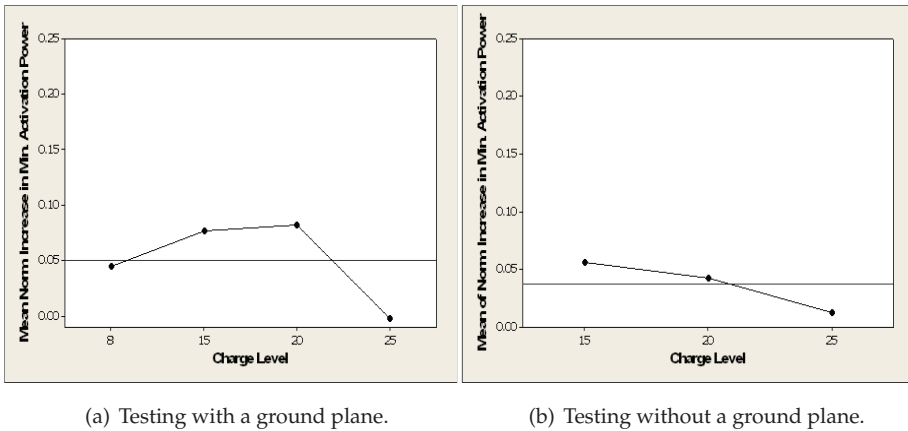
Fig. 4. The mean change in the minimum activiation power as a function of the magnitude of the discharge. (©2007 IEEE (Bauer-Reich et al., 2007))



(a) Testing with a ground plane.                    (b) Testing without a ground plane.
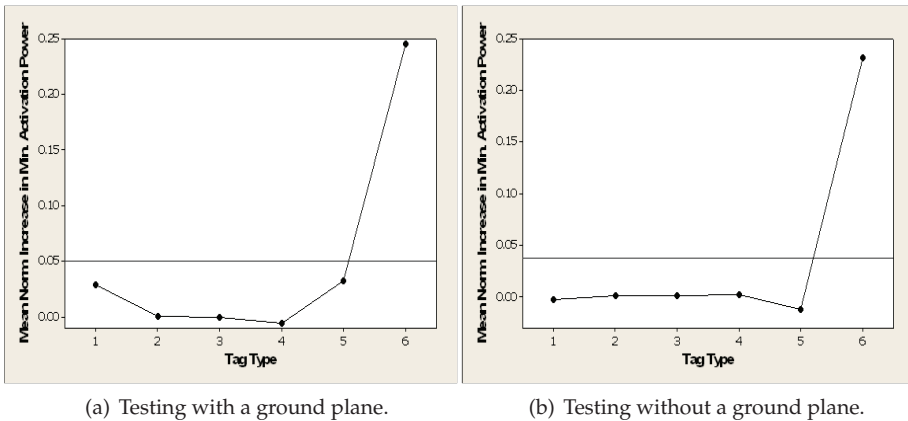
Fig. 5. The mean change in the minimum activiation power as a function of the tag type. (©2007 IEEE (Bauer-Reich et al., 2007))

In brief, the EPCglobal Class 1 Gen 1 standard was one of the first UHF RFID standards to see a significant deployment in terms of numbers of tags. The EPCglobal Class 1 Gen 2 standard (also incorporated as the ISO standard ISO 18000-6C) was developed in order to address a number of shortcomings in previous first generation protocols, including the EPCglobal Class 1 Generation 1 protocol. A more readable description of both protocols than that found in the applicable standards documents is given in (Dobkin, 2008).

It was found that the tags conforming to the EPCglobal Class 1 Gen 2 standard had a lower failure rate (6). In order to examine the issue, tag inlays, i.e., tags without the label covering, were tested. The inlays had the same antenna but some had EPCglobal Class 1 Generation 1 ICs while the rest had EPCglobal Class 1 Generation 2 ICs. The result is that there was significantly more variability in the EPCglobal Class 1 Generation 1 ICs after discharge. It

appears that the EPCglobal Class 1 Generation 2 tags may have incorporated better ESD protections on chip.
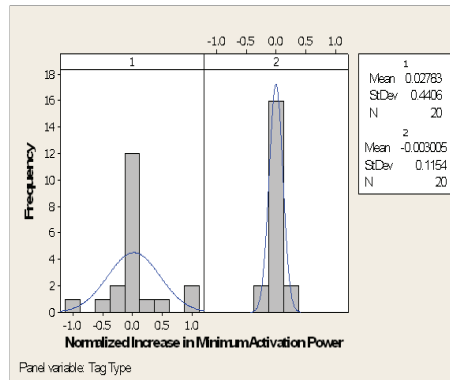


Fig. 6. The distribution of the change in normalized minimum activation power for Generation 1 ICs (left) compared with Generation 2 ICs (right). (©2007 IEEE (Bauer-Reich et al., 2007))

Overall results indicate that RFID tags could have failure rates as high as 4%. The failure rates, however, are dependent on several factors such as the environment, proximity of discharge to the IC, and type of IC utilized. Significantly, this is the failure level when the tag is not in the presence of an ambient field, such as that created by a reader antenna. It seems reasonable to expect that this level would be higher if an ESD event were to occur when a tag is actively communicating.

The results of this study were necessarily narrow; they did not address any type of tag beyond adhesive-paper label tags that operate at UHF frequencies. They also were limited to two ICs. Since this paper was published, there have been many new types of tags and ICs introduced into the marketplace. There are also tags that are manufactured for considerably different uses. The authors are unaware of any additional studies dealing with the interaction between RFID and ESD, indicating that there are many areas where this behavior is still unquantified.

## 6. Minimizing ESD in the RFID manufacturing and testing environment

In any electronics manufacturing environment, there are certain precautions which should be taken to prevent damage to the product. Fairly universal solutions should include static dissipative counter-tops and floors, ESD-safe office equipment, and use of static dissipative clothing for personnel. Indeed, precautions such as these are called out by an RFID IC manufacturer in Impinj (2005).

In RFID processing, however, there are additional issues which need to be taken into consideration (Blitshteyn, 2005). Processing tags into their final form, such as label conversion, is one area where ESD creates signficant product loss. RFID tags that are used in label form must be tested, converted to labels, and retested. All of these processes provide multiple opportunities for tags to fall victim to ESD.

One consideration is that roll-to-roll processes are used for manufacture and testing of RFID. These processes involve unrolling and re-rolling the product through several rollers. Both the machinery and local environment of these processes should be evaluated regularly for factors

which may increase susceptibility, especially to inlays. The machinery for the process should, of course, include a static dissipative coating on all surfaces that come into contact with tags. However, this static-dissipative coating should not be assumed to eliminate all possibilities of ESD. Coatings will prevent discharge from occurring if the static build-up on the device is not too large.

RFID tag antennas tend to be printed on materials such as polymers which are very prone to triboelectric charging. When this material is placed on a roll-to-roll device, large amounts of static can be accumulated and transferred from rollers and testing devices despite the presence of static dissipative surfaces. Sometimes this static can build up faster than it can be removed safely from the equipment.

The reader should note that a large number of synthetic materials have a strong affinity for negative charge, as shown on Table 1. There are also specialized triboelectric series to deal with such materials. A series of guidelines was published in (Diaz & Felix-Navarro, 2004), suggesting that nitrogen containing polymers generated a strong positive charge, halogenated polymers resulted in strong positive charge, and hydrocarbon-based polymers were nearly neutral. Although considerations such as cost play into selection of materials for manufacturing, the probability of triboelectric charging should be one consideration when choosing materials which will be used in manufacturing electronics.

ESD events in the manufacturing environment are likely to affect neighboring tags through field induction. Because tags are often placed closely together, a large ESD event may be sufficient to damage not only the tag directly affected but nearby tags, as well. Therefore preventing a single ESD event may prevent damage on several tags.

There are several ways to deal with ESD in manufacturing. One of the most effective methods is to reduce the speed of the process. Triboelectric charging increases as the rate of separation increases, so keeping the rate low will reduce charging. Another possibility, although more difficult to implement, is changing the substrate of the RFID tags to one that is not as prone to generating charge, such as a hydrocarbon-based polymer. Increasing humidity near the process is another way to dissipate charge. It is important in any electronics manufacturing environment to make sure that humidity levels are sufficiently high, but a second step is to make sure that the humidity level is constant throughout the area. A process which is placed a long way from a humidifier and perhaps near a window that may contribute to temperature swings will be more likely to have ESD issues than a process in a well-controlled area. The use of ionizers is also popular, but their placement should be carefully determined as improper positioning will cause more problems than it solves. For instance, an ionizer which neutralizes charge at one point in the process may adversely affect the process if the roll threads through an area underneath the ionizer where remnant charge may fall. Finally, keeping other equipment away from the process is often necessary. To monitor processes, display screens and other computer equipment may be placed near or integrated into the process. However, this equipment can often generate an electromagnetic field and, when not properly shielded, can create areas of large static build-up despite all other preventative measures.

One method of monitoring processes is through the use of a field meter, such as (StaticSolutions, n.d.). Field meters can detect an ambient electromagnetic field created by accumulation of static electricity. Areas where ESD events are likely to occur to transfer charge that may later be involved in an ESD event can be identified with a field meter and then neutralized. A field meter is meant to be used as a preventative measure as it cannot detect actual ESD events.

Another way to identify problem areas is an ESD event detector or monitor. These sensors detect discharge events above a user-defined threshhold. Devices can be connected to a computer to record data or hand-held devices. The devices cannot detect the exact location where ESD is occuring but are useful in locating problem areas. These are able to detect events and therefore not useful as a preventative measure. They also cannot determine whether damage has occurred, therefore making it difficult to assess whether a specified level of event is an issue of concern. Finally, these may be useful in determining the relationship between ESD activity and process speed. If one wishes to avoid events above a specified level, ESD monitors may be used to assess the speed at which event levels are unacceptably high.

Through the combined use of equipment designed to prevent and detect ESD and regular monitoring, ESD in the manufacturing and testing environment can be minimized. Each company will have to determine what rate of loss is acceptable and choose their materials and equipment accordingly.

## 7. Conclusion

Dealing with ESD in the RFID industry is a challenge which can be approached from several perspectives. Care should be taken in the manufacturing environment, but reducing ESD susceptibility of relevant circuitry is also useful. Based on studies performed by the authors, however, it appears that these challenges are still present in the manufacturing and usage environment. Given up to 4% of tags the tags tested failed, the prevalence of RFID technology in the current economy could imply significant losses. Therefore, it is necessary to understand the factors which can cause tag failure and try to find a means to prevent it.

## 8. References

AlienTech (2008). Higgs-3 product overview, *Alien Technology Datasheet* .
URL: *http://www.alientechnology.com/docs/products/DS_H3.pdf*.

Amerasekera, A. & Duvvury, C. (2002). *ESD in Silcon Integrated Circuits*, 2nd edn, John Wiley and Sons Ltd., Baffins Lane, Chichester, West Sussex PO 19 1UD, England.

Ames, B. (2005). Pentagon continues its push on suppliers to use RFID, *Military and Aerospace Electronics* 16.
URL: *http://www.militaryaerospace.com/index/display/article-display/236294/articles/ military-aerospace-electronics/volume-16/issue-9/news/pentagon-continues-its-push-on- suppliers-to-use-rfid.htmld*.

Barnett, R., Lazar, S. & Liu, J. (2006). Design of multistage rectifiers with low-cost impedance matching for passive RFID tags, *Radio Frequency Integrated Circuits (RFIC) Symposium, 2006 IEEE*, pp. 1–4.

Bauer-Reich, C., Nelson, R. & Vaselaar, D. (2007). The effects of ESD in multiple testing environments on adhesive-label RFID tags, *IEEE International Symposium on Electromagnetic Compatibility, 2007. EMC 2007*, pp. 1–6.

Bergeret, E., Gaubert, J., Pannier, P. & Rizzo, P. (2006). Power generation system for UHF passive RFID, *Electronics Letters* 42(25): 1452 –1454.

Blitshteyn, M. (2005). Mastering RFID label converting, *Paper, Film and Foil Converter* .

Bo, F., Yujie, D., Xiaoxing, Z. & Yingjie, L. (2009). A RF to DC voltage conversion model for multi-stage rectifiers in UHF RFID transponders, *Journal of Semiconductors* 44(2): 354–370.

Bustillo, M. (2010). Wal-mart radio tags to track clothing, *The Wall Street Journal* .
URL: *http://online.wsj.com/article/SB10001424052748704421304575383213061198090. html? mod=WSJ_article_related*.

Curty, J.-P., Joehl, N., Dehollain, C. & Declercq, M. J. (2005). Remotely powered addressable UHF RFID integrated system, *IEEE Journal of Solid-State Circuits* 40(11): 2193–2202.

Diaz, A. & Felix-Navarro, R. (2004). A semi-quantitative tribo-electric series for polymeric materials: the influence of chemical structure and properties, *Journal of Electrostatics* 62: 277–290.

Dobkin, D. M. (2008). *The RF in RFID: Passive UHF RFID in Practice*, Communications Engineering Series, Newnes, an imprint of Elsevier, 30 Corporate Drive, Suite 400, Burlington, MA 01803.

EPCglobalGen1 (2002). *860 MHz - 930 MHz Class 1 Radio Frequency Identification Tag Radio Frequency and Logical Communication Interface Specification Candidate Recommendation, Version 1.0.1*, 1.0.1 edn, EPCglobal.
URL: *http://www.epcglobalinc.org/standards/specs/860MHz_930_MHz_Class_1_RFID _ Tag_ Radio_Frequency_Logical_Communication_Interface_Specification.pdf*.

EPCglobalGen2 (2008). *EPC™Radio-Frequency Identity Protocols Class-1 Generation-2 UHF RFID Protocol for Communications at 860 MHz - 960 MHz, Version 1.2.0*, EPCglobal.
URL: *http://www.epcglobalinc.org/standards/uhfc1g2/uhfc1g2_1_2_0-standard-20% 080511.pdf*.

Evers, J. (2006). RFID passports take off, *CNET News* .
URL: *http://news.cnet.com/RFID-passports-take-off/2100-7348_3-6130016.html*.

Facen, A. & Boni, A. (2006). Power supply generation in CMOS passive UHF RFID tags, *Research in Microelectronics and Electronics 2006, Ph. D.*, pp. 33–36.

Finkenzeller, K. (2003). *RFID Handbook: Fundamentals and Applications in Contactless Smart Cards and Identification*, 2nd edn, John Wiley and Sons Ltd., The Atrium, Southern Gate, Chichester, West Sussex PO19 8SQ, England.

Glidden, R., Bockorick, C., Cooper, S., Diorio, C., Dressler, D., Gutnik, V., Hagen, C., Hara, D., Hass, T., Humes, T., Hyde, J., Oliver, R., Onen, O., Pesavento, A., Sundstrom, K. & Thomas, M. (2004). Design of ultra-low-cost UHF RFID tags for supply chain applications, 42(8): 140–151.

Glover, B. & Bhatt, H. (2006). *RFID Essentials*, O'Reilly Media Inc., 1005 Gravenstein Highway North, Sebastopol, CA 95472.

Greason, W. D. (1989). Influence of a ground plane on the ESD event in electronic systems, 25(2): 224–229.

IEC61000-4-2 (2005). *International Standard 61000-4-2, Electromagnetic Compatibility (EMC)-Part 4-2: Testing and Measurement Techniques - Electrostatic Discharge Immunity Test*, 1.1 edn, International Electrotechnical Commission.

Impinj (2005). ESD and the RFID tag, *Impinj Whitepaper* .
URL: *http://www.impinj.com/WorkArea/linkit.aspx?LinkIdentifier=id&ItemID=253%9*.

Impinj (2010). Monza 3 tag chip datasheet, *Impinj Datasheet* .
URL: *http://www.impinj.com/WorkArea/linkit.aspx?LinkIdentifier=id&ItemID=4157*.

Karthaus, U. & Fischer, M. (2003). Fully integrated passive UHF RFID transponder IC with 16.7-$\mu$W minimum RF input power, *IEEE Journal of Solid-State Circuits* 38(10): 1602–1608.

Nikitin, P. V., Rao, K. V. S., Lam, S. F., Pillai, V. andMartinez, R. & Heinrich, H. (2005). Power reflection coefficient analysis for complex impedances in RFIDtag design, *IEEE Transactions on Microwave Theory and Techniques* 53(9): 2721–2725.

Ott, H. W. (1988). *Noise Reduction Techniques in Electronic Systems*, 2nd edn, John Wiley and Sons Inc.

Shaw, M. (2004). Pushing past paper, *Pulp and Paper* .

Sood, B., Das, D., Azarian, M., Pecht, M., Bolton, B. & Lin, T. (2008). Failure site isolation on passive RFID tags, *15th International Symposium on the Physical and Failure Analysis of Integrated Circuits, 2008, IPFA 2008*, pp. 1–5.

StaticSolutions (n.d.). Ohm-stat™FM-1125 digital ESD field meter, *FM-1125 Datasheet* .
   URL: *http://www.staticsolutions.com/products/data/FM-1125.pdf*.

Torrance, R. (2009). RFID s power themselves, *EDN* May 4.
   URL: *www.edn.com/article/458664-RFIDs_power_themselves.php*.

# Part 2

# Advanced RFID Applications

# Privacy-enhanced RFID Tag Search System

Ji Young Chun[1], Jung Yeon Hwang[2] and Dong Hoon Lee[3]

[1]*Graduate School of Information Management and Security,Korea University*
[2]*Electronics and Telecommunications Research Institute (ETRI)*
*Republic of Korea*

## 1. Introduction

Radio frequency identification (RFID) technology is used to identify RFID-tagged objects automatically. An RFID system generally consists of three components: an RFID tag, an RFID reader, and a backend system. An RFID tag is a small device for identification, which is attached to or embedded in an object. It has an unique identifier and may optionally hold additional product information for the object. An RFID reader is a device used to interrogate RFID tags. It can be fixed or portable. It passes communication messages between an RFID tag and a backend system. A backend system stores and manages the online data which are associates with RFID tags. Since the communication between an RFID tag and an RFID reader occurs without optical line of sight, RFID tags can be read much longer and much faster than other automatic identification and data capture (AIDC) technologies such as Bar-codes and smartcards. Thanks to these advantages, RFID technology has various applications.



Fig. 1. RFID Tag Search System

Recently, RFID technology has been applied to many real-life applications such as asset management, supply chain, and product maintenance, etc. Especially, RFID tag search system

which can be used to find RFID-tagged objects is one of the promising applications of RFID technology. For example, this system can be used to search for missing children and find books in a library (See Fig. 1). This system also can be used to find and monitor an offender who has an electronic tag. Consider the situation which can easily happen in the library. Everyday librarians arrange books in order in its place. However, since they may be handled by many people, books are constantly misplaced on the shelves. When someone wants to borrow a book which is not checked out, if the book is not where it should be one must scan the entire shelves to find the misplaced book. Fortunately if the book is nearby, the search is quickly ended. Otherwise, one should do an exhaustive search. This is too time-consuming. If RFID tag search system is used in the library, one can efficiently find the misplaced book among extensive RFID-tagged books.

Although RFID technology provides various benefits because of its convenience, there is growing concern about RFID security and privacy. When someone holds RFID-tagged objects, attackers can discover his personal information which is stored in RFID tags and can track his movement using IDs of RFID tags. Besides these attacks, there are many security and privacy threats. Therefore, when we implement RFID technology, we should consider security and privacy threats. There are numerous researches focusing on RFID security and privacy issues (Burmester et al., 2008; Gilbert et al., 2008; Juels & Weis, 2005; Ohkubo et al., 2003; Paise & Vaudenay, 2008; Rotter, 2008; Rieback et al., 2006; Tsudik, 2006; Vaudenay, 2007). Recently, secure protocols for RFID tag search system are proposed for the first time (Tan et al., 2007; 2008). After that, various RFID tag search protocols have been proposed (Ahamed et al., 2008;a; Hoque et al., 2009; Won et al., 2008; Zuo, 2009). Even though these protocols are designed to enhance the security and privacy of RFID tag search system with its own requirements, there still exist vulnerabilities. Therefore, we first analyze the vulnerabilities of the previous works and then discuss the corresponding countermeasures.

The remainder of this chapter is organized as follows. We introduce RFID tag search system in Section 2 and classify some protocols which have been proposed in this area in Section 3. In Section 4, we point out the vulnerabilities of the previous works, and then analyze the security and privacy requirements of the RFID tag search system in Section 5. Finally, we conclude the chapter with future works in Section 6.

## 2. RFID Tag search system

In this section, we describe the RFID tag search system and the threat model in RFID systems. Before describing the threat model, we describe system configurations and the basic RFID tag search protocol to clarify the roles of three components in RFID tag search system. We then describe the threat model in RFID systems.

### 2.1 System configurations
RFID tag search system also consists of three components: an RFID tag, an RFID reader, and a backend system.

- RFID Tag: RFID tags are categorized into two groups, active and passive, according to whether they have their own battery or not. While an active tag has its own battery, a passive tag does not have an internal battery and passively obtain the operating power from an RFID reader. In RFID tag search system, it is reasonable that tags are assumed to be passive. Since tags are usually attached to cheap objects like books or goods, passive tags are more suitable

than rather expensive active tags in RFID tag search system. We assume that tags are passive in this chapter. It is known that the communication range of passive tags is 3*m* or less (OECD, 2007).

- RFID Reader: An RFID reader can interrogate RFID tags and transfer communication messages between an RFID tag and a backend system. It supplies the operating power to passive tags. To give enough operating power to passive tags, the signal strength of an RFID reader should be strong. Therefore, the communication range of an RFID reader is much stronger than that of a passive tag, it is about 100*m* (OECD, 2007). There are two kinds of RFID readers, fixed and portable. Fixed reader is installed where data capture is required and it sends and receives RFID tag data to a backend system through the wired networks (See Fig. 2). Portable reader which can be mounted in a mobile phone or personal digital assistant (PDA) uses the wireless networks to communicate with a backend system (See Fig. 3). Therefore, fixed reader can be assumed that it has a persistent connection with a backend system while a persistent connection between portable reader and a backend system cannot be guaranteed due to unstable wireless connection or distance limitation, etc.

- Backend System: A backend system stores and manages online data of RFID tags. It is assumed to be trusted and do not compromised.

Fig. 2. Fixed Reader

Fig. 3. Portable Reader

## 2.2 Basic RFID tag search protocol

RFID tag search is to find a particular RFID tag using an RFID reader. In more detail, an RFID reader can determine whether a particular tag exists nearby the RFID reader using RFID tag

search system. Next we present a simple protocol to realize 'RFID tag search'. This basic RFID tag search system operates as follows:

| | | | |
|---|---|---|---|
| (1) $B \leftarrow R$ | : | Search request about a particular tag | |
| (2) $B \rightarrow R$ | : | A tag identifier $ID_j$ | |
| (3) | $R \rightarrow T^*$ : | $ID_j$ | |
| (4) | $T^*$ : | Check $ID^* = ID_j$ | |
| (5) | $R \leftarrow T_j$ : | Reply | |

Fig. 4. Basic RFID Tag Search Protocol

(1) When the reader $R$ wants to find a particular tag, it sends a request message about a particular tag to the backend system $B$.

(2) The backend system $B$ sends a tag identifier $ID_j$ which the reader wants to find to the reader $R$.

(3) After receiving $ID_j$, the reader $R$ broadcasts $ID_j$ to find the tag.

(4) One of arbitrary tags $T^*$ nearby the reader $R$ replays when its own identifier is equal to the broadcasted identifier $ID_j$.

(5) If the reader receives the reply from the tag $T_j$, the reader $R$ can know the existence of the tag $T_j$.

Despite the simplified structure for a tag search the above basic protocol does not have any considerations for RFID security and privacy problems. There exist various threats through malicious attacks in RFID systems. We should consider RFID security and privacy problems to use RFID tag search system in real-life.

### 2.3 Threat model

In this subsection, we describe various security and privacy threats in RFID systems and analyze the basic RFID tag search protocol in terms of these threats. An adversary can mount the following attacks.

- Eavesdropping Attack: An adversary can eavesdrop all the communication messages between an RFID reader and RFID tags. When a portable reader is used, an adversary can also eavesdrop all the communication messages between a portable reader and a backend system.

- Intercept Attack: An adversary can intercept the messages in transmission between RFID readers and RFID tags. If a message from a reader is intercepted, a tag cannot get this intercepted message.

- Replay Attack: An adversary can replay the messages which were previously eavesdropped or intercepted.

- Tampering Attack: An adversary can modify, add, and delete data stored in RFID tags.

- Physical Attack: An adversary can compromise RFID tags. Once tags are compromised physically, an adversary can know all the secret information stored in RFID tags. An adversary

can also do a physical attack to portable readers, since portable readers can be easily lost or stolen. However, a backend system and fixed readers are not compromised.

Using these attacks, an adversary threatens security and privacy in RFID systems as follows.

- Impersonation: An adversary can impersonate a legitimate tag or a legitimate reader. After an adversary intercepts valid messages from a legitimate tag/reader, she replays these intercepted messages to a legitimate reader/tag.

- Information Leakage: An adversary can identify a specific tag using eavesdropping attacks. This attack can breach the privacy of a tag holder.

- Tracking: An adversary can track the movements of an RFID-tagged object such as a tag or a portable reader using eavesdropping attacks.

- Cloning: An adversary can clone a specific tag using physical and tempering attacks. To make a clone tag, an adversary physically accesses the secret information of a tag, and then creates a fake tag which stores this secret information. Using this attack, the adversary can change an expensive product into a cheap one.

- Denial of Service (DoS): An adversary sends a large amount of requests to a backend system to disable the RFID tag search system. Under this attack, a backend system cannot respond to the request of readers.

- Desynchronization: An adversary can make a tag and a backend system/reader be desynchronized by intercepting communication messages. Once a desynchronization happens, a tag and a backend system/reader cannot communicate with each other any more.

In the basic RFID tag search protocol in Fig. 4 an adversary can eavesdrop all communication messages between $R$ and $T^*$. An adversary can impersonate a legitimate tag $T_j$ after eavesdropping the communication messages in step (3) and (5). An adversary can also impersonate a legitimate reader $R$ just by replying identifier, $\text{ID}_j$. The basic protocol leaks the information of tags like IDs. This leads the privacy breaches of a tag holder. An adversary can know the sensitive information of a tag holder, such as what a tag holder has and what a tag holder wears. More serious problem of the basic protocol is location tracking. If an adversary constantly observes the replies of a particular tag, she can track the movements of this tag and also the movements of a tag holder. Another security problem is tag cloning since low-cost passive tags cannot be protected with a temper-proof mechanism. The basic protocol is vulnerable to DoS attacks. If a backend system is disabled because of DoS attacks, then $R$ cannot get any tag identifier in step (1) and (2), and so the RFID tag search system cannot be available.

These threats are general threats in RFID systems. However, there may exist other threats to be considered especially in the RFID tag search system. For instance, in the RFID tag search system, it could be important information to an adversary whether an RFID reader finds a specific tag or not. This threat is restricted to the RFID tag search system. Therefore, to design secure protocols in the RFID tag search system, we need to identify threats which are restricted to the search system. We will analyze previous RFID tag search protocols in the next section and then identify threats in the RFID tag search system.

## 3. Classification of previous RFID tag search protocols

In this section, we classify previous RFID tag search protocols (Ahamed et al., 2008;a; Hoque et al., 2009; Tan et al., 2007; 2008; Won et al., 2008; Zuo, 2009) which are designed to overcome various threats in the previous section.

### 3.1 Criteria for classification
We classify previous RFID tag search protocols according to the following criteria which reflect fundamental design considerations.

1) Movement of Readers: What kinds of RFID readers are used? Fixed or Portable?

2) Secret Update: Does each tag update its own secret value after every session?

3) Response of Tags: Do all tags respond to the request of an RFID reader? or Does the specific tag respond to the request of an RFID reader while the others keep silent?

4) Reveal Reader ID: Does an RFID reader reveal its identifier without any manipulation?

We will describe each criterion in more detail.

### 3.1.1 Movement of readers
As we described in Section 2, fixed readers use wired networks while portable readers use wireless networks. Since portable readers are hardly assumed that they have a persistent connection with a backend system, the search protocol with portable readers should consider this situation when portable readers cannot connect to a backend system. Another problem is that portable readers are easily lost or stolen. Once the readers are compromised, all the secret information in readers are revealed. Therefore, the search protocol with portable readers should also consider this situation.

### 3.1.2 Secret update
When each tag updates its own secret value after every session, a backend system should update the secret value of this tag at the same time. In this case, synchronization between a tag and a backend system is important. If a tag and a backend system are desynchronized, then this tag cannot be searched any more. Secret update is necessary to be secure against a physical attack. If an adversary is assumed to be able to mount a physical attack, an adversary can get the secret information of a tag. After that, an adversary can trace the communication messages of the tag in previous sessions using the current secret value of a tag if each tag does not update its own secret value after every session in the search protocol. This means that the protocol does not provide forward secrecy.

### 3.1.3 Response of tags
In the RFID tag search protocol, if the specific tag which an RFID reader wants to find responds to the request of an RFID reader, an adversary can learn whether the reader finds the specific tag or not. However, if all the tags including the specific tag respond to the request of an RFID reader, an adversary cannot decide whether the reader finds the specific tag or not. Therefore, by adjusting the number of responses of tags, we can protect the privacy of an RFID reader holder. Beside this problem an adversary can trace a tag. If only a specific tag always responds to a particular message, by sending this particular message repeatedly to the tag, an adversary

can trace this tag. However, if all tags respond to a particular message, an adversary cannot trace the tag.

### 3.1.4 Reveal reader ID

This criterion is about whether an RFID reader reveals its own ID or not. This is only for the protocols using portable readers. Since fixed readers passively relay communication messages between tags and a backend system, tags do not have to know IDs of fixed readers. However, since portable readers should handle the situation that portable readers cannot connect to a backend system, they should store secret information of tags. Therefore, tags have to know IDs of portable readers to communicate with them. To let tags know an ID of a portable reader, a portable reader sends its own ID to tags. In some circumstance, a revealment of reader's ID is not desirable. If an RFID reader sends its own ID without any manipulation, an adversary can identify this reader and also trace the movement of the reader holder.
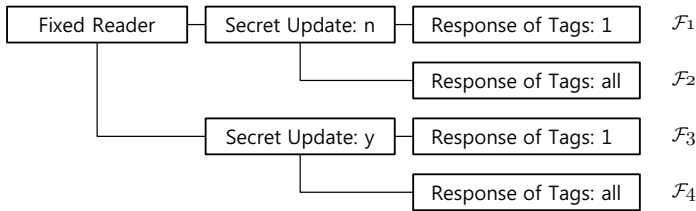


Fig. 5. Classification of Previous RFID Tag Search Protocols with Fixed Readers
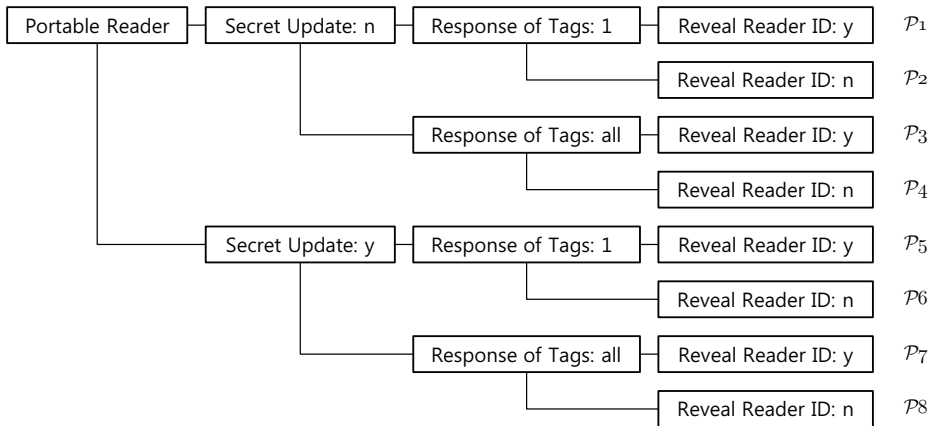


Fig. 6. Classification of Previous RFID Tag Search Protocols with Portable Readers

| Fixed Reader | | Portable Reader | | | |
|---|---|---|---|---|---|
| Secret Update: $n$ | Secret Update: $y$ | Secret Update: $n$ | | | Secret Update: $y$ |
| | | 3): 1 | | 3): *all* | |
| | | 4): $y$ | 4): $n$ | 4): $y$ | |
| $\mathcal{F}1$ | $\mathcal{F}3$ | $\mathcal{P}1$ | $\mathcal{P}2$ | $\mathcal{P}3$ | $\mathcal{P}8$ |

Table 1. 6 kinds of previous protocols

### 3.2 Classification

The classification of RFID tag search protocols based on criteria is shown in Fig. 5 and 6. In Fig. 5 and 6, "Secret Update: y/n" means that each tag updates/does not update its own secret value after every session in RFID tag search protocol. When all tags respond to the request of an RFID reader, this is denoted by "Response of Tags: all". If the specific tag responds to the request of an RFID reader, this is denoted by "Response of Tags: 1". "Reveal Reader ID: y/n" means that the reader ID is revealed/is not revealed from the communication messages in RFID tag search protocol. This means that an RFID reader sends its own ID to tags without any manipulation. Based on these criteria, search protocols are divided into 12 categories. Protocols using fixed readers have 4 categories from $\mathcal{F}1$ to $\mathcal{F}4$ and protocols using portable readers have 8 categories from $\mathcal{P}1$ to $\mathcal{P}8$.

There are 6 kinds of previous protocols in (Ahamed et al., 2008;a; Hoque et al., 2009; Tan et al., 2007; 2008; Won et al., 2008; Zuo, 2009) (See Table 1). We select one protocol from each type as follows.

- Protocol 1   in category $\mathcal{F}1$: Protocol one in (Zuo, 2009)

- Protocol 2   in category $\mathcal{F}3$: Protocol three in (Zuo, 2009)

- Protocol 3   in category $\mathcal{P}1$: First protocol in (Tan et al., 2008)

- Protocol 4   in category $\mathcal{P}2$: Fourth protocol in (Won et al., 2008)

- Protocol 5   in category $\mathcal{P}3$: RFID search protocol in (Tan et al., 2008)

- Protocol 6   in category $\mathcal{P}8$: Enhanced search protocol in (Hoque et al., 2009)

In Table 1, 3) means the third criterion, Response of Tags and 4) means the fourth criterion, Reveal Reader ID.

## 4. Analysis of previous RFID tag search protocols

In this section, we analyze previously selected RFID tag search protocols. We do not present the protocols in detail but describe main features and drawbacks.

### 4.1 Protocol 1 in $\mathcal{F}_1$

In (Zuo, 2009), there is no mention about the movement of readers. However in the Protocol 1 disconnection of an RFID reader is not considered. This is why we classify Protocol 1 as $\mathcal{F}1$. Since tags do not update their secret information, Protocol 1 does not provide forward secrecy. That is, an adversary can trace the movement of a tag $T_i$ in the previous sessions using compromised secret information $k_i$ and $id_i$ of a tag $T_i$. The secret information can be obtained through physical attacks. If an adversary stored all communication messages in the

| Reader $R$ | Tag $T^*$ |
|---|---|
| calculate $F_{k_i}(id_i \oplus H(n_1))$ | |
| send $\theta = F_{k_i}(id_i \oplus H(n_1))\|n_1$ $\xrightarrow{\quad \theta \quad}$ | calculate $F_{k^*}(id^* \oplus H(n_1))$ |
| | test if $F_{k^*}(id^* \oplus H(n_1)) = F_{k_i}(id_i \oplus H(n_1))$ |
| | if so, calculate $H(id_i\|F_{k_i}(n_1))$ |
| verify $H(id_i\|F_{k_i}(n_1))$ $\xleftarrow{\quad \lambda \quad}$ | send $\lambda = H(id_i\|F_{k_i}(n_1))$ |

Fig. 7. Protocol 1

previous sessions, she can check whether a previous communication message $(\theta, \lambda)$ is from a tag $T_i$ or not. After she gets $n_1$ from $\theta$, she can check whether $\lambda = H(id_i\|F_{k_i}(n_1))$.

Besides the tracing problem through physical attacks, there is another tracing problem through replay attacks in the protocol. If an adversary repeatedly sends the same request $\theta$, a tag $T_i$ always sends same response $\lambda$. Therefore an adversary can trace a specific tag. If all tags except a tag $T_i$ respond to the request of a reader with random values, then Protocol 1 becomes secure against replay attacks. This modified protocol can be classified as $\mathcal{F}2$.

### 4.2 Protocol 2 in $\mathcal{F}_3$

| Reader $R$ | Tag $T^*$ |
|---|---|
| calculate $F_{k_i}(id_i \oplus H(n_1))\|F_{k_i^N}(id_i \oplus H(n_1))$ | |
| send $\theta = F_{k_i}(id_i \oplus H(n_1))\|$ | |
| $F_{k_i^N}(id_i \oplus H(n_1))\|n_1$ $\xrightarrow{\quad \theta \quad}$ | calculate $F_{k^*}(id^* \oplus H(n_1))$ |
| | test if $F_{k^*}(id^* \oplus H(n_1)) = F_{k_i}(id_i \oplus H(n_1))$ |
| | or $F_{k^*}(id^* \oplus H(n_1)) = F_{k_i^N}(id_i \oplus H(n_1))$ |
| | if either condition is true, |
| | calculate $H(id_i\|F_{k_i}(n_1))$ |
| verify $H(id_i\|F_{k_i}(n_1))$ $\xleftarrow{\quad \lambda \quad}$ | send $\lambda = H(id_i\|F_{k_i}(n_1))$ |
| if $k_i$ was used to verify $\lambda$ | update $k_i \leftarrow H((k_i \gg L)\|n_1)$ |
| update $k_i \leftarrow H((k_i \gg L)\|n_1)$ | |
| if $k_i^N$ was used to verify $\lambda$ | |
| update $k_i \leftarrow H((k_i^N \gg L)\|n_1)$ | |

Fig. 8. Protocol 2

Protocol 2 is similar to Protocol 1, but each tag updates its own secret key after every session. Therefore this protocol satisfies forward secrecy. Since each tag's secret key is updated using a hash function like SHA-1, an adversary cannot know the previous secret key because of the one-wayness of a hash function. However, the protocol should consider the synchronization between a reader and a tag. If an adversary mounts an intercept attack to the communication message $\lambda$, a tag $T_i$ and a reader are desynchronized. To be secure against intercept attacks, $k_i^N$ is used for the situation when $T_i$ updated the secret key but a reader did not update the

secret value. Therefore a reader should store two secret keys of a tag $T_i$, current key and next should-be key.

We can simply modify Protocol 2 to be secure against replay attacks using the same response technique in the Protocol 1. Then the modified protocol can be classified as $\mathcal{F}_4$.

### 4.3 Protocol 3 in $\mathcal{P}_1$

| Reader $R_j$ | | Tag $T^*$ |
|---|---|---|
| calculate $h(f(r_j, t_i)\|n_r) \oplus id_i$ | | |
| send $\theta = h(f(r_j, t_i)\|n_r) \oplus id_i\|n_r\|r_j$ | $\xrightarrow{\theta}$ | calculate $h(f(r_j, t^*)\|n_r)$ |
| | | if $id^* = h(f(r_j, t^*)\|n_r) \oplus h(f(r_j, t_i)\|n_r) \oplus id_i$ |
| | | calculate $h(f(r_j, t_i)\|n_t\|n_r) \oplus id_i$ |
| verify $h(f(r_j, t_i)\|n_t\|n_r) \oplus id_i$ | $\xleftarrow{\lambda}$ | send $\lambda = h(f(r_j, t_i)\|n_t\|n_r) \oplus id_i\|n_t$ |

Fig. 9. Protocol 3

This protocol provides serverless RFID search which does not require a persistent connection to a backend system. A holder of a portable reader may go to a remote location where a portable reader cannot connect to a backend system to find an RFID-tagged object. To overcome this problem, if portable readers download all the secret information of tags, then portable readers can always find particular tags even if they cannot connect a backend server. However, this approach is not secure against physical attacks. Since portable readers are easily lost or stolen, an adversary can know all the secret information of tags. Therefore, in Protocol 3, a portable reader $R_j$ stores the information $f(r_j, t_i)\|id_i$ of each tag $T_i$ where $r_j$ and $id_i$ are IDs of a portable reader $R_j$ and a tag $T_i$, respectively, and $t_i$ is a secret key of a tag $T_i$. Even if an adversary gets the information $f(r_j, t_i)\|id_i$ of each tag $T_i$ from compromised portable reader $R_j$, she cannot get a secret key $t_i$ of a tag $T_i$ due to the one-wayness of the function $f(\cdot, \cdot)$.

This protocol is vulnerable to replay attacks. By sending an eavesdropped message $\theta$ repeatedly, an adversary can trace a specific tag. The responses $\lambda$ of a specific tag vary in every session, but a specific tag always sends a response to the same request.

In Protocol 3, a portable reader $R_j$ sends its own identifier $r_j$. This breaches the privacy of the reader holder. An adversary can trace the movement of a reader holder just eavesdropping an ID of a portable reader. Since the signal strength of a reader is much stronger than that of a tag, an adversary can eavesdrop a message from a reader more easily. Therefore, revealing IDs of readers may be more serious than revealing IDs of tags in RFID tag search system, since tags are usually attacked to goods while portable readers are handled by people in RFID tag search system.

### 4.4 Protocol 4 in $\mathcal{P}_2$

This protocol does not reveal IDs of readers, hence this protocol protects the privacy of a reader holder. To let tags know an ID of a reader, the authors use a symmetric encryption (Feldhofer & Wolkerstorfer, 2007). By decrypting a received message with its own identifier, a tag can know an ID of a reader. This protocol is also secure against replay attacks. Since each tag stores *ltime* which is the last time to communicate with a reader, tags can check whether a received message is replayed or not using this value. If *ctime* from a received message is less than *ltime*, tags do not respond to the request of a reader.

| Reader $R_j$ | Tag $T^*$ |
|---|---|
| generate $ctime$ | |
| calculate $S_1 = E_{id_i}(ctime \oplus r_j)$ | |
| calculate $S_2 = E_{ctime \oplus r_j}(E_{t_i}(r_j \oplus id_i))$ | |
| send $\theta = ctime \| S_1 \| S_2 \xrightarrow{\ \theta\ }$ | if $ctime > ltime$ then |
| | calculate $D_{ownid}(S_1) \oplus ctime = r_j$ |
| | calculate $D_{ownt}(D_{ctime \oplus r_j}(S_2)) \oplus r_j = id_i$ |
| | if $id_i = ownid$ then |
| | generate $n_t$ |
| | calculate $S_3 = E_{ownid \oplus n_t}(S_1)$ |
| verify $S_1 = D_{id_j \oplus n_t}(S_3) \xleftarrow{\ \lambda\ }$ | send $\lambda = S_3 \| n_t$ |
| | $ltime \leftarrow ctime$ |

Fig. 10. Protocol 4

While *ctime* is useful to defeat replay attacks, it can be used for malicious attacks. After stealing a portable reader, an adversary sends a request message $\theta$ with *ctime'* which is much bigger than current time. A tag $T_i$ accepts this message since *ctime'* is much bigger than *ltime*. And then updates *ltime* with *ctime'*. After that, a tag $T_i$ cannot communicate with honest portable readers until *ctime'*.

### 4.5 Protocol 5 in $\mathcal{P}_3$

| Reader $R_j$ | Tag $T^*$ |
|---|---|
| calculate $h(f(r_j, t_i) \| n_r) \oplus id_i$ | |
| send $\theta = h(f(r_j, t_i) \| n_r) \oplus id_i \| n_r \| r_j \xrightarrow{\ \theta\ }$ | calculate $h(f(r_j, t^*) \| n_r)$ |
| | if $id^* = h(f(r_j, t^*) \| n_r) \oplus h(f(r_j, t_i) \| n_r) \oplus id_i$ |
| | calculate $\lambda = h(f(r_j, t_i) \| n_t) \oplus id_i$ |
| $\xleftarrow{\ \lambda\ }$ | then send $\lambda = h(f(r_j, t_i) \| n_t) \oplus id_i \| n_t$ |
| | else choose random number *rand* and $n_t$ |
| $\xleftarrow{\ \lambda\ }$ | then send $\lambda = rand \| n_t$ |
| verify $h(f(r_j, t_i) \| n_t) \oplus id_i$ | with the predefined probability |

Fig. 11. Protocol 5

Protocol 5 improves Protocol 3 in that Protocol 5 is secure against replay attacks. Since all tags respond to the request of a reader with the predefined probability, an adversary cannot trace a specific tag using replay attacks. However, alike Protocol 3, Protocol 5 has the privacy problem that the protocol reveals the IDs of readers. And Protocol 3 and Protocol 5 do not provide forward secrecy for such a reason as mentioned in section 4.1.

| Reader $R_j$ | | Tag $T^*$ |
|---|---|---|
| calculate $\mathcal{P}(seed_{T_i})$ | | |
| send $n_i = \mathcal{P}(seed_{T_i})$ | $\xrightarrow{\;n_i\;}$ | calculate $a = \mathcal{P}(seed_{T*})$ |
| | | if $a = n_i$ then |
| | |   calculate $k = \mathcal{M}(seed_{T*})$, $x = \mathcal{P}(k)$ |
| | |   and $seed_{T_i} = \mathcal{M}(k)$ |
| | $\xleftarrow{\;x\;}$ |   send $x$ |
| | | else choose random number $rand$ |
| calculate $s = \mathcal{M}(seed_{T_i})$ and $m = \mathcal{P}(s)$ | $\xleftarrow{\;rand\;}$ |   send $rand$ with probability $\lambda$ |
| if $m = x$, $seed_{T_i} = \mathcal{M}(s)$ | | |
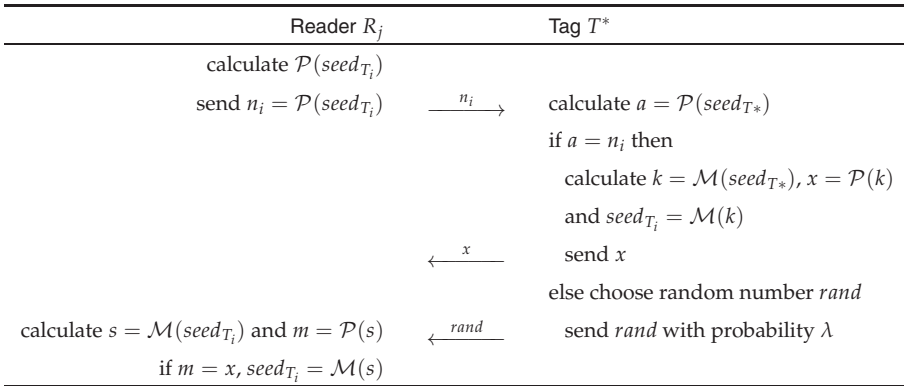
Fig. 12. Protocol 6

### 4.6 Protocol 6 in $\mathcal{P}_8$

Protocol 6 does not reveal an ID of a reader and provides forward secrecy. And the protocol is also secure against replay attacks since all tags respond to the request of a reader. However, Protocol 6 is not secure against intercept attacks. If an adversary intercepts a communication message $x$, a tag $T_i$ and a reader $R_j$ are desynchronized. After this session, they cannot communicate with each other. If Protocol 6 uses the technique in Protocol 2, Protocol 6 can become secure against intercept attacks.

Another drawback of the protocol is a storage cost. In the protocol, tags should store seeds as many as the number of portable readers. This can be a burden to resource constraint tags. This protocol is not designed for scalability. To use a new portable reader $R'$, all tags should store a seed for the reader $R'$. This may take much time when huge tags are used in this search system.

### 5. Security & privacy requirements in RFID tag search system

We previously described threats in RFID systems in Section 2. These threats are still major threats in RFID tag search system. However, there may exist other threats to be considered in RFID tag search system. In this section, we analyze security and privacy requirements in RFID tag search system based on the analysis of previous protocols.

We first simply describe security and privacy requirements which are analyzed based on the threats in Section 2.

1) Authentication: A backend system and a portable reader must be convinced that tags who communicate with them are legitimate. If authentication is not provided in the protocol, an adversary can impersonate a legitimate tag using malicious attacks such as intercept attacks and replay attacks.

2) Confidentiality: An adversary should not be able to extract any information from eavesdropped messages. If an RFID tag search protocol does not provide confidentiality, the protocol leaks secret information.

3) Anti-tracking: An adversary should not be able to trace the movements of RFID-tagged objects.

4) Anti-cloning: An adversary should not be able to make cloned tags.

5) Anti-DoS attacks: Even if an adversary mounts DoS attacks, an RFID tag search system should not be disabled.

6) Synchronization: Tags and a backend system/ a reader are always synchronized even if an adversary tries to break the synchronization.

To find a particular tag, both fixed reader and portable reader can be used. A fixed reader is installed at location where searches of RFID-tagged objects are required. Therefore a fixed reader can find a specific tag that is nearby a fixed reader. For example, to cover all area in a library, 15 fixed readers are needed (See Fig. 13). However portable reader provides more flexible searches. To find a particular tag, a user just moves around with a portable reader.
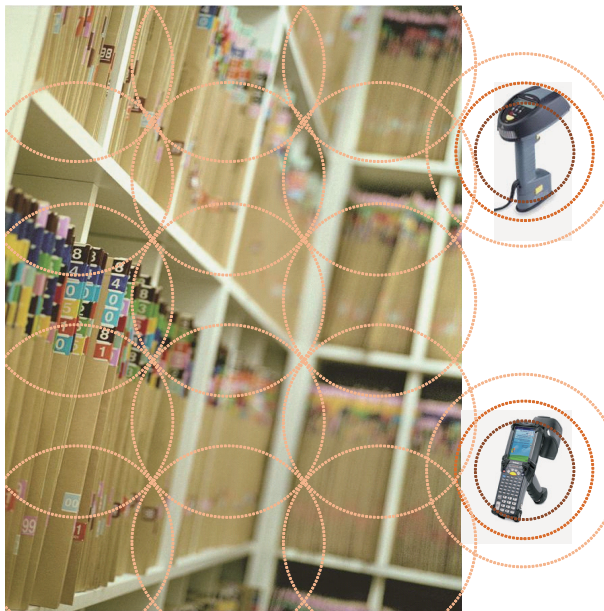


Fig. 13. Fixed reader and Portable reader

When a portable reader is used in RFID tag search system, we should consider the privacy of an RFID reader holder. The communication range of a tag is $3m$, while the communication range of a reader is $100m$ (See fig. 14). The area where an adversary can eavesdrop a message from a tag is $9\pi m^2$ and the area where an adversary can eavesdrop a message from a reader is $10000\pi m^2$. Therefore, a message from a reader can be eavesdropped much easier than a message from a tag. Moreover, since tags usually are attached to goods in RFID tag search system while readers are handled by people, the privacy breaches of a portable reader can be more serious than that of a tag.

100m

3m
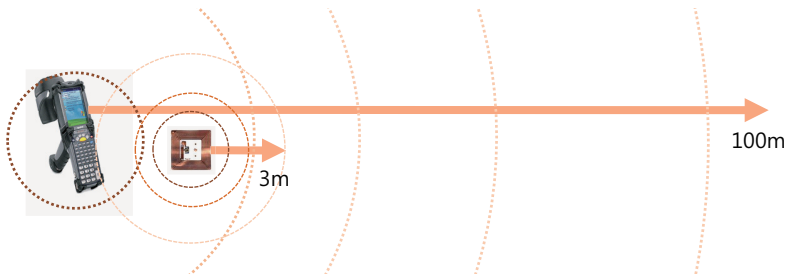
Fig. 14. Communication ranges of a tag and a reader

| Requirements | P 1 | P 2 | P 3 | P 4 | P 5 | P 6 |
|---|---|---|---|---|---|---|
| 1) Authentication | x | √ | x | √ | √ | √ |
| 2) Confidentiality | √ | √ | √ | √ | √ | √ |
| 3) Anti-tracking | x | √ | x | √ | √ | √ |
| 4) Anti-cloning | x | x | x | x | x | x |
| 5) Anti-DoS attacks | x | x | √ | √ | √ | √ |
| 6) Synchronization | — | √ | — | — | — | x |
| 7) Reader ID privacy | — | — | x | √ | x | √ |
| 8) Availability | — | — | √ | √ | √ | √ |
| 9) Leakage Resilience | — | — | √ | √ | √ | √ |
| 10) Protect response of tags | x | x | x | x | √ | √ |

Table 2. Security and Privacy Properties

Besides the security and privacy requirements which are mentioned above, additionally required requirements in RFID tag search system are as follows.

7) Reader ID privacy: In an RFID tag search protocol, an ID of a reader should not be revealed. If a portable reader sends its own ID in every session, an adversary can identify the reader and trace a portable reader holder using this static value.

8) Availability: Even if a portable reader cannot connect to a backend system, an RFID reader should be able to find a particular tag which a reader wants to find.

9) Leakage Resilience: Even if a portable reader is compromised, an adversary should not be able to know secret information of tags.

10) Protect response of tags: If a particular tag responds to the request of a reader, an adversary can trace this tag using replay attacks. Therefore, an RFID search protocol protects the response of tags.

The security and privacy properties of selected 6 protocols are summarized in Table 2. The only one requirement which is not satisfied by selected 6 protocols is anti-cloning. To design a secure protocol against cloning, physical unclonable functions (PUFs) are proposed (Tuyls & Batina, 2006). PUFs are used as a secure memory to store a secret key on a tag. It will

be an interesting work to design an RFID tag search protocol secure against cloning using the idea of PUFs.

## 6. Conclusion

In this chapter, we introduce privacy-enhanced RFID tag search system. After describing the threat model in RFID systems, we classify previous RFID tag search protocols which are designed to overcome various threats. And we analyze these protocols and draw security and privacy requirements in RFID tag search system based on the analysis. Our analysis is helpful to researchers who want to design secure protocols in RFID tag search system. Our future work is to improve some protocols which have drawbacks in 6 selected protocols.

## 7. References

Ahamed, S.I.; Rahman, F.; Hoque, E.; Kawsar, F. & Nakajima, T. (2008). S3PR: Secure Serverless Search Protocols for RFID, *Proceedings of Information Security and Assurance(ISA)*, pp. 187-192, Apr. 2008.

Ahamed, S.I.; Rahman, F.; Hoque, E.; Kawsar, F. & Nakajima, T. (2008) Secure and Efficient Tag Searching in RFID Systems using Serverless Search Protocol, *International Journal of Security and Its Applications*, Vol. 2, No. 4, pp. 57-66, Oct. 2008.

Burmester, M.; Medeiros, B. & Motta, R. (2008) Provably Secure Grouping-Proofs for RFID Tags, *Proceedings of CARDIS*, LNCS 5189, pp. 176-190, Sep. 2008.

Feldhofer, M. & Wolkerstorfer, J. (2007) Strong crypto for RFID tags-A comparison of low-power hardware implementations, *Proceedings of IEEE International Symposium on Circuits and Systems(ISCAS)*, pp. 1839-1842, May. 2007.

Gilbert, H.; Robshaw, M. & Seurin, Y. (2008) HB ♯: Increasing the Security and Efficiency of HB+, *Proceedings of Advances in Cryptology - EUROCRYPT*, LNCS 4965, pp. 361-378, Apr. 2008.

Hoque, Md.E.; Rahman, F.; Ahamed, S.I. & Park, J.H. (2009) Enhancing Privacy and Security of RFID System with Serverless Authentication and Search Protocols in Pervasive Environments, *Proceedings of Wireless Personal Communications*, pp. 1-15, Jul. 2009.

Juels, A. & Weis, S.A. (2005) Authenticating Pervasive Devices with Human Protocols, *Proceedings of Advances in Cryptology - Crypto*, LNCS 3621, pp. 293-308, Aug. 2005.

Ohkubo, M.; Suzuki, K. & Kinoshita, S. (2003) Cryptographic Approach to "Privacy-Friendly" Tags, *RFID Privacy Workshop*, Nov. 2003.

Paise, R. & Vaudenay, S. (2008) Mutual authentication in RFID: security and privacy, *Proceedings of ACM Symposium on Information, Computer and Communications Security (ASIACCS)*, pp. 292-299, Mar. 2008.

Rotter, P. (2008) A Framework for Assessing RFID System Security and Privacy Risks, *IEEE Pervasive Computing*, Vol. 7, No. 2, pp. 70-77, Apr. 2008.

Rieback, M.R.; Crispo, B. & Tanenbaum, A.S. (2006) The Evolution of RFID Security, *IEEE Pervasive Computing*, Vol. 5, No. 1, pp. 62-69, Jan. 2006.

Tuyls, P. & Batina, L. (2006) RFID-tags for Anti-counterfeiting, *Proceedings of CT-RSA*, LNCS 3860, pp. 115-131, Feb. 2006.

Tsudik, G. (2006) YA-TRAP: Yet Another Trivial RFID Authentication Protocol, *Proceedings of Pervasive Computing and Communications(PerCom) Workshops*, pp. 640-643, Mar. 2006.

Tan, C.; Sheng, B. & Li, Q. (2007) Serverless Search and Authentication Protocols for RFID, *Proceedings of Pervasive Computing and Communications(PerCom) Workshops*, pp. 3-12, Mar. 2007.

Tan, C.; Sheng, B. & Li, Q. (2008) Secure and Serverless RFID Authentication and Search Protocols, *Proceedings of IEEE Transactions on Wireless Communications*, vol. 7, no. 4, pp. 1400-1407, Apr. 2008.

Vaudenay, S. (2007) On Privacy Models for RFID, *Proceedings of Advances in Cryptology - ASIACRYPT*, LNCS 4833, pp. 68-87, Mar. 2007.

Won, T.Y.; Chun, J.Y. & Lee, D.H. (2008) Strong Authentication Protocol for Secure RFID Tag Search Without Help of Central Database, *Proceedings of IEEE/IFIP International Conference on Embedded and Ubiquitous Computing*, Vol. 2, pp. 153-158, Dec. 2008.

OECD (2007) Radio Frequency Identification (RFID): A Focus on Information Security and Privacy, OECD Working Party on Information Security and Privacy, DSTI/ICCP/REG(2007)9/FINAL, 70 pages, Jan. 2008.

Zuo, Y. (2009) Secure and private search protocols for RFID systems, *Information System Frontier*, Vol. 0, pp. 0-0, August. 2009.

# Improving Position Estimation of the RFID Tag Floor Localization with Multiple Recognition Ranges

Youngsu Park, Je Won Lee, Daehyun Kim, Sang-woo Kim
*Electronic and Electric Engineering department, POSTECH*
*Korea, South*

## 1. Introduction

This chapter introduces the RFID tag floor localization method with multiple recognition ranges and its mathematical formulation to improve position estimation accuracy. Using the multiple recognition ranges of RFID reader, the reader can obtain more information about the distances to the tags on the tag floor. The information is used to improve the position estimation performance. At first, this chapter reviews the RFID tag floor localization method with single recognition range for mobile robots(Park et al., 2010) and The performance measure based on the position estimation error variance for the localization method. For the second, this paper extends the mathematical formulation of the localization method and the performance measure for the case of multiple recognition ranges. This work is related to the previous work(Park et al., 2009) that used multiple powers to improve position estimation performance. However, previous work lacks analysis and mathematical formulation of general RFID tag recognition models. We extend the mathematical formulation and the analysis of the single recognition range RFID tag floor localization method (Park et al., 2010) to the multiple recognition range case. Then the minimum error variance of multiple recognition range is introduced as a lower bound of position estimation error variance. Finally, it presents performance improvement of proposed localization method via the Monte-Carlo simulation and simple experiments. The analysis for the simulation and experimental results and the consideration for real application will be given.

This chapter is organized as follows; This section discusses sensor systems used in the mobile robot localization. Then the advantages of the RFID systems as sensor systems for localization are discussed and the researches on the systems are reviewed. Section 2 introduces the RFID tag floor localization, its mathematical formulation and its performance index. Section 3 represents the motivation of introducing the use of multiple recognition ranges for the RFID tag floor localization method, and extend the mathematical formulation and the error variance for the multiple recognition range case. Section 4 conducts the Monte-Carlo simulation to show the improvement of the position estimation performance when the multiple recognition range is used. Section 5 represents experimental results that support the simulation results. In Section 6, the minimum error variance(Park *et al.*, 2010) as a lower bound of error variance is extended to the multiple recognition range case. Section 7 gives the conclusions, discussions and tasks for the further researches.

## 1.1 Sensor systems for indoor mobile robots

The localization is essential problem for the mobile robots to navigate a working area and to accomplish their work. For the localization problem, many researchers used various types of sensor systems to solve it.

The dead reckoning systems utilize the movement of actuators by encoders to estimate the relative changes of position and heading angle(Everett, 1995). However, the sensor systems accumulate the errors that induced by the mismatches between real robot and models, slippage of wheels, and variance of wheel diameter due to the air pressure during the navigation.

The localization systems with inertial navigation system (INS) utilize the linear accelerations and angular velocities of the mobile robot(Borenstein and Feng, 1996). The systems integrate these informations to estimate the current position and the heading angle. The cost of the INS systems was very high and the size was large for the indoor mobile robots, until the advances of the micro-electromechanical systems (MEMS). The MEMS based INS have low cost and small size relative to mechanical INS systems. However, the INS suffers from noise and bias that lead to drift of integrated results (Sasiadek *et al.*, 2000). Some INS packages include magnetic sensors to detect the terrestrial magnetism, to reduce the pose or heading angle error. However, there are many sources that can distort the terrestrial magnetism for indoor environments.

The ultra sonic ranging system and the lager range finder (LRF) are range detecting sensors. The mobile robot matches range information with the map which they have, to estimate their positions. These range sensors can measure the range of objects very accurately. But, under some surface conditions, they can't detect objects and can suffer from multipath problems(Everett, 1995).

The ultra sonic satellite systems, such as CRICKET triangulate a moving node's position with distances from fixed nodes by time of flight(Priyantha, 2005). However, the system is hard to scale up for the large work area and the many mobile robots. When the numbers of fixed nodes and mobile robots are increased, the localization takes longer time due to the arbitration processes.

The radio-frequency-based ranging systems such as chirp spread spectrum (CSS) and received signal strength (RSS) are used for localization of the mobile robots(Inácio *et al.,* 2005; Patwari and Hero III, 2003), however, they have relatively large errors for the indoor mobile robot applications. The ultra-wideband (UWB) communication systems are also used for the indoor localization problem and have good resolution, however, the system cost is still high and each fixed nodes needs to be synchronized by wires(Gezici *et al.*, 2005). Moreover, they use the wide frequency bands that can be the reason of the signal interference, therefore, it requires the permission of the relevant government ministries when it is use.

## 1.2 RFID systems for indoor mobile robots

The RFID based localization systems are also used by several researches to localize the indoor mobile robots. The RFID systems as localization sensor systems for mobile robots have several advantages.

First, the systems are robust to the external environments such as light condition, surface condition of objects, dirts on the landmarks, and distortion of the terrestrial magnetism. Vision-based localization systems suffer from illumination and color changes, bad focused images, image distortions, motion bluer and so forth. The ultra sonic sensor systems and the LRF sensor systems can not detect obstacles or walls, under some surface conditions.

Second, the RFID systems can handle numerous unique landmarks. The landmark is the simplest way to locate the current position, however, the vision sensor based localization

systems have limitations on the numbers of landmarks or features. Moreover, they need heavy image process routines for finding features in images. The RFID tags have their unique identification information in their memories and some of the RFID tags have configurable memories which can be written while or after the landmark installation.

Third, they can handle many tags in a short time. Most of RFID readers are equipped with anti-collision algorithms such as ALOHA, slotted ALOHA, and binary search tree algorithm. It reduces the user's consideration for handling the collisions and arbitrations.

Finally, the installation cost and the maintenance cost of RFID systems are relatively low. The price of tags have been dropping. Nowdays, a 96-bit EPC tags cost 7 to 15 U.S. cents and the EPCglobal tries to reduce the price of tags to 5 cents(RFID journal, nd). After the installation of RFID tags, the efforts to maintain the landmarks are barely needed. These utilize the transmitted power from readers to respond to the reader. They will work normally under harsh conditions.

For these reasons, the RFID systems are used for the mobile robot localization problem by many researchers. Burgard *et al.* (2004) and Kim and Chong (2009) used directional antennas to estimate the current position and target objects. Jia *et al.* (2008) used multiple antennas to locate RFID tags accurately. Ni *et al.* (2004), Shih *et al.* (2006), Zhao *et al.* (2007), and Sue *et al.* (2006) used active RFID tags for indoor localization of target object. Some of them have names such as LANDMARC, VIRE, FLEXOR. Kulyukin *et al.* (2004) and Kulyukin *et al.* (2006) used the passive RFID system with the LRF for guiding visually impaired. Chae and Han (2005) and Kamol *et al.* (2007) used vision information to improve the position estimation performance. Zhou *et al.* (2007) and Zhou and Liu (2007) used active RFID tags that have LEDs on it. Using vision sensors fond the light of tag and aim the laser to the tags to activate it.

## 2. RFID tag floor localization

The RFID tag floor localization method is one of the RFID based localization method that utilize massive passive tags installed on the working area. The RFID readers are attached under the mobile robot's chassis and the tags are placed on the certain points on a working area. While the mobile robot moves, the reader detects tags near the mobile robot and estimates the position from the detected tags' positions. The RFID tag floor localization method has several advantages. It is easy to scale up the work space and number of robots. Most RFID system still need some arbitration process when multiple readers in a work area. However, the antennas for the RFID tag floor localization face down to the floor. Therefore, they need little consideration for the reader arbitration. Moreover, it rarely require maintenance after installation and does not require power to maintain the tag infrastructure.

The concept of the RFID tag floor localization that called the super-distributed RFID infrastructures, is firstly proposed by Bohn and Mattern (2004). They also propose the criteria to classify the tag placement by the density of tags and the regularities of tag positions. Several researchers managed their works to apply the concept to their application and to improve the position estimation accuracy. Park and Hashimoto (2009a) proposed a simple algorithm that combined rotations and linear movements sequentially to reach the goal position. Lee *et al.* (2007) and Park and Hashimoto (2009b) used weighted mean algorithm to estimate the position of mobile robots. Park *et al.* (2010) investigated the performance of the RFID tag floor localization algorithm with various reader recognition ranges and tag placements. Han *et al.* (2007) used a cornering motion to gather information of robot's position and direction. Senta *et al.* (2007) used support vector machine (SVM) to learn the accurate tag positions from

pseudo table of the tag positions. Choi *et al.* (2008) augmented the ultra sonic sensors and the RFID tag floor localization method for efficient localization.

## 2.1 Mathematical formulation of the RFID tag floor localization
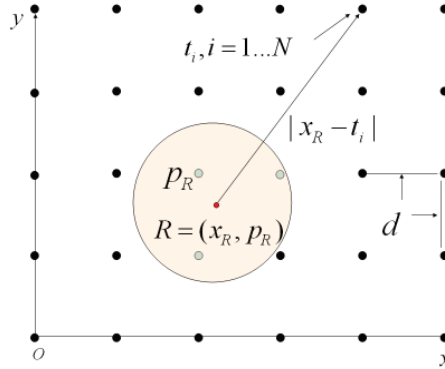


Fig. 1. Concept of the RFID tag floor localization method.

To formulate the RFID tag floor localization (RTFL), it is required to define the representation of the RFID reader and the Tag floor. The RFID reader detects the tags on the RFID tag floor to estimate its position. The RFID tag floor is defined as a set of tags which have their own identities and positions, installed on a work area with some geometric pattern(Fig. 1). The tags are detected by the reader stochastically. The probability of tag recognition can be described as a function of distance and directions between tag and reader. Moreover, the recognition probability is also a function of the RFID reader's transmission power, the number of tags, and other various environmental conditions. Most RFID based localization methods, however, assume that the recognition probability is only a function of distance and the transmission power is fixed for the simplicity of the algorithms.
Therefore, the RFID reader can be described as follows:

$$R = (\mathbf{x}_R, p_R(\cdot)), \tag{1}$$

where $\mathbf{x_R}$ is the position of the RFID reader and $p_R(\cdot)$ is a recognition probability function of distances between the RFID reader and tags.
Tags in tag floor can be described as a tag set $T$,

$$T = \{t_i | i = 1, \cdots, N\}, \tag{2}$$

where $N$ is the number of tags in the tag floor and $t_i$ is the position of $i$-th tag.
The result of a recognition process is a set of recognized tags or combination of tags. This set must be one of subsets of $T$. $Y$ is defined as a set of all subsets of $T$, and it can be expressed as follows:

$$Y = \{\phi, \{t_1\}, \{t_2\}, \cdots, \{t_1, t_2\}, \cdots, T\}, \tag{3}$$

where $\phi$ means the empty set that corresponds to the case in which no tag is recognized. The number of elements of $Y$ is $2^N$.
However, for a recognition function of a reader, many elements of $Y$ have zero probability, or cannot be happened. For example, in large tag floor, tags in rightmost end and leftmost

end cannot be recognized simultaneously. So, $Z$ is defined as the set of elements of $Y$, whose elements are the tag set that can be detected at the same time.

$$
\begin{aligned}
Z &= \{\phi, \{t_1\}, \cdots\} \\
&= \{\phi, z_1, \cdots, z_K\}.
\end{aligned}
$$

(4)
(5)

$K$ is the number of elements of $Z - \{\phi\}$. $\phi$ means the case in which no tag is recognized, but it does not mean that probability is zero. So, $\phi$ is also a element of set of realizable outputs, $Z$. The set $Z$, the set of recognition outputs with nonzero probability, has finite size. In general triangulation problem, there can be additional information such as signal strength, time of flight. However, that the recognition process of RTFL gives only tag's identity and its position. In consequence, only finite number of estimation points can exist. Exactly saying, the number of position estimation points is the same as the number of elements of $Z - \{\phi\}$.

We define the set of mapping or estimation points:

$$
\hat{X} = \{\hat{\mathbf{x}}_1, \cdots, \hat{\mathbf{x}}_K\},
$$

(6)

where $\hat{x}_k$ is position estimation points.

In RTFL, the position estimation using recognition output is mapping from $Z$ to $\hat{X}$,

$$
f : Z - \{\phi\} \to \hat{X},
$$

(7)

$$
f(z_k) = \hat{\mathbf{x}}_k.
$$

(8)

This mapping is called position estimation function. In other words, the estimated point $\hat{\mathbf{x}}_k$ is the representative position of the domain where the recognition output $z_k$ occurs.

## 2.2 Performance index based on position estimation error variance

Main problem in RTFL is making proper position estimation function. To evaluate how proper the function is, performance index is needed. Performance index generally used is average of squared error. The error is difference between the real reader's position and the estimated position. To calculate performance the index, the conditional probability $p(\hat{x}_k|\mathbf{x}_R)$ should be calculated. This probability function represents the probability of detecting the tags, $z_k$, corresponding to the mapping point, $\hat{\mathbf{x}}_k$, when the tag is on the position $\hat{\mathbf{x}}_R$. It can be described as follows:

$$
p(\hat{x}_k|\mathbf{x}_R) = \prod_{t_i \in z_k} p(t_i|\mathbf{x}_R) \times \prod_{t_j \in z_k^c} (1 - p(t_j|\mathbf{x}_R)),
$$

(9)

where $p(t_i|\mathbf{x_R})$ is the probability function in which tag $t_i$ is detected if the reader is on a position $\mathbf{x_R}$. If there is proper number of RFID tags, the recognition probability of a tag is independent of other tags.

Using the conditional probability, the expected value of squared error in position $\mathbf{x}_R$ can be calculated as follows:

$$
V_{\mathbf{x}_R} = \sum_{\hat{\mathbf{x}}_k \in \hat{X}} |\mathbf{x}_R - \hat{\mathbf{x}}_k|^2 p(\hat{\mathbf{x}}_k|\mathbf{x}_R).
$$

(10)

The average of squared error, or the error variance, as a performance index is an average of the expected value over the domain of the RFID tag floor. It can be expressed as follows:

$$V \quad = \quad \frac{1}{W} \iint_W V_{\mathbf{x}_R} dx dy \tag{11}$$

$$= \quad \frac{1}{W} \sum_{\hat{\mathbf{x}}_k \in \hat{X}} \iint_W |\mathbf{x}_R - \hat{\mathbf{x}}_k|^2 p(\hat{\mathbf{x}}_k | \mathbf{x}_R) dx dy, \tag{12}$$

where $W$ is the work area. By using the performance index, the optimal estimation position set can be found. Moreover, the accuracy of various position estimation functions can be evaluated by the performance index. In general, mean based or weighted mean based position estimation functions are used in RFID tag floor localization method.

Another aspect of the performance of the RFID tag floor localization is the success rate. The success rate means the ratio of successful localization. The localization fails if there is no detected tag by the reader. The success rate, however, is not dependent on a position estimation function, but the recognition range and distance of grids. For the continuous localization and for avoiding the localization failure, the reader recognition range should contain at least one tag for every position of reader on the work area.

## 3. RFID tag floor localization with multiple recognition ranges

Most of UHF RFID readers can control power of transmission signal by changing the antenna attenuation of readers Narayanan *et al.* (2005) and it means the reader can change recognition range shown as (Fig.2). We can obtain more information about the distances between reader and tags with multiple power, that is multiple recognition ranges. With low transmission power, only the tags near the reader are detected. The recognition range is increased as the transmission power is increased. By giving more weight for the estimated positions for the lower power, the position estimation error can be reduced.

In previous studies such as the study of Luo *et al.* (2007), multiple power is just used for robust recognition of tag but not used for nearness information. In the studies of Park et al.(2009), they use the nearness information obtained by multiple recognition range to improve the position estimation.

### 3.1 Mathematical formulation of RFID tag floor localization with multiple recognition ranges

Multiple recognition ranges mean that there are multiple recognition probability functions. We can extend the description of the RFID reader of with single recognition range to the multiple recognition ranges as follows:

$$R = (\mathbf{x}_R, \{p_R^m(\cdot) | m = 1, 2, \cdots, M\}), \tag{13}$$

where $M$ is the number of the ranges and $p_m^R(\cdot)$s are corresponding recognition functions. Also, there exist $M$ sets of recognition outputs with nonzero probability, or $Z$.

$$Z^m \quad = \quad \{z_0^m, \cdots, z_{K_m}^m\}, \tag{14}$$

$$= \quad \{z_k^m | k = 0, 1, \cdots, K_m\}, \tag{15}$$

where $z_0^m = \phi$ and $z^m$ is a possible recognition output with nonzero probability at $m$-th recognition range. As like single range case, output of recognition process with $m$-th range is one of elements of $Z^m$. $K_m$ is the number of possible elements at the $m$-th range.
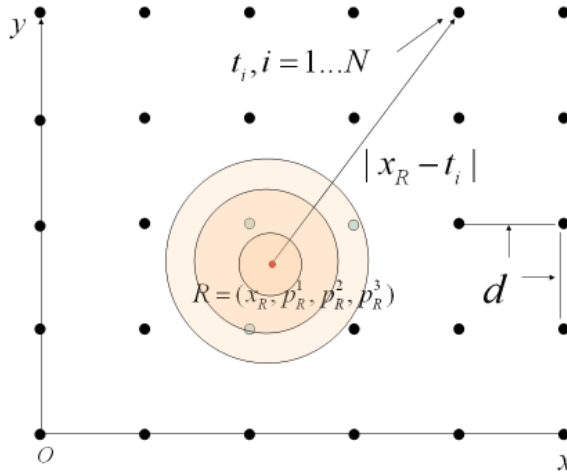
Fig. 2. The concept of the RFID tag floor localization method with multiple recognition ranges.

Define a set $\bar{Q}$ as follows:

$$\bar{Q} = \{(z^1, z^2, \cdots, z^m, \cdots, z^M) | z^1 \in Z^1, z^2 \in Z^2, \cdots, z^M \in Z^M\}. \tag{16}$$

Hence, recognition output with multiple recognition ranges must be one of elements of $\bar{Q}$. But, some elements of $\bar{Q}$ cannot happen. $Q$ is defined as a sub set of $\bar{Q}$ whose elements are occurred with nonzero probability. Then,

$$Q = \{q_0, q_1, \cdots, q_l, \cdots, q_L\}, \tag{17}$$

where,

$$q_0 = \{\phi^1, \phi^2, \cdots, \phi^M\}. \tag{18}$$

$q_0$ means that there is no recognized tag in recognition process for all recognition ranges. $L$ is the number of all possible combination of tags for the multiple recognition ranges.

In RTFL with multiple recognition ranges, elements of $Q$ instead of $Z$ are the outputs of recognition process. The others are the same as the things in recognition process with single recognition range as follows:

$$\hat{X}_M = \{\hat{x}_1, \hat{x}_2, \cdots, \hat{x}_l, \cdots \hat{x}_L\}, \tag{19}$$

$$f_M : Q - \{q_0\} \rightarrow \hat{X}_M, \tag{20}$$

where $M$ is the number of recognition ranges .

Generally, the size of $Q$ is much larger than the size of $Z$. So, there are much more estimated points in multiple ranges case and each estimated point is representative to narrower area. In result, error variance is smaller than error variance of single range, it means accuracy of position estimation is improved.

### 3.2 Performance indexes for position estimation performance

In multiple ranges case, definition of error variance is the same as the definition in single range case as follows:

$$V \quad = \quad \frac{1}{W} \sum_{\hat{\mathbf{x}}_k \in \hat{X}_M} \iint_W |\hat{\mathbf{x}}_k - \mathbf{x}_R|^2 p(\hat{\mathbf{x}}_k|\mathbf{x}_R) dx dy. \tag{21}$$

However, as using $Q$ instead of $Z$, calculating $p(\hat{x}_k|x_R)$ need modification as follows:

$$p(\hat{\mathbf{x}}_l|\mathbf{x}_R) = \prod_{z^m \in q_l} \big( \prod_{t_i \in z^m} p_R^m(t_j|\mathbf{x_R}) \quad \times \prod_{t_j \in (z^m)^c} (1 - p_R^m(t_j|\mathbf{x_R}) \,), \tag{22}$$

Multiple recognition ranges give good success rate as well as accuracy improvement. The accuracy improvement will be verified by simulations and experiments in Section 4 and Section 5.

## 4. Simulation for the two RFID tag floor localization methods

This section provides and compares the simulation results for the tag floor localization method and the method with multiple recognition ranges to show the performance improvement of the proposed method. The Monte-Carlo method is used for the simulation and the position estimation error variance is used as a performance index.

### 4.1 Simulation settings
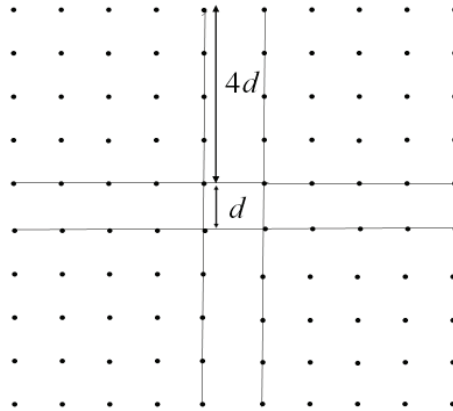


Fig. 3. The tag grid used for the RFID tag floor localization simulation.

For this simulation, $9 \times 9$ tag grid is used as shown in Fig. 3. To compare the two type of RFID tag floor localization methods, 400,000 sample points are generated in the $1 \times 1$ center grid cell. The approximation of the position estimation error variance is calculated as following equation:

$$\hat{V}(\mathbf{x_R}) = \frac{1}{M-1} \sum_{j=1}^{M} | \mathbf{x_{R,j}} - \mathbf{x_{k,j}} |^2. \tag{23}$$

The $M$ is the number of samples that succeed to detect at lease one tag. If the recognition range is small, there may be no detected tag, and we call that the sample is failure point. The rate of failure is also one of the performance index for the position estimation as mentioned before.

If the sample point succeed to detect a tag set or tag sets with multiple recognition ranges, the estimation point is determined by the position mapping function. For the single recognition range case, the estimation point is determined by $f(z_{k,j}) = \hat{\mathbf{x}}_{\mathbf{R},\mathbf{j}} = \mathbf{x}_{\mathbf{k},\mathbf{j}}$. In this simulation, we take mean of the detected tag positions to estimate the reader position. For the multiple recognition range case, we use following position estimation function: $f_M(q_{l,j}) = \hat{\mathbf{x}}_{\mathbf{R},\mathbf{j}} = \mathbf{x}_{\mathbf{k},\mathbf{j}}$. In this simulation, the mean value of the mean position of recognized tags for each level is used for position estimation function.

In general, the recognition range of a tag from the position of RFID reader can not be defined clearly, since the probability of a tag recognition gradually decreases from a certain range near the recognition boundary. However, the recognition model $p_R(\cdot)$ used in this section is circular model as follows, for simplicity of the simulation:

$$p_R(\mathbf{x_i} \mid \mathbf{x_R}) = \begin{cases} 1 & \text{for } \mid \mathbf{x_i} - \mathbf{x_R} \mid \leq r \\ 0 & \text{for } \mid \mathbf{x_i} - \mathbf{x_R} \mid > r. \end{cases} \tag{24}$$

The recognition ranges $r$ changed from 0.5 to 4.0. For the multiple recognition range case, the number of recognition ranges is 3 and the recognition range set $(r_1, r_2, r_3)$ is defined $(0.3r, 0.7r, r)$.

### 4.2 Simulation results

Figure 4 and 5 shows the simulation results. Figure 4 represents the error variances of position estimation. The line and broken line respectively represents the approximation of position estimation error variance of the RFID tag floor localization method and the method with multiple recognition ranges. It shows the improvement of the position estimation performance when the multiple recognition ranges are used. Both error variances are
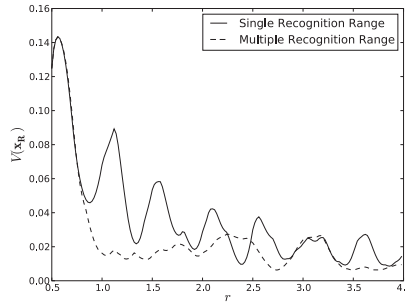


Fig. 4. The position estimation error variance of the RFID tag floor localization methods.

decreasing as the recognition range is increasing. The reason of the decrease of the error variance is the increase of the number of the estimation or mapping points. For the larger recognition range, the more tags are detected by the RFID reader. Figure 5 shows the number of the mapping points. The numbers of mapping points increase as the recognition range increase. Each mapping point corresponds a partition that divided by the recognition boundaries. If the number of partitions increases, the error variance is decreased. In Fig.
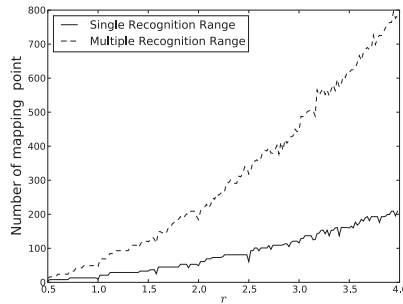
Fig. 5. The number of mapping points that corresponds the number of the detected tag combinations.

5, we can find the fluctuations on the error variances. The reason of the fluctuations is the balance between each partitions. If the partitions are relatively even, the error variance is low, otherwise, the error variance is high. More illustrative explanation will be given in Section 6.

## 5. Experimental results of multiple recognition range RFID tag floor localization

This section provides the experimental results that support the performance improvement of the proposed RFID tag floor localization method with multiple recognition ranges. The settings for the experiment of the tag floor localization methods are explained. Then, the result of experiment is processed with random sampling algorithm to get meaningful data. Finally, the meaning of the results are discussed.

### 5.1 Experimental settings
In this experiment, $9 \times 9$ tags were placed with the 20cm$\times$20cm grid. And the reader detected the nearby tags at every 2cm grid points inside the 65cm$\times$62cm work area of the experimental equipment. At each point, the reader changed the transmission power from 15dBm to 25dBm by 1dBm and read the tags 10 times for each power.
After gathering the sample data, we used random sampling algorithm to process the data. For each point, the recognition probability of each tag was defined by the data. Then, at each sample point, tags were detected with the recognition probability and conducted the position estimation process based on it. It was repeated 1000 times at each sample points.
Figure 6 shows the equipments and setting that we used in this experiment. Figure 6(a) is the experimental equipment. It was made by wood to avoid the effects of metallic objects on the RFID reader performance. It can move the reader along $x$ and $y$ direction with 2mm accuracy in the 65cm$\times$62cm work area. Figure 6(b) shows the tag placement and Fig. 6(c) represents the tags used in this experiment. All of the tags were aligned with one direction to reduce directional difference of tag antenna sensitivity. However, the directional sensitivity of the tag in this experiment was not significant and was ignorable. Next subsection will illustrate the recognition of the tag and other sticker type tags. Figure 6(d) is the small portable type RFID reader that can alter its transmission power from 15dBm to 30dBm. The antenna was 8cm$\times$8cm ceramic antenna and faced down to the floor at the 10cm above the floor.

(a) The experimental equipment.



(b) Tag placement for the experiment.



(c) The UHF RFID with casing
tag(CONFIDEX
MICRO).



(d) The portable UHF RFID readers
STEELWAVE used in the experiment.
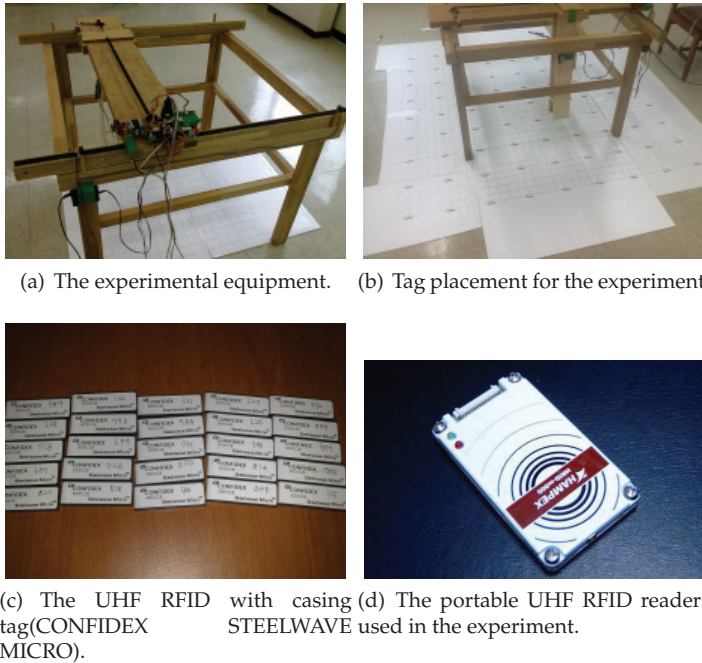
Fig. 6. The experimental settings.

## 5.2 Experimental results for localization

Figure 7 shows the recognition ranges of a tag used in the experiment with different RFID reader transmission powers. We can find that the recognition range increases according to the power. The patterns are slightly ellipsoidal shape, however, we fit these patterns to circles and estimate the recognition ranges. Figure 8 represents the fitting result. The relation between the reader transmission power and the reader recognition range seems to be linear, but we can not have strong confidence to the linear relation in this experiment. Moreover, under the different conditions such as different tags, antennas and height of antenna from the floor, different relation can be found.

However, due to the relation linear like relation, Fig. 9, the error distance which is the square root of the error variance can be interpreted without additional works. The relative recognition range with respect to the tag grid (20cm) is (0.25,0.9). The simulation results that we conducted have the data from recognition range is 0.5. Therefore, we can find the trend of the position estimation error variance in Fig. 9 shows similar trends of the position estimation error variance in Fig. 4 only in the range of 0.5 to 0.9. But the rest of recognition range need more investigation. However, due to the relation linear like ship, Fig. 9, the error distance which is the square root of the error variance can be interpreted without additional works. The relative recognition range with respect to the tag grid (20cm) is (0.25,0.9). The simulation results that we have starts from 0.5. Therefore, we can find the trend of Fig. 9 shows similar trends of the position estimation error variance in Fig. 4 in the range of 0.5 to 0.9. But the rest of recognition range need more investigation.

Figure 11 and Fig. 12 show the recognition ranges of other tags. The tags placed each conner of the work area of the experimental equipment . The recognition data is sampled with

power: 15,tag: 705 / (a) 15dBm
power: 16,tag: 705 / (b) 16dBm
power: 19,tag: 705 / (c) 17dBm
power: 25,tag: 705 / (d) 18dBm
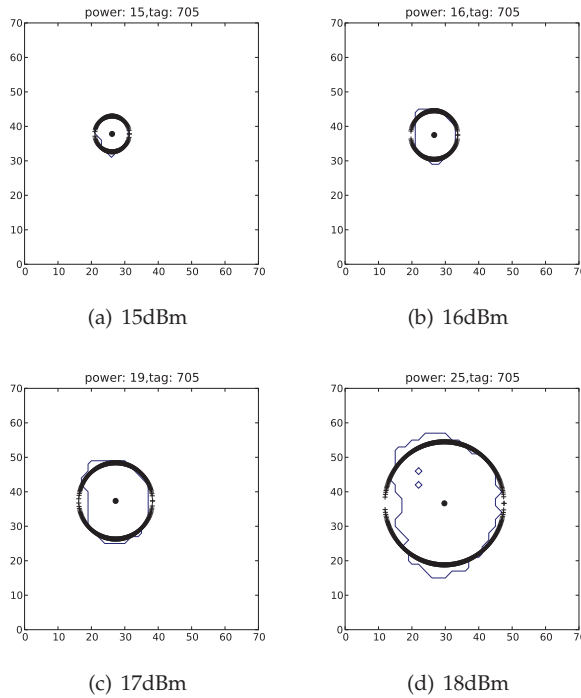
Fig. 7. A Recognition range of a tag with different transmission powers.
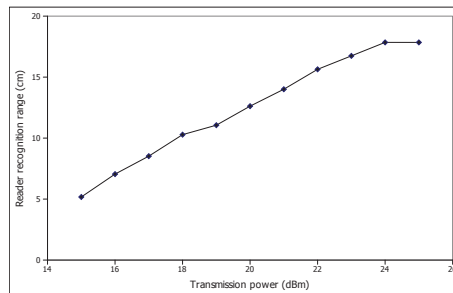


Fig. 8. Experimental result of the relation between reader transmission power and reader recognition range

5cm×5cm grid. These are "Inray" sticker type UHF RFID tags with 7cm×1.7cm dimension. The tags have supreme recognition ranges. At the power of 15dBm, their recognition range are already over 50cm. Long recognition range is good for the tag installation cost. However, these tags have irregular recognition patterns and large difference of recognition ranges between each tags. Tags of "Inray" types are hard to used for the RFID tag floor localization. Figure 10 represents the fail rate which is the ratio of the number of samples that failed to recognize tags, to the sample points. For the small powers, due to the small recognition
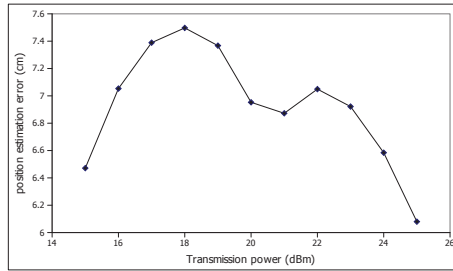
Fig. 9. Experimental result of the relation between the position estimation error(square root of the position estimation error variance) and the reader transmission power.
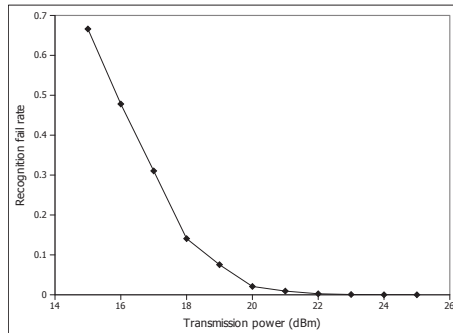


Fig. 10. Experimental result of recognition fail rate for the experiment.
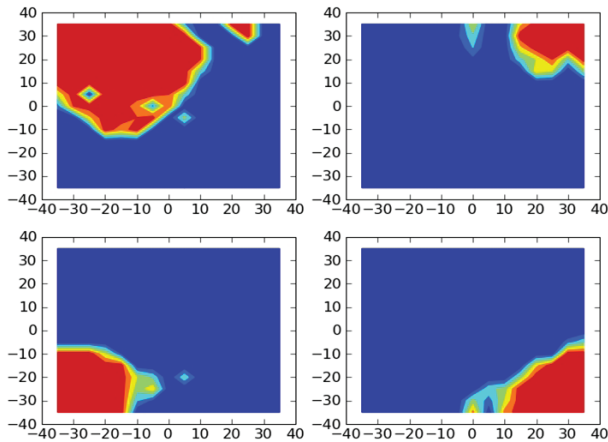


Fig. 11. The recognition patterns of a "Inray" type tags with 15dBm transmission power of RFID reader

ranges, the fail rate is high. High fail rate reads to error accumulation during the mobile robot navigation application .

Table 1 shows the results of the random sampling post process of the acquired data previously mentioned. We use three power levels for the multiple recognition ranges. However, in
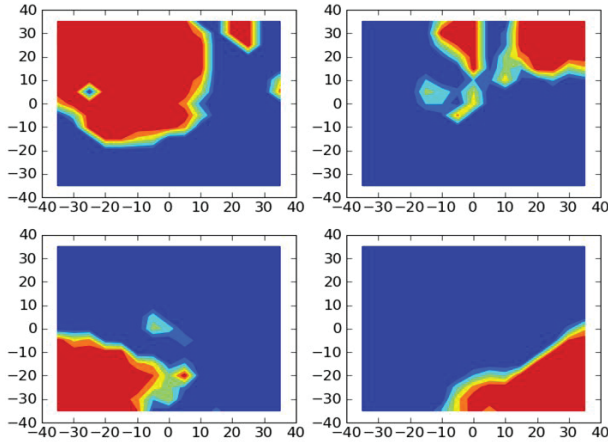
Fig. 12. The recognition patterns of a "Inray" type tags with 17dBm transmission power of RFID reader

| Power combination(dBm) | Position estimation error(cm) | fail rate |
|---|---|---|
| (15,15,15) | 6.471 | 0.6661 |
| (16,16,16) | 7.053 | 0.4781 |
| (17,17,17) | 7.389 | 0.3104 |
| (18,18,18) | 7.497 | 0.1407 |
| (19,19,19) | 7.367 | 0.0754 |
| (20,20,20) | 6.953 | 0.0209 |
| (21,21,21) | 6.872 | 0.0093 |
| (22,22,22) | 7.049 | 0.0025 |
| (23,23,23) | 6.922 | 0.0007 |
| (24,24,24) | 6.584 | 3.9E-005 |
| (25,25,25) | 6.080 | 2.7E-005 |
| (16,19,25) | 5.590 | 0.0009 |
| (15,20,25) | 5.634 | 0.0005 |
| (15,19,25) | 5.650 | 0.0011 |
| (15,18,25) | 5.674 | 0.0012 |

Table 1. The experimental results after the random sampling post process of the acquired data. The position estimation errors are shown in cm.

real applications, the number of power levels and the combination of powers should be determined with various considerations. The first eleven rows in Table 1 can be seen as the result of the RFID tag floor localization with single recognition range. Since the multiple sampling reduces the sample error variance, we used three same power levels for the single power case, for the fair comparison with multiple recognition range case. The last four rows represent the RFID tag floor localization method with multiple recognition ranges. The combinations of the powers are selected by the position estimation errors.

We can see that the position estimation errors with the multiple recognition ranges are smaller than the position estimation errors with single power. The recognition fail rates are smaller than single recognition range cases with powers under 23dBm. The improvement of position

estimation error of (16,19,25) case with respect to (25,25,25) is about 8%. Moreover, it can save the energy of the RFID reader.

## 6. Minimum variance of position estimation as a bound of error



(a) Single power ($r = 0.76$)



(b) Single power ($r = 1.12$)



(c) Multiple power ($r = 0.76$)



(d) Multiple power ($r = 1.12$)
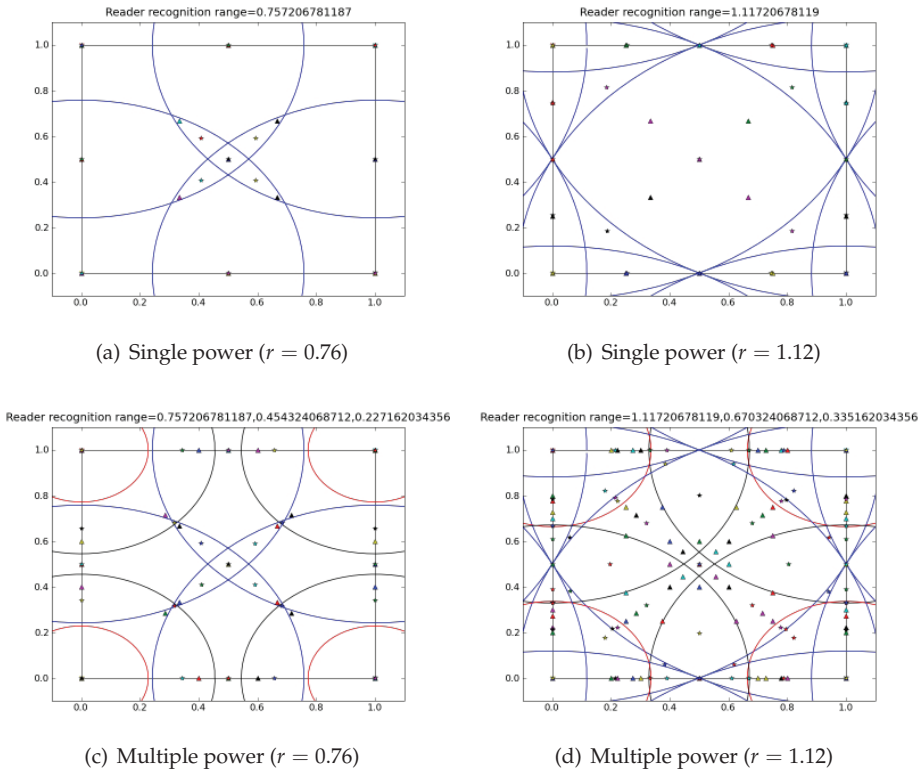
Fig. 13. Mapping points by the mean method and minimum variance method.

In this section, we will introduce the minimum variance of position estimation as the bound of the position estimation error and extend it to the multiple recognition range case. Figure 13 shows the motivation of introducing the minimum variance of position estimation. As the recognition range also grows, the number of mapping points that correspond to the partitions is grows. As the number of partitions grows and the balance between each partitions are more even, the position estimation error variance gets smaller.

In each figure in Fig 13, the $\triangle$ marks represent the mapping points produced by the mean algorithm and the $\star$ marks represent the mapping points produced by the minimum variance criteria. The mapping points based on the mean algorithm does not changed even if the recognition range is changed. Moreover, for the some recognition ranges such as $r = 1, 12$ in Fig. 13(b), the mapping points are out of their corresponding partitions. It leads to increase of the error variance. If the mapping points are on the center of mass of the each partitions,
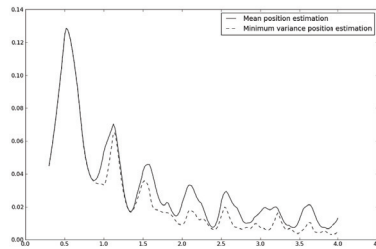
Fig. 14. The error variance and the minimum error variance of single power case.
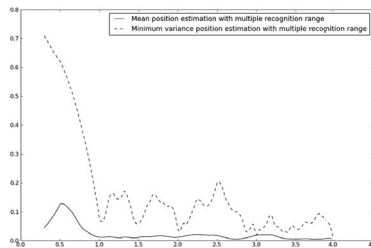


Fig. 15. The error variance and the minimum error variance of multiple power case.

the position estimation error variance will be minimized and it is the motivation of minimum error variance of position estimation.

However, in general, to find the minimum variance error bound analytically is not easy. We used the Monte-Carlo simulation to find the minimum variance of position estimation of RFID tag floor localization methods. The simulation setting is the same as Section 4.1. In addition, we calculate the center of mass and the variances of the sample point of each partitions. The results are represented in Fig. 14 and Fig. 15.

The minimum error variance can be used for the bound of position estimation error. The position estimation based on the minimum variance mapping point has lower error variance than the mean based position estimation. However, to find the minimum variance mapping points, we should know exact recognition model of tags and properties of tags in the tag floor must be even. The approximation of the dual problem of the minimum variance position estimation can be found in (Bouet and Pujolle, 2009a;b). They estimated the moving RFID tag with the fixed tags by approximating the center of mass with the virtual RFID tags.

## 7. Conclusion

In this chapter, we reviewed the researches on the RFID based localization methods, especially the RFID tag floor localization methods. Then we introduced the mathematical formulation of the RFID tag floor localization method and its performance index based on the position estimation error variance. Moreover, we extend it to the multiple recognition range case. Then, the improvement of the RFID tag floor localization system with multiple recognition ranges is shown by the simulation results and the experimental results. And we extend the error bound to the multiple recognition range case.

However, for the practical application of mobile robots, we need to solve some problems. There are still little researches on the effects of chassis, wheels, and metallic object on the floor on recognition. Antenna emission patterns of the tags and the readers need to be studied more and controlled for some ranges. Moreover, researches on effects of and counter plans to irregularities of tags are required.

## 8. References

Bohn, J. and Mattern, F. (2004). Super-distributed RFID tag infrastructures. *Lecture notes in computer science*, pages 1–12.

Borenstein, J. and Feng, L. (1996). Gyrodometry: A new method for combining data from gyros and odometry in mobile robots. *Ann Arbor*, 1001, 48109–2110.

Bouet, M. and Pujolle, G. (2009a). L-VIRT: a 3-D range-free localization method for RFID tags based on virtual landmarks and mobile readers. In *Proceedings of the 6th IEEE Conference on Consumer Communications and Networking Conference*, pages 159–163. Institute of Electrical and Electronics Engineers Inc., The.

Bouet, M. and Pujolle, G. (2009b). L-VIRT: Range-free 3-D localization of RFID tags based on topological constraints. *Computer Communications*, 32(13-14), 1485–1494.

Burgard, D., Fox, D., and Philipose, K. (2004). Mapping and localization with RFID technology. In *IEEE International Conference on Robotics and Automation*, pages 1015–1020.

Chae, H. and Han, K. (2005). Combination of rfid and vision for mobile robot localization. pages 75 – 80.

Choi, B., Lee, J., and Lee, J. (2008). An improved localization system with RFID technology for a mobile robot. In *34th Annual Conference of IEEE Industrial Electronics, 2008. IECON 2008*, pages 3409–3413.

Everett, H. (1995). *Sensors for mobile robots: theory and application*. AK Peters, Ltd.

Gezici, S., Tian, Z., Giannakis, G., Kobayashi, H., Molisch, A., Poor, H., and Sahinoglu, Z. (2005). Localization via ultra-wideband radios. *IEEE Signal Processing Magazine*, 22(4), 70.

Han, S., Lim, H., and Lee, J. (2007). An efficient localization scheme for a differential-driving mobile robot based on RFID system. *IEEE Transactions on Industrial Electronics*, 54(6), 3362–3369.

Inácio, J., Gerald, J., and Ortigueira, M. (2005). New PN even balanced sequences for spread-spectrum systems. *EURASIP Journal on Wireless Communications and Networking*, 2005(3), 458.

Jia, S., Sheng, J., and Takase, K. (2008). Improvement of performance of localization id tag using multi-antenna rfid system. pages 1715 –1718.

Kamol, P., Nikolaidis, S., Ueda, R., and Arai, T. (2007). Rfid based object localization system using ceiling cameras with particle filter. *Future Generation Communication and Networking*, 2, 37–42.

Kim, M. and Chong, N. Y. (2009). Direction sensing rfid reader for mobile robot navigation. *Automation Science and Engineering, IEEE Transactions on*, 6(1), 44 –54.

Kulyukin, V., Gharpure, C., Nicholson, J., and Pavithran, S. (2004). RFID in robot-assisted indoor navigation for the visually impaired. In *2004 IEEE/RSJ International Conference on Intelligent Robots and Systems, 2004.(IROS 2004). Proceedings*, pages 1979–1984.

Kulyukin, V., Gharpure, C., Nicholson, J., and Osborne, G. (2006). Robot-assisted wayfinding for the visually impaired in structured indoor environments. *Autonomous Robots*, 21(1), 29–41.

Lee, H.-J., Kim, M. S., and Lee, M. C. (2007). Technique to correct the localization error of the mobile robot positioning system using an rfid. pages 1506 –1511.

Luo, R., Chuang, C.-T., and Huang, S.-S. (2007). Rfid-based indoor antenna localization system using passive tag and variable rf-attenuation. pages 2254 –2259.

Narayanan K., Ramakrishnan M., and Dr. Demarest K. (2005). Performance Benchmarks for Passive UHF RFID Tags by,

Ni, L., Liu, Y., Lau, Y., and Patil, A. (2004). LANDMARC: indoor location sensing using active RFID. *Wireless Networks*, 10(6), 701–710.

Park, S. and Hashimoto, S. (2009a). Autonomous mobile robot navigation using passive rfid in indoor environment. *Industrial Electronics, IEEE Transactions on*, 56(7), 2366 –2373.

Park, S. and Hashimoto, S. (2009b). Indoor localization for autonomous mobile robot based on passive RFID. In *Proceedings of the 2008 IEEE International Conference on Robotics and Biomimetics*, pages 1856–1861. IEEE Computer Society.

Park, Y., Lee, J., and Kim, S. (2009). Improving position estimation on RFID tag floor localization using RFID reader transmission power control. In *Proceedings of the 2008 IEEE International Conference on Robotics and Biomimetics*, pages 1716–1721. IEEE Computer Society.

Park, Y., Lee, J. W., Kim, D., Jeong, J. J., and Kim, S.-W. (2010). Mathematical formuation of rfid tag floor based localization and performance analysis for tag placement. ICARCV 2010, Singapore.

Patwari, N. and Hero III, A. (2003). Using proximity and quantized RSS for sensor localization in wireless networks. In *Proceedings of the 2nd ACM international conference on Wireless sensor networks and applications*, pages 20–29. ACM.

Priyantha, N. (2005). *The cricket indoor location system*. Ph.D. thesis, Citeseer.

RFID journal (n.d.). Frequently asked questions: The cost of rfid equipment. http://www.rfidjournal.com/faq/20.

Sasiadek, J., Wang, Q., and Zeremba, M. (2000). Fuzzy adaptive Kalman filtering for INS/GPS data fusion. In *Proceedings of the 15th IEEE International Symposium on Intelligent Control*, pages 17–19. Rio, Patras, GREECE.

Senta, Y., Kimuro, Y., Takarabe, S., and Hasegawa, T. (2007). Machine learning approach to self-localization of mobile robots using rfid tag. pages 1 –6.

Shih, S.-T., Hsieh, K., and Chen, P.-Y. (2006). An improvement approach of indoor location sensing using active rfid. *Innovative Computing ,Information and Control, International Conference on*, 2, 453–456.

Sue, K., Tsai, C., and Lin, M. (2006). FLEXOR: A flexible localization scheme based on RFID. *Information Networking. Advances in Data Communications and Wireless Networks*, pages 306–316.

Zhao, Y., Liu, Y., and Ni, L. M. (2007). Vire: Active rfid-based localization using virtual reference elimination. *Parallel Processing, International Conference on*, 0, 56.

Zhou, Y. and Liu, W. (2007). Preliminary research on indoor mobile robot localization using laser-activated rfid. pages 78 –85.

Zhou, Y., Liu, W., and Huang, P. (2007). Laser-activated rfid-based indoor localization system for mobile robots. pages 4600 –4605.

# Pseudorandom Tag Arrangement for Accurate RFID based Mobile Robot Localization

Sungbok Kim and Hyunbin Kim
*Department of Digital Information Engineering*
*Hankuk University of Foreign Studies*
*Republic of Korea*

## 1. Introduction

The localization of a mobile robot is one key ingredient for autonomous navigation, along with map building and obstacle detection/avoidance (Borenstein, J., et al., 1996). Several sensors have long been used for mobile robot localization, but all of them are confronted with their own inherent limitations. Encoder suffers from error accumulation, ultrasonic/laser sensor demands the line of sight, camera expends complicated processing, and GPS works at low resolution. To cope with these problems of typical sensors, new attempts have been made, which use the RFID system consisting of tags, antenna, and reader for mobile robot localization (Finkenzeller, K., 2000).

There have been two different research groups of working on the RFID based mobile robot localization. Both groups assume that a set of tags storing the absolute positional information are deployed throughout a navigation environment. In one group, either active or passive tags are installed along the wall and they are used as beacons or landmarks to guide the navigation of a mobile robot (Kubitz, O., et al., 1997; Kantor, G., et al., 2002; Hahnel, D., et al., 2004; Kulyukin, V., et al., 2004; Penttila, K., et al., 2004; Yamano, K., et al., 2004; Kim, B.K., et al., 2006; Vorst, P., et al., 2008). However, in the other group, passive tags are installed on the floor and they are used to indicate the current position of a mobile robot (Bohn, J., et al., 2004; Choi, J., et al., 2006; Kim, B.K., et al., 2006; Han, S., et al., 2007; Kodaka, K., et al., 2008). This paper belongs to the latter group.

When an antenna senses a tag on the floor, there involves the positional uncertainty within the sensing range, which degrades the performance of RFID based mobile robot localization. One simple way of alleviating such a limitation may be to increase the tag distribution density on the floor. If more than one tag is sensed by an antenna at one instant, the current position of a mobile robot can be estimated more accurately by utilizing multiple tag readings (Han, S., et al., 2007; Kodaka, K., et al., 2008). However, the increased tag distribution density may be accompanied by the economical problem of high tag installation cost and the technical problem of incorrect tag readings.

For a given tag distribution density, the performance of RFID based mobile robot localization is affected by how a set of tags are arranged over the floor. There have been a variety of tag arrangements considered so far, which can be categorized into three repetitive arrangements, including square, parallelogram, and tilted square. Depending on the

localization method, the tag arrangement can be optimized for improved localization performance. It is claimed that the triangular pattern is optimal in (Han, S., et al, 2007).

In this paper, we present a pseudorandom RFID tag arrangement for improved performance of mobile robot localization. This paper is organized as follows. With the underlying assumptions, Section 2 describes a mobile robot localization method using spatial and temporal information. Section 3 examines four repetitive tag arrangements, including square, parallelogram, tilted square, and equilateral triangle, in terms of tag installation and tag invisibility. Inspired from the Sudoku puzzle, Section 4 proposes the pseudorandom tag arrangement for reduced tag invisibility without increased installation difficulty. Section 5 gives some experimental results. Finally, the conclusion is made in Section 6.

## 2. Mobile robot localization

In RFID based mobile robot localization, a mobile robot equipped with an antenna at the bottom navigates over the floor covered with a set of tags. As a mobile robot moves around, an antenna often senses tags that are located within the sensing range. For simplicity, let us assume that the sensing range of an antenna is circular and the shape of a tag is a point. For explanation, it is convenient to exchange the roles between antenna and tag, in such a way that a point shape antenna passes through the circular range of a sensed tag. This is illustrated in Fig. 1.
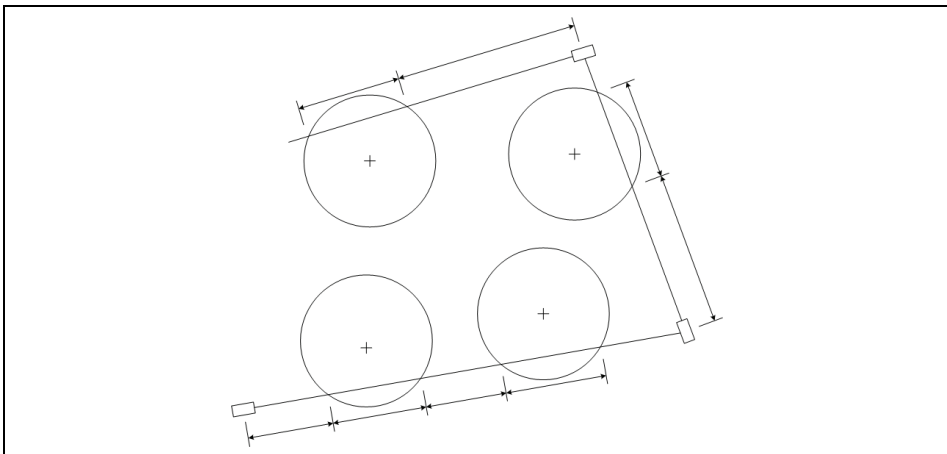


Fig. 1. Mobile robot trajectory over the floor covered with tags

The number of tags sensed by an antenna at one instant is assumed to be either one or zero. This assumption of low tag distribution density will be valid especially for lower end personal/service robots in home/office environments. Next, a mobile robot is assumed to travel along a trajectory consisting of a series of linear segments, as shown in Fig. 1. For each linear segment, a mobile robot standing still at the beginning changes the steering angle, then forwards at a constant speed, and finally stops at the end. It is also assumed that a mobile robot moves at a human walking speed, so that the time required for self-rotation or acceleration/deceleration is negligible compared with the constant speed line traveling time along the linear segment.

## 2.1 Velocity estimation

Fig. 2 depicts the situation where a mobile robot initially standing at a priori known position moves straight across the sensing range of a tag at a constant speed. Let us consider the mobile robot localization under this situation, which is effective for all but first linear segment. Suppose that a pair of temporal information on the traverse of a mobile robot across the sensing range are given: the elapse time from starting to entering and the elapse time from entering and exiting. Given these two timing information, the velocity of a mobile robot, that is, the steering angle and the forwarding speed, can be determined. Note that there are two constraints for two unknowns.

For convenience, the local coordinate system is introduced, in such a way that the tag position is defined as the coordinate origin, $O = \begin{bmatrix} 0 & 0 \end{bmatrix}^t$, and the starting position is defined at $A = \begin{bmatrix} -l & 0 \end{bmatrix}^t$, as shown in Fig. 2. Let $r$ be the radius of the circular sensing range centered at a tag. Let $t_1$ be the elapse time during which a mobile robot starts to move and then reaches the sensing range. Let $t_2$ be the elapse time during which a mobile robot enters into the sensing range and then exits out of it. Let $\theta (= \angle OAB)$ be the steering angle of a mobile robot, and $v$ be the forwarding speed along the linear segment. Let us denote $\overline{OA} = l$, $\overline{OB} = \overline{OC} = r$, $\overline{OF} = c$, $\overline{AB} = a (= vt_1)$, and $\overline{BC} = b (= vt_2)$.
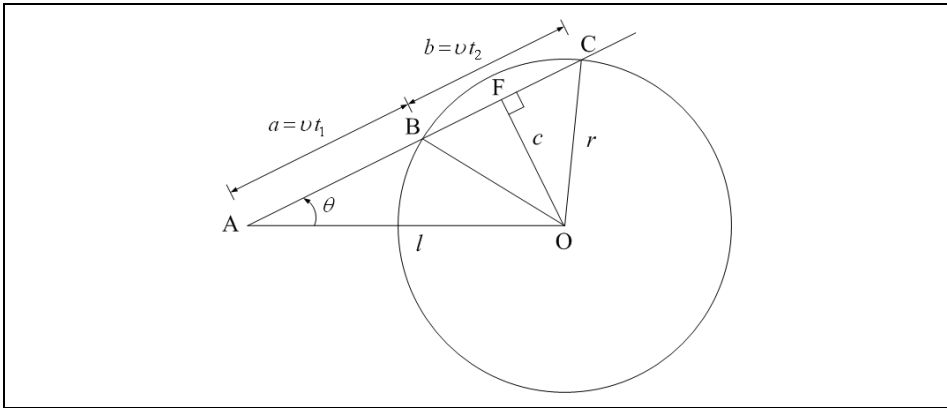


Fig. 2. Mobile robot traversing across tag sensing range

First, from $\triangle OAF$ and $\triangle OBF$, using Pythagoras' theorem,

$$l^2 = c^2 + \left( a + \frac{b}{2} \right)^2 \tag{1}$$

$$r^2 = c^2 + \left( \frac{b}{2} \right)^2 \tag{2}$$

From (1) and (2), we can have

$$a(a+b) = l^2 - r^2 \tag{3}$$

so that the forwarding speed, $v$, of a mobile robot can be obtained by

$$v^2 = \frac{l^2 - r^2}{(t_1 + t_2)t_1} \tag{4}$$

where $a = vt_1$ and $b = vt_2$ are used.

Once $v$ is known using (4), applying the law of cosines to $\Delta OAB$, the steering angle, , of a mobile robot can be determined:

$$\cos\theta = \frac{(vt_1)^2 + l^2 - r^2}{2(vt_1)l} \tag{5}$$

which leads to

$$\theta = \text{atan2}(\pm\sqrt{1 - \cos^2\theta}, \cos\theta) \tag{6}$$

Seen from (6), there are two solutions of $\theta$, which are illustrated in Fig. 3. Although both solutions are mathematically valid, only one of them can be physically true as the velocity of a mobile robot. This solution duplicity should be resolved to uniquely determine the velocity of a mobile robot. One way of resolving the solution duplicity is to utilize the information from the encoders that are readily available. For instance, the estimated steering angle using the encoder readings can be used as the reference to choose the true solution out of two possible solution.
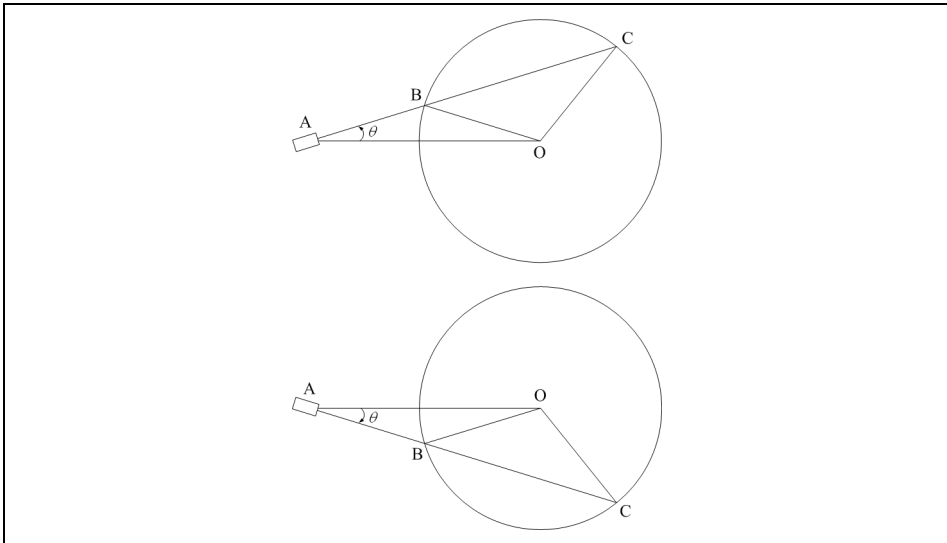


Fig. 3. Solution duplicity of mobile robot velocity

Let us briefly discuss the case where the starting position of a mobile robot is not known a priori, which is true for the first linear segment, that is, at the start of navigation. Now, there are four unknowns: two for the starting position and two for the velocity, which implies that four constraints are required. One simple way of providing four constraints is to command a mobile robot to move straight at a constant speed across the sensing ranges of two tags, as shown in Fig. 4. The detailed procedure will be omitted in this paper, due to space limit.
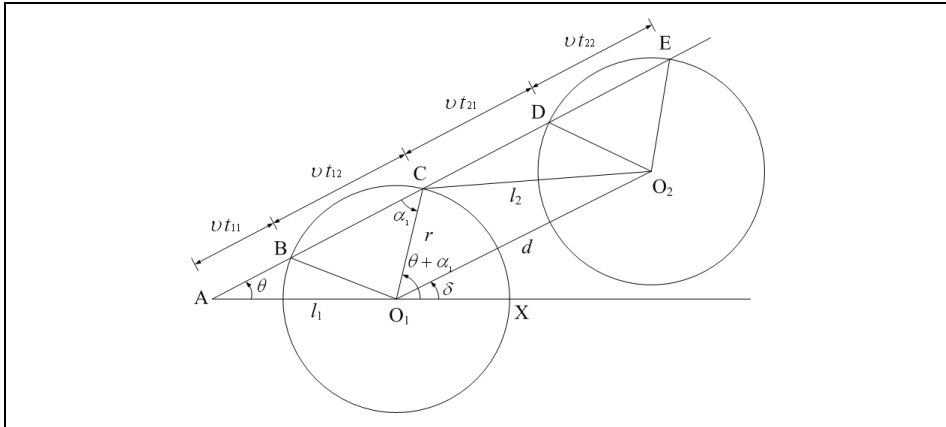
Fig. 4. Velocity estimation for the first linear segment

## 2.2 Position estimation

At each sampling instant, the current position of a mobile robot will be updated using the velocity information obtained at the previous sampling instant. Unfortunately, this implies that the RFID based mobile robot localization proposed in this paper suffers from the positional error accumulation, like a conventional encoder based localization. However, in the case of RFID based localization, the positional error does not keep increasing over time but is reduced to a certain bound at each tag traversing. Under a normal floor condition, RFID based localization will work better than encoder based localization in term of positional uncertainty, while the reverse is true in terms of positional accuracy.

## 3. Repetitive tag arrangements

The performance of RFID based mobile robot localization is heavily dependent on how densely tags are distributed over the floor and how they are arranged over the floor. As the tag distribution density increases, more tag readings can be used for mobile robot localization, leading to better accuracy of localization. However, the increased tag distribution density may cause the economical problem of excessive tag installation cost as well as the technical problem of duplicated tag readings.

For a given tag distribution density, the tag arrangement over the floor affects the performance of RFID based mobile robot localization. Several tag arrangements have been considered so far, however, they can be categorized into four repetitive arrangements, including square, parallelogram, tilted square, and equilateral triangle. For a given tag distribution density, it is claimed that the tag arrangement can be optimized for improved mobile robot localization, which depends on the localization method used (Han, S., et al., 2007; Choi, J., et al., 2006).

### 3.1 Tag installation

One important consideration in determining the tag arrangement should be how easily a set of tags can be installed over the floor. Practically, it is very difficult or almost impossible to precisely attach many tags right on their respective locations one by one. To alleviate the

difficulty in tag installation, two step procedure can be suggested. First, attach each group of tags on a square or rectangular tile in a designated pattern. Then, place the resulting square tiles on the floor in a certain repetitive manner.

First, consider the case in which a group of four tags are placed on a square tile of side length of $2s(\geq 4r)$, where $r$ is the radius of the circular tag sensing range, under the restriction that all four sensing ranges lie within a square tiles without overlapping among them. Note that the maximum number of tags sensed at one instant is assumed to be one in this paper. Fig. 5 shows three square tag patterns, including square, parallelogram, and tilted square. Fig. 5a) shows the square pattern, where four tags are located at the centers of four quadrants of a square tile.
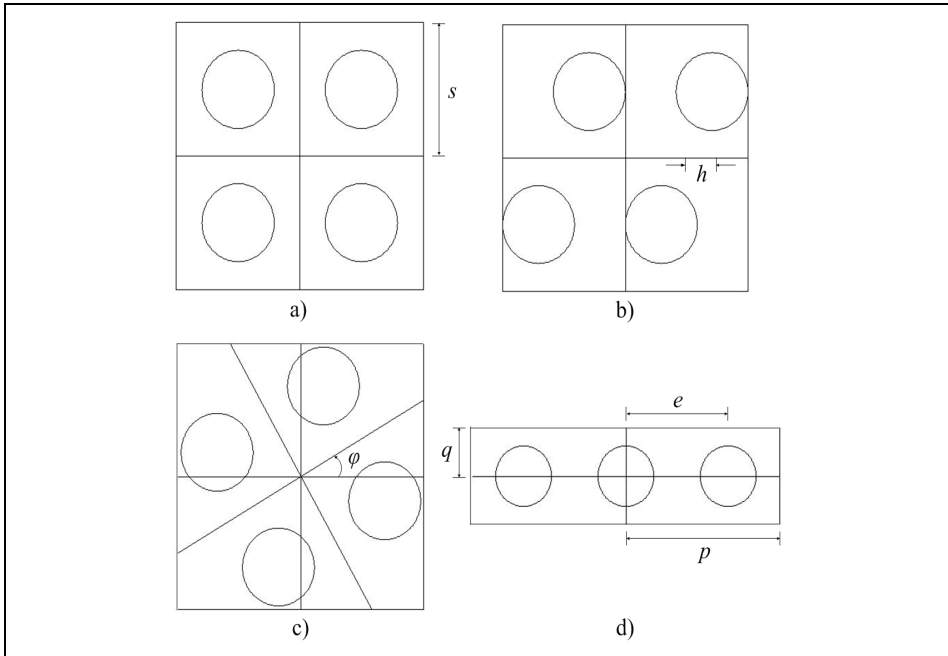


Fig. 5. Four tag patterns: a) square, b) parallelogram, c) tilted square, and d) line

Fig. 5b) shows the parallelogram pattern, which can be obtained from the square pattern shown in Fig. 5a) by shifting upper two tags to the right and lower two tags to the left, respectively. The degree of slanting, denoted by $h$, is the design parameter of the parallelogram pattern. In the case of $h = \frac{s}{4}$, the parallelogram pattern becomes an isosceles triangular pattern (Han, S., et al., 2007). And, in the case of $h = 0$, the parallelogram pattern reduces to the square pattern.

Fig. 5c) shows the tilted square pattern (Choi, J., et al., 2006), which can be obtained by rotating the square pattern shown in Fig. 5a). The angle of rotation, denoted by $\varphi$, is the design parameter of the tilted square pattern. Note that the tilted square pattern returns to the square pattern in the case of $\varphi = 0, \frac{\pi}{2}$.

Next, consider the case in which a group of three tags are placed in a line on a rectangular tile of side lengths of $2p\,(\geq 6r)$ and $2q\,(\geq 2r)$, under the same restriction imposed on three square tag patterns above. Fig. 5d) shows the line tag pattern. For later use in equilateral triangular pattern generation, we set

$$2p = 3e$$
$$2q = \frac{\sqrt{3}}{2}e \tag{7}$$

where $e$ denotes the tag spacing, that is, the distance between two adjacent tags. For the line pattern to have the same tag distribution density as three square patterns,

$$4s^2 : 4pq \; = \; 4 : 3 \tag{8}$$

From (7) and (8), it can be obtained that

$$e^2 = \frac{2}{\sqrt{3}}s^2 \tag{9}$$

Fig. 6 shows four different tag arrangements, each of which results from placing the corresponding tag pattern in a certain repetitive manner.
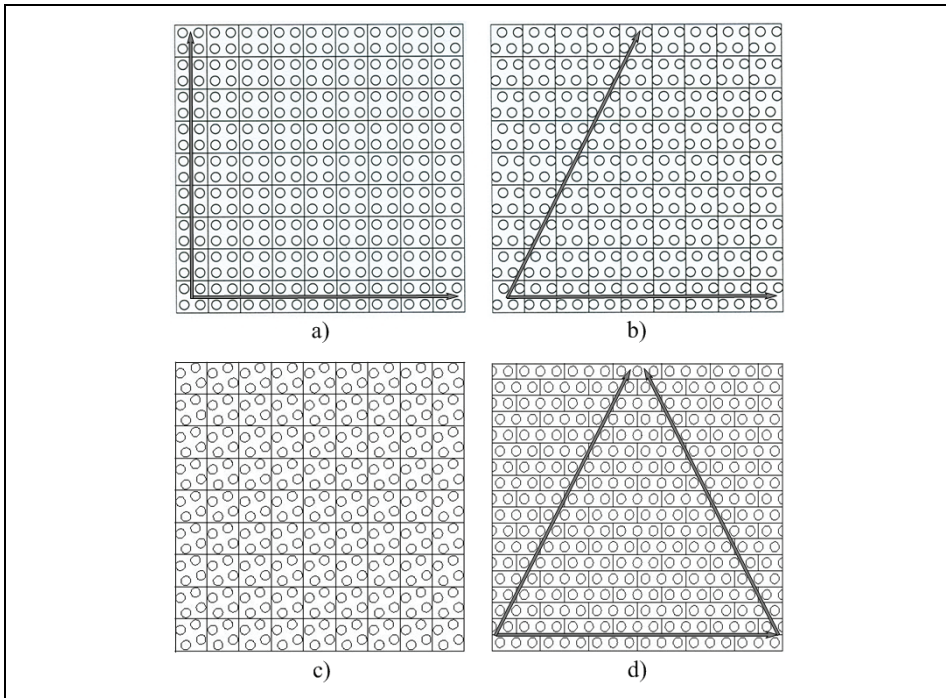


Fig. 6. Four repetitive tag arrangements: a) square, b) parallelogram, c) tilted square, and d) equilateral triangle

### 3.2 Tag invisibility

In RFID based mobile robot localization, it may happen that an antenna cannot have a chance to sense any tag during navigation, referred here to as the tag invisibility. If the tag invisibility persists for a long time, it may lead a mobile robot astray, resulting in the failure of RFID based localization. The tag invisibility should be one critical factor that needs to be taken into account in determining the tag arrangement. For a given tag distribution density, it will be desirable to make the tag visibility, which is the reverse of tag invisibility, evenly for all directions rather than being biased in some directions.

The square and the parallelogram tag arrangements, shown in Fig. 6a) and Fig. 6b), have been most widely used. In the case of square arrangement, tags cannot be sensed at all while a mobile robot moves along either horizontal or vertical directions. As the sensing radius is smaller compared to the tag spacing, the problem of tag invisibility becomes more serious. In the case of parallelogram arrangement, the problem of tag invisibility still exists along two but nonorthogonal directions, which results in a slightly better situation compared with the case of square arrangement. One the other hand, in the case of tilted square tag arrangement, shown in Fig. 6c), the situation gets better along both horizontal and vertical directions. Finally, in the case of equilateral triangular tag arrangement, shown in Fig. 6d), the problem of tag invisibility exists along three equiangular directions, however, the range of tag invisibility becomes smaller compared to the cases of both square and the parallelogram arrangements.

## 4. Pseudorandom tag arrangement

To significantly reduce the tag invisibility in all directions, the random tag arrangement, shown in Fig. 7, seems to be best. Note that each four tags are placed on a square tile under the same restriction imposed on three square tag patterns shown in Fig. 5. Due to highly expected installation difficulty, however, it is hard to select the random tag arrangement in practice.

Taking into account both tag invisibility and installation difficulty, a pseudorandom tag arrangement is proposed using a set of different tilted squares that have different angles of rotation, shown in Fig. 5c). It is expected that the proposed pseudorandom tag arrangement exhibit randomness to some extent without increasing the difficulty in installation.



a)                                    b)
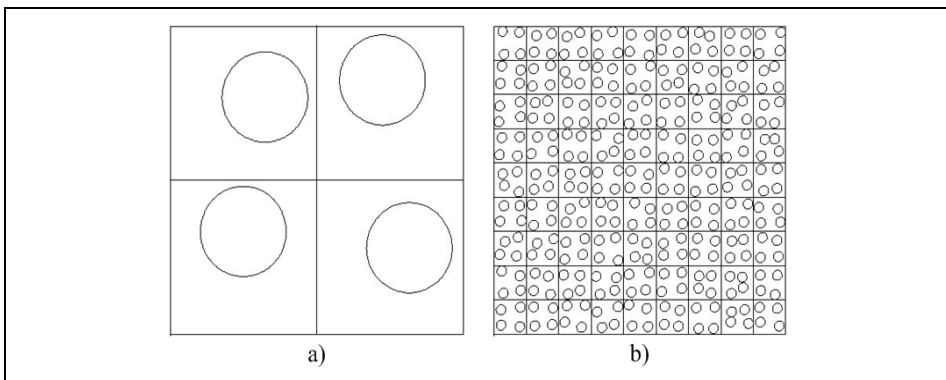
Fig. 7. Random tag arrangement: a) random pattern and b) random arrangement

First, let us define a set of nine different tilted square tag patterns as follows. Since the rotation by 90° makes the resulting tilted pattern back to the original one, we propose to use the set of discrete angles of rotation, given by

$$\Phi_K = (K-1)\frac{\pi}{2}\frac{1}{9} = (K-1)\frac{\pi}{18}, \qquad K = 1, \cdots, 9 \qquad (10)$$

where $K = 1$ corresponds to the square pattern shown in Fig. 5a). Fig. 8 shows the set of nine different tilted square patterns, given by (10). After making nine copies of each set of nine different tilted square tag patterns, we place them on the floor side by side, according to the number placement in the Sudoku puzzle. In the Sudoku puzzle, the numbers '1' through '9' should be placed in a 9×9 array without any duplication along horizontal, vertical, and diagonal directions.



Fig. 8. The set of nine different tilted square patterns



Fig. 9. Pseudorandom tag arrangement: a) one solution to the Sudoku puzzle and b) the corresponding tag arrangement

Fig. 9 shows one solution to the Sudoku puzzle and the corresponding tag arrangement. Compared to the random tag arrangement shown in Fig. 7b), it can be observed that the tag arrangement shown in Fig. 9b) exhibits randomness successively, which is called the pseudorandom tag arrangement.

## 5. Experimental results

In our experiments, a commercial passive RFID system from Inside Contactless Inc. is used, which consists of M300-2G RFID reader, circular loop antenna, and ISO 15693 13.56 MHz coin type tags. Fig. 10 shows our experimental RFID based localization system, in which the reader and the antenna are placed, respectively, on the top and at the bottom of a circular shaped mobile robot. The antenna is installed at the height of 1.5 cm from the floor, and the effective sensing radius is found to be about 10 cm through experiment. For experimental flexibility, each tag is given a unique identification number, which can be readily mapped to the absolute positional information.



Fig. 10. The experimental RFID based localization system

As a mobile robot navigates over the floor covered with tags, the antenna reads the positional information from the tag within the sensing region, which is then sent to the reader through the coaxial cable. The reader transmits the positional data to the notebook computer at the rate of 115200 bps through RS-232 serial cable. Using a sequence of received data, the notebook computer executes the embedded mobile robot localization algorithm described in this paper.

To demonstrate the validity and performance of our RFID based mobile robot localization, extensive test drives were performed. First, Fig. 11 shows the pseudorandom tag arrangement on the floor that is used in our experiments. For easy installation, each four tags having 10 cm sensing radius are attached on a 70×70 cm square tile in a titled square pattern. With different angles of rotation, given by (10), nine different square tiles are constructed and their copies are made. Then, a total of sixteen square tiles are placed side by side in a 4×4 array, resulting in a 280×280 cm floor with the pseudorandom tag

arrangement. At each test drive, a mobile robot is to travel along a right angled triangular path shown in Fig. 11, where two perpendicular sides are set to be parallel to the $x$ axis and the $y$ axis. A mobile robot is commanded at a constant speed of 10 cm/sec along three linear segments, starting from (30,30), passing through (250,250) and (250,30), and returning to (30,30).
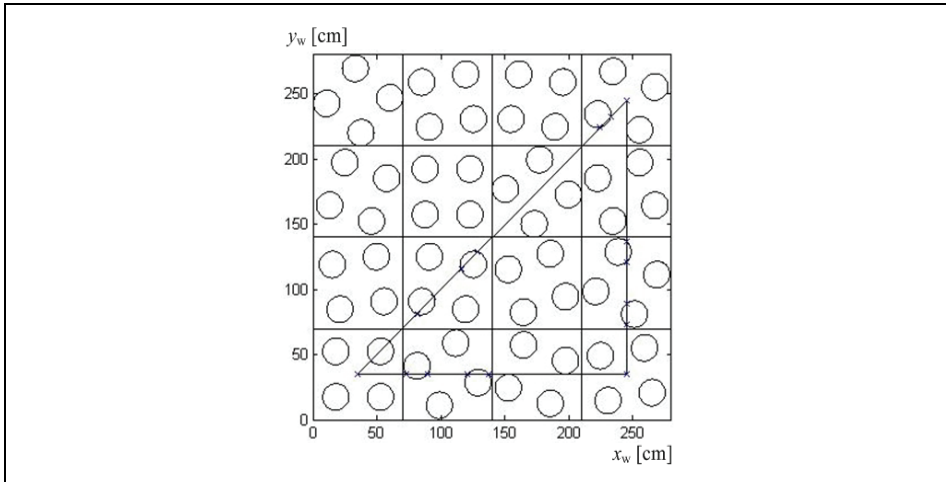


Fig. 11. The experimental pseudorandom tag arrangement and the closed path trajectory
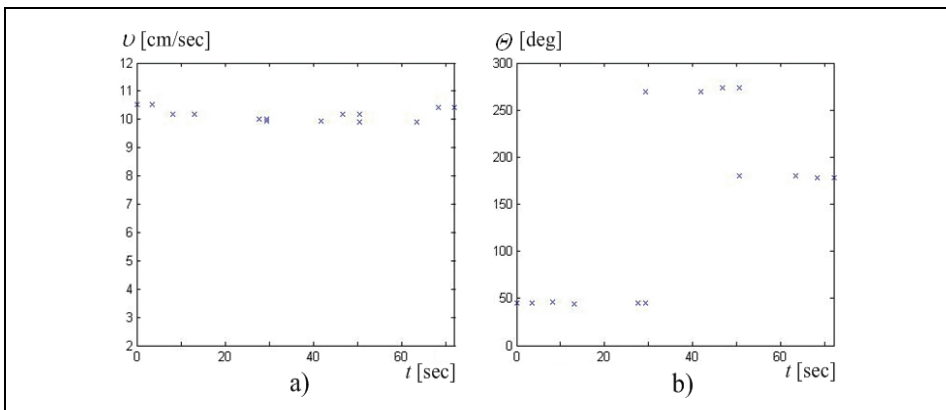


Fig. 12. The mobile robot velocity estimates: a) the forwarding speed and b) the steering angle

Fig. 12 shows the componentwise plots of the estimated mobile robot velocities along the right angled triangular path, obtained based on (4) and (6). Small difference between the estimated and the actual mobile robot velocities can observed, which seem to be largely attributed to measurement noises involved. Next, Fig. 13 shows the componentwise plots of the estimated mobile robot positions along the right angled triangular path, which are computed from the mobile robot velocity estimates. The deviations from the actual mobile

robot positions are also plotted in Fig. 13, which are again relatively small. Fig. 14 shows the estimated and the actual mobile robot trajectories on the floor, marked by 'x', and 'o', respectively. It can be observed that the estimated mobile robot trajectory is fairly close to the actual one.
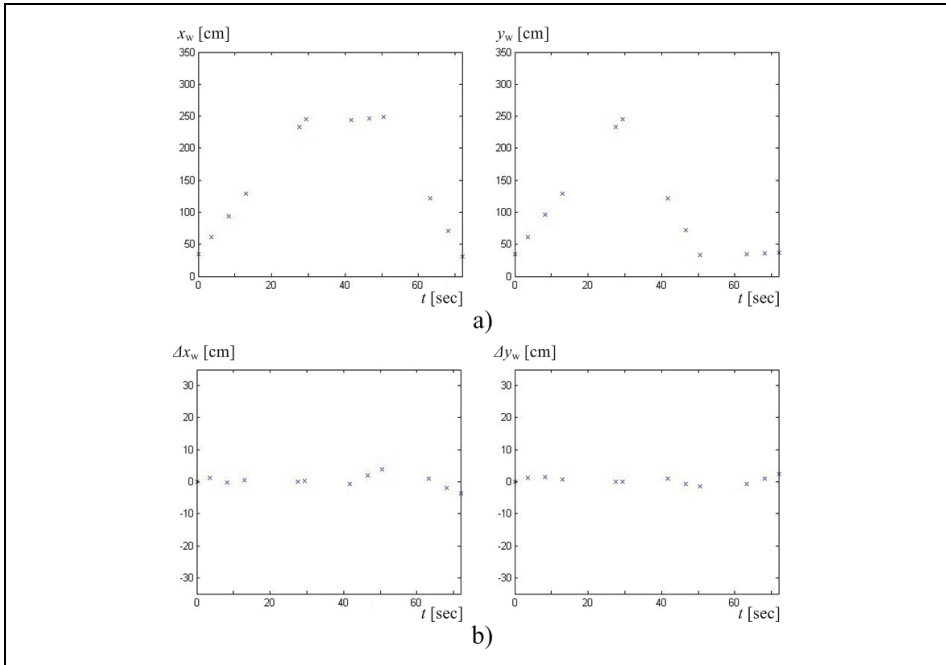


Fig. 13. The mobile robot localization: a) the componentwise positional estimates and b) the deviations from the actual values
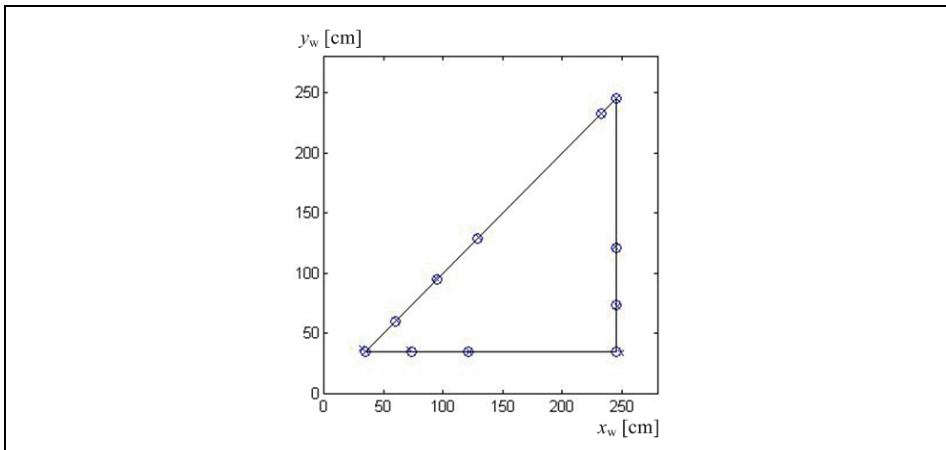


Fig. 14. The estimated trajectory, marked by 'x', and the actual trajectory, marked by 'o'

Finally, the same test drive above was repeated 50 times to see how closely a mobile robot can return to the starting position after the closed path navigation. Fig. 15 shows the plot of the positional homing errors, which are the differences of the returning positions from the starting position. It can be observed that the positional homing errors are kept less than 5 cm. Considering that the tag distribution density is relatively low, this result seems quite satisfactory.
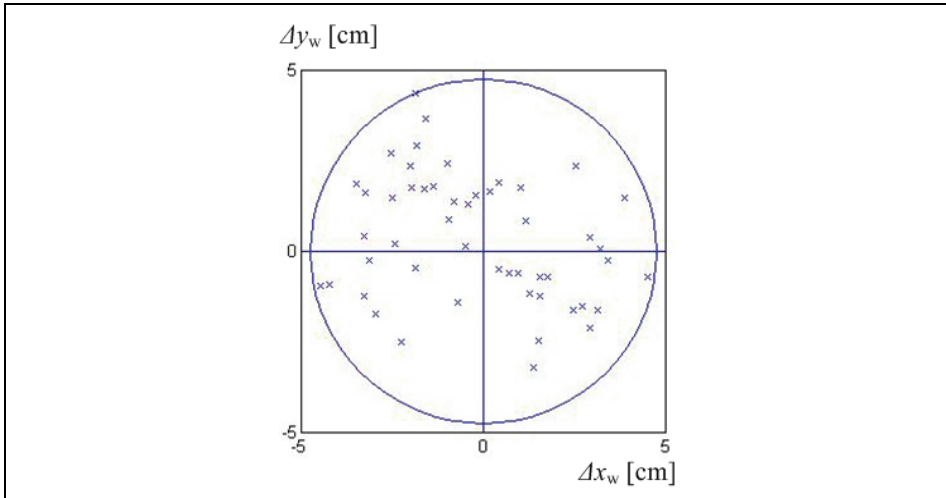


Fig. 15. The positional homing errors after the closed path navigations

## 6. Conclusion

This paper presented a pseudorandom RFID tag arrangement for improved performance of mobile robot localization. First, using temporal as well as spatial information on tag traversing, we developed a simple but effective mobile robot localization method. Second, we examined four repetitive tag arrangements, including square, parallelogram, tilted square, and equilateral triangle, in terms of tag installation and tag invisibility. Third, taking into account both tag invisibility and tag installation, we proposed the pseudorandom tag arrangement, inspired from the Sudoku puzzle. Currently, a study is under way for the quantitative evaluation and optimal design of tag arrangements. We hope that the results of this paper can provide an effective solution to the indoor localization of personal/service robots.

## 7. Acknowledgement

## 8. References

Borenstein, J., Everett, H. R., & Feng, L. (1996). Where am I? Sensors and Methods for Mobile Robot Positioning, The University of Michigan

Finkenzeller, K. (2000). RFID handbook: Fundamentals and Applications, Wiley.

Kubitz, O., Berger, M. O., Perlick, M. & Dumoulin, R. (1997). Application of radio frequency identification devices to support navigation of autonomous mobile robots, Proc. IEEE Vehicular Technology Conf., pp. 126-130

Kantor, G. & Singh, S. (2002). Preliminary results in read-only localization and mapping, Proc. IEEE Int. Conf. Robotics and Automation, pp. 1818-1823

Hahnel, D., Burgard, W., Fox, D., Fishkin, K., & Philipose, M. (2004). Mapping and localization with RFID technology, Proc. IEEE Int. Conf. Robotics and Automation, pp. 1015-1020

Kulyukin, V, Gharpure, C., Nicholson, J. & Pavithran, S. (2004). RFID in robot-assisted indoor navigation for the visually impaired, Proc. IEEE/RSJ Int. Conf. Intelligent Robots and Systems, pp. 1979-1984

Penttila, K., Sydanheimo, L. & Kivikoski, M. (2004). Performance development of a high-speed automatic object identification using passive RFID technology, Proc. IEEE Int. Conf. Robotics and Automation, pp. 4864-4868

Yamano, K., Tanaka, K., Hirayama, M., Kondo, E., Kimura, Y., & Matsumoto, M. (2004). Self-localization of mobile robots with RFID system by using support vector machine, Proc. IEEE/RSJ Int. Conf. Intelligent Robots and Systems, pp. 3756-3761

Kim, B.K., Tomokuni, N., Ohara, K., Tanikawa, T., Ohba, K., & Hirai, S. (2006). Ubiquitous localization and mapping for robots with ambient intelligence, Proc. IEEE/RSJ Int. Conf. Intelligent Robots and Systems, pp. 4809-4814

Vorst, P., Schneegans, S., Yang, B., & Zell, A. (2008). Self-localization with RFID snapshots in densely tagged environments, Proc. IEEE/RSJ Int. Conf. Intelligent Robots and Systems, pp. 1353-1358

Bohn, J. and Mattern, F. (2004). Super-distributed RFID tag infrastructure, Lecture Notes in Computer Science, vol. 3295, pp. 1-12

Choi, J., Oh, D., & Kim, S. (2006). CPR Localization Using the RFID Tag-Floor, Lecture Notes in Computer Science, vol. 4099, pp. 870-874

Han, S., Lim, H., & Lee, J. (2007). An Efficient Localization Scheme for a Differential-Driving Mobile Robot Based on RFID System, IEEE Trans. Industrial Electronics, vol. 54, no. 6, pp. 3362-3369

Kodaka, K., Niwa, H., Sakamoto, Y., Otake, M., Kanemori, Y., & Sugano, S. (2008). Pose estimation of a mobile robot on a lattice of RFID tags, Proc. IEEE/RSJ Int. Conf. Intelligent Robots and Systems, pp. 1385-1390

# RFID Tags to Aid Detection of Buried Unexploded Ordnance

Keith Shubert and Richard Davis
*Battelle Memorial Institute*
*United States*

## 1. Introduction

Detecting buried unexploded ordnance (UXO) at military firing ranges and elsewhere is very difficult and expensive. To enable the military to conduct cost-effective training and research missions in the future, with increased safety for personnel and property without negative environmental impact, significant advances in detection and identification of buried UXO must be pursued and implemented.

This chapter presents the results of analytical and experimental efforts that demonstrated the viability of using munition-mounted radio frequency identification (RFID) tags as buried ordnance detection and identification aids. RFID tagging of ordnance can provide a high probability of detection and a near-zero false alarm rate. The tag provides discrimination between UXO and clutter items, a capability that is critical to reducing the cost of UXO remediation. This work was pursued because state-of-the-art passive RFID tags can potentially provide information on the munitions' locations while maintaining compatibility with operational deployment. To ensure success, however, detection range below the ground had to be investigated quantitatively.

The analysis was performed in the context of a UXO searching process that included the movement of the transmit and receive coils in pre-defined lanes across a large land parcel. The term "overlap" refers to the amount of overlap in two adjacent search lanes, i.e., the portion of area retraced by the coil. This planned movement of the interrogation system's transmit and receive coils will reduce the impact of isolated nulls or minima within the field patterns at both the tag and receive coil locations.

The operational concept calls for fastening tags to the exterior of candidate ordnance item as part of the manufacturing process. During the detection segment of the UXO remediation process, the UXO interrogation module provides energy to the tag by emitting a large magnetic field. The munition-mounted tag responds by emitting a low-level digital signal that is sensed by receivers on the UXO interrogation module. This research focused on low-frequency, passive (non-battery) RFID tags, a choice made early in the investigation. Extensive modeling of the RFID tag on the metal munition was performed to aid in understanding the tag mounting parameters. The critical mounting concern is the required separation between the tag and the metal of the munition because the customer required detection of munitions buried as deep as one meter. For safety reasons, the transmitting coil and RFID tag must be shown not to induce a large electric field near the munition because too large a field might cause the munition to detonate.

## 2. Background

Various methods for detecting buried unexploded ordnance at military firing ranges have been investigated (GAO, 2004), (Halman, et al., 1998). These techniques involve scattering energy off the munition and resolving the modified signal. Unfortunately, achieving consistent results using these methods has proved to be difficult and expensive. The techniques have also resulted in an unacceptable number of false-positive indications that will significantly increase the cost of remediation because of the expense of excavating non-UXO items. Using RFID tags, false alarms can occur only when a munition explodes and the RFID tag survives. This event is thought to have such a low likelihood of occurring that a statistical investigation of this scenario was not performed.

The method examined here differs from previous methods in that detection of the munition is based on the energy received from a transmitting RFID tag affixed to the munition, as depicted in Figure 1. The detection signal does not result from energy scattered by the munition itself.
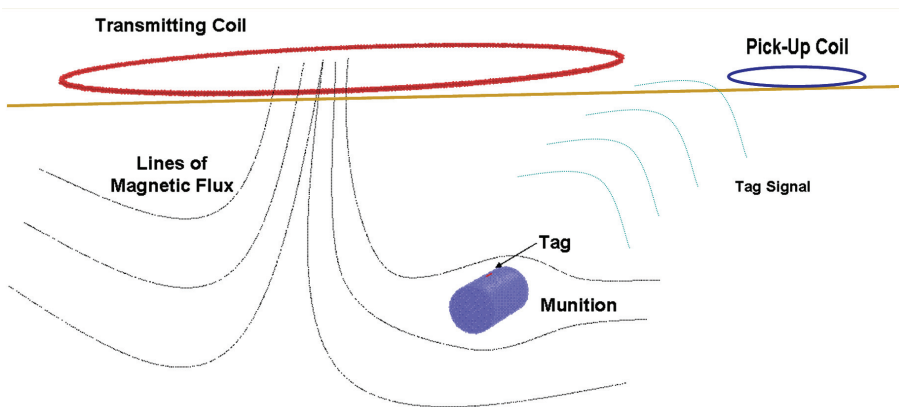


Fig. 1. Depiction of the tagged munition technique.

The ordnance detection system comprises an interrogation module and the RFID tag. The above-ground interrogation module, used to search for tags, generates a large magnetic field. The tag harvests the transmitted energy to power its integrated circuit and replies with a digital signal. The interrogation module's receive coil senses the digital signal transmitted by the tag, then reports detection and any embedded digital data, which might include information such as the munition type, serial number, and date of manufacture. One meter deep detection of UXO was deemed necessary to demonstrate feasibility.

After determining which passive RFID tags offer the highest probability of success in this application, additional electromagnetic and mechanical constraints were analyzed. Electromagnetic considerations involved characterization of the ability to energize and receive the reply from a passive RFID tag one meter from the excitation coil, the effect of the presence of the munition's metal on tag functionality, and the danger of the high-energy transmitting coil setting off buried munitions. Mechanical considerations involved finding ways to mount the RFID tags on existing metal munitions that allow RFID tag survival and functionality, subject to the extreme accelerations associated with munitions and ordnance.

## 3. System design

### 3.1 RFID tag choice

According to Faraday's and Lenz' Law, the eddy currents induced on a conductive munition will tend to oppose the magnetic field perpendicular to its surface. This opposition becomes greater nearer the munition's surface. Therefore, magnetic fields very near the munition will tend to be parallel to its surface. This condition suggests choosing a solenoidal-shaped tag mounted with its core parallel to the surface, allowing the most efficient harvesting of energy from the interrogation module's magnetic field.

One candidate solenoidal tag was the Texas Instruments (TI) Tiris RFID tags. The decision was made to exploit these tags because of their operating frequency near 130 kHz and their reliance on the magnetic field, both of which were favorable for maximum ground penetration of the transmitted energy. Figure 2 shows the Texas Instruments' Tiris solenoid tags employed during this study on the left and the in the larger "pancake" geometry on the right. The solenoid tags comprise a copper coil wrapped around a ferrite core, other circuit elements, and a digitally-based integrated circuit that functions as a receiver, transmitter, and processor with 64 bits of user-written data. The tags and readers employ frequency-shift keying (FSK) between 123 kHz and 134 kHz to transmit the tag's data to the reader.
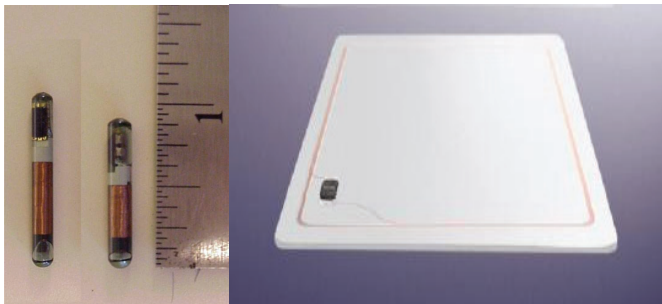


Fig. 2. Two examples of the low-frequency passive tags. The photo on the left shows the solenoid tag design; the coil wire is wrapped around a small permeable core. The photo on the right shows the "pancake" coil design used in non-contact facility access applications. The small black objects in the figures are the integrated circuits.

The RFID system choice was influenced by the Tiris tag's response mechanism being more favorable in this application. The Tiris tags do not reply until after the interrogation module's transmitter has turned off, which allows detection of the weak tag signal in a quieter spectral environment. Alternative RFID systems have tags that reply during reader interrogation, generally at half the reader's transmitted frequency. This simultaneous transmit and receive process in non-Tiris systems forces their readers' detection systems to detect very small signals in the presence of very large signals. Although this detection can be accomplished, it requires very precise relative positioning of the transmitting and receiving coils to minimize the magnitude of the transmitted signal cross-coupled into the receiving coil. It was anticipated that maintaining the relative positions of the coils precisely would be very difficult while traversing artillery and bomb ranges. The required positioning accuracy is much less for the Tiris system because the transmitter is turned off while the receiver is enabled.

## 3.2 The transmit coil

The passive Tiris tags used in this study were intended to function with a separation between the reader and the tag of about one meter under certain conditions. Because budgetary constraints required that no changes be made to the RFID tags themselves, the interrogation module would have to be modified and made larger to achieve the required separation of one meter in the presence of the metal munition. The basic magnetic field equations were examined to determine the possible ways to increase the field levels at longer ranges. The magnetic field emitted in the z-direction, $Bz$, by a circular loop of radius $a$ in the x-y plane at a point located a distance $r$ from the origin can be expressed in μW/m² as

$$B_z = \frac{\mu_0 I N a^2}{2(a^2 + r^2)^{\frac{3}{2}}} \tag{1}$$

This relationship simplifies when the point $r$ is located far from the coil as

$$B_z = \frac{\mu_0 I N a^2}{2}(\frac{1}{r^3}) \qquad for \qquad r \gg a \tag{2}$$

Equation (1) holds in regions near the coil, where the reduction as a function of $r$ is slightly less than $1/r^3$. The magnetic field increases linearly with the area of the coil, with the current, and with the number of turns. For a given value of $r$ (one meter) and a given value of area (radius of one-half meter to keep the interrogating module from being too large), it appears that one can arbitrarily increase $B$ by either increasing the number of turns, $N$, or the current, $I$. Practical considerations will limit the amount of current that can be employed but it still appears that arbitrary increases in the number of turns will yield increasingly large values of the magnetic field. Unfortunately, increasing the number of turns increases the inductance of the coil. The value of the inductance can be seen in equations (3) and (4) to increase as the square of the number of turns. The voltage across the coil is proportional to the inductance as seen in equation (5). This relationship implies that the voltage is proportional to $N$ squared. Thus, for a given coil current, an arbitrary increase in $N$ can quickly drive the voltage across the coil to impractical values. An optimum combination of $N$ and $I$ must be determined given the amount of current the batteries and drive circuit can provide and the maximum tolerable voltage across the coil.

$$L = \frac{0.31(aN)^2}{6a + 9h + 10b} \tag{3}$$

$$L = \frac{0.31aN^2}{6} \qquad for \qquad a \gg h, b \tag{4}$$

$$V = L\frac{dI}{dt} \tag{5}$$

The final interrogation coil design included a diameter of one meter and Litz wire with 270 strands of 38 American wire gauge (AWG) magnet wire. The coil design employed 10 turns of Litz wire ($N$=10) and approximately 16 amps-rms, for a magnetomotive force of 160 ampere-turns-rms. These design values were confirmed to be effective through

laboratory experimentation and electromagnetic modeling of the interrogation system and munition-mounted tag. No analytical optimization was attempted.

The laboratory investigation provided insight into potential detection ranges but it did not answer the basic physics question of whether or not the tag mounted on or near a metallic munition could function as needed.

## 3.3 Modeling approach

Knowledge of the magnetic field's behavior is essential in understanding the overall system designs required to transmit energy from the above-ground interrogator to the tag and from the tag back to the above-ground receiver. Quantities of interest, such as signal strength, can be calculated from these fields.

In the absence of the munition, the tag system's general behavior is well known. However, the tag's necessarily close proximity to the metallic munition will affect its operation. These passive tags are activated when there is sufficient magnetic energy linking its circuit's pick-up coil. Getting the requisite level of magnetic field to the tag for activation will be impeded by the munition. Once activated, the tags generate a transmitted field that is altered by the presence of the metal munition also.

Furthermore, the operational circuitry of the tag requires a specific quality factor ($Q$) to operate (Shubert, 2007, 2008). The $Q$-value depends on the inductance and resistance of the tag's pick-up coil. These values will be distorted in the presence of the munition. If the $Q$-value for the tag is too low, the tag cannot operate. There are of course other electromagnetic factors interfering with the tag's operation, but proximity to the munition is primary.

Figure 1 shows the basic geometry of the system as it was modeled. A transmitting coil sends out a signal. If a tagged munition is within its range, the tag is activated and sends out its own signal. The tag's output signal is picked-up by a receiving coil.

For purposes of the modeling investigation, this basic system was decoupled into two separate cases; (1) transmitting a signal to the tag and (2) receiving a signal from the tag. These two cases are independent because the amplitude of the signal received by the munition-mounted tag and the amplitude of the field transmitted by the tag are not related. In both cases, the electric field was examined for Hazards of EM Radiation to Ordnance (HERO) issues (Davis et al., 2006). The changes in Q-value of a tag were also examined separately.

## 3.4 Magnetic modeling

The models consisted of two- and three-dimensional finite element models. For this task, the commercially available finite element software package, Vector Fields, was used. Battelle has successfully employed this type of modeling in other studies. Those results were validated in both laboratory and field experiments.

Because the practical range of frequencies that will be used are on the order of a 100 kHz and because the system antennas are in the near field, the models were solved using the low-frequency Maxwell's equations. For the two-dimensional models, equation (6) was solved subject to appropriate boundary conditions. Here, $A$ is the magnetic vector potential, $J_s$ is the source current density, $\sigma$ is the conductivity, and $\mu$ is the magnetic permeability.

$$\nabla \times (\frac{1}{\mu} \nabla \times A) = J_S - \sigma \frac{\partial A}{\partial t} \tag{6}$$

The curl of the vector potential, *A*, yields the magnetic field, *B* and its negative partial time derivative yields the electric field, *E*. These two-dimensional models were used to provide quick qualitative insights into the basic behavior of this system.

Although more time consuming, the three-dimensional models provided more useful quantitative information. Equation (6) was used in the conductive regions and regions near conductive materials. In all other regions, the magnetic scalar potential shown in equation (7) was solved. Here, $\Phi_m$ is the magnetic scalar potential. The solutions are matched at the interfaces and are subject to appropriate boundary conditions. The gradient of the magnetic scalar potential, $\Phi_m$, yields the magnetic field, *B*.

$$\nabla^2 \Phi_m = 0 \tag{7}$$

Rather than employ an open-boundary technique, the mesh was extended to a reasonable distance, a minimum of five times the distance between the munition and the transmit coil, with a scalar potential boundary condition applied to the outer surface. This method ensures that truncation has an insignificant effect on the region of interest. Although requiring larger model sizes than the open-boundary technique, past experience indicates that it provides a more accurate solution. The effect of truncation was estimated by calculating the tangential component of the field on an open boundary with a derivative boundary condition. Here, one-half the field observed on such a boundary is being reflected back from the exterior. Combining this value with knowledge of the probable decay in the exterior space gave an order of magnitude for the effect of the truncation on the regions of interest. The effect of truncation was less than one part in a hundred.

In general, the two-dimensional models consisted of about 100,000 elements and had an error relative to element size less than 0.25 percent. The three-dimensional models consisted of about 800,000 elements and had an error relative to element size less than 1.0 percent.

Figure 3 shows an example of the basic three-dimensional models used for these calculations including the cylindrical munition, a solenoid tag mounted on the munition, and the transmit coil. The soil and air are not shown, but their interface is located along the transmit coil's plane.

For calculating the fields from the transmitting coils and tags, a uniform and constant source current of 1 amp-turn was defined. The individual turns of transmitting coil wires need not be modeled, provided the individual wire size is small compared to the coil diameter and wavelength. Note that the source input is defined in terms of a constant current and not voltage. The relationship between voltage and current input depends on the circuitry used to drive the coils and is not important in modeling the fields.

Practically, the magnetic field levels generated will be such that the magnetic permeability of all likely materials is constant. Therefore, the electromagnetic field results, upon which all quantities of interest are calculated, will be linear with the number of amp-turns defined. The calculated results can then be scaled for any strength transmitting coil or tag.

Once field levels are determined, signals to and from the tags can be calculated using equation (8). Here *S* is the signal strength, N is the number of turns in the receiving coil, *B* is the magnetic field linking the receiving coil, and *a* is the area of the coil. If a sinusoidal waveform is assumed, the right hand side of equation (8) is obtained. Here $u_{eff}$ is the effective permeability of a receiving coil's permeable core, $\omega$ is the angular frequency, and $B_o$ is the calculated magnetic field linking the circuit in the absence of core permeability.

$$S = N \int_{Coil} \frac{d\vec{B}}{dt} \cdot d\vec{a} = N\mu_{eff}B_o\omega a \tag{8}$$

The Texas Instruments tags specify a minimum *Q* to respond to an interrogating signal. Models of the tags near the munitions were used to calculate the changes in the *Q*-value due to their proximity to the metallic munition (Skilling, 1957). *Q* can be defined in several ways but two definitions stand out in this application. It is useful to define it as proportional to the ratio of the inductance to the resistance of the tag's receiving coil. It can also be defined as the ratio of the resonance frequency to the bandwidth, which is a measure of the relative narrowness of the resonance curve.
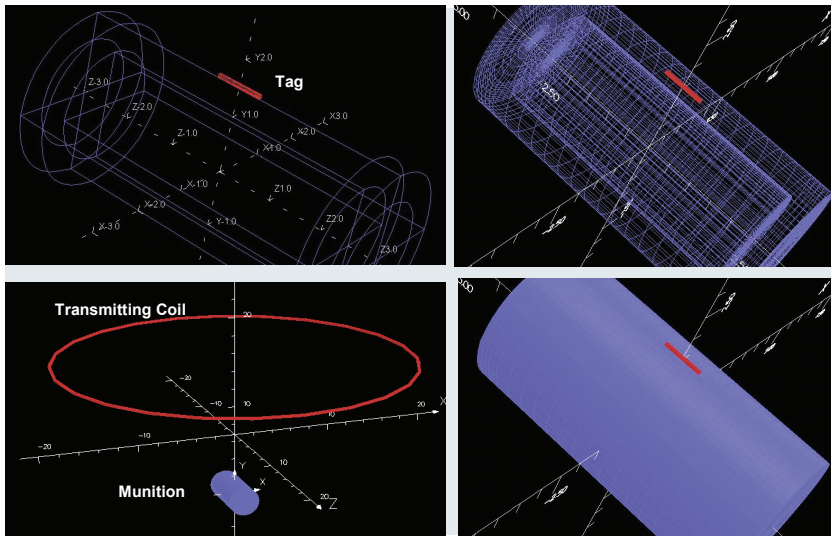


Fig. 3. The basic models for the munition, solenoid tag, and transmitting coil. The bottom left figure shows the transmitting coil and munition. Here the coil is centered directly over the munition and the ground is not shown. The other figures show the geometry (top-left and bottom-right) and mesh (top-right) for the munition model. The tag is also shown centered on the top surface of the model.

The resistance, $R_c$, of the tag in free space is known *a priori*. Using the value of the inductance, L, and resistance, R, caused by the nearby munition, the *Q*-value is defined as

$$Q = \omega L / (R + R_c) \tag{9}$$

The value of *Q* is dimensionless. The L and R values can be calculated from the electromagnetic fields. The value of R is related to the power loss of the tag caused by induced eddy current density, *J*, in the munition. If *I* is the constant source current, the value of R is given by

$$R = \frac{1}{|I|^2} \int_{volume} \frac{J^2}{\sigma} dV \tag{10}$$

The value of $L$ is related to the magnetic energy created by the tag for a constant source current. If $B$ is the magnetic field as a function of space, the value of $L$ is given by

$$L = \frac{1}{\mu |I|^2} \int_{volume} B^2 \, dV \qquad (11)$$

The integrals are over all space containing conductive and/or permeable material.

The following parameters were examined to provide insight into the system with the intent of proving feasibility and optimizing the system. These parameters were studied for all three situations modeled using both two- and three-dimensional models. The parameters being varied included:

- Above-ground transmitter and receive coil positions relative to the munition
- Soil type and conductivity (dry dirt to salt water)
- Effect of nearby metallic or permeable materials
- Munition depth
- Munition orientation
- Munition shape
- Munition material
- Tag type (solenoid or pancake)
- Tag position on munition
- Tag orientation
- Tag mounting options such as tag offset from and "grooves" on the munition
- Frequency of operation (both transmitter and tag)

For each situation, a baseline model was defined. These parameters were varied relative to this baseline model to determine their effects.

### 3.4.1 Models for transmitting the signal from the tag

The fields at the munition surface near the above-ground receiving coil are critical to understanding behavior. The flux from the tag linking the receiving coil's windings will determine whether the tag's output signal can be detected.

The same basic munition geometry defined in the signal-to-the-tag case was used. The effects of the transmit coil were ignored. A specific tag was modeled as being fastened to the munition. Its location was variable. Both types of tags were modeled for baseline. Baseline was a tag centered on the top of the munition with the same offset.

A receive coil does not need to be specifically modeled. The signal received from the tag by a receive coil depends only on the magnetic field linking the receiver's coil windings. This value can be calculated independently using equation (8) once the model is solved.

### 3.4.2 Models for estimating effects on Q-values

Examination of the tags' changes in $Q$-value due to the proximity of metallic munition was done using two- and three-dimensional modeling. The model's field output was calibrated to commercial tags. Effects of various mounting techniques including separation (lift-off) from the metallic surface were examined. The electromagnetic fields solved for these cases were used to calculate the $Q$-value through the inductance and resistance using equations (9) through (11).

### 3.5 Magnetic modeling
### 3.5.1 Signal to the tags

Modeling did provide insight into behavior of the fields near the munition generated by the transmitting coil.

As expected, the field amplitudes dropped significantly near the munition's conductive surface. The decrease in field and resulting signal to the tag can be as much as two orders of magnitude in going from a lift-off of 2.5 mm (0.1 inch) to the munition surface. In general, a 6.3-mm (0.25-inch) gap increases the field by a factor 2.5 over a 2.5-mm separation. The exact change depends on the munition material. As expected, lower conductivity in the metal ordnance object results in lower eddy current amplitudes and therefore lower loss in field level at the munition. Also, higher permeability of the material tended to increase the field near the munition. Nonetheless, the proximity of the tag to the munition will decrease the magnetic field near the tag. Therefore, the separation between the metallic surface and the tag is critically important.

In order to accommodate this required separation, the idea of grooves into which the tags would be placed was considered. Modeling indicated that groove shape has minimal influence on the field coupled into the tag. The important parameters were groove depth and groove length and width. Separation requirements were identical. The length and width of the groove should be such that there is about 5 mm (0.2 inch) of clearance between the tag's coil and the sides of the groove. This requirement holds for both tag types. The effect of the composition of the material potting the tag in the groove was also investigated. Nonconducting, permeable material will aid in coupling the interrogation signal into the tag.

Near the munition, the magnetic field lines tend to be parallel to the conductive surface. For a surface lift-off of 2.5 mm, the magnetic field parallel to the munition surface can be as much as five times larger than the magnetic field perpendicular to the surface. This fact indicates that a tag with solenoid geometry will receive a much higher input signal than a tag with the pancake geometry.

Figure 4 shows the magnetic vector equipotential lines from a transmitting coil near the munition as it passes by. The magnetic field is parallel to these lines. Here, the metallic munition is oriented vertically and the coil passes over its centerline. Regardless of the coil position, the field lines tend to be parallel to the munition.

This behavior is a consequence of the electromagnetic boundary condition associated with conductive surfaces and strongly suggests that the pancake coil tag would not be feasible for this application because it requires magnetic fields perpendicular to the surface of the munition to be activated. It would be helpful to orient two solenoid tags axially and circumferentially on the munitions with circular cross-section. However, because of practical constraints, the solenoid tags can only be oriented axially on the munition. Therefore, the transmitting coil will have to produce sufficient axial field on the surface of the munition for this system to be feasible. The other parameters examined focused on this geometry.

The angular orientation of the ordnance item (vertical to horizontal) as the above-ground coils are moved, as they would be in a large ground-area survey, were examined. For a coil centered over the munition, the two extremes, vertical and horizontal, were modeled. In the first case the magnetic field on the surface of the munition is vertical. In the second case, the field is mostly circumferential, albeit larger in magnitude.
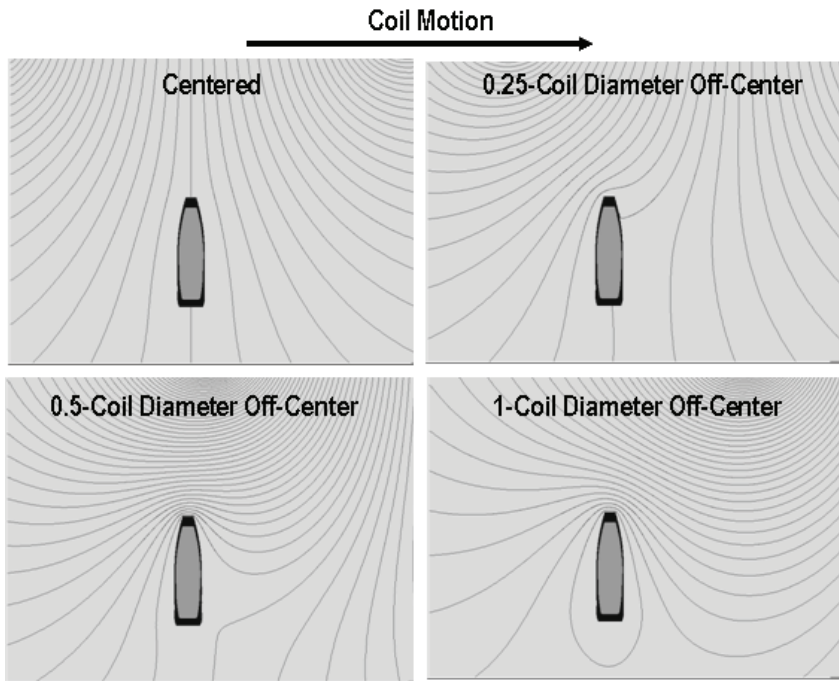
Fig. 4. Two-dimensional modeling results showing the magnetic vector equipotential lines from the transmitting coil as it passes directly over a vertically oriented munition. The magnetic field is tangential to these equipotential lines. The coil is not shown, but it is located one-half meter above the munition. The center of the coil is designated in the figures.

However, the orientation of the field on the munition will change as the transmitting coil passes over the ordnance item. Figure 5 shows an example. In all cases examined, there were at least some points along the coil motion that caused an axial field somewhere along the surface of the munition.

The relative signal received by an axially-oriented solenoid tag, for a munition whose axis is parallel to the surface, is shown in Figure 6. The two cases shown are for the coil passing parallel and perpendicular to the munition's axial axis.

In the first case, sufficient field can exist to activate the solenoid tag, although the transmitting coil will be off-center from the munition. In the second case, sufficient field can only exist if the tag is near the ends of the munition. In this case, a tag centered on the munition cannot receive any activating field and the munition will not be detected. Placement of the tag on the munition is important. It is preferable to place it near the edge of the munition.

Notice also that the peak activating fields for a tag occur at different transmitting coil positions depending on munition orientation and how the transmitting coil passes over the munition. For the above example, in the first case, the tag receives its peak activating field when the transmitting coil is roughly one-half diameter off-center from the munition; in the second case the peak activating field occurs when it is centered.

Centered          0.3X Coil Diameter          0.5X Coil Diameter
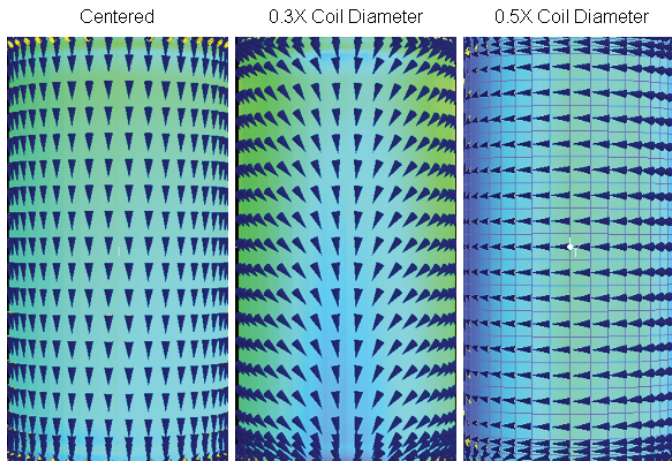


Fig. 5. The direction of the magnetic field on the surface of a vertically-oriented cylindrical munition with a one-meter diameter transmitting coil located 0.38-meters above the munition, centered (left), 0.3-meter off-center (middle) and 0.5-meter off-center (right).
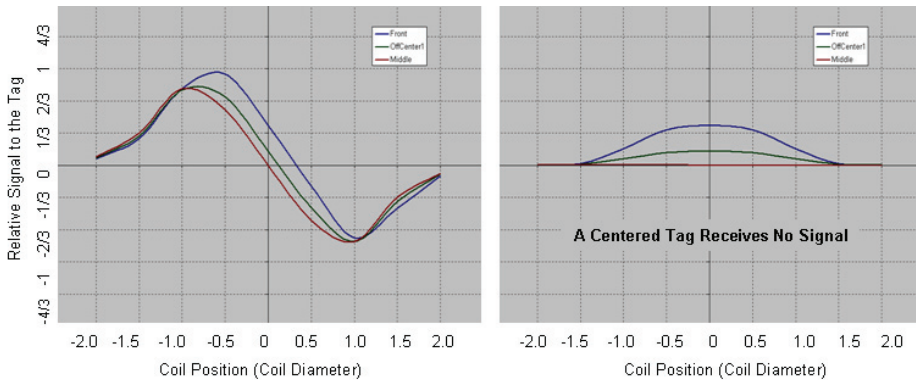


Fig. 6. Responses calculated as the interrogating coil moved past a horizontally-oriented munition. The left curves correspond to the transmitting coil moving parallel to the axis of the munition. The right curves correspond to the coil moving perpendicular to its axis.

For a given munition depth, the strength of the activating field varies only by about a factor of three depending on munition orientation, tag location, and where the transmitting coil passes. A vertical munition orientation provides the largest activating field. A horizontal orientation is more affected by coil motion and tag location.

For any given case, the magnitude of the field levels on the munition change only slightly as a function of the angular position. For a vertically oriented munition, the peak signal strength is independent of angular orientation. The worst case is for a horizontally oriented munition. In the horizontal case, the signal for a tag on the bottom of munition remains about one-half the magnitude at the top of the munition, which was encouraging because the munition's tag could be on the "underneath" side of the tag and still, be detectable.

The basic behavior and orientation of the magnetic fields on the surface of the munitions do not change as a function of munition depth in the range of 0.3 to 1.5 times the transmitting coil diameter. The only change in field is the amplitude. In general, if a solenoid tag is mounted near the edge of the munition with at least a 6.3-mm lift-off, a signal should be detected by the tag for all cases up to a one-meter depth. If the solenoid tag is mounted at the center of the munition, the average maximum depth for tag activation reduces to about 0.5 meters; however, there are certain cases in which the tag will not receive any signal regardless of depth. For the pancake coil tag, the maximum depth is about 0.1 meters.

Figure 7 shows the amplitude of the peak axial field on the top surface of a horizontally-oriented munition. Assuming 100 amp-turns for a one-meter diameter transmitting coil and a solenoid tag, equation (8) suggests a field level of 8.5 pT is required for tag activation. For this case, a maximum depth of more than 1 meter is possible. If the tags were located on the bottom of the munition, field levels for the horizontal case would be roughly halved, but still a one-meter deep tag can be activated. A vertically oriented munition would have a somewhat larger field.
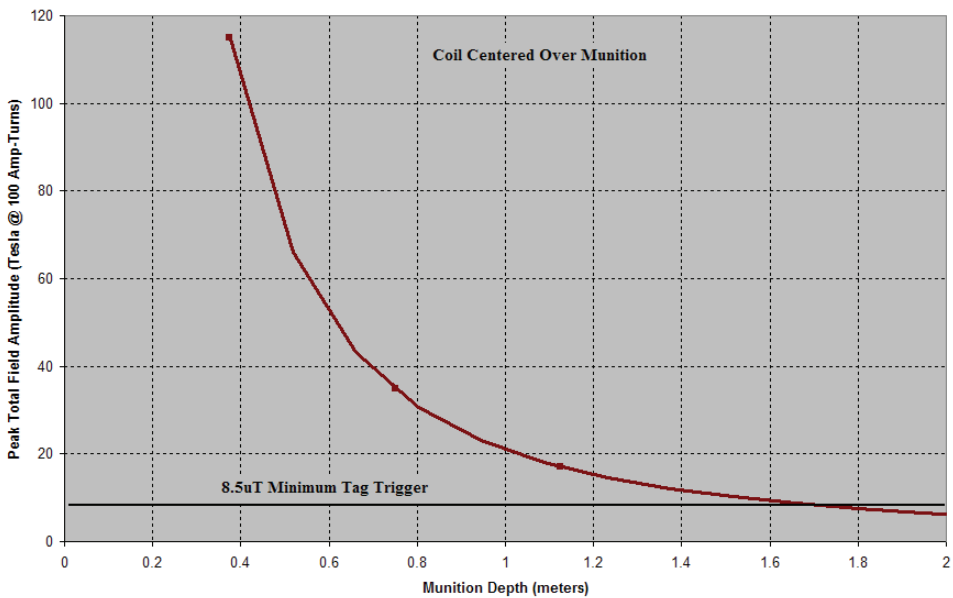


Fig. 7. The maximum field level on the surface of the munition as a function of munition depth. The coil is centered over munition.

Frequency of the transmitting coil's signal is also important. For practical considerations, the frequency range between 50 and 300 kHz was examined because most commercial tags of interest fall into this range. In all cases, the field levels near the munition slightly decreased with increases in frequency. However, because the signals to the tags are linear with frequency, the signal increased monotonically. Commercially available tags are set to receive a fixed frequency. But, this information indicated that use of a higher frequency signal has advantages.

Munition geometry was also studied. In general, there was no appreciable change in the behavior of the fields for the geometries analyzed. Smaller munitions allowed larger field levels near its surface. For a cone shaped munition, the field was slightly larger near the smaller diameter ends.

There are other factors that can alter the field on the surface of the munition. For example, the presence of other permeable or conductive material, such as the remnants of exploded ordnance items nearby, can shield the tag from the input signal. Modeling indicates that if larger pieces of ordnance items are at least 0.1 meter from the munition and each other, field levels near the munition will not be significantly affected. Otherwise, the conductive material will shield the munition's tag from the field.

Soil conductivity is generally of concern for higher frequency systems but it was examined in our study. The results indicate that if the frequencies are on the order of 150 kHz and the munition depth is less than one coil diameter, soil conductivity does not affect the signal transmitted to the tag much. For a 0.38-meter deep munition and a frequency of 150 kHz, the difference between a dry soil and one saturated with salt water was a decrease in field amplitude of less than 20 percent.

If the tag mounting is optimized, modeling suggests that an overlap for the transmit coil of a half-coil diameter will be sufficient for ensuring that there is enough magnetic energy to actuate a tag at a one-meter depth.

The electric field at the munition produced by the transmitting coil was also calculated. Using these models, the current design of our one-meter diameter coil has been predicted to be about 0.5 V/m at 100 kHz immediately below the coil, which lies well below the HERO safety level. The HERO curves specify the maximum safe level at 100 kHz to be between 10 and 40 V/m (rms), depending on the sensitivity of the munition.

### 3.5.2 Signal from the tags

Once a tag has been activated, in generates its own output signal that is picked up at the surface using a receive coil. The magnetic field generated from both the pancake and solenoid tag geometries were examined. Figure 8 shows the magnetic vector equipotential lines from both tag types, in air and in a groove on the munition. The magnetic field is parallel to these lines and larger when the lines are closer together. The presence of the conductive munition reduces the field output of the pancake coil tag significantly while slightly boosting the output from the solenoid tag. The pancake coil tag generates a field normal to the surface of the munition that is reduced because of the electromagnetic boundary conditions. The effect on the solenoid is somewhat reversed, the metallic munition repels the magnetic field, which increases the signal transmitted by the tag boosting the effective signal output by as much as 20 percent.

Just as with receiving the signal from a transmitting coil, the solenoid tag performs better in outputting a signal. For these reasons, the solenoid geometry was the focus of the rest of this study. Because of practical constraints, these tags must be axially oriented on the munition so only axially oriented tag results are presented here.

Unlike inputting a signal to the tag, the effect of munition materials examined had little effect on solenoid tag output.

Soil conductivity has minimal effects on the tag's output signal as with the tags input signal. Again, the tag location on the ordnance item was found to be important with a tag position closer to the end of the munition increasing signal at the pick-up coil a maximum of 10 percent, depending on the specific case.
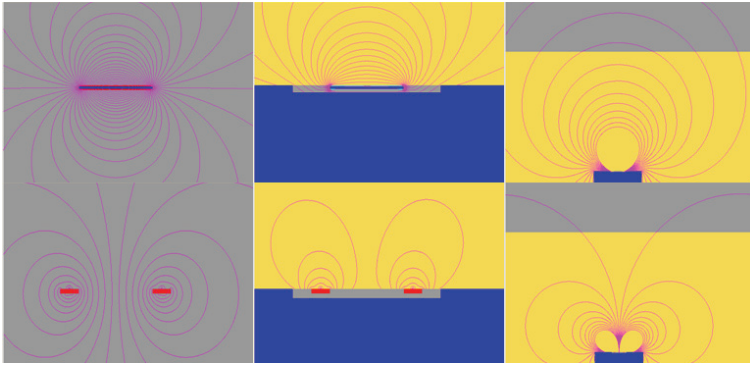
Fig. 8. Magnetic vector equipotential lines from the transmission of the solenoid (top row) and the pancake coil (bottom row) tags. The left column shows the results for the tags in air. The middle column shows the results for the tags in a grooved munition in dirt. These two columns are the same scale. The pancake coil tag's signal output is severely damped compared to the solenoid tag's signal because of the munition's presence. The right column shows the same results as the center column, but on a larger scale to see the impact near the surface.

When the tag is embedded in a groove, a wider and deeper groove is important but the shape of the groove is less important. Lift-off is not as much of a factor in getting signal to the surface as it was in getting signal to the tag. Here, a lift-off of only 2.5 mm is sufficient. A lift-off of 6.3 mm was required to receive the signal. The permeable filler placed in a groove to help increase input signal to the tag has little effect on tag output.

As in the case of the signal to the RFID tag, the tag's transmitted signal frequency was influential. As stated previously, the frequency range between 50 and 300 kHz was examined during this work to correspond with commercial tag availability. While the magnetic field amplitude at the ground's surface slightly decreased as frequency increased, the signal in the above-ground receive coil increased monotonically with frequency.

The length of the solenoid tag was also examined. The longer tags produced a larger amplitude field at the ground surface. The commercial tags examined varied from 10 to 40 mm in axial length.

Figure 9 shows the peak amplitude of the three components of the magnetic field generated in a plane 0.38 meters above an off-centered, axially-oriented, solenoid tag. The columns show the axial, normal, and circumferential components, respectively. Two horizontal and one vertical munition orientations are shown. The red color is a positive and the blue color is a negative.

The basic field distributions depend only on munition orientation. The field amplitude decreases in amplitude as munition depth increases and as the tag angular location approaches the far side (bottom) of the munition.

These field distributions have significant consequences for the signal received by and the design of the receive coil. Only the field linking the receive coil's windings will be detected. For a point-coil receiver, the magnetic field amplitude is linearly proportional to the signal. However, because the coil will have a finite diameter, the average field level linking that coil area will determine the signal.

In practice, it will be easier to position the above-ground receive coil oriented parallel to the surface, so approach will focus on this case. In this situation, the normal component of flux induces the signal.

Generally, a larger coil diameter will capture more flux and produce a larger signal for detection. However, the unique features in the tag's surface field distribution indicate that a coil diameter less than one meter should be sufficient given the munition sizes and depths of interest. Larger coil diameters would add little benefit.

Referring to Figure 9, the normal flux distributions are shown in the center column. The following arguments can be applied to any component of the flux detected by a pick-up coil. For a vertically oriented munition, the normal field distribution from the tag at the surface is a monopole. However, for a munition oriented parallel to the surface, this field distribution is a dipole.
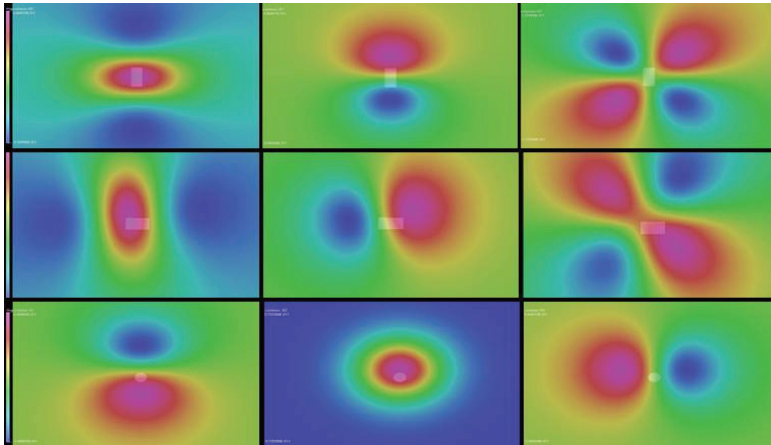


Fig. 9. The axial (left), normal (middle), and circumferential (right) components of the peak magnetic field transmitted by the solenoid tag at the surface. The top, middle, and bottom rows show the munition orientation parallel to the surface with centered tag on top of munition, same orientation rotated 90 degrees with the tag position off center on the side, and a vertically oriented munition with the tag centered, respectively. The munition is shown as a rectangle (parallel to surface) in the first two rows and a circle (vertical) in the last.

A problem arises with dipole distributions. Depending on the direction of the motion of the receive coil as it passes over the dipole field, the dipole field could tend to cancel itself as it links the coil windings. Therefore, it is very important that the receive coil have an overlap as it is scanning. This overlap will reduce the impact of isolated nulls inherent in the dipole field patterns because the system will be taking data continuously at nearby locations that are not within the null. Modeling suggests that the receive coils should have an overlap no less than one-half the coil diameter.

The models can be calibrated to any commercial tag. For example, the Texas Instruments' Tiris 32-mm long solenoid tag's specifications state that it has a field output between 80.5 and 102.5 Amps/meter at 50 mm with an output frequency of 134 kHz. The calibration data are used to determine the maximum munition depth that can be detected realistically.

The field at the receive coil is dependent on the discussed parameters. It is also dependent on the receive coil's electronic design. Electronics associated with the receive coils can generally measure minimum signal strengths of about 5.0 µV. For practical purposes,

assume the receiver has 20 turns, a coil area of 0.3 m², and an effective core permeability of one. For this case, equation (8) suggests an average field strength of 6 picoTesla (pT) at the receiver is required for detection.

If the lower value for the tag output is used and the above receive coil is assumed, analysis indicates that a signal from the tag can be detected for a munition depth of least one meter, for all cases considered. The average field linking this receive coil as a function of munition depth is shown in Figure 10.
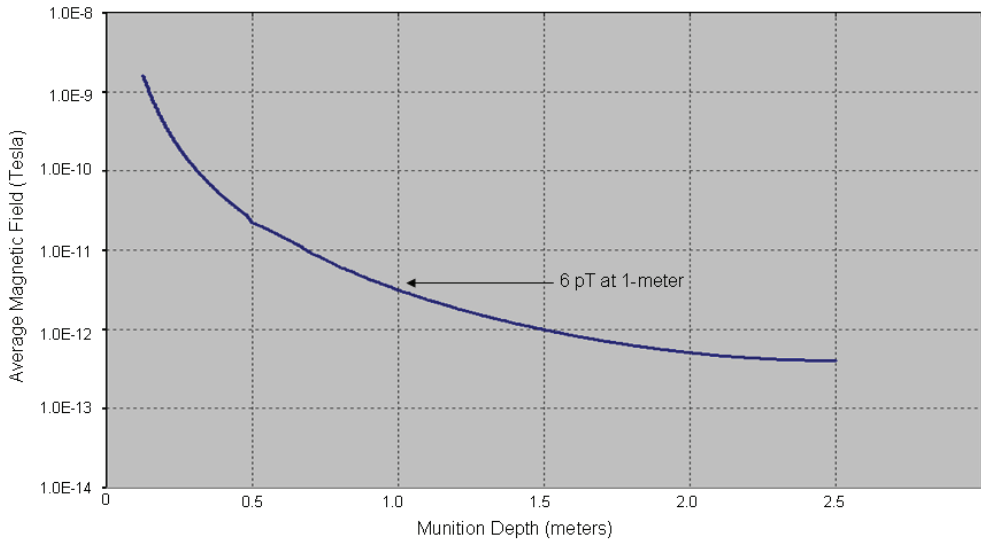


Fig. 10. The average field as a function munition depth. The munition is oriented parallel to the surface. For a typical receive coil, a field of 6 pT is required.

The electric field produced by the tags at the munition was also calculated. The models indicate that the tags would produce electric field amplitudes less than 0.01 V/m at 100 kHz on the munition, far below the HERO safety levels.

### 3.5.3 Q-value of the tags

The Texas Instruments' tags specify a minimum quality factor above 60 to respond to an interrogating signal. In free space, the $Q$ of the transponder coils was found to be about 94. The modeled results were calibrated with respect to these commercial tag values.

Modeling studies indicated that the metal of the munition casing had a significant impact on the $Q$ of the tag. As expected, the presence of the munition decreased the inductance and increased the resistance of the tag's circuit, thereby lowering the $Q$-value.

Figure 11 shows the induced eddy currents that change the resistive value of the circuit. Modeling indicates that in general a lift-off greater than 6 mm from the munition surface is required to keep the $Q$-value above 60.

If the tag is placed in a groove, not only is this lift-off still required, but the tag should be separated from the walls of the groove by about 5 mm. The nonconducting, permeable material used to aid in coupling the interrogation signal into the tag did not lower the $Q$-value.
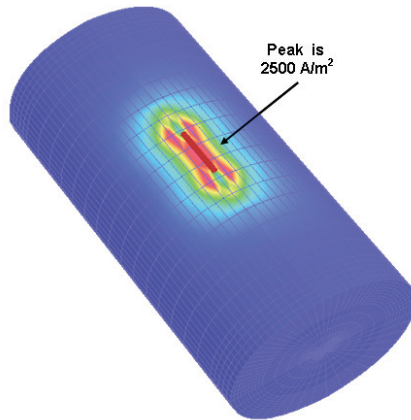
Fig. 11. The induced eddy currents from a solenoid tag on the surface of the munition. The peak current density for a typical commercial tag is about 2500 amps per square meter.

### 3.6 Experimental verification

Experimental efforts involved the design, fabrication, and tuning of the custom coil circuits. The tuning circuits for the high-voltage, one-meter diameter transmit coil and the corresponding receive coil were built.
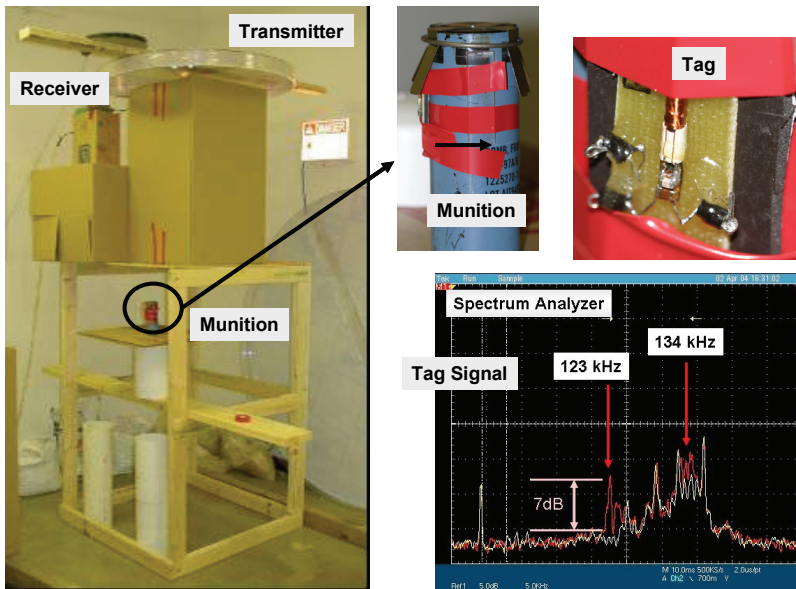


Fig. 12. The laboratory setup for obtaining experimental data. The left picture shows a one-meter diameter transmitting coil centered over a munition. The top right pictures show a close-up of this munition and the RFID tag. The lower right graphic is a spectrum analyzer screen shot displaying the two frequencies transmitted by the tag.

Lab and field testing were conducted. The basic results of the modeling were verified, although not every parameter was examined in the lab and field. Tag proximity to the munition surface was important not only for receiving a signal but also maintaining a high $Q$-value. The separation distance of 6.3 mm (0.25 inch) for good tag performance was found to be adequate.

The solenoid tag and the one meter diameter coil in the laboratory using the set-up shown in Figure 12 were characterized. The solenoid Tiris tags from Texas Instruments have been used exclusively.

Experiments were performed to determine the distance from a transmitting coil that a tag could be activated by measuring the voltage level at the tag coil without a munition item. Ranges greater than 2 meters were observed. These experiments were repeated with the tag near a munition. Similar results were seen as long as the tag separation from the munition was sufficient.

Later experiments observed the field generated by the tag at the above-ground receiving coil. For optimized conditions, munition depths greater than one meter were detectable in the lab.

Tagged munitions were also detectable in the experimental field trials in dry clay soils. These findings also supported the modeling results.

### 3.7 Modeling conclusions

This modeling effort suggests that munition tagging, making use of current passive RFID tag technology, as a method to improve locating UXO and discriminating UXO from clutter is feasible.

In tagging the munition, a solenoid type tag was found to be preferable. The tag separation from the metallic munition surface is important for ensuring acceptable operation of the tag. A separation distance of 6.3 mm is required. If it is placed in a groove, separation of the tag from the groove walls should be about 5 mm.

For practical reasons, the tag will be oriented axially on the munition and should be place near the ends of the munition so that the tag can receive a signal from the transmitting coil regardless of munition orientation. If centered on the munition, there are circumstances that would prevent a tag from receiving a signal. The tag can still receive and transmit sufficient signals regardless of its angular position on the munition, i.e., top or bottom.

The receive coil should be less than one meter in diameter. The transmit and receive coils should have an overlap of about one-half coil diameter. Soil conductivity did not present a problem.

For an optimized system, a detectable munition depth of a one meter is likely.

## 4. Mechanical considerations

The mechanical considerations were two-fold. First, the tag had to survive launch acceleration and impact. Second, the tag had to be mountable on existing munitions without significant modification to the munition.

Launch acceleration and velocity testing explored tag survivability potential. These tests were conducted at Battelle's West Jefferson, Ohio munitions testing facilities. A "soft catch" was employed using a combination of Styrofoam and duct tape to reduce deceleration forces. Tiris tags were removed from their glass containers, potted, and placed inside polypropylene cylinders that were inserted as shotgun shell loads. Tag survival was

determined using a Tiris reader to monitor the tag's digital response. Initial results were encouraging. A single tag was fired 11 times; it survived the first 10 events. The results are listed in Table 1. The final firing at 67,000 g's allowed the polypropylene slug to strike a steel plate, which did incapacitate the tag. Shot number 8 is highlighted in the table. The tag described in this line survived accelerations up to 43,000 g's and a maximum velocity of 247 meters per second (809 feet per second). Informal discussions with ordnance experts indicated the highest acceleration/deceleration levels experienced by U.S. munitions were in the low 20,000 g's (anecdotal information did not indicate if this value was acceleration or deceleration). Further testing and analysis would be needed to ensure tag functionality meets acceleration/deceleration rates acceptable to the Government.

| Shot Number | In-Bore Acceleration (g's) | Velocity (feet/second) | Tag Response |
|---|---|---|---|
| 1 | 10,000 | 340 | Good |
| 2 | 27,000 | 277 | Good |
| 3 | 33,000 | 681 | Good |
| 4 | 12,750 | 375 | Good |
| 5 | 26,900 | 575 | Good |
| 6 | 10,800 | 381 | Good |
| 7 | 15,850 | 438 | Good |
| 8 | 43,100 | 809 | Good |
| 9 | N/A | 882 | Good |
| 10 | N/A | 475 | Good |
| 11 | 67,500 | 1158 | Bad* |
| * Load struck metal plate behind Styrofoam | | | |

Table 1. Summary of tag acceleration and velocity survivability testing

The initial research into the mounting feasibility and potential approaches was analytical; no physical testing was performed during this investigation. Five candidate munitions were considered for tagging. The candidates included munitions that were used at firing ranges and that stayed within one meter of the surface when they entered the ground and did not explode. These munitions were the BLU-97, MK-52 practice bomb, M720, M229, and 155 mm projectile. Because these munitions vary considerably in physical shape and size, no universal attachment method seemed realistic. However, mounting a tag to each munition type was deemed feasible with minor modifications to the munition. Distinct techniques were developed for each of these munitions. Figure 13 shows one potential approach for the MK-52 practice bomb.
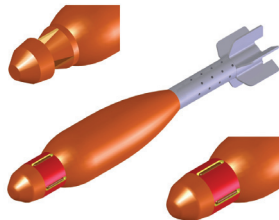


Fig. 13. One example of mechanically mounting a tag on a munition .

## 5. Evaluation and testing

Experimental efforts involved the design, fabrication, and tuning of the custom coil circuits. The tuning circuits for the high-voltage, one-meter diameter transmit coil and the corresponding receive coils were built. The basic results of the modeling were verified, although not every parameter was examined in the lab and field.

### 5.1 Lab evaluation

Figure 12 shows the laboratory setup for characterizing the one-meter transmit coil and the Tiris tags. The Tiris tag was mounted on a BLU-97 munition 4.3 mm (0.17 inch) from the steel body using a 2.8-mm thick ferrite spacer and a 1.5-mm thick circuit board spacer. The circuit board allowed probes to be attached for monitoring voltage levels. The frequency-domain view of the Tiris tag's response shows the frequency shift keying between 123 kHz and 134 kHz.

Experiments were performed to determine the distance from a transmitting coil that a tag could be activated by measuring the voltage level at the tag coil. Ranges greater than two meters were observed in this configuration. These lab experiments were repeated with the tag mounted on an inert munition. Similar results were seen as long as the tag separation from the munition was sufficient. Later experiments observed the field generated by the tag at the above-ground receiving coil. For optimized conditions, munition/detection coil separations greater than one meter were achieved in the lab with the tag on a munition. Tagged munitions were also detectable at one meter in the experimental field trials in dry clay soils. These findings supported the modeling results.

As expected and predicted by the modeling, the tag proximity to the munition surface was important not only for receiving a signal but also maintaining a high $Q$-value so the tag could respond. In the lab setting with the BLU-97 munition, a separation distance of 4.3 mm (0.17 inch) produced acceptable results. This separation was less than the 6 mm minimum predicted by theory because a layer of ferrite 2.8 mm thick was placed between the tag and the ordnance item.

Even at separations greater than two meters, signal-to-noise ratios greater than 5 dB were observed when averaging was performed. Figure 12 shows a spectrum analyzer view of the FSK signal with a 7-dB signal-to-noise ratio. The data sets were taken with a digital oscilloscope that measures voltage waveforms as a function of time. The digital portion of the integrated circuit in the Tiris tag outputs a digital data stream of 64 bits that include synchronization information and information stored in its memory. This digital waveform then drives modulation circuitry that, in simple terms, transmits a tone at 123 kHz to represent a logical "zero" and a tone at 134 kHz to represent a logical "one."

This type of frequency-domain plot is useful for detecting the presence of a digital FSK signal but it is not useful for determining the information content of the digital signal. The ultimate detection system will demodulate the FSK signal and determine the underlying data. Such detail was not necessary for this proof-of-concept program. In a future effort, processing could be added to the detection circuitry that would perform the Fourier transform to convert the data to the frequency domain and allow signal processing that would identify low-level signals in the presence of noise and interference.

### 5.2 Field testing

The tagged-ordnance system was tested at the Aberdeen Test Center (ATC) located at Aberdeen Proving Ground. Nine tagged surrogates were buried with three untagged

surrogates buried near the tagged surrogates to simulate the presence of buried clutter. ATC provided the location and depth information of the buried objects *after* their locations were predicted. The detection system shown in Figure 14 was used to transmit the tag activation signal and receive the tags' responses. The transmit coil is one meter in diameter and the receive coils are 30.5 cm (12 inches) in diameter.
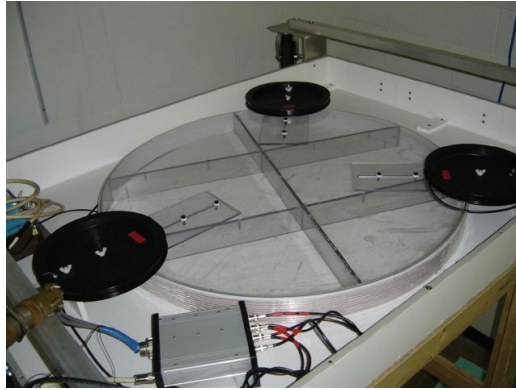


Fig. 14. The interior of the coil module showing the one-meter diameter transmit coil and the three separate receive coils.

The surrogates were solid steel cylinders that were 5 cm (2 inches) in diameter and 30.5 cm (12 inches) long. The nine surrogates had grooves milled into their surface into which tags were embedded. A photo of one of the tagged cylinders is shown in Figure 15. The tag had 5.65 mm (0.22 inch) of material between it and the surrogate munition including 2.85 mm of plastic next to the cylinder and 2.8 mm of ferrite next to the tag.



Fig. 15. Munition surrogate later buried at Aberdeen Test Center. The tag is evident below the red tape.

The nine targets were buried in a fairly small area because there was no need to test search rate at this point in the development cycle. ATC buried the objects in a four-meter by four-meter area.

The signals from the three receive coils were plotted on the oscilloscope after the scope performed Fourier transforms on the signals. Example frequency-domain plots are shown in

Figure 16. The left and right vertical yellow cursors are positioned at 120 and 130 kHz, respectively. The left figure shows the signal from an untagged surrogate (essentially background noise). The figure on the right represents the background noise-plus-interference environment; signal strength is significantly higher at the two cursors. The tag is replying to the interrogating signal by switching between 123 and 134 kHz.
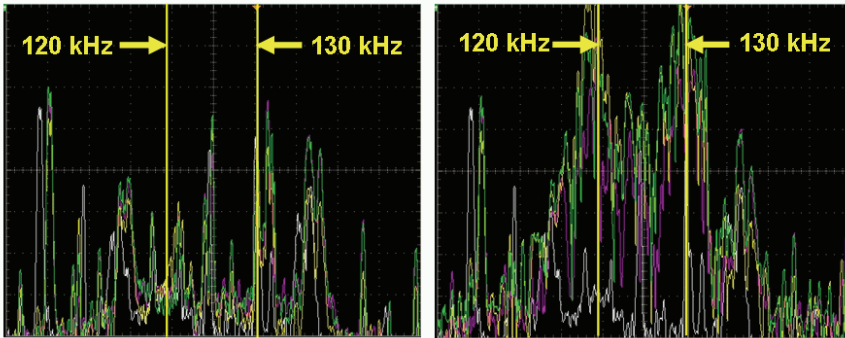


Fig. 16 (Left) Example data plot with no tagged surrogate present. (Right) Example data plot with coil module positioned above a tagged surrogate; signal strength is much higher at the two cursor positions.

The locations of the surrogates (tagged and non-tagged), Battelle's predicted positions, and data acquisition points are shown in the plot of Figure 11. The square markers indicate the positions of the tagged surrogates, the three triangles indicate where non-tagged surrogates were placed, the large circles represent Battelle's predicted positions of the tagged surrogates, and the diamonds indicate the position of the center of the transmit coil when data sets were recorded. The depth of each tagged surrogate is indicated with text. The predicted positions are indicated with large-diameter circles because of the large "footprint" of the coil module. The circle represents the uncertainty in the predicted position of the buried tag, an uncertainty similar to resolution cell size in an image. The actual resolution cell size was not determined experimentally, but modeling indicates it is a function of munition depth and orientation. A shallow munition might be detectable when the center of the coil module is one meter from the position of the buried tag but a one-meter-deep tag might only be detectable when the center of the coil is within 25.4 cm (10 inches) of a position directly over the tag.

Eight of the nine buried tagged surrogate positions were predicted. As stated previously, nine tagged surrogates were sent to ATC but the actual number buried was unknown at the time of the test. Figure 17 indicates the reasonable success in predicting the positions of the eight targets.

One tagged surrogate was missed completely by the predicting process. The missed surrogate, which was buried one meter below the surface, is shown in Figure 12 at position (0.5, 2.5). It was described by ATC personnel as "Tagged surrogate parallel to the surface with the *tag down.*" The phrase "tag down" implies the tag's position on the surrogate is underneath the item, as far from the surface and the coil module as possible and in the untagged surrogate's shadow. The untagged surrogate was 15.2 cm (6 inches) above and parallel to the tagged surrogate. The figure shows that a data set was taken directly over the missed surrogate. After Battelle provided its predictions and ATC supplied the actual

positions, the data set taken at (0.5, 2.5) was examined to see if the tag's signal existed in the data set. In fact, the tag's signal was very strong in the frequency-domain plot. It was concluded that the analysis and decision-making processes used for this test were too simplistic. An improved algorithm was needed.

Although this tagged surrogate's location was not predicted, it is encouraging that the tag's signal is very strong in the data even though it is at maximum depth at worst case position. Improved data presentation, analysis, and interpretation will allow similar tags to be correctly predicted in future assessment exercises.
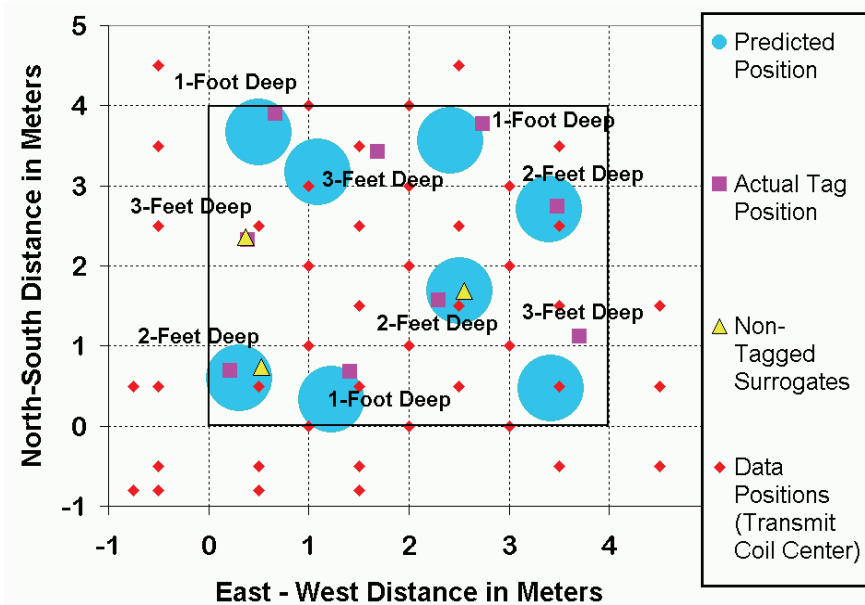


Fig. 17. Plan view of the test grid at Aberdeen Test Center showing the actual tagged munition positions, Battelle's predicted positions, and the positions where Battelle acquired data.

## 6. Summary

This study showed that the use of RFID tags to aid detection of UXO was feasible. Tags with solenoidal geometry, similar to the TI Tiris tag, are preferred for practical signal detection reasons. These tags show promise for being able to be mounted on munitions as well as surviving launch and impact. Analysis provided insight into the parameter variations necessary for optimizing the system, such as mounting the tags with some separation from the munition surface to allow sufficient magnetic energy into the tag and to allow the tag to operate properly. Field testing with the UXO interrogation system prototype was successful. Efforts incorporating further optimal design and detection algorithm adjustments remain.

## 7. Acknowledgements

## 8. References

Davis, R.; Shubert, K., Barnum, T. & Balaban, B. (2006). Buried Ordnance Detection: Electromagnetic Modeling of Munition-Mounted Radio Frequency Identification Tags, *IEEE Transactions on Magnetics*, Vol. 42, No. 7, (Jul. 2006) pp. 1883-1891, ISSN 0018-9464

GAO Report (2004). DoD Operational Ranges; More Reliable Cleanup Cost Estimates and a Proactive Approach to Identifying Contamination Are Needed, General Accounting Office Report GAO-04-601

Halman, J.; Shubert, K. & Ruck, G. (1998). SAR processing of ground-penetrating radar data for buried UXO detection: results from a surface-based system, *IEEE Transactions on Antennas Propagation*, Vol. 46, No. 7, (Jul. 1998), pp. 1023-1027, ISSN 0018-926X

Purello, M. (2002). New Maximum Allowable Environments (MAE) For HERO Unsafe Ordnance and HERO Susceptible Ordnance, Dahlgren Division, Naval Surface Warfare Center, Systems Electromagnetic Effects Branch (J52)

Shubert, K. ; Davis, R., Barnum, T., Balaban, B., Amdor, R., Sikorski, B., Peters, T., & Griffin, J. (2007). Enhanced Electromagnetic Tagging For Embedded Tracking Of Munitions And Ordnance During Future Remediation Efforts, Final Technical Report on Project MM-1272 prepared for the Strategic Environmental Research and Development Program

Shubert, K.; Davis, R., Barnum, T. & Balaban, B. (2008). RFID Tags to Aid Detection of Buried Unexploded Ordnance, *IEEE Antennas and Propagation Magazine*, Vol. 50, No. 5, (Oct. 2008), pp. 13-24, ISSN 1045-9243

Skilling, H (1957). *Electrical Engineering Circuits, Second Edition,* John Wiley and Sons, Inc., New York

# Reordering of Location Identifiers for Indexing an RFID Tag Object Database

Sungwoo Ahn and Bonghee Hong
*Pusan National University*
*Republic of Korea*

## 1. Introduction

Radio frequency identification (RFID) has become one of the emerging technologies for a wide area of applications such as automated manufacturing, inventory tracking, and supply chain management. RF technologies make it possible to identify individual items in real-time by means of automatic and fast identification. Besides the real-time identification, RF technologies give additional advantages for monitoring of field-based operation by tracking and tracing the location of tags attached to items. By using queries on trajectories of RFID tag data, RFID applications can get events about field-based situation and then respond to them.

To store and retrieve tag data efficiently, it is important to provide an index for the repository of tag data. The EPCglobal, being in charge of a standards management and development for RFID related technologies, proposes EPC Information Service (EPCIS) as the repository for tag events. The EPCIS is a standard interface for access and persistent storage of tag information. Tag data stored in the EPCIS consists of the static attribute data and the timestamped historical data. Historical information is continuously collected and updated whenever each tag is identified by an RFID reader. The EPCIS usually stores them at the base table of a database for efficient management of those data. It is necessary to execute queries on the EPCIS whenever applications want to retrieve the location history of specific tags. However, it is inefficient to look up all the records of the table because a large amount of historical information for tags is to be accumulated in the base table.

For efficient query processing of tracing tags, an index structure can be constructed based on tag events generated when a tag goes in and out a location where a reader places. Among timestamped historical information contained in tag events, an RFID application uses the location identifier (LID), the tag identifier (TID), and the identified time (TIME) as predicates for tracking and tracing tags. To index those values efficiently, we can define the *tag interval* by means of two tag events generated when the tag enters and leaves a specific location, respectively. The tag interval could be represented and indexed as a time-parameterized line segment in a three-dimensional domain which is constituted by LID, TID, and TIME axes.

Tag intervals in a three-dimensional index are sequentially stored and accessed in one-dimensional disk storage. Since logically adjacent tag intervals are to be retrieved together at a query, they should not be stored far away from each other in the disk to minimize the cost

of disk accesses. Logical closeness has been studied to determine the distance between domain values representing the coordinate of those objects. A logically adjacent object to a specific object on the data space has the shortest distance to that object by using some distance measure. Note that the change of the order of domain values results in the variation of distances between objects because of a different distribution of objects on the data space. Thus, domain values should be ordered properly in each domain in order to keep logical closeness between objects.

Most works for clustering spatial objects have used the spatial distance in the spatial domain as the distance measure. To diminish the number of disk accesses at answering spatial queries, they stored adjacent objects sequentially based on the spatial proximity. In addition to the spatial proximity, moving object databases M.F. Mokbel and Y. Theodoridis have applied the temporal proximity to the characteristic for the distance measure in the time domain. Previous works assumed that all domains on the data space provide the proper proximity about measuring the distance between domain values.

Since an LID represents the location where a tag stays or passes, the LID domain should provide logical closeness for the dynamic flow of tags along locations. The problem is that there is no rule of assigning LIDs to RFID locations in order to keep this property. If LIDs are arbitrarily arranged in the domain without considering tag flows, tag intervals would be scattered into the data space irrespective of logical closeness. Because this situation causes random disk accesses for searching logically adjacent tag intervals, the cost of query processing will be increased.

To solve this problem, we propose a reordering method for arranging LIDs in the LID domain. The basic idea is to compute the distance between two LIDs for preserving logical closeness of tag intervals. To do this, we define the proximity function based on a new *LID proximity* between two LIDs. The proximal distance between LIDs can be computed by the tag movements. To determine LID proximity, we need to examine *the path of tag flows* which is generated by tag movements. Then, we define the *LID proximity function* which computes the distance between LIDs with the dynamic flow of tags. To determine a sequence of LIDs based on LID proximity, we construct a weighted graph and generate the ordered LID set. It is possible to store logically adjacent tag intervals close to each other in the disk because our reordering method can keep the correlation between the distance and logical closeness of tag intervals. To prove this, we evaluate the performance of the index scheme using LIDs based on LID proximity as domain values. We also compare it with the index scheme using the numerical order of LIDs.

The reminder of this paper is organized as follows. Section 2 defines the problem of an LID as the domain value for tag intervals and describes the needs of reordering LIDs. Section 3 examines the path of tag flows based on the characteristics of RFID locations and tag movements, and then defines the LID proximity function. In Section 4, we propose a reordering scheme of LIDs using a weighted graph that is constructed by LID proximity. Section 5 presents some experimental results of performance evaluation for the proposed reordering scheme. A summary is presented in Section 6.

## 2. Problem definition

### 2.1 Target environment

Whenever the tag attached to an item passes through an RFID reader, the reader collects the tag's information within its interrogation zone. In an RFID middleware system, gathered

information are represented as *EPCIS tag events* and stored at the persistent storage in order to answer tag related queries. Since a tag event contains several timestamped historical information, it could represent the dynamic flow of tagged items between RFID locations placed along tag routes. If an RFID application wants to know a history of these items, a query processor can make an answer to the application by retrieving suitable tag events in a repository of tag events.

In timestamped historical information, a query processor usually employs the tag identifier (TID), the location identifier (LID), and the timestamp (TIME) as the predicates of queries for tracing tag locations. For efficient query processing of tracing tags, the tag trajectory should be modeled and indexed by using these predicates.

Note that RFID locations are different from the spatial locations to represent real positions on the map. There are two types of location related to EPCIS tag events according to a business perspective for an RFID location. One is the physical position which identifies the tag. We denote this position as the *read point* (RP). The read point does not provide the information where a tag visited or stays by itself because it designates only the place at which a tag was detected. The other is the region where a tag stays. We denote this region as the *business location* (BizLoc). The business location represents the place where a tag is assumed to be until a subsequent tag event is generated by a different business location. Since most of RFID applications trace a business flow of tagged items, they have an interest in the business location instead of the read point as the location type of the tag. Therefore, it is natural to use the business location as the LID predicate for tracing tag locations.

The EPCIS tag event could be modeled as the time parameterized interval in a three-dimensional domain whose axes are LID, TID, and TIME. We denote this interval as the *tag interval* (TI). The tag interval is a line segment that connects two coordinates in a three-dimensional space when the tag enters and leaves a specific business location. In this manner, the trajectory of a tag is represented as a set of tag intervals which are associated with the tag.

| Predicate | | | Query results | Query types |
|---|---|---|---|---|
| LID | TID | TIME | | |
| point/set/range | * | point/range | TID(s) | Observation Query (OQ) |
| * | point/set/range | point/range | LID(s) | Trajectory Query (TQ) |

Table 1. Query classification for tracing tag locations

Queries for tracing tags are classified into two types according to a kind of restricted predicate as shown in Table 1. An *observation query* (OQ) is used to retrieve the tag(s) that are identified by the specified business location(s) in the specified time period. A *trajectory query* (TQ) is used to retrieve the business location(s) that the specific tag(s) enters and leaves within the specified period. Queries in Table 1 can be extended to a combined query by performing two queries in the order OQ and TQ.

To support fast retrieving of desired trajectories of tags, it is necessary to store and search tag trajectories by means of an index structure. Each leaf node of the index references logically adjacent tag intervals on the data space by using minimum bounding box (MBB). Then, tag intervals referenced by index nodes are sequentially stored and accessed in one-

dimensional disk storage. Tag intervals on each leaf node are stored at the same disk page in order to minimize disk seeks.

## 2.2 Problem of using an LID as the domain value

(a) Logical closeness between tag intervals is very important for simultaneous accessing at the query. It gives a great influence on the performance of query processing because the cost of disk accesses depends on the sequence of storing tag intervals on the disk. For example, let us assume that a query, $Qi$, would search tag intervals by the index structure. If all tag intervals accessed by $Qi$ are stored in P3 as shown in Fig. 1-(a), a query processor needs to access just one disk page, P3. If those tag intervals are dispersed to disk pages, P2, P3, and P5 as shown in Fig. 1-(b), however, a query processor usually require the additional cost about accessing two pages, P2 and P5. To minimize the cost of disk accesses, logical closeness between tag intervals in the same disk page should be higher than logical closeness to others.

| P1 | P2 | **P3** | P4 | P5 | ••• |
| --- | --- | --- | --- | --- | --- |

| P1 | **P2** | **P3** | P4 | **P5** | ••• |
| --- | --- | --- | --- | --- | --- |

(a) All tag intervals accessed by the query $Q_i$ are stored in P3      (b) Tag intervals accessed by the query $Q_i$ are stored in P2, P3, P5
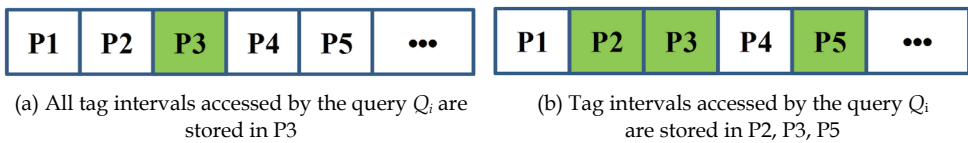
Fig. 1. An example of different access cost of the disk

Distance between two tag intervals on the data space should be computed for measuring logical closeness between them. If the distance measure keeps logical closeness between tag intervals, we can say that the nearest tag interval to a specific tag interval has the shortest distance to that tag interval. The distance is normally measured based on proximity between domain values on the data space. Thus, we need to examine the characteristic of each domain's proximity in order to keep correlation between the distance and the logical closeness.

The TIME domain in 3-dimensional space should provide chronological closeness between tag intervals. We usually achieve this closeness with assigning timestamps based on the temporal proximity in the TIME domain. The TID is the fixed identifier, which is related to Electronic Product Code (EPC), for a tagged item. The EPC can be composed of three parts – *Company*, *Product* and *Serial*. Since the EPC scheme assign an identifier to a tag by a hierarchical manner with three parts, the TID can imply logical closeness between grouped tags.

A tag produces a dynamic flow while moving between business locations. Since a query for tracing tags would give tag's traces, the LID domain should provide the closeness of tag intervals about tag movements. On the contrary to the TID, the LID is not the predefined identifier. We can assign business locations to LIDs by various numbering methods. For example, it can be some lexicographic method for measuring the distance in an RFID applied system. It is also possible to apply spatial distance measure such as Hilbert curve, Z-ordering, and Row-Prime curve. Figure 2 shows an example of numbering LIDs for describing business locations and read points.

Despite the existence of various LID numbering methods, the problem is that they do not have an inherence property of proximity for providing logical closeness related to the

dynamic flow of tags. If LIDs are assigned to business locations without considering tag's flows, each leaf node of the index may reference tag intervals irrespective of their logical closeness. This means that the index structure does not guarantee a query processor to retrieve results with minimal cost because logically adjacent tag intervals will be stored far away from each other at disk pages.



(a) The organization of RFID locations

(b) An example of assigning identifiers to business locations of (a)
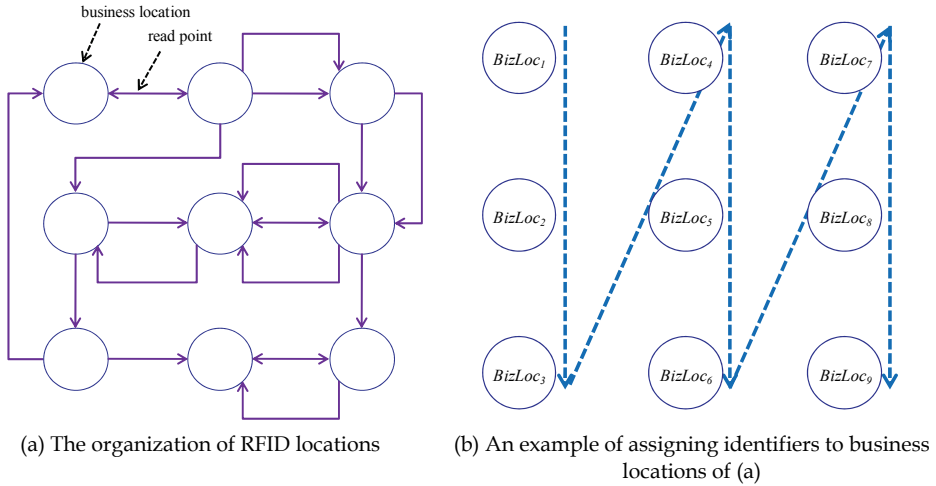
Fig. 2. An example of numbering method for business locations



(a) Assigning LIDs by some lexicographic method

(b) Assigning LIDs by the tag flow
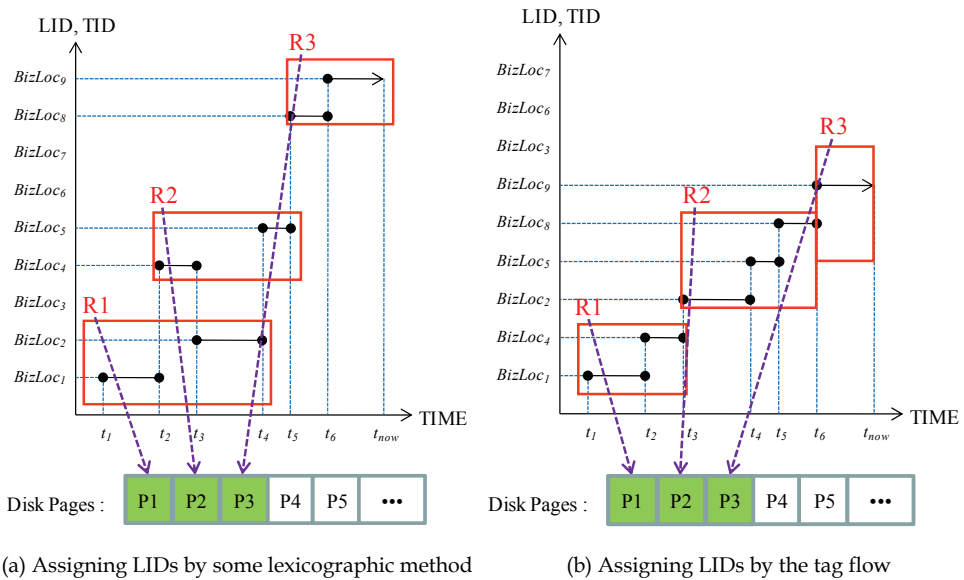
Fig. 3. Different organization of the index according to the order of LIDs

This situation is illustrated in Fig. 3. Assume that a tag, $TID_m$, passes through business locations of Fig. 2 in $BizLoc_1$, $BizLoc_4$, $BizLoc_2$, $BizLoc_5$, $BizLoc_8$, and $BizLoc_9$ order. If LIDs are arranged according to the order of Fig. 2-(b), tag intervals would be distributed on the data space and stored at disk pages as shown in Fig. 3-(a). Let $TQ_i$ = (*, $TID_m$, [$t_3$, $t_6$]) be the trajectory query for searching LIDs where $TID_m$ stayed during the period $t_3$ to $t_6$. When $TQ_i$ is processed at the index organized as shown in Fig. 3-(a), a query processor should access disk pages, P1, P2, and P3 because all tag intervals generated during the period $t_3$ to $t_6$ are dispersed to all MBBs, R1, R2, and R3. However, if we make LIDs reorder based on the order of $TID_m$'s movement as shown in Fig. 3-(b), tag intervals during the period $t_3$ to $t_6$ can be referenced by one leaf node having R2. A query processor needs to access only the page, P2 in order to process $TQ_i$ over the index of Fig. 3-(b).

We solve this problem by defining LID proximity. LID proximity determines the distance between two LIDs in the domain. If two LIDs have higher LID proximity than others, corresponding tag intervals could be distributed closely on the data space. In the remainder of this paper, we analyze factors to deduce LID proximity. Subsequently, we define the LID proximity function based on those factors. To determine the order of LIDs with LID proximity, we also propose the reordering scheme of LIDs.

## 3. Proximity between LIDs

### 3.1 LID proximity based on the path of tag flows

Tagged items always move between the business locations passing through the read points placed in the entrance of each business location. If there are no read points connecting with specified business locations, however, the tagged item cannot move directly between them. Although read points exist, the tag movement can also be restricted because of a business process of an applied system. According to these restrictions, there is a predefined path which a tag is able to cross. We designate this path as the *path of tag flows* (FlowPath). The items attached by the tags generate a flow of tags passing through the path. The FlowPath from $LID_i$ to $LID_j$ is denoted as $FlowPath_{i\,to\,j}$.



(a) A graph example for business locations connected by their read points

(b) A generation of FlowPaths between LIDs using the graph (a)
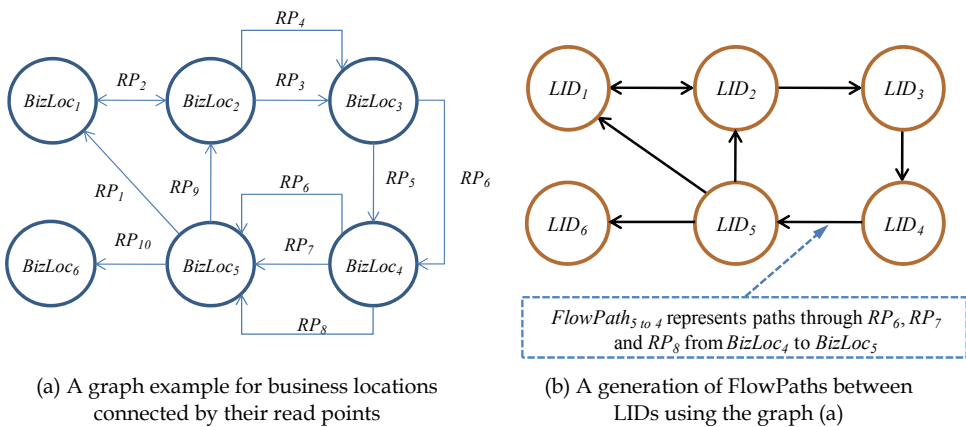
Fig. 4. An example of representing FlowPaths with business locations and their read points

The FlowPath is a simple method for representing the connection property between two business locations. It is possible to generate the FlowPath with a connected graph of business locations and read points as shown in Fig. 4. To do this, $BizLoc_1$ to $BizLoc_6$ in Fig. 4-(a) are corresponding with location identifiers, $LID_1$ to $LID_6$ in Fig. 4-(b), respectively. If one or more read points connect particular two business locations, they are represented as a single line connecting two LIDs as shown in Fig. 4-(b). Properties of a FlowPath are as follows.

1.  A FlowPath is a directional path because a read point has a directional property among three types of directions – IN, OUT, and INOUT.
2.  The number of FlowPaths connecting one LID with other LIDs is more than one because all business locations have one or more read points connecting other business locations.
3.  There may be no FlowPath which connect two particular LIDs directly. In this case, a tag should pass through another LIDs connected with those LIDs by FlowPaths in order to move from one to the other.

As mentioned in Section 2, a query for tracing tags is interested in a historical change of locations for the specific tag. This means that tag intervals generated by business locations along the specific FlowPath have higher probability of simultaneous access than others. Therefore, it is necessary to reorder LIDs based on the properties of a FlowPath for the efficient query processing. We first define the proximity between LIDs for applying to the LID reordering as follows.

**Definition 1. *LID Proximity (LIDProx)*** is the closeness value between two LIDs in the LID domain for tag intervals. We denote LID proximity between $LID_i$ and $LID_j$ as $LIDProx_{ij}$ or $LIDProx_{ji}$.

We also denote the LID proximity function for computing $LIDProx_{ij}$ as LIDProx($i$, $j$) or LIDProx($j$, $i$). LID proximity between two LIDs has following properties.

1.  Any $LID_i$ in the LID domain should have a LID proximity value to any $LID_j$ where $i \neq j$.
2.  $LIDProx_{ij}$ is equal to $LIDProx_{ji}$ for all LIDs.
3.  If $LID_k$, having the property LIDProx($i$, $j$) < LIDProx($i$, $k$), does not exist, the nearest LID to $LID_i$ is $LID_j$.

It is possible to represent LID proximity between all LIDs with a graph based on the FlowPath. To do this, a graph based on the FlowPath should satisfy following conditions. First, a graph should be a weighted graph that all edges in a graph have a weight value. Second, a graph should be a complete graph by the property (1) of LID proximity. Third, a graph should be an undirected graph by the property (2) of LID proximity. By these conditions, we define the graph G based on the FlowPath as follows.

- $G = (V, E, W)$
- $V$ = LIDSet = {$LID_1$, $LID_2$, …, $LID_n$} where $n$ is the number of LIDs in the LID domain
- $E = \{(LID_i, LID_j) \mid LID_i \in$ LIDSet, $LID_j \in$ LIDSet, $i \neq j\}$
- $w : E \rightarrow R$, $w(i, j) = $ LIDProx($i$, $j$) = LIDProx($j$, $i$) = $w(j, i)$

## 3.2 LID proximity function

The tag movements along FlowPaths and the frequency of their related queries are changed continuously over time. Consequently, the access probability of tag intervals generated by any two LIDs also changes as time goes by.

For applying dynamic properties of the FlowPath to LID proximity, we define the *LID proximity function* as shown in Eq. 1; we denote $T$ as the time to compute LID proximity, $\text{LIDProx}_T(i, j)$ as the LID proximity function at time $T$, $\text{LIDProx\_OQ}_T(i, j)$ and $\text{LIDProx\_TQ}(i, j)$ as proximity functions invented by properties of an observation query and a trajectory query, respectively.

$$\text{LIDProx}_T(i,j) = \alpha \times \text{LIDProx\_OQ}_T(i,j) + (1-\alpha) \times \text{LIDProx\_TQ}_T(i,j) \tag{1}$$

$\text{LIDProx}(i, j)$ is the time parameterized function that the closeness value between $LID_i$ and $LID_j$ changes over time. To consider the closeness value for an observation query and a trajectory query altogether, the function calculates the sum of $\text{LIDProx\_OQ}(i, j)$ and $\text{LIDProx\_TQ}(i, j)$ with the weight value. The weight $\alpha$ determines the applying ratio between two proximity functions as shown in Eq. 2; we denote $OQ_{ij,t}$ as the number of observation queries for $LID_i$ and $LID_j$ at time $t$ and $TQ_{ij,t}$ as the number of trajectory queries for $LID_i$ and $LID_j$ at time $t$.

$$\alpha = \begin{cases} 0 \text{ or } 1 & \begin{array}{l} \textit{if no queries are processed} \\ \textit{for } LID_i \textit{ and } LID_j \end{array} \\ \sum\limits_{t=1}^{T} OQ_{ij,t} \Big/ \sum\limits_{t=1}^{T} \left( OQ_{ij,t} + TQ_{ij,t} \right) & \textit{otherwise} \end{cases} \tag{2}$$

LID proximity for an observation query is proportionally influenced by the number of tag intervals generated by two LIDs which are predicates of the observation query. The function $\text{LIDProx\_OQ}(i, j)$ computes LID proximity for an observation query with the ratio of tag intervals generated by $LID_i$ and $LID_j$ to all tag intervals as shown in Eq. 3; we denote $TI_{i,t}$ as the number of tag intervals by $LID_i$ at $t$, and $\sigma_{OQ}$ and $\delta_{OQ}$ as weight values for $\text{LIDProx\_OQ}(i, j)$.

$$\text{LIDProx\_OQ}_T(i,j) = \frac{\delta_{OQ}}{\sigma_{OQ}} \times \left( \sum_{t=1}^{T} \left( TI_{i,t} + TI_{j,t} \right) \Big/ \sum_{t=1}^{T} \sum_{a=1}^{n} TI_{a,t} \right) \tag{3}$$

Because of the influence of the tag's flow on LID proximity, we should consider the distribution of tag intervals over time. Equation 4 represents dynamic properties of the tag interval distribution. The difference in the distribution of tag intervals in time domain can be represented by the standard deviation of tag intervals. To apply this property to LID proximity, the variable $\sigma_{OQ}$ in Eq. 4 is used as the inversely proportional weight to the number of tag intervals. This means that the lower standard deviation indicates that associated distribution of tag intervals is close to the uniform distribution; we denote $\sigma_{OQ}$ as the standard deviation of tag intervals by $LID_i$ and $LID_j$ and $\overline{TI_i}$ as the average number of tag intervals by $LID_i$ until $T$.

$$\sigma_{OQ} = \sqrt{\frac{1}{T} \times \sum_{t=1}^{T} \left\{ \left( TI_{i,t} + TI_{j,t} \right) - \left( \overline{TI_i} + \overline{TI_j} \right) \right\}^2}$$

$$\delta_{OQ} = \left( \sum_{t=1}^{T} \left( STI_{i,t} + STI_{j,t} \right) \Big/ \sum_{t=1}^{T} \left( TI_{i,t} + TI_{j,t} \right) \right) \times \left( 1 \Big/ \sum_{t=1}^{T} OQ_{ij,t} \right) \tag{4}$$

The hit ratio of tag intervals for an observation query is also the factor determining the LIDProx_OQ($i$, $j$). As opposed to the standard deviation $\sigma_{OQ}$, LID proximity for an observation query should be proportional to the hit ratio of tag intervals. The variable $\delta_{OQ}$ in Eq. 4 computes the proportional weight – the hit ratio of tag intervals for $OQ_{ij}$; we denote $OQ_{ij,t}$ as the number of observation queries for $LID_i$ and $LID_j$ at t and $STI_{i,t}$ as the number of results by $LID_i$ for $OQ_{ij,t}$.

$$\text{LIDProx\_TQ}_T(i,j) = \frac{\delta_{TQ}}{\sigma_{TQ}} \times \left( \sum_{t=1}^{T} \left( TM_{i\ to\ j,t} + TM_{j\ to\ i,t} \right) \middle/ \sum_{t=1}^{T} \left( \sum_{a=1}^{n} \sum_{b=1}^{n} TM_{a\ to\ b,t} - \sum_{c=1}^{n} TM_{c\ to\ c,t} \right) \right) \quad (5)$$

LID proximity for a trajectory query uses the pattern of tag movements along the FlowPath as the main factor because a trajectory query takes an interest in LIDs where a tag passes at the specified time period. Equation 5 shows the LID proximity function for a trajectory query retrieving tag intervals by $LID_i$ and $LID_j$. This function, denoted by LIDProx_TQ($i$, $j$), obtains the simultaneous access probability of $LID_i$ and $LID_j$ through the ratio of tag movements between $LID_i$ and $LID_j$ to the total number of tag movements for all LIDs; we denote $TM_{i\ to\ j,t}$ as the amount of tag movements from $LID_i$ to $LID_j$, and $\sigma_{TQ}$ and $\delta_{TQ}$ as weight values for LIDProx_TQ($i$, $j$).

Similar to the LID proximity function for an observation query, both the tag interval distribution over time and the hit ratio of tag intervals for a trajectory query have an influence on that for a trajectory query. Different with an observation query, however, a trajectory query should consider not the distribution of tag intervals for each individual LID but that of tag intervals between LIDs – the movements of the specified tag. To do this, we define the standard deviation, $\sigma_{TQ}$, for computing a degree of the difference in the distribution of tag movements between $LID_i$ and $LID_j$. We also define the hit ratio of tag intervals by $LID_i$ and $LID_j$ for a trajectory query as $\delta_{TQ}$.

## 4. Reordering scheme of LIDs

In this section, we define the reordering problem of LIDs based on the LID proximity function and propose the reordering scheme for solving this problem.

Let us assume that there is a set of LIDs, LIDSet = {$LID_1$, $LID2$, …, $LID_{n-1}$, $LID_n$}. To use the LIDSet for the coordinates in the LID domain, an ordered list of LIDs, $OLIDList_i$ = ($OLID_{i.1}$, $OLID_{i.2}$, …, $OLID_{i.n-1}$, $OLID_{i.n}$) should be determined first of all. It is possible to make $n!/2$ combinations of the OLIDList from $OLIDList_1$ to $OLIDList_{n!/2}$. To find out the optimal OLIDList that LID proximity for all LIDs are maximum, we first define the linear proximity as follows.

**Definition 2.** *Linear Proximity (LinearProx)* of $OLIDList_a$(*LinearProx$_a$*) is the sum of LIDProx between adjacent OLIDs for all OLIDs in OLIDLista such that

$$LinearProx_a = \sum_{i=1}^{n-1} \text{LIDProx}(i, i+1) \quad (6)$$

To get the optimal distribution of tag intervals in the domain space, LID proximity between two LIDs should be the maximum for all LIDs. That is, if a query accesses tag intervals generated by the LIDs in the query predicate, corresponding LIDs in the OLIDList should be

ordered closely. As a result, all of LID proximity between adjacent LIDs should also be maximum. With the definition of the linear proximity, we can define the problem for reordering LIDs in order to retrieve the OLIDList which has the maximum access probability as follows.

**Definition 3. *LID reOrdering Problem (LOP)*** is to determine an $OLIDList_o$ = ($OLID_{o.1}$, $OLID_{o.2}$, ..., $OLID_{o.n-1}$, $OLID_{o.n}$) for which $LinearProx_o$ is maximum where there is LIDSet = $\{LID_1, LID_2, ..., LID_{n-1}, LID_n\}$ and LID proximity for all LIDs.

To solve the LOP with LID proximity, the graph $G$ is formed by LIDs and their LID proximity values as shown in Fig. 5-(a). The LOP is to find out the optimal OLIDList which has the maximum linear proximity in the graph $G$ according to the Definition 3. In Fig. 5-(a), the optimal $OLIDList_o$ is ($LID_5$, $LID_1$, $LID_2$, $LID_4$, $LID_3$) or ($LID_3$, $LID_4$, $LID_2$, $LID_1$, $LID_5$) among 60 (5!/2) OLIDLists and its $LinearProx_o$ is 0.199.

The LOP is very similar to the well-known minimal weighted Hamiltonian path problem (MWHP) without specifying the start and termination points. The MWHP finds the Hamiltonian cycle which has a minimal weight in the graph. To apply the LOP to the MWHP, it is necessary to convert the LOP into a minimization problem because the LOP is a maximization problem for finding the order of having maximum LID proximity values for all LIDs. Therefore, the weight value for $LID_i$ and $LID_j$, $w(i, j)$ in the graph $G$ should be changed to 1 – LIDProx($i$, $j$) or 1 – LIDProx($j$, $i$). The LOP can be treated as a standard traveling salesman problem (TSP) by Lemma 1.



(a) A weighted graph $G$ representing LID proximity between LIDs

(b) The conversion of the graph $G$ into the graph $G'$ for solving the LOP
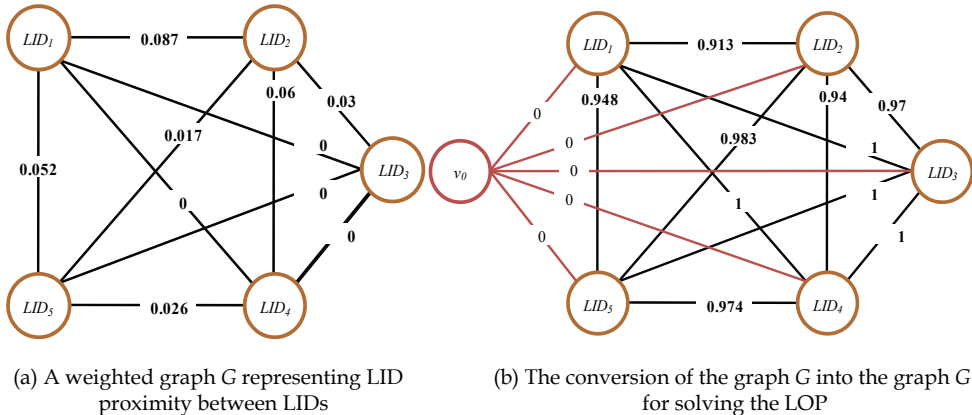
Fig. 5. An example of a weighted graph for reordering LIDs based on LID proximity

**Lemma 1.** The LOP is equivalent to the TSP for a weighted graph $G'$ = ($V'$, $E'$, $w'$) such that
$V'$ = $V$ $\cup$ $\{v_0\}$ where $v_0$ is an artificial vertex to solve the MWHP by the TSP
$E'$ = $E$ $\cup$ $\{(LID_i, v_0) \mid LID_i \in$ LIDSet$\}$
$w'$ : $E \to$ R, $w'(i, j)$ = 1 – LIDProx($i$, $j$) = 1 – LIDProx(j, i) = $w'$(j, i), $w'(i, v_0)$ = $w'(v_0, i)$ = 0
**Proof:** The graph $G'$ contains Hamiltonian cycles because $G'$ is a complete and weighted graph. Assume that a minimal weighted Hamiltonian cycle produced in $G'$ is $HC$ where $HC$ = (($v_0$, $OLID_{a.1}$), ($OLID_{a.1}$, $OLID_{a.2}$), ..., ($OLID_{a.n-1}$, $OLID_{a.n}$), ($OLID_{a.n}$, $v_0$)) and $OLID_{a.i} \in$ LIDSet. If two edges, ($v_0$, $OLID_{a.1}$) and ($OLID_{a.n}$, $v_0$), containing the vertex $v_0$ are eliminated from $HC$, we can get a minimal weighted Hamiltonian path $L$ in $G'$ from $OLID_{a.1}$ to $OLID_{a.n}$. A weight

of *HC* is identical with one of a path *L* because all of edges eliminated in order to produce the path *L* contain the vertex $v_0$ and weights of these edges are zero. The produced path *L* is translated as an ordered LID list, *OLIDList$_a$* where *OLIDList$_a$* = (*OLID$_{a.1}$*, *OLID$_{a.2}$*, …, *OLID$_{a.n-1}$*, *OLID$_{a.n}$*). By this reason, the reordering of LIDs can be defined as a solution of the corresponding TSP for obtaining *HC* in the weighted graph *G'*.

Figure 5-(b) shows an example of the weighted graph *G'* to determine the OLIDList for LIDs in Fig. 5-(a). To apply the WMHP to the LOP, weights of edges are assigned to *w'*, the weight of an edge assigned to one minus LID proximity value. It means that the lower the weight of an edge is, the higher the probability of simultaneously accessing tag intervals generated by the corresponding LIDs of two vertices at each end of the edge is. Since the start and termination points are not determined in the graph *G*, we insert an artificial vertex $v_0$ and edges from $v_0$ to all vertices with weight 0 into the graph *G'*. Each Hamiltonian cycle is changed to a Hamiltonian path by removing vertex $v_0$ in the Hamiltonian cycle with same weight because the weight of all edges incident with $v_0$ is 0.

Because the TSP is a NP-complete problem, exhaustive exploration of all cases is impractical. To solve the TSP, there have been proposed dozens of methods based on heuristic approaches such as Genetic Algorithms (GA), Simulated Annealing (SA), and Neural Networks (NN). Heuristic approaches, can be used to find a solution for NP-complete problems, takes much less time. Although it might not find the best solution, it can find a near perfect solution – the local optima.

We have used a GA among several heuristic methods to determine the ordered LIDSet by using the weighted graph *G'*. This algorithm has been very successful in practice to solve combinatorial optimization problems including the TSP.

## 5. Experimental evaluation

We have evaluated the performance of our reordering scheme by applying LIDs as domain values of an index. We also compared it with the numerical ordering scheme of LIDs using a lexicographic scheme. To evaluate the performance of queries, TPIR-tree, R*-tree, and TB-tree are constructed based on the data model for tag intervals with the axes being TID, LID, and TIME. Since indexes use original insert and/or split algorithms, it is possible to preserve essential properties of them.

Since well-known and widely accepted RFID data sets such as the GSTD do not exist, we conducted our experiments with synthetic data sets generated by the Tag Data Generator (TDG). The TDG generates tag events which can be represented as the time-parameterized interval based on the data model for tag intervals. To reflect the real RFID environment, the TDG allows the user to configure its specific variables. All variables of the TDG are based on properties of the FlowPath and tag movements along FlowPaths. According to user-defined variables, tags are created and move between business locations through FlowPaths. The TDG generates a tag interval based on a tag event occurring whenever a tag enters or leaves. We assigned an LID to each business location by a lexicographic scheme of the TDG based on the spatial distance. To store trajectories of tags over the index, the TDG produces tag intervals from 100,000 to 500,000. Since the LID proximity function uses the quantity for each query, OQ and TQ, as the variable, we should process queries during the TDG produces tag intervals. To do this, we processed 10,000 queries for tracing tags continuously and estimated query specific variables over all periods. Finally, the sequence of LIDs based

on LID proximity is determined by computing the proximity value between LIDs until all the tag events are produced.

Experiments of this paper used the TDG data set constructed with 200 business locations. To measure average cost, all experiments were performed 10 times for the same data set. In the figures for experimental results, we rename the index by attaching the additional word with a parenthesis in order to distinguish each index according to the arrangement of LIDs. "Original" means the index using the initial arrangement of LIDs on the LID domain. "Reorder" means the index based on LID proximity.

**Experiment 1:** Measuring the performance of each query type

In this experiment, we attempted to evaluate the performance of queries where only one query type is processed in order to measure the performance of each query type. To obtain the optimized order of LIDs for each query type, we processed 10,000 OQs in Fig. 6-(a) and 10,000 TQs in Fig. 6-(b) before reordering scheme is processed.

Figure 6 shows the performance comparison between "Original" and "Reorder" for each query type. Figure 6-(a) and 6-(b) are related to the performance of OQ and TQ, respectively. Each query set includes 1,000 OQs or TQs. We find out that "Reorder" can retrieve the results with lower cost of node accesses than "Original" for all comparison in Fig. 6. The performance of most "Reorder" is slightly better than the performance of "Original" for the data set of 100,000 tag intervals. Nevertheless, "Reorder" still outperforms "Original" during tag intervals are generated continuously and inserted at the index.



(a) The number of node accesses for OQ          (b) The number of node accesses for TQ
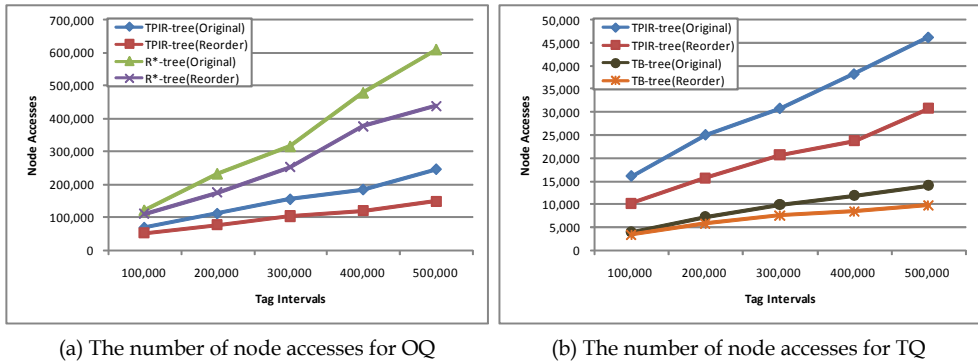
Fig. 6. Performance evaluation for indexes where only one type of query is used.

The search performance of OQ and TQ are improved up to 39% and 33%, respectively. This experiment tells us that LID proximity can measure the closeness between business locations more precisely if tag movements and queries happen continuously.

**Experiment 2:** Performance comparison in case of processing OQ and TQ altogether

Regardless of better performance than an initial arrangement of LIDs, Experiment 1 only evaluates the performance for individual query type. We need to measure the performance in case that OQ and TQ are processed altogether. To do this, we performed the experimental evaluation as shown in Fig. 7. Since LID proximity should reflect properties of all query types together, we processed both of 5,000 OQs and 5,000 TQs before the proximity is measured. Then, 1,000 OQs or TQs are processed for evaluating the performance of each query.

(a) The number of node accesses for OQ          (b) The number of node accesses for TQ
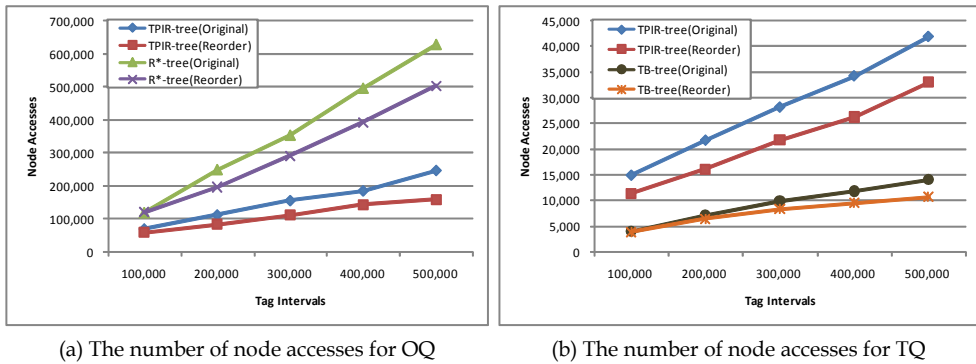
Fig. 7. Performance evaluation for indexes when processing both queries altogether

The result of Fig. 7 shows that the number of node accesses of "Reorder" is increased as compared with that in Fig. 6. The reason is that $LIDProx\_OQ_T(i, j)$ and $LIDProx\_TQ_T(i, j)$ in Eq. 2 have a negative effect on the performance of a query not related to each proximity under the condition that OQ and TQ are processed together. The performance of "Reorder" is nevertheless better than the performance of "Original" at processing all of OQ and TQ.

## 6. Conclusions

This paper has addressed the problem of using the location identifier (LID) as the domain value of the index for tag intervals and proposed the solution for solving this problem. The basic idea is to reorder LIDs by the LID proximity function between two LIDs. The LID proximity function determines which an LID to place closely to the specific LID in the domain. By using the LID proximity function, we can find out the distance of two LIDs in the domain so as to keep the logical closeness between tag intervals. Our experiments show that the proposed reordering scheme based on LID proximity considerably improves the performance of queries for tracing tags comparing with the previous scheme of assigning LIDs.

Since LID proximity is computed with the time parameterized properties, it changes over time. Therefore, it is necessary to reorder LIDs periodically or non-periodically for reflecting the changed LID proximity between LIDs. To process queries efficiently over all the time, the reconstruction of the tag interval index should also be required according to changing LID proximity. We are currently developing a dynamic reordering method of LIDs and a restructuring method of the index.

## 7. References

ChaeHoon , B.; BongHee, H. & DongHyun, K.(2005). Time Parameterized Interval R-tree for Tracing Tags in RFID Systems, International Conference on DEXA, pp.503-513

Dan. L.; HichamG, E.; Elisa, B. & BengChin, O. (2007). Data Management in RFID Applications, International Conference on DEXA, pp.434-444

Darrell, W.(1994). A Genetic Algorithm Tutorial, Statistics and Computing, Vol. 4, pp.65-85

EPCglobal.(2006). EPC Information Services (EPCIS) Specification, Ver. 1.0, EPCglobal Inc.

EPCglobal.(2006). EPC™ Tag Data Standards, Ver. 1.3, EPCglobal Inc.

Fusheng, W. & Peiya, L.(2005). Temporal Management of RFID Data, International Conference on VLDB, pp.1128-1139

HV,J.(1990). Linear Clustering of Objects with Multiple Attributes, ACM SIGMOD, Vol. 19(2), pp.332-342

Ibrahim, K.& Christos,F.(1993). On Packing R-trees, CIKM, pp.490-499

Mohamed F, M.; Thanaa M, G.&Walid G,A.(2003). Spatio-temporal Access Methods, IEEE Data Engineering Bulletin, Vol. 26(2), pp.40-49

Mark, H.(2003) EPC Information Service – Data Model and Queries, Technical Report, Auto-ID Center

Steven S, S.(1998). The Algorithm Design Manual, Springer-Verlag, New York Berlin Heidelberg

Yannis, T.;Jefferson R O, S.&Mario A, N.(1999). On the Generation of Spatiotemporal Datasets, International Symposium on Spatial Databases, pp.147-164

# An Efficient Cut-through Mechanism for Tree-based RFID Tag Identification Schemes

Nai-Wei Lo and Kuo-Hui Yeh
*Dept. of Information Management*
*National Taiwan Univ. of Science and Technology, Taipei,*
*Taiwan*

## 1. Introduction

Radio Frequency IDentification (RFID) technology successfully integrates radio transmitter and receiver, small size memory space and control circuitry to remotely store and retrieve data via wireless RF transceiver. As low-cost RFID tag can be massively manufactured by semiconductor industry, new applications associated with RFID technology have emerged rapidly such as inventory tracking, book storage and management, and airport baggage handling. Generally an RFID system is composed of many RFID tags (or tagged objects), at least one RFID reader, and one backend application system with database. An RFID tag gains its operation energy from query signals that are radio waves transmitted by RFID reader. Once a tag responds the query with its stored information to RFID reader, usually a unique identity number or string, the RFID system can recognize the tag carrier and perform required business logic operation.

As RFID technique is widely used in supply chain management, the corresponding RFID application systems are expected to process and manage large amount of tagged objects at a predefined period of time regularly. Therefore, for large-scaled RFID applications, tag reading throughput is very critical since it will affect the total data processing time. To measure tag reading throughput of a RFID system, two performance criteria are usually adopted: tag reading delay and reader energy consumption [5]. As RFID reader and tag always communicate over a shared wireless channel, it is very easy to have signal collisions during a normal tag identification process when multiple tags exist in reader's interrogation area. Signal collision results in query or data retransmission and eventually increases communication overhead and time delay of tag identification. Hence, an efficient tag collision arbitration mechanism is very important and critical for RFID systems to achieve effective performance.

Existing RFID tag identification schemes can be classified into aloha-based solutions [3, 10, 12-13, 16, 21, 23-24] and tree-based solutions [1, 2, 4, 6-9, 14-15, 17-20, 22]. In aloha-based schemes, a reader estimates the number of tags in its interrogation area and broadcasts the total number of timeslots to each tag. Then each RFID tag randomly selects its own timeslot to transmit its ID without knowing which timeslots have been selected by other tags. By distributing tag responses to distinct timeslots instead of getting all tag responses at the same time, aloha-based schemes effectively reduce the probability of signal collision. However, aloha-based schemes have tag starvation problem in which certain tags may not

be identified for a long period of time and consequently the predefined processing time for a RFID application system to recognize all existing tags may not be achieved. Tree-based schemes are based on tag-set splitting mechanism. When querying RFID tags, the RFID reader continuously splits signal-collided tags into two subsets until each tag set contains only one tag. This technique guarantees that every tag can be identified in a certain period of query time. As tree-based schemes are based on current tag responses to determine how tag subset should be formed and queried, higher energy consumption and increase of query time due to vast splitting and querying operations are emerged.

In this study, we introduce a cut-through mechanism (*CM*) to avoid serious signal collision cases in advance and improve tag identification efficiency for RFID system in consequence. From the viewpoint of tree structure, all tag IDs can be represented as leaf nodes of the abstract tree. When the number of tags to be queried is large, intermediate branch nodes of the abstract tree, that represent partial tag IDs sent in tag responses and locate only several levels above the leaf level, will have a significant probability to be visited during a tag identification process. By adopting *CM*, a tag identification scheme can bypass these colliding intermediate nodes during a tag recognition process. In addition, *CM* is a generic mechanism and it can be embedded with any given tree-based RFID tag identification protocol.

## 2. Cut-through Mechanism (*CM*)

Fig. 1 shows the scenario in a traditional binary-tree based tag identification protocol, once all current tags are spread in the lowest layer, i.e. leaf node, the upper several layers of the abstract tree structure will be full of collided nodes. The higher identification efficiency can be expected if we can ignore the visiting on these collided intermediate nodes. In other words, if we start the binary-tree based tag identification protocol from each node at the 4th layer instead of the root node, we will reduce all collided nodes (i.e. collided cycles) located at the first 3 layers. This leads to another interesting question: which is the best layer to start performing the tag identification procedure? For our analysis and simulation results, the solution depends on the number of tags, i.e. *q*, and the position of these tags, i.e. which leaf nodes they are located. Moreover, the impact weight of the number of tags is more important than the other one. Hence, the number of tags will be the main factor while considering how much layers (or collided intermediate nodes) we should cut off to pursue better system efficiency in a tag identification session.

The goal of *CM* is to avoid more collided nodes in the abstract tree structure before performing a tree-based tag identification protocol. This will make the whole tag identification process smoother and accordingly complete the tag recognition in a shorter time. More specifically, if we can recognize more readable nodes without visiting their collided ancestor nodes, the system throughput during the tag identification procedure will be better. This indicates that we can save all collision resolution operations which are supposed to perform on each of such collided ancestor nodes. On the other hand, in a tree based tag recognition protocol, the identification efficiency will be decreased if the reader has to visit some idle nodes without any useful feedback. As a result, it is critical to find the target layer *h* which possesses the best trade-off between the number of collided nodes and the number of idle nodes in such layer. If we cut off more collided (and useless) nodes, the better identification efficiency is obtained. However, the idle nodes should be carefully handled as the elimination of them may result in poor performance. This is because each idle node is produced by at least one descendant idle node in the abstract tree structure

corresponding to the target tag identification scheme. In the following, we present our simulation results to show how many layers should be eliminated before invoking a tree based tag identification protocol to pursue better efficiency.
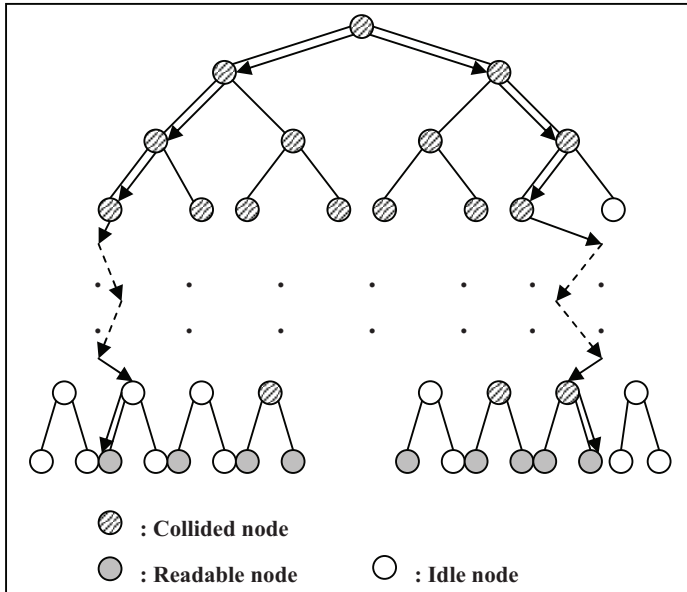


Fig. 1. A scenario in traditional binary-tree based tag identification protocol.
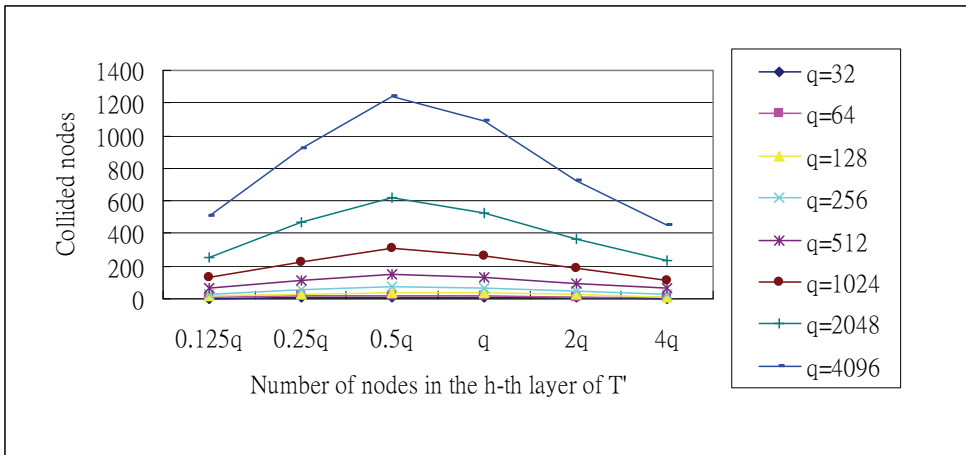


Fig. 2. Collided nodes in the $h^{th}$ layer of $T'$ with different number of tags. Note that the length of ID is 96 bits.

From Fig. 2 and 3, we find that the $h^{th}$ layer, where the number of nodes ($2^h$) is closest to $0.5q$, is the best candidate layer to start the target tag identification scheme. In such layer, the

ratio of the number of collided nodes to the number of total nodes, i.e. $2^h$, is the highest, and at the same time the number of idle nodes is not so large (within an acceptable level). If we invoke the target tree based tag identification protocol on each node of the $h$th layer instead of root node, all collided intermediate nodes in the ancestry layers of the $h$th layer can be ignored to visit. More precisely, performance improvement can be gained by ignoring the visiting on the collided nodes located from the 1st to the $(h-1)$th layers. Meanwhile, the reader only wastes a little time to visit few idle nodes at the target layer $h$. This interesting finding is utilized to construct the detailed procedure of *CM* in the next subsection.
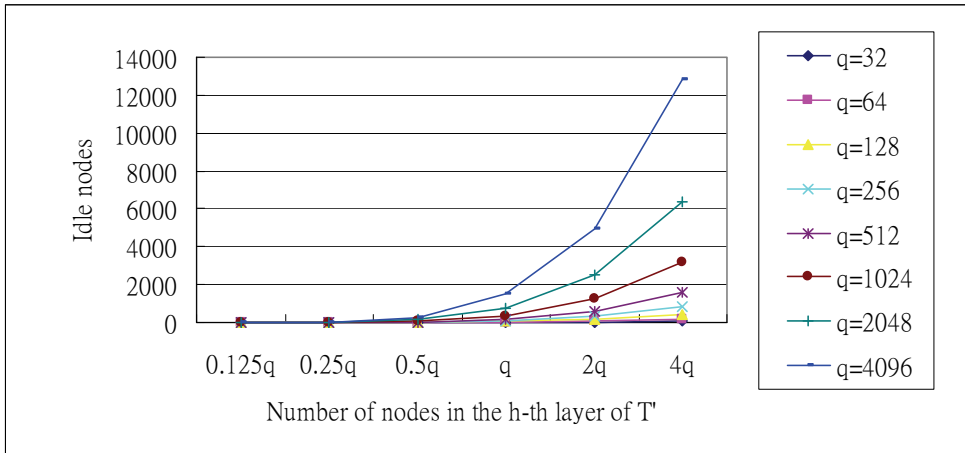


Fig. 3. Idle nodes in the $h$th layer of $T'$ with different number of tags. Note that the length of ID is 96 bits.

Cut-Through Mechanism (the operation at reader side)
/* Cut off useless collided nodes of target tree *T*/

1    Input the number of current tags $q$
2    Search the left-most readable node *LN* and the right-most readable node *RN* of *T*
3    Construct a new tree *T'* with the trajectory of finding *LN* and *RN*
4    Search the $h^{th}$ layer of *T'* in which the value of $2^h$ is the closest one compared to $0.5q$
5    For each node in the $h^{th}$ layer of *T'*
         Invoke "targeted tree-based tag identification
            protocol such as QT, BS and *k*-TAS"

Fig. 4. *CM* algorithm at RFID reader side.

As mentioned before, this study focuses on solving the tag signal collisions in the circumstances of the RFID applications in section II. In such applications, it is reasonable to assume that the number of tags is known. Under this assumption, we present the detail of *CM* in Fig. 4. The reader first probes the left-most readable node and right-most readable node in sequence. With the retrieval trajectory of these two nodes, a new tree structure $T'$, which is contained in the target tree $T$, can be constructed. An example of $T'$ is referred to the partial tree structure surrounded by the black arrow lines (and black dotted arrow lines) in Fig. 1. Next, as the number of current tags, i.e. $q$, is known in *CM*, the reader searches the $h$th layer of $T'$ in which $0.5q$ is closest to $2^h$. Finally, for each nodes on the $h$th layer of $T'$, the reader recursively invoke the target tag identification schemes such as Query Tree (QT) [1, 4, 8, 15, 22], Binary Search (BS) [7, 11], ETIP [25] and k-TAS [26].
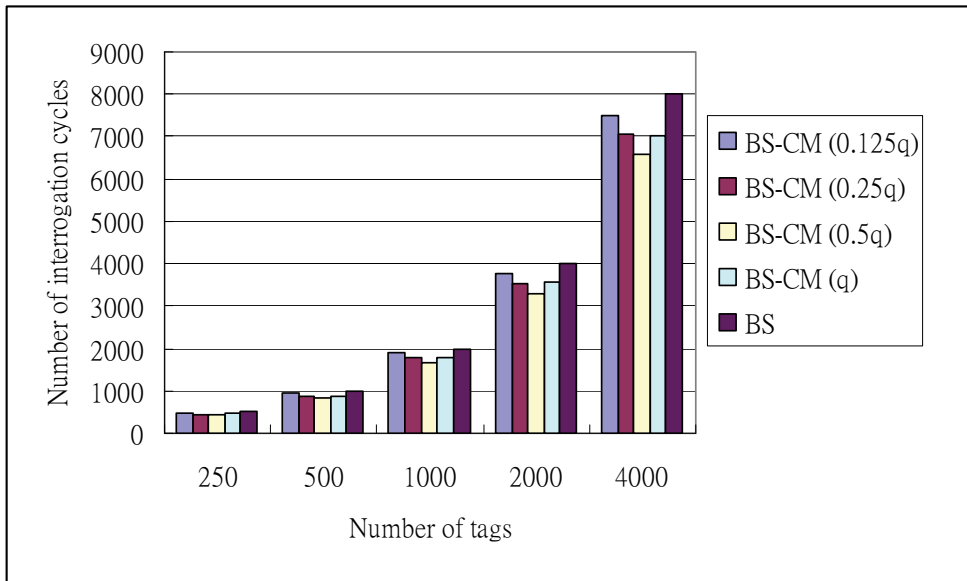


Fig. 5. The communication overhead of BS protocol embedded with *CM*. Note that the length of ID is 96 bits.

Fig 5 and 6 present the identification delay and communication overhead of BS embedded with *CM* in terms of the total interrogation cycles and the amount of transmitted bits. Note that BS-CM (0.25$q$) denotes the BS protocol is invoked at each node in the $h$th layer of target tag identification tree in which $2^h$ is closest to 0.25$q$. For the aspect of the identification delay (Fig. 5), BS-CM (0.5$q$) shows the best performance as the total interrogation cycles for identifying all tags is reduced between 15.5% ($q$=250) and 17.7% ($q$=4000). As the number of tags rises, the improvement is more significant. This results from that the rise of the number of tags will increase the number of collided cycles, and accordingly complicate the tag identification procedure itself. Since the focus of *CM* is to cut off unnecessary collided nodes, the reader embedded with *CM* can obtain better performance by avoiding more collided cycles (i.e. collided intermediate nodes in the abstract identification tree structure). In Fig. 6, BS-CM (0.5$q$) and BS-CM ($q$) both show performance improvement by eliminating

4.8%-6.2% and 6%-10% of total transmitted bits, respectively. Similarly, *CM* is more efficient on the communication overhead when the number of tags becomes larger (i.e. the number of collided nodes rises). Based on these two results, we can conclude that *CM* is significantly effective in reducing the collided cycles during a tag identification process. As *CM* is simple and independent of existing protocol properties, any tree-based arbitration protocol can easily embed *CM* for better performance. This embeddedness characteristic of *CM* is valuable.
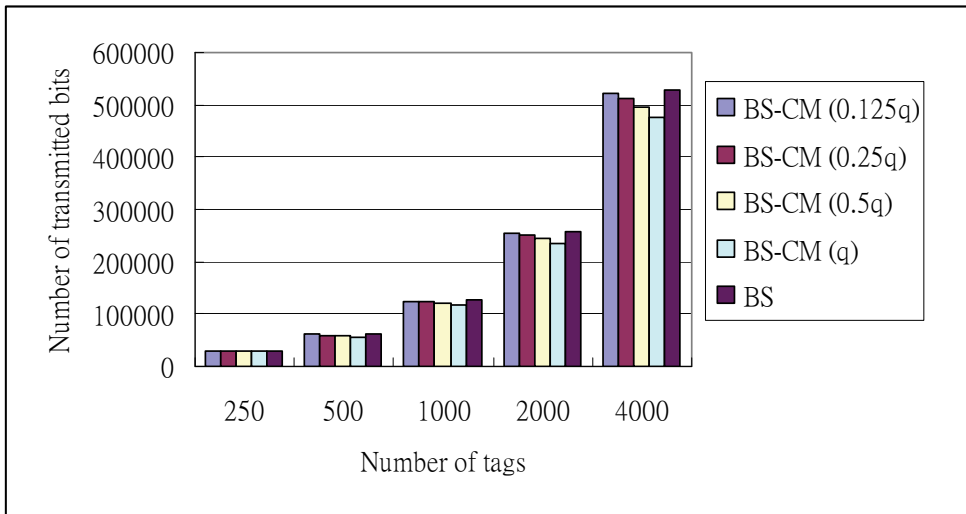


Fig. 6. The identification delay of BS protocol embedded with *CM*. Note that the length of ID is 96 bits.

In the following, we evaluate the performance of *k*-TAS scheme embedded with *CM* (0.5*q*) in terms of identification delay and communication overhead, where *q* is the number of current tags. From the simulation results in Fig. 7 and 8, we summarize four interesting findings. First of all, the efficiency improvement of embedding *CM* into a tree-based tag identification protocols such as *k*-TAS and BS is significant. In Fig.7, *CM* can improve system performance for *k*-TAS (*i*=2) scheme between 8% and 9.9% and for BS scheme between 15.3% and 18.3% in terms of reduction on total interrogation cycles. Secondly, we discover that the improvement ratio of *CM* depends on the structure of target tag identification tree, i.e. how many degrees each node has. With the increase of node degree, the improvement ratio is decreased. That is, *CM* can enhance more efficiency when the node degree in the target identification tree is smaller. From Fig.7, *CM* reduces identification delay for *k*-TAS (*i*=2) protocol between 8% and 9.9% and for *k*-TAS (*i*=3) between 2% and 4%, respectively. Since in BS each node possesses only two degrees, efficiency improvement is the most significant, i.e. between 15.3% and 18.3%. This phenomenon is because that *CM* always cuts a fixed number, i.e. 0.25*q*, of collided intermediate nodes (or cycles) in each identification session. Since these 0.25*q* collided nodes will actually appear in the abstract tree structure corresponded to BS, the performance improvement of BS-CM is better. As the nature of *k*-TAS is to efficiently reduce many collided nodes by utilizing a synchronized data sequence,

only some parts of these $0.25q$ collided nodes emerge in $k$-TAS. Therefore, efficiency improvement is comparatively smaller. In brief, if more collided nodes are contained in the several top layers of abstract tree structure when performing a tree based tag identification scheme, adopting $CM$ into such tree-based tag identification protocol can still gain some extra performance.
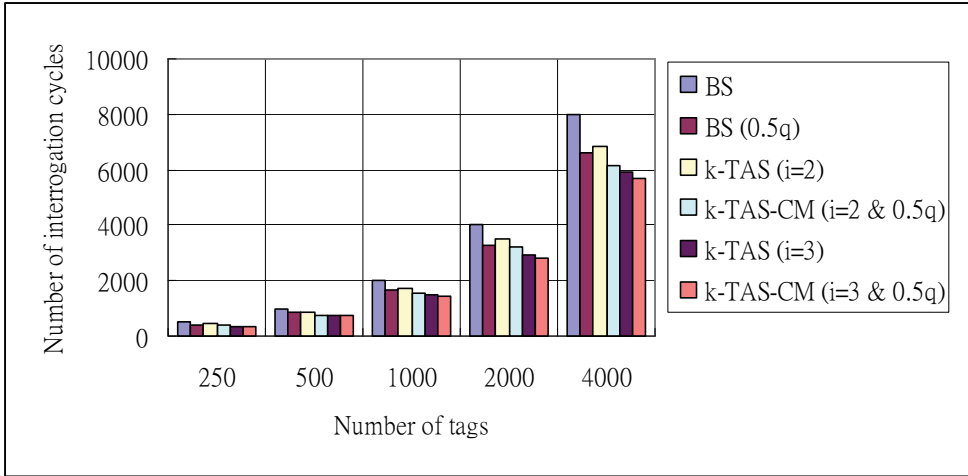


Fig. 7. The identification delay of $k$-TAS embedded with $CM$ in which the length of ID is 96 bits.
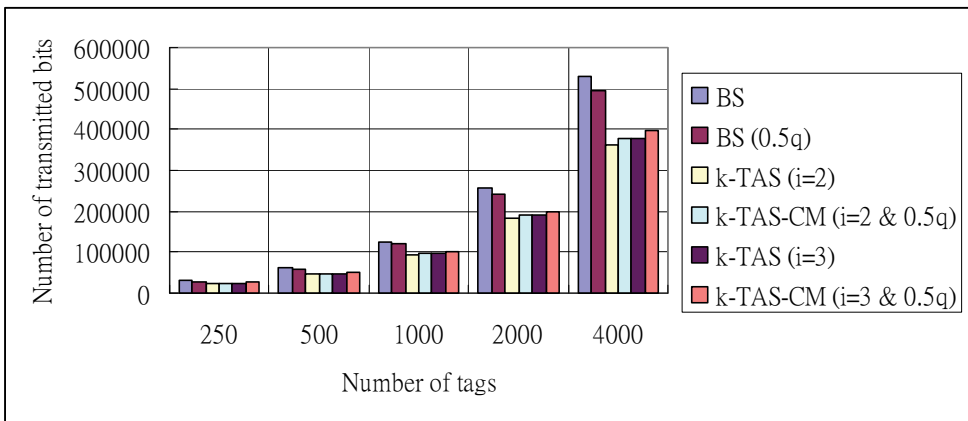


Fig. 8. The communication overhead of $k$-TAS embedded with $CM$ in which the length of ID is 96 bits.

Thirdly, Fig. 7 shows that the performance of BS ($0.5q$) is similar to the results in $k$-TAS ($i$=2), $k$-TAS-CM ($i$=2 & $0.5q$) and $k$-TAS ($i$=3). These results show performance obstacle in $k$-TAS scheme when many collided nodes appear at the top several layers of the corresponding abstract tree structure. If we intend to improve the performance of $k$-TAS, we should modify

the tag identification procedure corresponding to the top several layers instead of the middle layers or the bottom layers. We mark this open question as our future research direction. Fourthly, for the aspect of communication overhead, Fig. 8 demonstrates that overhead reduction is not significant when embedding *CM* into *k*-TAS. Protocol performance between pure *k*-TAS and *k*-TAS with *CM* is almost the same. This is because the reader in *k*-TAS with *CM* has to visit some idle nodes on the $h^{th}$ layer, where $2^h$ is the closest value to $0.5q$ and $q$ is the number of tags. In such idle nodes, some basic inquiry commands (bit strings) are required to be broadcast to all tags. This will increase the amount of transmitted bits. We infer that the total transmitted bits collected from all idle nodes at the $h^{th}$ layer is almost equal to bits collected from all collided nodes from the $0^{th}$ layer to the $(h-1)^{th}$ layer. However, in general performance improvement is significant in terms of the transmitted bits for existing binary tree-based tag identification protocols (such as BS and QT) to embed with *CM*.

## 3. Conclusion

Efficient collision resolution is critical for an RFID tag identification protocol. In this study, we present a cut-through mechanism to enhance the performance of current existing anti-collision protocols in which a significant portion of signal-collided query cycles can be removed from tag identification protocols such as QT, BS and *k*-TAS. In the future, we would like to investigate how to effectively remove signal-collided nodes in the top node levels of the abstract tree structure to pursue better protocol efficiency; especially in the category of *k*-ary tree based anti-collision schemes.

## 4. Reference

[1] 860 MHz – 930 MHz Class 1 Radio Frequency Identification Tag Radio Frequency and Logical Communication Interface Specification Candidate Recommdation Version 1.0.1, Auto-ID Center, 2002.

[2] J. I. Capettanakis, "Tree Algorithms for Packet Broadcast Channels," IEEE Trans. on Information Theory, vol.25, 1979, pp.505-515.

[3] T. Cheng and L. Jin, "Analysis and Simulation of RFID Anti-Collision Algorithms," in proc. of 9th International Conference on Advanced Communication Technology, 2007, pp.697-701.

[4] K. W. Chiang, C. Hua and T. S. Peter Yum, "Prefix-Randomized Query-Tree Protocol for RFID Systems," in proc. of IEEE International Conference on Communications, 2006, pp.1653-1657.

[5] Chamtac, C. Petrioli and J. Redi, "Energy-Conserving Access Protocols for Identification Networks," IEEE/ACM Trans. on Networking, vol.7, no.1, 1999, pp.51-59.

[6] J. S. Cho, J. D. Shin and S. K. Kim, "RFID Tag Anti-Collision Protocol: Query Tree with Reversed IDs," in proc. of 10th International Conference on Advanced Communication Technology, 2008, pp.225-230.

[7] H. S. Choi, J. R. Cha and J. H. Kim, "Fast Wireless Anti-Collision Algorithm in Ubiquitous ID System," in proc. of IEEE 60th Vehicular Technology Conference, 2004, pp.4589-4592.

[8] J. H. Choi, D. Lee and H. Lee, "Query Tree-based Reservation for Efficient RFID Tag Anti-Collision," IEEE Communications Letters, vol.11, no.1, 2007, pp.85-87.

[9] Draft Protocol Specification for a 900MHz Class 0 Radio Frequency Identification Tag, Auto-ID Center, 2003.

[10] EPCTM Radio-Frequency Identification Protocols Class 1 Generation-2 UHF RFID Protocol for Communication at 860-960 MHz Version 1.0.9, EPCGlobal Inc., Dec. 2005.

[11] K. Finkenzeller, RFID Handbook: Radio-Frequency Identification, Fundamentals and Applications, John Wiley & Sons Ltd, 1999.

[12] Information Technology-Radio Frequency Identification for Item Management-Part 6: Parameters for Air Interface Communications at 860 MHz to 960 MHz, Amendment 1: Extension with Type C and Update of Types A and B, ISO/IEC 18000-6:2004/Amd. 1:(E), Jun. 2006.

[13] D. K. Klair and K. W. Chin, "A Novel Anti-Collision Protocol for Energy Efficient Identification and Monitoring in RFID-enhanced WSNs," in proc. of 17th International Conference on Computer Communications and Networks, 2008, pp.1-8.

[14] Y. C. Lai and C. C. Lin, "Two Blocking Algorithms on Adaptive Binary Splitting: Single and Pair Resolutions for RFID Tag Identification," IEEE/ACM Trans. on Networking, vol.17, no.3, 2009, pp.962-975.

[15] C. Law, K. Lee and K. Y. Siu, "Efficient Memoryless Protocol for Tag Identification," in Proc. of the 4th International Workshop on Discrete Algorithm and Methods for Mobile Computing and Communication, 2000, pp.75-84.

[16] Y. Maguire and R. Pappu, "An Optimal Q-algorithm for the ISO 18000-6C RFID Protocol," IEEE Trans. on Automation Science and Engineering, vol.6, no.1, 2009, pp.16-24.

[17] J. Mosely and P. Humblet, "A Class of Efficient Contention Resolution Algorithms for Multiaccess Channels," IEEE Trans on Communication, vol.33, no.2, 1985, pp.145-151.

[18] J. Myung, W. Lee and T. K. Shih, "An Adaptive Memoryless Protocol for RFID Tag Collision Arbitration," IEEE Trans. on Multimedia, vol.8, 2006, pp.1096-1101.

[19] J. Myung, W. Lee, J. Srivastava and T. K. Shih, "Tag-Splitting: Adaptive Collision Arbitration Protocols for RFID Tag Identification," IEEE Trans. on Parallel and Distributed Systems, vol.18, no.6, 2007, pp.763-775.

[20] H. S. Ning, Y. Cong, Z. Q. Xu, T. Hong, J. C. Chao and Y. Zhang, "Performance Evaluation of RFID Anti-Collision Algorithm with FPGA Implementation," in proc. of 21st International Conference on Advanced Information Networking and Applications Workshops, 2007, pp.153-158.

[21] F. Schoute, "Dynamic Frame Length Aloha," IEEE Trans. on Communication, vol.31, no.4, 1983, pp.565-568.

[22] T. P. Wang, "Enhanced Binary Search with Cut-Through Operation for Anti-Collision in RFID Systems," IEEE Communications Letters, vol.10, no.4, 2006, pp.236-238.

[23] J. E. Wieselthier, A. Ephremides and L. A. Michaels, "An Exact Analysis and Performance Evaluation of Framed Aloha with Capture," IEEE Trans. on Communication, vol.37, no.2, 1989, pp.125-137.

[24] C. P. Wong and Q. Feng, "Grouping based Bit-Slot ALOHA Protocol for Tag Anti-Collision in RFID Systems," IEEE Communications Letters, vol.11, no.12, 2007, pp.946-948.

[25] K. H. Yeh, N. W. Lo and E. Winata, "An efficient tree-based tag identification protocol for RFID systems," in proc. of 22nd International Conference on Advanced Information Networking and Applications Workshops, 2008, pp.966-970.

[26] Chia-Chun Lin, A Tree-based Anti-collision Protocol for RFID Tag Identification in Supply Chain Network (master's thesis), National Taiwan Univ. of Science and Technology, Taipei, Taiwan, 2010.

# Design and Implementation of a Multi-protocol UHF RFID Tag Simulation Platform

Bo Zhang, Dongkai Yang and Qishan Zhang

*School of Electronics and Information Engineering, Beihang University*
*China*

## 1. Introduction

To raise the RFID UHF reader's performance, a test environment must be established. Using a lot of real tags to establish a test bed may induce some demerits, such as high resources costs and so on. So some institutions which engaged in RFID research developed some simulation systems for algorithm designing to provide reference information and technical support.

1.    TI Gen2 standard tag simulator

TI (Texas Instrument Company) which is the world's largest RFID reader and transponder producer,  develops a Gen2 standard tag simulator and provides to 5 main RFID reader and printer producers. This research is going on with the Gen2 standard product development in parallel, aiming to keep the compatibility between the transponder with the RFID reader and printer based on the UHF Gen2 standard. The tag simulator can generate 96bit codes and has other abilities defined by the EPC Gen2 protocol, is very helpful to the EPC Gen2 standard products development.

2.    RFID tag simulator by CISC

The main part of the CISC RFID tag simulator is a high power and multifilament FPGA chip. The sensor modules are connected to the simulation tools. These sensor modules play a very important role in many simulations and tests.

The tag simulator has an unprecedented creativity virtue that the user can determine the tag's parameters based on different applications. Tags simulated can be completely controlled by setting the parameters to determine the worst and best cases. The simulator can not only be used for general tests, but can also be used for the reader's test at the case of boundary defined. The real tags can't be used for this test because the boundary parameters can't be adjusted. So, CISC sensor modules and tag simulator can be used together to emulate the UHF RFID tag to verify and analysis the UHF RFID system.

CISC tag simulator can emulate at most 16 tags, each tag have a separate RF module, to be equivalent to 16 real tags.

3.    MATLAB used for RFID anti-collision simulation

Besides the tag simulators produced by the TI and CISC, there are several ways of RFID simulation reported, such as the way of using MATLAB to emulate the anti-collision algorithm, the way of using DSP and FPGA to establish a RFID system, and so on, and provide some reference values to the tag simulation design.

In this chapter, a tag simulator which can emulate the ISO/IEC 18000-6 type B and type C tags is introduced, and the parameters and numbers of the tags can be set also. It has the virtues such as:

1.    Better for research and improvement of the collision algorithm

ISO 18000-6 Type B and Type C protocols are all involved in the anti-collision algorithm, Type B protocol is based on the Binary tree principle, and the Type C protocol is based on the ALOHA principle. With the tag simulator, the two protocols can all be tested and analyzed in convenient.

2.    Emulates the actual situation

Signal's parameters (such as $t_{ari}$ tolerance, RTcal tolerance and TRcal tolerance the timing parameters; Reverse scattering signal intensity and the signal's accuracy) can be directly modified and set for some specific scenes to emulate the real situation. Compared with the software simulator, the simulator introduced in this chapter is more reliable.

3.    Compatible with various standards

The DSP and FPGA system both have the strong programmable and portable abilities, so the improvement and redevelopment based on it become more convenient. The tag simulator is compatible with various standards, has a higher reference value to consummate the standards.

## 2. RFID tag simulator hardware design

The general structure of the tag simulator is shown in Fig. 1, the whole system is divided into two major parts, the RF board PCB2 and the baseband board PCB1. The PCB2 board is mainly composed of antenna and RF module. And the PCB1 board is composed of DSP, FPGA, ADC, DAC and some other peripheral modules.
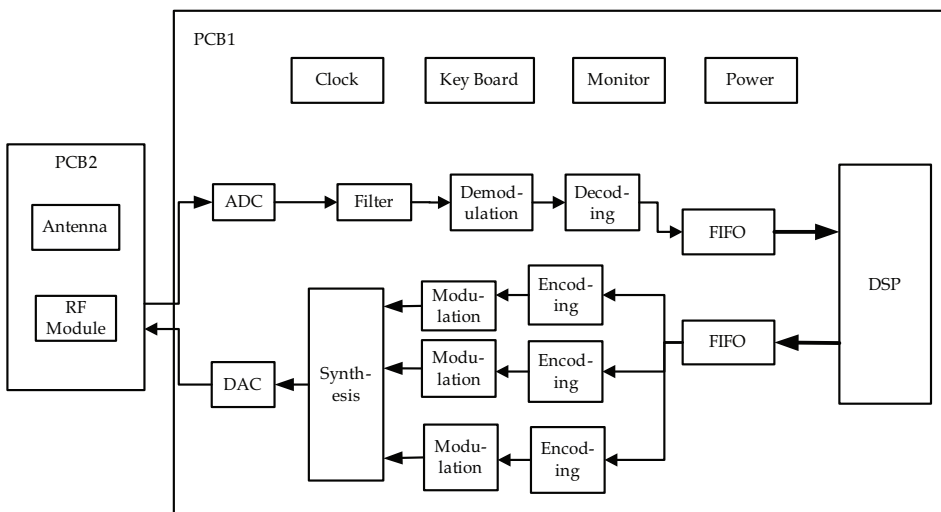


Fig. 1. General structure of the tag simulator

The RF module is mainly used for the RF and IF signals' frequency conversion. The baseband module is mainly used to realize the IF signals' demodulation, decoding and

radiation. The RF module and the IF module are connected via the ADC and DAC. In some process, it can be realized in digital way and is so called software radio technology. The virtue of digital frequency mixer is that it can avoid the discord between the I Q branches, but needs a high quality AD converter.

The DSP and FPGA chips are the cores of the baseband board, and this kind of system scheme is more and more prevalent and efficient now. The DSP chip can be used to realize the tag's protocol switching, state transferring, and data response. And the FPGA is mainly used in the signal's encoding, decoding, modulation, demodulation, data inspection, synthesis of multi channel and so on, and can also provide a stable clock, for its advantages in data processing speed.

### 2.1 Main hardware module
### 2.1.1 DSP and FPGA Interface

Connection between the DSP and FPGA includes the 32 bit data line evm_D[31:0], 20 bit address line evm_A[22:3], the DSP's general interface general_port[10:0], Serial Port 0 and Serial Port 2, control signal AWE, ARE, AOE and the chip select signal ACE2_n, ACE3_n, external interrupt signal EXT_INT[7:4], DSP's external input clock signal DSP_ECLKIN, DSP's external output clock signal TAECLKOUT2, and the DSP's reset signal evm_RESET.

The corresponding BEA mounts' level can be set as shown in Table 1.

| mounts | functional description |
|---|---|
| **BEA[19:18]** | Bootmode [1:0]<br>00 – No boot<br>01 − HPI boot<br>10 − EMIFB 8-bit ROM boot with default timings (default mode)<br>11 − Reserved |
| **BEA[17:16]** | EMIFA input clock select<br>Clock mode select for EMIFA (AECLKIN_SEL[1:0])<br>00 – AECLKIN (default mode)<br>01 − CPU/4 Clock Rate<br>10 − CPU/6 Clock Rate<br>11 − Reserved |
| **BEA[15:14]** | EMIFB input clock select<br>Clock mode select for EMIFB (BECLKIN_SEL[1:0])<br>00 – BECLKIN (default mode)<br>01 − CPU/4 Clock Rate<br>10 − CPU/6 Clock Rate<br>11 − Reserved |

Table 1. Settings of the DSP

### 2.1.2 ADC module

AD9433 is an Anolog to Digital converter chip produced by ADI company, it is a 12 bit sampling AD converter, and it also has the tracking/maintaining circuit on the chip. The conversion speed is as high as 125MSPS, and some optimize designs are made to adapt to the broadband and the dynamic performance of the high IF carrier system.

AD9433 needs a 5V analog power and a differential encoding clock to fit the chip's whole performance. In many applications, it does not require external benchmark and drive units. The digital output of the converter is compatible with the TTL/CMOS level. The proprietary circuit on chips can optimize the relationship between the spurious free dynamic range (SFDR) and the signal to noise and distortion ratio (SINAD) performance when input different frequency signals, the SFDR is up to 83dBc in the bandwidth from DC to 70MHz.

The chip has a 16 bit data line, each power mount of the chip is equipped with a filtering capacitance, the analog signal passing through the SMA interface is converted into digits by the AD converter after a 2 level transformer, a LVPECL difference clock and a matching network are adopted also.

### 2.1.3 DAC module

AD9777 is a 16bit DAC produced by ADI company, the input maximum data rate is 160MSPS (no interpolation) and 400MSPS (8 times interpolation). It has a optional interpolation ratio(2x/4x/8x) and a complex modulation. The direct IF pattern allows the synthetic intermediate frequency (IF) up to 70MHz.

The Designing of the DAC module is similar with the ADC module, but have several more serial peripheral interface configuration lines, and are connected to the FPGA, to configure the DAC's controlling memory.

### 2.1.4 User's interface module

The user's interface module is composed of keys and LED, the keys are input tools for users to choose the protocol (ISO 18000-6 Type B or Type C) and the tag numbers, LED is used to show the corresponding content, such as the status of collision, empty, successfully read, and so on.

### 2.2 FPGA circuit design
### 2.2.1 FPGA transmit link design

Parameters comparison of the two protocols in the transmit link are shown in table 2.

|  | Type B | Class 1 Gen2（Type C） |
|---|---|---|
| **Modulation Mode** | Bi-state Amplitude scattering modulation | ASK or PSK |
| **Encoding Mode** | FM0 | FM0 or Miller |
| **Data Rate** | 40 or 160kbit/s | FM0: 40 to 640kbit/s Miller: 5 to 320kbit/s |
| **Preamble** | 16 bit Scattering modulation sequence | depends on command |
| **Debugging Mode** | 16 bit CRC | CRC-16 |

Table 2. Parameters Comparison of the Tag -> Reader Link

The transmit link module of the FPGA includes FIFO, CRC check, FM0 and Miller encoding module, Digital Direct Frequency Synthesis (DDS), and Multi-channel synthesis module.

1.   Transmit link FIFO design

FIFO is a first in first out data buffer, the difference with the general register is that it has no external address lines, so it can be used in a very simple way. The data address can be established by the internal reading and writing pointer automatically, and it can not read or write into an appointed address settled by the address line as the general register.

The FIFO can be used as the data buffer in different clock domain, and it can be used in the different width data interface too. In this chapter, data transferred between the DSP and FIFO are all in 32bit pattern, as shown in Fig. 2, but in the FPGA, most data are in serial pattern, the FIFO is used here to match the data transferred between the FPGA and DSP.
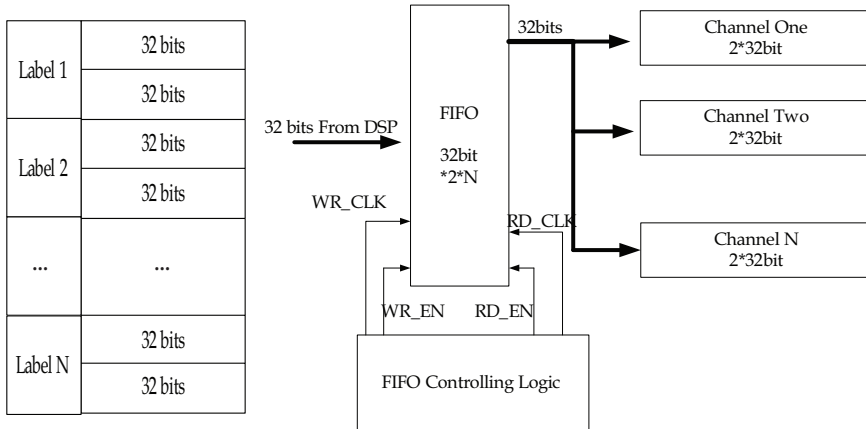
Fig. 2. Transmitting FIFO and the channel assignment principle

In the DSP commands, each tag needs to write the replied data into the FIFO, and the width of the data is 32bit, the width of the replied data is 64bit. But in Type C protocol, most data is not as wide as 32bit, only apart of it is used. For Type B protocol, the replied data's width is limited into 64bit, the CRC-16 data is also calculated and added in the FPGA. Each tag would write data into the FIFO in 2 times when replying, in the second time, if there is no additional data, 0x0000_0000 can be used to fulfill it.

When the assignments of writing the FIFO in all tags are finished, a signal is given to the FGPA, and when the FPGA gets the signal, it begins to assign the data for the FIFO. Each tag channel has a 64bit buffer. A synchronous clock (40kHz or 80kHz) is generated after the assignment, then it begins to process the data right shift, encoding and CRC generation and checking.

2.   CRC-5 and CRC-16 checking

The main purpose of the Cyclic Redundancy Check (CRC) is to use the linear encoding theory to generate an n bit CRC checking codes in a certain standard based on the k bit transmitting binary message sequence end, it is attached behind the message, and is made up to a (k+n) bit binary sequence. In the receiving end, the message sequence in a standard way with the CRC checking codes is checked to make sure the message is right or not.

3.   FM0 encoding module

FM0 is a kind of bi-phase space encoding method. The command from tag to reader begins with 2 preamble codes, which preamble code is chosen depends on the value of the TRext specified by the Query command.

The simulated waveform of the FM0 is shown in Fig. 3, including preamble code 1010v1 (v means the phase should be reversed but not), data_out is the output of serial data converted from the parallel data fm0_out[1..0].
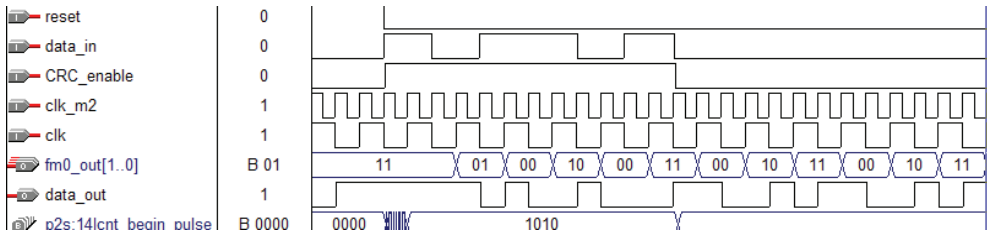


Fig. 3. Waveform of the FM0 encoding module

## 4. Miller Encoding module

In the ISO 18000-6 Type C protocol, the Miller Encoding performance is promoted by setting different sub_carrier wave frequency. By setting the 1X, 2X, 4X and 8X sub_carrier wave frequency, the reading scope, speed, and signal's bandwidth can be optimized, simulation in Fig. 4 shows the preamble code of the Miller Encoding, data_out is the output of serial data converted from the parallel data miller_out[1..0].
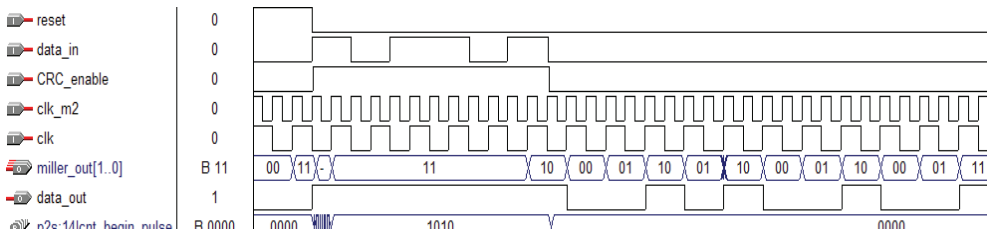


Fig. 4. Waveform of the Miller encoding module
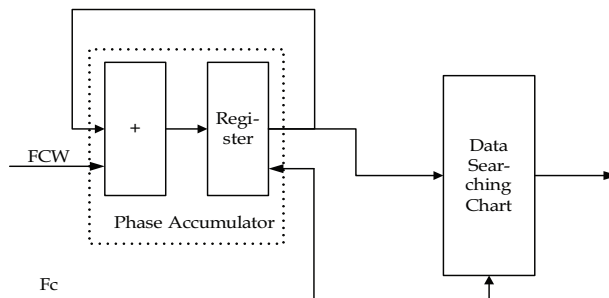


Fig. 5. Block Diagram of the DDS

## 5. DDS module

DDS is a new kind of frequency synthesizer invented in recent years, with applications of all digital large scale integration technology, it has some prominent characteristics such as low cost, high frequency resolution, fast switching, easy to be controlled and so on. And the

output signal's phase can be kept in continuous when frequency is switched into another one, and has low phase noise too. So it can be used to improve the reference frequency source's performance, and to be used to generate random waveform. The DDS module is composed of freqency controlling words (FCW), phase accumulator and data searching chart, as shown in Fig. 5.

6.    Multi-channel synthesizer module

Multi-channel synthesizer is used to combine each channel which is simulated as a tag to one output.

### 2.2.2 FPGA receive link design

The receive link module of the FPGA including Low Pass Filter (LPF), Demodulation Module, Receive link FIFO and PIE decoding module.

1.    Low Pass Filter

The design of Low Pass Filter (LPF) has many kinds of methods including Intellectual Property (IP) core from ALTERA with automatic COE parameters generation, or COE file data introduced from other sources.  MATLAB Filter Design Toolbox was used in this LPF design as there are many functions to simplify the design and give quantitative effect analysis.  Such parameters as filter type, order, sampling frequency and cutting frequency, amplitude attenuation could be configured during the design phase.  And the various properties are shown with the graph like Fig. 6.
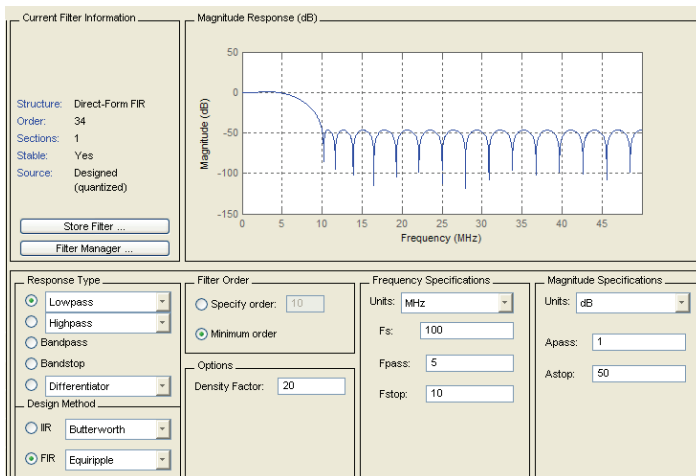


Fig. 6. Filter design interface

The proposed filter with valid specifications could be transferred from MATLAB to VHDL through assembling in FDA toolbox.

2.    Demodulation module

Tag received the radio signals from the reader with different carrier phase changing over time delay.  Orthogonal demodulation algorithm was used for ASK signal in the tag simulator [1].  Given the signal is expressed as equation (1),

$$S(t) = A\cos(\omega t) \tag{1}$$

The local in-phase and quadrature carrier are $\cos(\omega t + \varphi)$ and $\sin(\omega t + \varphi)$. $out\_I$ and $out\_Q$ are as follows after multiplier operation,

$$out\_I = S(t) * \cos(\omega t + \varphi) = \frac{A}{2}\left[\cos(2\omega t) + \cos(\varphi)\right] \tag{2}$$

$$out\_Q = S(t) * \sin(\omega t + \varphi) = \frac{A}{2}\left[\sin(2\omega t) + \sin(\varphi)\right] \tag{3}$$

The two signals will be remained phase related through this designed LPF and shown as in equation (4) (5),

$$filter\_I = \frac{A}{2}\cos(\varphi) \tag{4}$$

$$filter\_Q = \frac{A}{2}\sin(\varphi) \tag{5}$$

After squared and summed, we will get the constant $\dfrac{A^2}{4}$, i.e. correct signal could be got by judging this signal. ASK demodulation algorithm model is shown in Fig. 7.
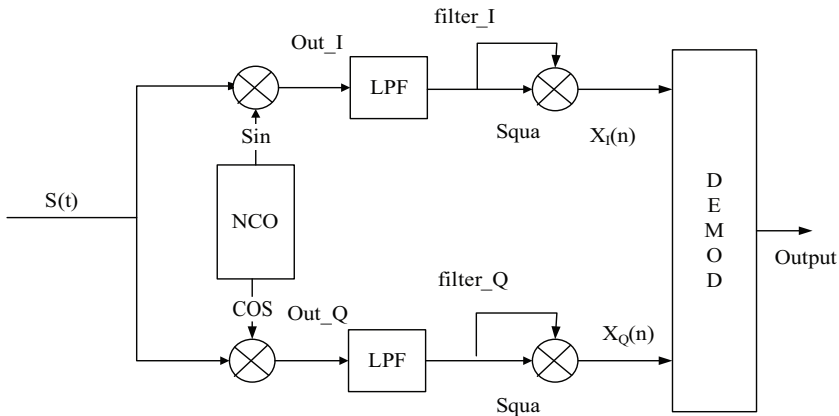


Fig. 7. ASK demodulation algorithm model

3.   Receive link FIFO

In receive link, the FIFO has no multiple channels. All the 32bit data of one word would be written into FIFO in order. As the command length is no more than $32 \times 5 = 160 bits$, FIFO depth is set to be 6 and the data are expressed by $data[0] - data[5]$. FIFO architecture is described in Fig. 8.

FIFO control module select PIE decode or Manchester decode to write into FIFO, where $data[0]$ stores the current protocol (i.e. Type B or C), tag number and some operation parameters. Several unoccupied bit in $data[0]$ are reserved for extension, whereas $data[1] - data[5]$ are used for command data.
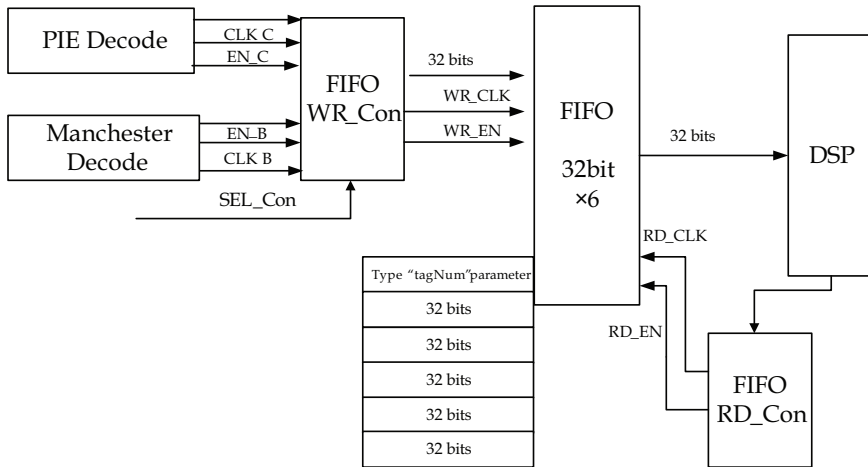
Fig. 8. Receive link FIFO design

After FIFO was written, external interrupt signal would be sent to DSP for specific command operation and state transit.

4.    PIE decoding module

Pulse Interval Encode (PIE) distinguish 0 and 1 by different pulse interval, with one phase transit in the middle of any symbol. It has clock information to maintain better data synchronization and robust transmission under wireless environment.

Given $Tari = 12.5us$, length of 0 is $1Tari$ and length of 1 is $2Tari$. Detect CLOCK could be selected as follows,

$$f = \frac{1}{12.5} \times 1000 \times 2KHz = 160KHz \tag{6}$$

Pre-amble from reader to tag is shown as in Fig. 9.
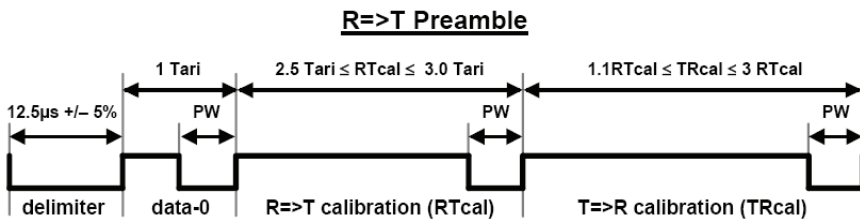


Fig. 9. Preamble for PIE

When one data, i.e. pulse arrives at the tag, its width was compared with the reference (half of the sum of "1" and "0" width). If the pulse width is larger than reference width, when the received data is "1", otherwise it is "0".

To make the two protocols, i.e. Type B and C share the same architecture FIFO, the data frame is designed as follows,

1st 32bit are protocol control and tags number;
2nd and 3rd 32 bit are command data;
And the last 3*32bit are reserved for backup.

## 3. Software design

### 3.1 Architecture

In the proposed tag simulator, the DSP exchange data only with FPGA, where FPGA chipset completes the protocol detection, tag number detection, however, quick command response, protocol switch, state transition, data feedback are finished by the DSP chipset. The whole simulator software workflow is shown as in Fig. 10.
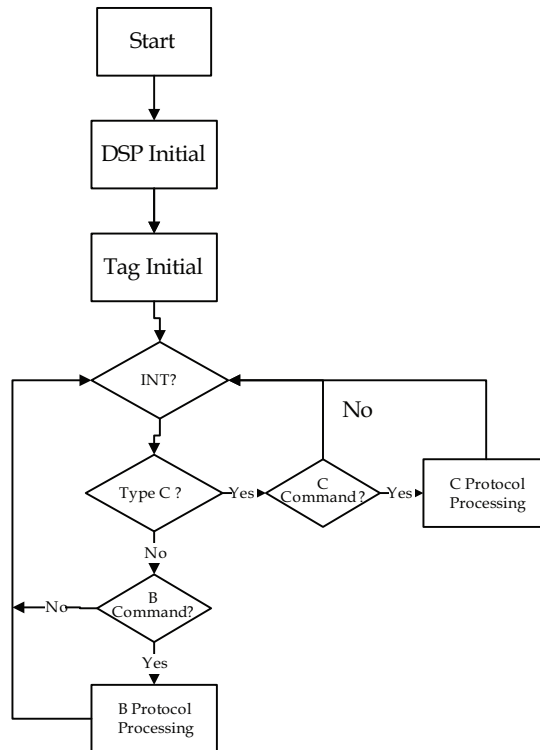
Fig. 10. Protocol processing workflow

### 3.2 Initialization of DSP

The DSP chipset has many peripherals and various registers, whose manually configuration will be complicated. Chip Support Library (CSL) function could be used to conveniently access DSP register and hardware resources to improve the development efficiently, where CSL_init () function is for loading and initializing these libraries. And PER_config () is mainly for configuration of given parameters,

PER_config([handle], *config Structure)

1.   General purpose Input/Output

There are sixteen pins GPIO[15:0] to be set Input or Output. As Output, it could be used to control its driven state by writing inner register, while as input it could be used to detect input state by reading inner register.

Here, GPIO[11:9] are output for DSP to notice FPGA that all these tags response, and finish writing FIFO. FPGA could allocate FIFO data to each tag channel for FM0, Miller encoding, modulation and synthesizer. GPIO[7:4] is multiple used as EXT_INT [7:4], i.e. external interrupt, besides general purpose I/O.

2.   External memory interface A/B

This simulator makes use of TMS320C6416 from TEXAS INSTRUMENT, which has EMIFA and EMIFB. EMIFA has 64pin memory bus with four spaces ACE0-ACE3 separately configurable and could be connected with SRAM, ROM or SDRAM. EMIFB has 16pin memory bus with BCE0-BCE3 four spaces. Both A and B have one external clock and two internal clock, CLK/4 and CLK/6.

3.   Interrupt register

Interrupt is C6416's main work mode to control the peripheral device by executing the interrupt service routine. All the interrupt have priority level used by central processor to select. The main interrupt type is reset, NMI (non-mask interrupt) and mask interrupt, i.e. INT4-INT15.

- Reset interrupt

  It is the highest priority in the DSP to halt the processor's work and return to one known state. There are ten clock cycles before this interrupt signal change from valid low level into high level to guarantee successful configuration. The reset operation stops all the executed command and all these registers returns to the default state. In addition, it is not affected by transition command.

- Non –mask interrupt (NMI)

  It has one enable bit set to 1 for NMI work, which warns CPU the serious hardware interrupt.

- INT4-INT15

  These 12 interrupts are mask connecting to the peripheral, and they could also be controlled through software or made to be unused. The processor replies INT4-INT15 only when the following conditions are well met:

  a) Interrupt Flag=1
  b) No higher interrupts occur
  c) Enabler bit =1
  d) Global interrupt enabler bit=1

## 3.3 Tag initialization

Each tag in the working environment should be configured as known state including its register and memory through a loop process. For Type B, state register, random number register and 64bit ID are to be set, while for Type C, counter, Handle are also to be set besides what is similar as Type B.

## 3.4 Interrupt response

In the tag simulator, FPGA chipset get the command data and write the protocol type, tag number into FIFO, INT4 is set to 1 so that DSP call interrupt void c_extint4() to response.

All the command data in Type B are 8 bit, and if-else sentence is used to inquiry one by one. Flag_B is set to 1 if the command is coming.

However, in Type C there are many commands with less than 8 bit. They are stored in one byte from the most significant bit (MSB). And the Flag_c is set to 1 if the command is coming whatever it has 2 bit, 4 bit or 8 bit.

### 3.5 State transition for different protocol

Both Type B and Type C have the same process architecture for the state transition, where current status and the coming new command with parameters are response to feedback new data and transit into a new state. For example, ID state in Type B is processed as the following routine.

```
case state_b_ID:// unselect ->state_b_ready
   switch(the_com_typeb.COMMAND)
   {
   case bcmd_FAIL:  //for FAIL Command
      if (mytag_b[i].count != 0)
      {
         mytag_b[i].count++; // Not zero, plus 1
      }
      else //random Number 0 or 1
      {
         mytag_b[i].count=random_counter_gen();//give random number
         if (mytag_b[i].count==0)
         {
            Write_FIFO(mytag_b[i].TID[0]);//reply the TID
            Write_FIFO(mytag_b[i].TID[1]);
         }
      }
      mytag_b[i].state=state_b_ID; //Next state
      break;
   case bcmd_SUCCESS: // SUCCESS command
      mytag_b[i].count--; //minus 1
      if (mytag_b[i].count==0)
      {
         Write_FIFO(mytag_b[i].TID[0]); // reply the TID
         Write_FIFO(mytag_b[i].TID[1]);
      }
      mytag_b[i].state=state_b_ID;  //Next state
      break;
```

## 4. Experiment result

The main circuit board for tag simulator is shown as in Fig. 11.

SignalTap II in Quartus II is a practical tool to analyze the signal state by collecting internal node or I/O pins signal. CCS is used for DSP to compile, load and debug the program with step by step, register result tracking and set breakpoint etc.

In the FPGA chipset, FIFO get the DSP written data and allocate to each transmit link. At the same time, FIFO_buffer could know how many tags response based on the times reading FIFO and record this value. Signal synthesizer module gives the combined signal of multiple tags shown as in Fig. 12 in SignalTap II, i.e. two tags.



Fig. 11. Tag simulator main circuit board
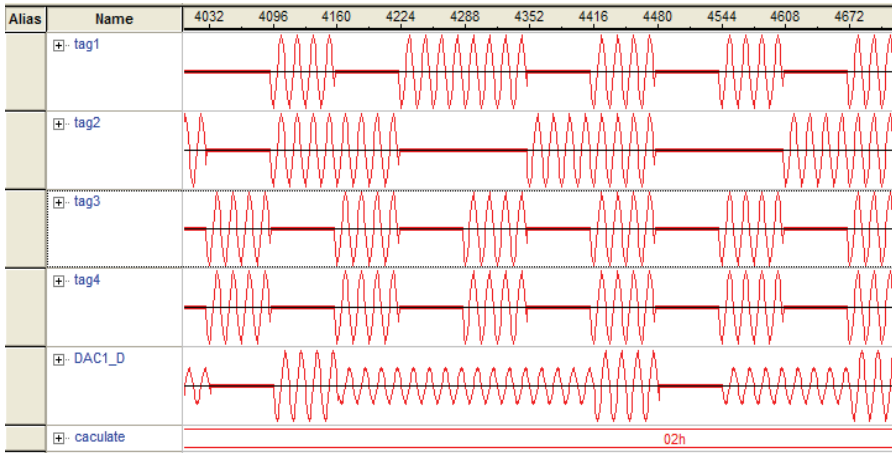


Fig. 12. Two tags synthesizer signal

If single tag returns data, the synthesizer signal will be tag1. When there are two tags response simultaneously, both tag3 and tag4 have no data and enencoding a series of "01".

If only one of the two tags has modulation data, then the synthesizer signal is half of the original magnitude; If both the two tags are 0, final signal is also 0 as the combined output to the reader.

## 5. Summary

In this chapter, the UHF RFID tag simulator is designed for the anti-collision algorithm study and simulation, and even the application system architecture design. The key technologies including the protocol analysis, the hardware design, software design, debug and simulation, practical test result are given as a whole.

The traditional software radio method is adopted, that is, the FPGA and DSP chipset are selected as the main components to work as tag simulator. Both Type B and Type C protocol are implemented, and the signal synthesize is given for more than one tag. The circuit design in FPGA chipset and the work flow in DSP chipset are well introduced, such as the transmission link, receive link, the low pass filter module, digital orthogonal demodulation etc. The work mode based on the interrupt is also given in this Chapter. And finally the test result is shown as verification of the proposed tag simulator.

## 6. Reference

Zhang Yang, Wang Hui(2008). Design and Simulation of FIR Digital Filter Based on MATLAB and Quartus II. *Electronic Engineering*, Vol.34, No.8, pp.25-27 ,ISSN 1006-7787.

YUAN Jie,ZHAO Zhi-jin,ZHANG Fu-hong (2008). Design of Modem of RFID Based on FPGA. *Chinese Journal of Electron Devices*, Vol.31, No.5, pp. 1635-1638, ISSN 1005-9490

Shi Jingzhuo, Xu Meiyu, Xu Dianguo (2006). Manchester Encoder and Decoder Based on CPLD. *Electrotechnical Application*, Vol.25, No.5, pp.62-64, ISSN 1672-9560

TI Company(2004). TMS320C6000 DSP General-Purpose Input/output (GPIO) Reference Guide[J]. Literature Number: SPRU584A

TI Company(2003). TMS320C6000 Chip Support Library API Reference Guide. Literature Number: SPRU401

TI Company(2001). TMS320C6000 Peripherals Reference Guide. Literature Number: SPRU190